Contactless Excitation for Electric Machines: High Temperature Superconducting Flux Pumps

Zezhao Wen

School of Engineering

The University of Edinburgh

This dissertation is submitted for the degree of

Doctor of Philosophy

2022

Declaration

1) I declare that this thesis has been composed solely by myself and that it has not been submitted, in whole or in part, in any previous application for a degree. Except where states otherwise by reference or acknowledgment, the work presented is entirely my own.

2) I confirm that this thesis presented for the degree of PhD in Energy System, has
   - i) been composed entirely by myself
   - ii) been solely the result of my own work
   - iii) not been submitted for any other degree or professional qualification.

3) I declare that this thesis was composed by myself, that the work contained herein is my own except where explicitly stated otherwise in the text, and that this work has not been submitted for any other degree or professional qualification except as specified. Parts of this work have been published in the work stated in the list of publications.

Abstract

With the intensification of global warming and climate change, the pace of transformation to a neutral-emission society is accelerating. In various sectors, electrification has become the absolute tendency to promote such a movement, where electric machines play an important role in the current power generation system. It is widely convinced that electric machines with very high power density are essential for future applications, which, however, can be hardly achieved by conventional technologies. Owing to the maturation of the second generation (2G) high temperature superconducting (HTS) technologies, it has been recognized that superconducting machine could be a competitive candidate to realize the vision.

One significant obstacle that hinders the implementation of superconducting machines is how to provide the required magnetic fields, or in other words, how to energise them appropriately. Conventional direct injection is not suitable for HTS machines, because the current leads would bridge ambident temperature to the cryogenic environment, which can impose considerable heat load on the system and increase the operational cost. Thus, an efficient energisation method is demanded by HTS machines. As an emerging technology that can accumulate substantial flux in a closed loop without any physical contact, HTS flux pumps have been proposed as a promising solution.

Among the existing developed HTS flux pumps, rotary HTS flux pumps, or so-called HTS dynamo, can output non-zero time-averaged DC voltage and charge the rest of the circuit if a closed loop has been formed. This type of flux pump is often employed together with HTS coils, where the HTS coils can potentially work in the persistent current mode, and act like electromagnets with a considerable magnetic field, having a wide range of applications in industry. The output characteristics of rotary HTS flux pumps have been extensively explored through experiments and finite element method (FEM) simulations, yet the work on constructing statistical models as an alternative approach to capture key characteristics has not been studied. In this thesis, a 2D FEM program has been developed to model the operation of rotary HTS flux pumps and evaluate the effects of different factors on the output voltage through parameter sweeping and analysis of variance. Typical design considerations,

including the operating frequency, air gap, HTS tape width, and remanent flux density have been investigated, in particular, the bilateral effect of HTS tape width has been discovered and explained by looking at the averaged integration of the electric field over the HTS tape. Based on the data obtained from various simulations, regression analysis has been conducted through a collection of machine learning methods. It has been demonstrated that the output voltage of a rotary HTS flux pump can be obtained promptly with satisfactory accuracy via Gaussian process regression, aiming to provide a novel approach for future research and a powerful design tool for industrial applications using rotary HTS flux pumps.

To enhance the applicability of the proposed statistical models, an updated FEM program has been built to take more parameters into account. The newly added parameters, namely the rotor radius and the width of permanent magnet, together with formerly included ones, should have covered all the key design parameters for a rotary HTS flux pump. Based on data collected from the FEM model, a well-trained semi-deep neural network (DNN) model with a back-propagation algorithm has been put forward and validated. The proposed DNN model is capable of quantifying the output voltage of a rotary HTS flux pump instantly with an overall accuracy of 98% with respect to the simulated values with all design parameters explicitly specified. The model possesses a powerful ability to characterize the output behaviour of rotary HTS flux pumps by integrating all design parameters, and the output characteristics of rotary HTS flux pumps have been successfully demonstrated and visualized using this model. Compared to conventional time-consuming FEM-based numerical models, the proposed DNN model has the advantages of fast learning, accurate computation, as well as strong programmability. Therefore, the DNN model can greatly facilitate the design and optimization process for rotary HTS flux pumps. An executable application has been developed accordingly based on the DNN model, which is believed to provide a useful tool for learners and designers of rotary HTS flux pumps.

A new variant inspired by the working principles of rotary HTS flux pumps has been proposed and termed as stationary wave HTS flux pumps. The superiority of this type is that it has a simple structure without any moving components, and it utilises a controllable current-driven electromagnet to provide the required magnetic field. It has been demonstrated that the origin of the output voltage is determined by the asymmetric distribution of the dynamic resistance in the HTS tape, for which the electromagnet must be placed at such a position that its central line is not aligned with that of the HTS tape. A numerical model has been built to simulate the operation of a stationary wave HTS flux pump, based on which the output characteristics and dynamic resistance against various parameters have been investigated. Besides, accurate and reliable statistical models have been proposed to predict the open circuit voltage and effective dynamic resistance by adapting the previously developed machine learning techniques.

The work presented in this PhD thesis can bring more insight into HTS flux pumps as an emerging promising contactless energisation technology, and the proposed statistical models can be particularly useful for the design and optimization of such devices.

Lay Summary

The increasingly acute climate change has prompted the urgency of seeking clean and efficient energy, in order to transfer human society into a more environmental-friendly and sustainable mode. One commonly recognized mainstream trend for future energy usage is that fossil fuels should be replaced by electricity, wherever possible. However, traditional electric machines have been proven not suitable for providing the high power density, i.e. high power density with light weight and compact size, required in some dominant industrial sectors, such as aviation propulsion systems and large-scale wind turbines. As an alternative, high temperature superconducting (HTS) electric machines were believed to be a competitive solution, owing to their superior capabilities of maintaining high power density and low loss.

Energising the HTS coils for an HTS electric machine has been a critical concern, because the energy injection (conventionally by current leads) can impose a heavy heat load on the cryogenic system, and hence result in significant additional operation costs. Aiming to address these challenges, HTS flux pumps, which can controllably accumulate magnetic flux in a closed loop without physical connections, have been proposed as a promising excitation system for HTS electric machines.

In this thesis, a critical review of the technology of HTS flux pumps has been presented in the beginning, which introduced a variety of HTS flux pumps in detail. The focus was then put on the rotary HTS flux pump that utilises rotating a permanent magnet to induce a voltage in the HTS tape, from where the output characteristics and the influences of different parameters have been analysed. In addition, artificial intelligence techniques have been innovatively applied and demonstrated to predict the output voltage of a rotary HTS flux pump in a fast and accurate manner. Based on that, an executable application has been developed and validated, which can substitute for complicated and time-consuming experimental tests and numerical simulations. Such an application can serve as a powerful design tool to facilitate the design and optimisation of rotary HTS flux pumps.

Different from the rotary HTS flux pumps, a novel stationary wave HTS flux pump that employs no moving components has been proposed. The effectiveness of such an HTS flux

pump has been verified, and its output characteristics have also been investigated. Besides, the previously implemented artificial intelligence techniques have been successfully reapplied to construct statistical models for predicting the output voltage and the effective dynamic resistance of the newly proposed stationary wave HTS flux pumps. Hence, it has been further strengthened that the artificial intelligence-based approaches demonstrated in this thesis were highly extendable to a wide range of practical applications.

In a word, this thesis contains original and inspirational work associated with the design and operation of HTS flux pumps. Therefore, this work is helpful for bringing a deeper insight into this emerging technology for future development.

Acknowledgement

I would like to express my warmest gratitude to my supervisor Prof. Markus Mueller, who offered me the original concept of this project and considerable guidance throughout the research. It is his professional expertise and cordial solicitude as well as selfless support that helped me tackle the difficulties that occurred in my PhD studies, allowing me to pursue unlimited possibilities. This project can be hardly accomplished without him, and it has been my great honour to work with him.

I sincerely appreciate the advice, cooperation, and other forms of help that I have received from Dr. Chris Bumby and Dr. Ratu Mataria at the Victoria University of Wellington, Dr. Mengyuan Tian and Dr. Guoliang He at the University of Cambridge and Prof. Francesco Grilli at the Karlsruhe Institute of Technology. I am also grateful to my colleagues at the University of Edinburgh, in no specific order, Dr. Kevin Kalis, Dr. Giorgos Skarmoutsos, Dr. Joe Burchell, and Dr. Konstantions Gyftakis, working alongside them was truly inspiring and enjoyable.

In particular, I shall acknowledge Dr. Hongye Zhang at the University of Manchester. Zhang has not only always been generous to share his brilliant ideas and proficient skills, but also provide helpful suggestions and kind encouragement for me, which contributes significantly to the conduction of this project.

I do, if entitled still, wish to thank Ms. Wei and Ms. Cao, respectively, for their affectionate company at different times of the journey of my PhD, who brought me love and hope when there was none, and that has meant a lot to me.

Though there are names of my family and dearest friends that have not been indicated in this statement, they are deeply rooted in the bottom of my heart. My gratitude towards them is well beyond any linguistic description -- they are the meaning of my existence.

List of Publications

- **Z. Wen**, H. Zhang and M. Mueller. "Sensitivity Analysis and Machine Learning Modelling for the Output Characteristics of Rotatory HTS Flux Pump." *Superconductor Science and Technology*, vol. 34, no. 12, 125019, 2021.

- **Z. Wen**, H. Zhang and M. Mueller. "High Temperature Superconducting Flux Pumps for Contactless Energization." *Crystals*., vol. 12, no. 6, p.766, 2022. (Invited)

- **Z. Wen**, H. Zhang, M. Tian, F. Grilli, and M. Mueller. "A Statistical Model for the Design of Rotary HTS flux pumps based on deep-learning neuron networks." *Superconductivity*., vol. 3, 100017, 2022.

- H. Zhang, **Z. Wen**, F. Grilli, K. Gyftakis, and M. Mueller. "Alternating current loss of superconductors applied to superconducting electrical machines." *Energies*., vol. 14, no. 8, p.2234, 2021.

Table of Contents

Acronyms and Abbreviations

2G	second generation
HTS	high temperature superconducting
FEM	finite element method
DNN	deep neural network
IEA	international world agency
IPCC	intergovernmental panel on climate change
HTSC	high temperature superconductors
CC	coated conductors
PM	permanent magnet
LTSC	low temperature superconductors
REBCO	bismuth strontium calcium copper oxide
MRI	magnetic resonance imagining
NMR	nuclear magnetic resonance
YBCO	yttrium barium copper oxide
LHC	large hardon collider
LTS	low temperature superconducting
MEMEP	minimum electromagnetic entropy production
IE	integral equation
VIE	volume integral equation
DPC	double pancake coil
HIA	homopolar inductor alternator
PID	proportion-integral-differential
VP	vector potential
SP	scalar potential
MLP	multi-layer perception
SVM	support vector machine
GPR	Gaussian process regression
DT	decision tree
KNN	k-nearest neighbour
NSE	Nash-Sutcliffe efficiency coefficient

RMSE	root mean square error
MAE	mean absolute error
MAPE	mean absolute percentage error
ANN	artificial neural network
SGD	stochastic gradient descent
Adam	adaptive moment estimation
L-BFGS	limited-memory Broyden-Fletcher-Goldfarb-Shanno
ReLU	rectified linear unit
MLE	maximum likelihood estimation
RBF	radial-basis function
MSE	mean squared error
F-MSE	Friedman-mean square error
GPU	graphics processing unit
CPU	central processing unit

List of Figures

List of Tables

Chapter 1

Introduction

1.1 Thesis background

With the worldwide advancement of urbanization and modernization, energy consumption has seen continuous growth, especially in the sector of industry and transport. According to the documentation (World Energy Balances 2022 [1]) of the International Energy Agency (IEA), the total final consumption by industry and transport both reached 120 million TJ, which has doubled since 1990. Under such a high level of energy consumption, the total CO_2 emissions have increased by 63.92% since 1990, which has become a dominant cause of global warming and climate change. For the past decade, the global mean sea level has increased 20 cm due to the temperature rise [2]. It was recommended by the Intergovernmental Panel on Climate Change (IPCC) that global warming should be limited below 1.5 ℃ to mitigate catastrophic climate change issues [3]. Therefore, it is of great importance that actions need to be taken to reduce anthropogenic emissions while maintaining the almost irreversibly increasing energy consumption required by the whole society.

On one hand, since currently about 5% of the anthropogenic climate change comes from global aviation and it is expected to continually increase [4], the sector set targets in 2001 of reducing CO_2 emissions by 75% and NO_x emissions by 90% by 2050 to reduce aviation emissions (Flight Path 2050) [5]. Replacing traditional fuel combustion engines with electrical propulsion systems is believed to be a promising method to meet these targets [6, 7]. In such scenarios, the propulsion motors require a very high power density, in the range of 20kW/kg to 40 kW/kg, to provide an equivalent thrust. However, it is very challenging to achieve this goal through conventional motor technologies. On the other hand, in 2021 wind electricity generation increased by a record 273 TWh, which was 45% higher growth than that achieved in 2020 and was the highest among all renewable power technologies [8]. Findings of IEA [8] have indicated that sustained capacity growth is required to get on track with the Net Zero Emissions by 2050 Scenario through the exploitation of wind energy. However, wind turbines with high capacity typically have an extremely bulky size and heavy weight, which can result in critical difficulties for manufacturing, assembling, and maintenance [9].

High temperature superconducting (HTS) technologies provide the possibility for satisfying those ambitious targets, and hence solving challenges. As a superior alternative, high temperature superconductors (HTSCs) possess a much higher current capacity than normal conductors, e.g., coppers, which can generate very strong magnetic fields that are not achievable for the same amount of normal conductors or even rare-earth permanent magnets. More importantly, HTSCs have practically zero DC resistance [10] under proper cryogenic environments, which is helpful for reducing the associated losses. As a result, HTSCs are promising for designing electric machines that not only have high power density with compact size, but also high capacity and efficiency.

Tremendous efforts have been put into the investigation of applying HTS technologies in electric machines. Concepts of bulk superconductors and stacks of HTS tapes, being able to trap high magnetic fields [11, 12], have been proposed by the research community, which can be potential candidates for field sources in electric machines. However, they can experience demagnetization and lack precise control during operation, in addition to the constraints of weight and size [13]. Thus, HTS coils enabled by the production of long-length superconducting coated conductors (CCs) with robust bending tolerance become a more competitive candidate.

To energise a coil, the traditional approach is direct injection, which directly injects currents into the coil via conductive current leads. Since HTSCs must be strictly operated in cryogenic environments, current leads can bring considerable heat loads because they bridge the ambient temperature with the cryogenic system. In the case of rotating coils, the direct injection can be more suffering, because the additional challenge of transferring large DC currents across a rotating joint has to be dealt with. These factors are critical drawbacks in HTS applications because they can result in significant additional capital and operational cost, whilst undermining the overall performance. Consequently, direct injection is not the most desirable option for energising HTS coils.

In response to the aforementioned issues, HTS flux pumps have drawn appealing attention. The most attractive advantage of this technology is that it can realize controllable energisation without any physical connection, by the utilization of peculiar properties of HTSCs. Owing to the contactless mechanism, HTS flux pumps can be applied to energise both static and rotating HTS coils. The operation of HTS flux pumps is a persistent and periodical process, which can effectively compensate the flux decay [14] presented in HTSCs. Currently, remarkable progress has been achieved in the investigation of HTS flux pumps, and a series of variants have been proposed. The various HTS flux pumps are different from each other, in terms of their structure, operation as well as underlying physics. One of the most typical types is the rotary HTS flux pump, which has a very simple structure and mainly consists of a permanent magnet (PM) and a piece of HTS tape. By rotating the PM, an effective DC voltage can be consistently induced across the HTS tape beneath it, which can then energise HTS coils if a closed loop is formed. This type of HTS flux pumps is particularly conspicuous for electric machines, since its rotating operation perfectly matches with electric machines, such as synchronous generators. Except for the HTS rotary HTS flux pumps, other types of HTS flux pumps have also seen substantial potentials in a wide range of applications.

Experimental tests and theoretical analyses have been conducted by worldwide researchers, some of whose excellent works have brought out inspiring findings. However, most previous work primarily focused on a specific aspect of HTS flux pumps. Considering the fact that HTS flux pump is a complicated system, it is of great necessity to investigate its characteristics more comprehensively, and further explore its mechanism. Moreover, existing studies of HTS flux pumps are majorly based on traditional research methods, including experiments and numerical models. These methods are useful for replicating and investigating key processes during the operation of such devices, but less efficient when it comes to the scenario of industrial design and optimisation. On one hand, arranging tests in a laboratory requires expensive HTS materials and strict experimental environments. On the other hand, numerical models are subjected to abundant professional knowledge that may not be guaranteed by designers. Besides, the simulation process to solve numerical models can be extremely time consuming, which is not preferable for realizing efficient design. Thus, it leads to the dominant research question of the thesis: how can we put forward alternatives to replacing the traditional methods, and then provide feasible solutions to facilitating the design and optimisation of HTS flux pump devices?

1.2 Contributions of the thesis

The most important aim of the thesis is to broaden the border of knowledge about HTS flux pumps and find practical solutions to facilitating the design and optimization of such devices, especially at the level of industrial applications. HTS flux pump is an emerging and promising technology, which has considerable prospects in the transformation to electrification and clean energy. Despite the remarkable efforts that have been put into the investigation of HTS flux pumps by worldwide researchers, there is yet more to be discovered. The main contributions of the thesis can be concluded as below:

- The thesis has presented a critical review of HTS flux pump, which summarized the most-up-to-date advances of this emerging technology, clarified the working mechanisms, and commonly adopted modelling approaches, presented objective analyses of the applicability of various HTS flux pumps, specified the primary challenges for implementing HTS flux pumps, and proposed useful suggestions for improvements.
- This thesis has investigated the output characteristics of rotary HTS flux pumps, where the focus was mainly put on how the open circuit voltage is influenced by a set of design parameters. Each parameter effect has been clearly demonstrated, and it has been found that the output voltage can be increased or decreased with the HTS tape width in certain situations. This discovery has implied that there should be an optimal tape width for the rotary HTS flux pump to achieve maximum output voltage.
- The novel stationary wave HTS flux pump has been put forward, which possesses simple structure as the rotary HTS flux pump but evades the rotating components. Numerical models have been built to simulate the operation of this type of flux pump, and also verify the effectiveness and explore the output characteristics.
- Artificial intelligence techniques have been innovatively introduced to model the output characteristics of rotary and stationary wave HTS flux pumps. Commonly used machine learning-based algorithms have been tested, and the feasibility of such a modelling approach has been confirmed by obtaining regression models that can accurately correlate the target outputs with a set of design parameters.

1.3 Outline of the thesis

Except for this introductory chapter, the main context of this thesis consists of seven chapters. A summary for each chapter is presented below.

Chapter 2 is a literature review, where the first few sections present the fundamental knowledge of superconductivity. After that, it briefly introduces the early flux pumps developed for low temperature superconductors (LTSCs) and explains the factors that motivate the evolution to HTS flux pumps. Then, it focuses on the travelling wave type flux pump, which is currently one of the most popular HTS flux pumps and provides detailed information for its underlying physics and modelling techniques. After that, another important category of HTS flux pumps that has attracted increasing research interest, named as switched transformer-rectifier flux pump, is described. A set of other variants of HTS flux pumps, such as the thermally actuated, electronic-switch-based and pulse-type HTS flux pumps, whose working principles can be readily understood in the scope of those introduced above, are also listed. Following on, all the existing HTS flux pump technologies are compared and summarized. Besides, the exploitation of HTS flux pumps in practical applications for various scenarios is elaborated. On the basis of the aforementioned contents, potential challenges are discussed, and recommendations are proposed for the future development of HTS flux pump technologies.

Chapter 3 pays particular attention to the HTS rotary flux pumps. In this chapter, a 2D ***T-A*** formulation-based numerical model is constructed to simulate the operation of a rotary HTS flux pump, which is validated by experimental results. It is pointed out that the field dependence of critical current density tends to increase the dynamic resistance for the HTS tape region beneath the PM, where the forward eddy current flows, and elimination of such dependence, e.g., assume a constant critical current density, will result in a smaller output voltage. Based on this numerical model, a comprehensive sensitivity analysis of the open circuit voltage is conducted. The individual effect of each parameter on the open circuit voltage is investigated, in which it is found that the superconductor width has a bilateral effect on the output voltage. Lastly, a new numerical model based on ***H-A*** formulation, which is different from the previously utilised ***T-A*** formulation-based model, is built to simulate the operation of a rotary HTS flux pump. Instead of approximating the HTS tape to a straight line without thickness in the ***T*-*A*** model, the multilayer structure of the HST tape, is considered in the ***H*-*A*** model. By doing so, the current interactions with different layers of the HTS tape can be reflected, and output characteristics of rotary HTS flux pumps at high frequencies are demonstrated.

Chapter 4 proves the feasibility of utilizing machine learning techniques to develop regression models as a substitution for numerical models, for the purpose of capturing key output characteristics. Considering the air gap, HTS tape width and remanent flux density of the PM as inputs, the best selected model achieved an average accuracy as high as 97%, with respect to the simulated values from numerical models. Furthermore, a semi-deep neural network model was successfully obtained, which can predict the output voltage of a rotary HTS flux pump with an average accuracy of nearly 98%, while additionally taking the operating frequency, rotor radius and width of the PM into account. Such a model allows fast tests on the open circuit voltage of a rotary HTS flux pump under different configurations, from where the optimal HTS tape width can be examined. In addition, the model can not only predict the output voltage given a set of design parameters, but also can inversely produce proper values for each design parameter by specifying the output voltage.

Chapter 5 proposes a novel HTS flux pump without involving any moving components. This concept of replacing the rotating PM with a controllable electromagnet is verified by simulation results from an ***H*-*A*** formulation-based numerical model. The origin of the output voltage is discussed, and the formation of the circulating currents within the HTS tape is revealed. The impact of each design parameter of a stationary wave HTS flux pump on its dynamic resistance, which is closely related to its output voltage, is investigated. Besides, the machine learning techniques adapted in last chapter are re-applied to search for statistical models that are capable of predicting the open circuit voltage and effective dynamic resistance of a stationary wave HTS flux pump, whose results are also presented.

Chapter 6 summarizes the key findings and outcomes achieved throughout the completion of this thesis. The limitations alongside some tasks conducted during the PhD project are discussed, and some hints for future work that can take a step on existing work to make further improvements are also presented.

Chapter 2

Literature Review

Superconductivity was first discovered in 1911 by Heike Kamerlingh Onnes at Leiden University [15], when he observed that the resistance of solid mercury abruptly disappeared at the temperature of 4.2 K. In following decades, a similar phenomenon has been found in a variety of other materials, which are referred as superconductors.

2.1 Fundamental properties of superconductivity

2.1.1 Zero DC resistance

For a superconductor transporting a pure DC current, without any external interference, no voltage will be generated within the superconductor. According to the basic definition of resistance given by Ohm's law as $R = V/I$, if the voltage equals to zero, the resistance must be zero consequently.

Due to the zero-resistance property, superconductors are able to maintain a current in the absence of a power supply. It has been experimentally demonstrated that currents in superconducting coils can persist for years without any detachable degradation. This persistent current is theoretically estimated to have a lifetime that can exceed the predicted lifetime of the universe [16]. In superconducting gravimeters [17, 18], where the measurement is performed by monitoring the levitation of a superconducting niobium sphere with a mass of 4 grams, it has been recorded currents injected in superconducting coils have lasted more than 26 years.

2.1.2 Meissner effect

In 1933 [19], Meissner and Ochsenfeld found that no magnetic fields can be detected inside a superconductor with the existence of applied fields and then discovered that superconductors can expel applied magnetic fields, which was termed as 'Meissner effect'. This remarkable discovery has widely broadened people's understanding of superconductivity and paved the way for many influential works. According to Lenz's law, when a conductor is exposed to a changing magnetic field, an electric current will be induced within the conductor to create an opposite magnetic field to attempt to maintain its original magnetic flux. Thus, arbitrary electric current can be induced to cancel the applied fields given the perfect conductivity of superconductors. However, the Meissner effect is distinct from this kind of diamagnetism. As illustrated in figure 2.1.1, if a superconductor is placed in a magnetic field before it enters the superconducting state, the penetrated magnetic flux will still be expelled when the superconductor is driven to its superconducting state. On the contrary, if considering the superconductor as a perfect conductor, the penetrated magnetic flux will remain the same. Hence, superconductors should not be simply considered as conventional conductors with perfect conductivity.

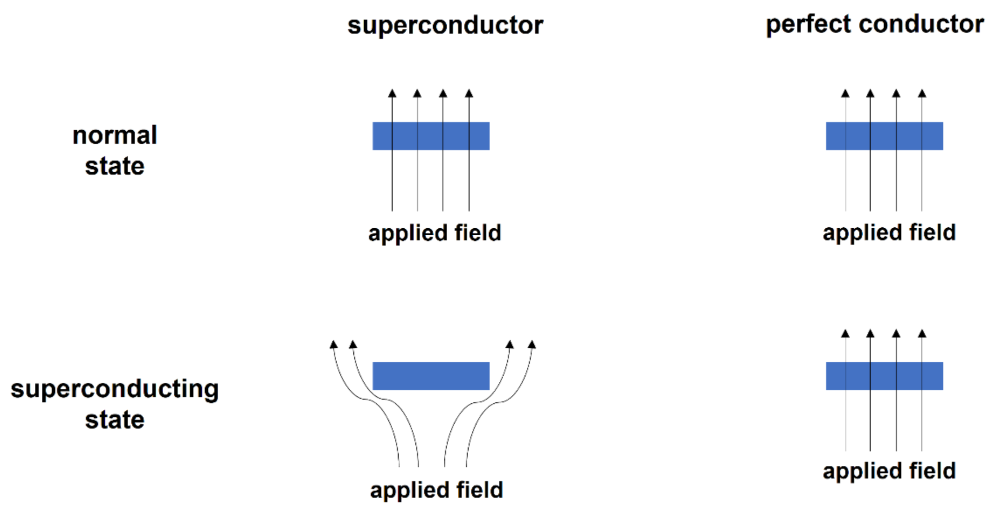

Figure 2.1.1. Illustration of Meissner effect by comparing the field variation for a superconductor and a perfect conductor under an external field.

2.1.3 Preconditions for superconductivity

For any superconducting materials, the characteristics of superconductivity can appear only if certain preconditions are satisfied, so that these materials can be maintained in the superconducting state. Unlike a normal conductor, where the electric current can be considered as a fluid of individual electrons, the electric fluid in a superconductor consists of bounded pairs of electrons, so-called Copper pairs [20]. According to quantum mechanics, there exists an energy gap ΔE in the energy spectrum of the Copper pairs flow. As long as the thermal energy of the lattice is smaller than ΔE, the fluid will not be scattered by the lattice [10]. However, the bounding force is caused by weak attractions between electrons from the exchange of phonons, so it is valuable to any thermal vibrations. Therefore, there is a maximum temperature for the superconductors to maintain superconductivity, which is known as the critical temperature T_c.

Even at a fixed temperature below the critical temperature, the applied magnetic field must not go beyond a certain point in order to let the superconductor remain superconducting. It is because the Gibbs free energy of the superconducting phase increases considerably with the magnetic field, whilst the free energy of the normal phase is relatively independent of the magnetic field [21]. That is to say, if one gradually increases the magnetic field applied to a superconductor in the superconducting state, the superconductor will end up losing its superconductivity and transiting to the normal state. The magnetic field at which point the phase transition occurs is known as the critical field H_c. Similarly, if the transport current that flows in a superconductor tends to induce a magnetic field greater than the critical field, the superconductor will also lose its superconductivity. This is also the reason why superconductors cannot deliver unlimited power even if they possess zero resistance. The maximum current that is allowed to flow in a superconductor while the superconductivity will not be terminated is known as the critical current I_c. In order to ensure a superconductor exhibits superconductivity, the temperature, magnetic field, and transport current must be kept below the critical values, as indicated in figure 2.1.2. It should be noted that the critical current is influenced by the mechanical strain, which may also be considered as a precondition. Breaking any of these conditions can lead the superconductor to quench, i.e., the materials lose their superconductivity and exhibit considerable resistance.

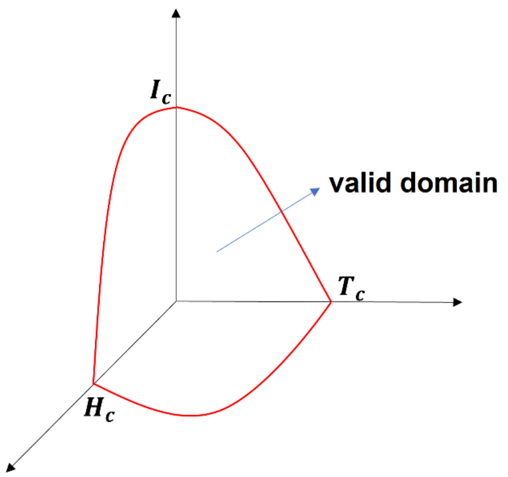

Figure 2.1.2. The valid domain for superconductors to exhibit superconductivity (enclosed by the red surface).

2.2 Classifications of superconductors

Since the first discovery of superconductivity in solid mercury, worldwide researchers have been continuously seeking for new materials that can superconduct under certain conditions and various superconductors have been reported over the past century-long period. Traditionally, superconductors can be classified into different categories based on their critical temperatures and characteristic behaviour against external magnetic fields, which are introduced below.

2.2.1 Low temperature superconductors & high temperature superconductors

Accompanied by the first record of superconductivity for solid mercury at the temperature of 4.2 K, a great number of materials were observed to establish superconductivity at similarly low temperatures, such as helium, lead and niobium were found to superconduct at 2.2K, 7K, 16K, respectively. Such low temperature puts costly requirements on the coolant to provide a proper cryogenic environment. As shown in figure 2.2.1, different classes of superconducting materials have been discovered over the last century, including the Bardeen-Cooper-Schrieffer (BCS) based, heavy-fermions-based, Cuprate, buckminsterfullerene-based, carbon-allotrope, iron-pnictogen-based, strontium-ruthenate, nickel-based. In general, it can be easily observed that these newly discovered materials have gradually increasing critical temperature. An important step in the development of superconductors took place in 1986 [22], when the metallic oxygen-deficient compounds in the La-Ba-Cu-O system, fabricated by Mueller and Bednorz, were found to have a transition temperature at 30 K. The same series of materials has been discovered with a transition temperature at 100 K level. In order to distinguish the newly discovered superconducting materials, which have much higher critical current than the ones discovered at the beginning, a standard us required to classify these superconductors into different categories based on their critical temperature. By academic convention, any superconducting materials with a critical temperature above 30 K are termed as HTSCs, otherwise are termed as LTSCs. Due to the wide availability and low cost of liquid nitrogen coolant (boiling point at 77K, saturation vapor pressure), HTSCs with T_c greater than 77 K have seen continuously increasing interests in the past decades. Commercial specifications for some of the typical superconductors are represented in table 2.2.1.

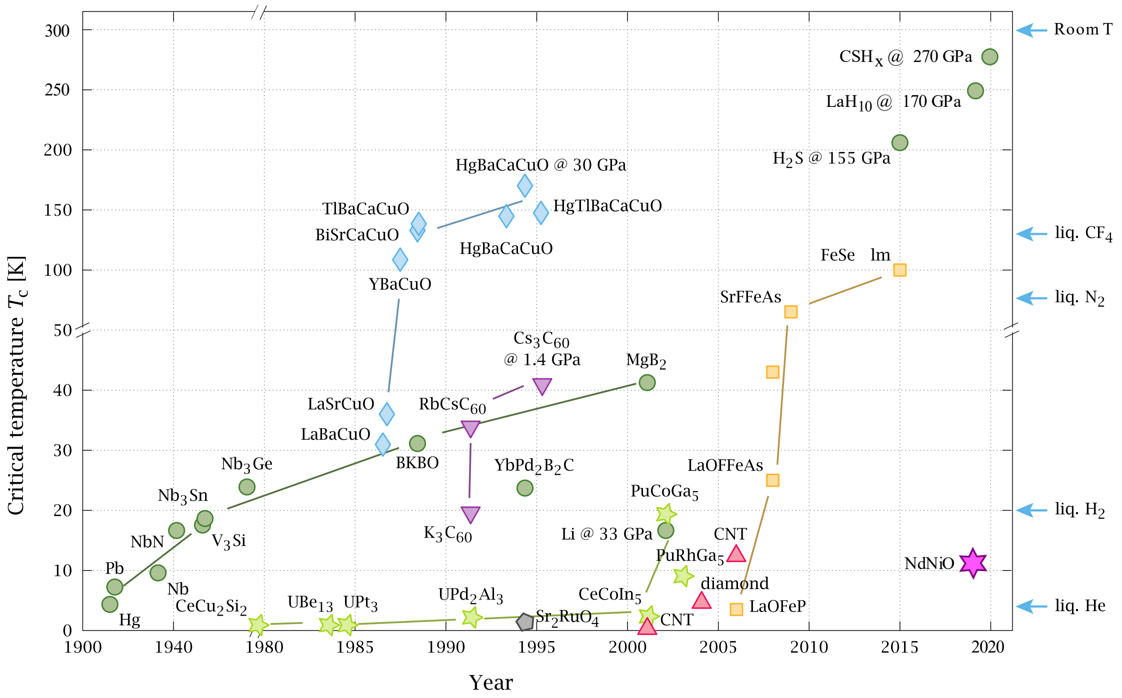

Figure 2.2.1. Timeline of superconducting materials. Colours represent different classes of materials: BSC (dark green circle), heavy-fermions-based (light green star), Cuprate (blue diamond), buckminsterfullerene-based (purple inverted triangle), carbon-allotrope (red triangle), iron-pnictogen-based (orange square), strontium-ruthenate (grey pentagon), nickel-based (pink six-point star). Adapted from [23].

Table 2.2.1. Reported commercial superconductor specifications. Data are from [24].

Material	Unit Cost	T_c	I_{c0}
REBCO (12mm-wdith)	~227 $/(kA · m)	up to 119K	400-600 A (SuperPower, at 77 K)
REBCO (4mm-width)	~230 $/(kA · m)	up to 119K	min. 130A (AMSC, at 77K)
Bi-2223	17.4 $/(kA · m)	110K	~170A-~200A (SEI, at 77 K)
MgB_2	20 $/(kA · m)	39K	~157 A (Ga(30), at 4.2 K)
NbTi	0.8 $/(kA · m)	9.5K	up to 3kA (SuperCon, at 4.2K)

2.2.2 Type I & type II superconductors

In addition to the critical temperature T_c that categorizes superconductors as HTSCs and LTSCs, superconducting materials can be identified as type I or type II superconductors based on their reactions to external magnetic fields. As discussed in section 2.1.3, the magnetic field applied to a superconductor should not exceed the critical field H_c, otherwise the superconductor will transit to the normal state. Those superconductors that lose superconductivity completely once the applied magnetic field goes beyond H_c are defined as type I superconductors. However, some superconducting materials will not experience an instant elimination of superconductivity with the increase of external magnetic fields, instead, they will gradually transit from the superconducting state to the normal state. As shown in figure 2.2.2 (a), for type I superconductors, they can only be either in the superconducting state or the normal state (ignoring the intermediate state that only subjects to specific conditions), and thus their internal magnetic fields show a discontinuously sudden change at the moment when the state transition occurs. Figure 2.2.2 (b) illustrates that type II superconductors tend to enter the mixed state if the magnetic field reaches the first critical field H_{c1}, where some of the flux lines can penetrate the superconductors. Equivalently, the superconductors do not expel all flux lines, meaning that the Meissner effect still holds partially. If the magnetic field increases further and exceeds the second critical field H_{c2}, the type II superconductors will be fully penetrated by flux lines, as the same as the normal state for type I superconductors. As a result, the internal fields in a type II superconductor will not see a step change but a relatively smooth ramp.

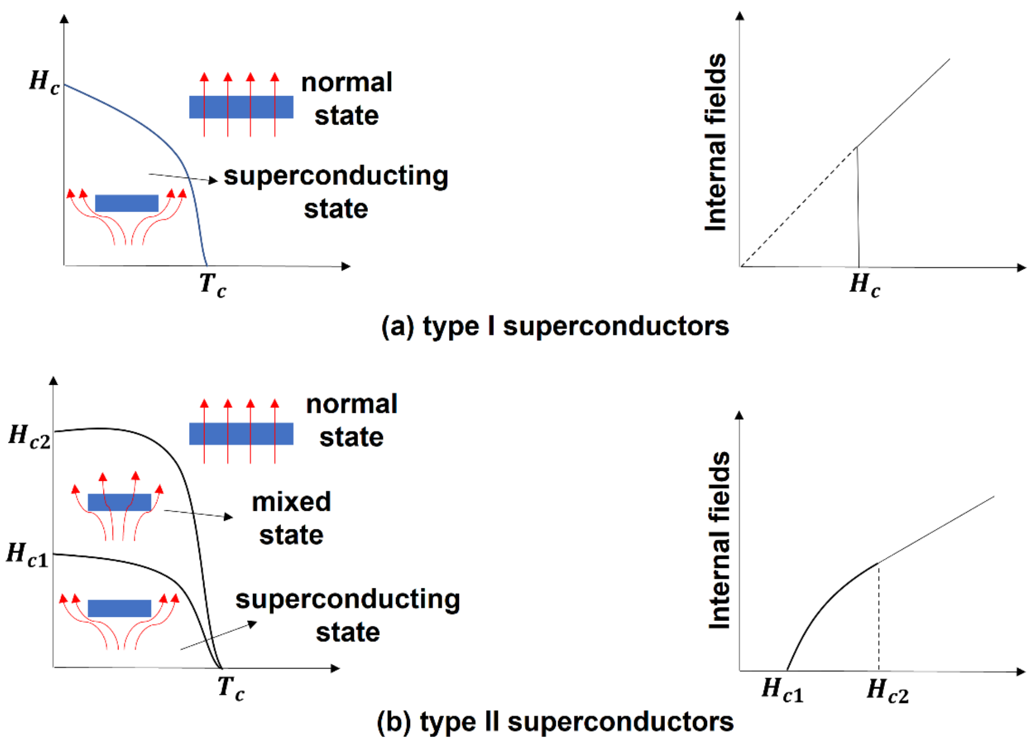

Figure 2.2.2. Reactions to applied magnetic fields for (a) type I, (b) type II superconductors.

The distinct behaviour of type I and type II was firstly described by Abrikosov [25], based on the analysis of GL lengths. An exact breakpoint that separates the two types of superconductors was identified as the Ginzburg-Landau parameter k equals to $1/\sqrt{2}$, namely for materials with $k > 1/\sqrt{2}$ the breakdown of superconductivity occurs in a first-order transition at H_c and are classified as type I superconductors, while for materials with $k < 1/\sqrt{2}$ the breakdown of superconductivity occurs in a second-order transition and are classified as type II superconductors. Most pure elemental superconductors, except niobium and carbon nanotubes, are type I. Almost all impure and compound superconductors, including all known HTSCs, are type II.

2.3 Bean model

As discussed in the last section, type II superconductors can be magnetized in a continuous manner due to the existence of the mixed state. In 1962 [26, 27], Bean proposed a critical state model to describe the magnetization behaviour of type II superconductors. Two assumptions are made in the Bean model, the first assumption is that the superconductor always stays in the critical state, where the current density within the superconductor can only be one of the three values: $+J_c$, $-J_c$, 0, the second assumption is that the critical current density J_c is constant. Under the two assumptions, the unreversible magnetization of type II superconductors can be clearly described.

Assume an infinitely long type II superconducting slab with $2a$ width, exposed to a perpendicular magnetic field as shown in figure 2.3.1.

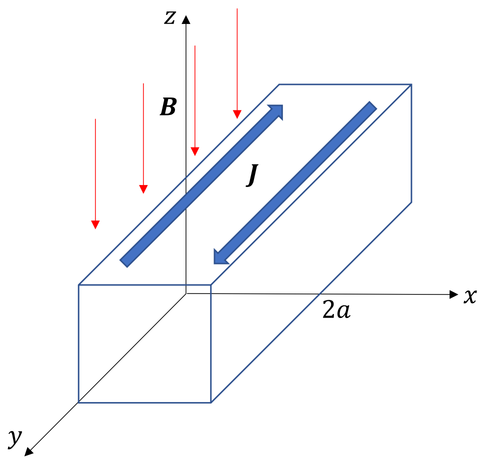

Figure 2.3.1. An infinitely long type II superconductor in a perpendicular magnetic field.

The one-dimensional representation of Ampere's law under such a geometry is:

$$\frac{dB}{dx} = \mu_0 J \tag{2.4.1}$$

Therefore, the magnetic field (where there exists one) in the superconductor varies linearly along the slab width, because J is fixed by the value of critical current density. If the applied field initially increases from zero, part of the magnetic flux will penetrate into the edges of the superconductor, and currents will be induced in corresponding regions, which flow in opposite directions (perpendicular to the $x-z$ plane), as shown in figure 2.3.2 (a). With the increase of applied field, the magnetic flux will penetrate more and more into the superconductor slab, meanwhile more proportions of the superconductor slab are occupied by the critical current. Eventually, the superconductor slab will be uniformly fulfilled by the positive and negative induced current, and hence fully penetrated by the magnetic flux when the applied field reaches a threshold value H_{th}, as shown in figure 2.3.2 (b). Further increase of the applied magnetic field above H_{th} will not affect the current distribution, but it will lift the magnetic field in the superconductor slab, accordingly, as shown in figure 2.3.2 (c). If one then decreases the applied magnetic field, the induced current near the edges of the superconductor slab will be reversed first, and the previously established current and magnetic field in the middle of the superconductor remain unchanged, as shown in figure 2.3.2 (d). The current distribution is continuously reshaped with the decrease of applied magnetic field, until the applied magnetic field arrives at the negative threshold field $-H_{th}$. At that moment, the whole superconductor slab is again fully occupied by the positive and negative induced current as shown in figure 2.3.2 (e). Similar to the process in figure 2.3.2 (c), further decreasing the applied magnetic field below the negative threshold field $-H_{th}$ will not affect the current distribution, but only reversely lift the magnetic field in the superconductor slab, as shown in figure 2.3.2 (f).

It should be pointed out that a uniform distribution of critical current density with a constant value is, in most cases, not the situation in real practice. However, the Bean's critical state model has provided a useful tool to microscopically explain the unreversible magnetization of type II superconductors.

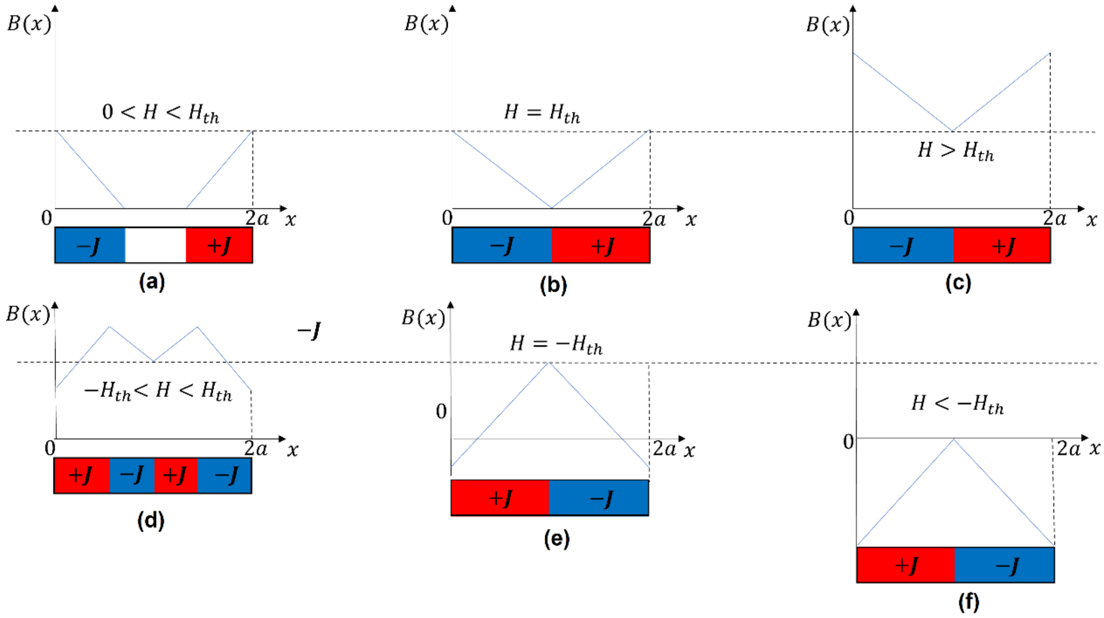

Figure 2.3.2. Magnetization process of type II superconductor under Bean's model.

2.4 $J_c(B)$ dependence

Unlike the assumptions for Bean's model, the critical current density J_c of superconductors is not consistently constant under different magnetic fields. In fact, J_c is highly dependent on the magnetic field. An empirical model, expressed as equation (2.4.1) was proposed by Kim and Anderson [28, 29] to consider the magnetic field dependence of J_c:

$$J_c(B) = \frac{J_{c0}}{1 + \frac{B}{B_0}} \tag{2.4.1}$$

where J_{c0} is the critical current density under zero applied field and B_0 is a fixed coefficient relating to the material properties. This so-called Kim-Anderson model straightforwardly points out that the critical current density is suppressed by the magnetic fields in an inverse relationship.

For some superconductors in regular shapes, e.g., REBCO tapes, it was found that magnetic field dependence of critical current density is dominated by the magnetic field components that are perpendicular to the current flowing plane, whilst the parallel components impose a relatively much lower impact. This anisotropic phenomenon is often described by another empirical expression, which has been widely used [30]:

$$J_c(B) = \frac{J_{c0}}{\left(1 + \frac{\sqrt{k^2 {B_{para}}^2 + {B_{perp}}^2}}{B_0}\right)^{\alpha}} \tag{2.4.2}$$

where B_{para} and B_{perp} represent the parallel and perpendicular components of the magnetic flux density with respect to the wide face of superconducting tape, respectively. J_{c0}, B_0, k and α are materials-related constant coefficients.

Apart from the magnetic field, the critical current density is also influenced by the temperature. There are several models in existing literature that account for the temperature dependence of critical current density. Chan [31, 32] formulated the critical current density as a function of temperatures T:

$$J_c(T) = \begin{cases} J_{c0}\left(\frac{T_c - T}{T_c - T_0}\right)^{\beta} & T > T_c \\ 0 & T \le T_c \end{cases} \tag{2.4.3}$$

Note that J_{c0} here is the critical current density at operating temperature T_0 and β is a constant associated with the materials. Fujishiro [33] also described the temperature dependence of J_{c0} by the following equation:

$$J_{c0}(T) = \alpha\left\{1 - \left(\frac{T}{T_c}\right)^2\right\}^{\frac{3}{2}} \tag{2.4.4}$$

where α is also a constant associated with materials.

In addition, the critical current density is also sensitive to internal mechanical strain. This is an important factor that has to be considered for high field superconducting magnets, because the superconductors in intensive magnetic fields will inevitably experience strong mechanical stresses due to Lorentz forces. It has been experimentally demonstrated in [34] that the critical current density of a REBCO coated conductor decreases with the increase of the applied tensile strain. In their experiments, the critical current density decreases smoothly with the applied tensile strain increasing from zero, and it sees a sharp drop when the stain reaches 0.74%.

2.5 Dynamic resistance

Current can flow without resistivity in superconductors, which is one of the fundamental properties of superconductors. However, if an HTSC is carrying a DC current under an AC magnetic field, it will experience noticeable resistance [35].

Let us consider an HTS thin film with the width of $2w$, thickness of h and length of l, transporting a DC current I_t. The critical current density J_{c0} is simply the critical current divided by the cross-section area $I_{c0}/2wh$. An external magnetic field B_{ext} is applied perpendicular to its wide surface, as shown in figure 2.5.1.

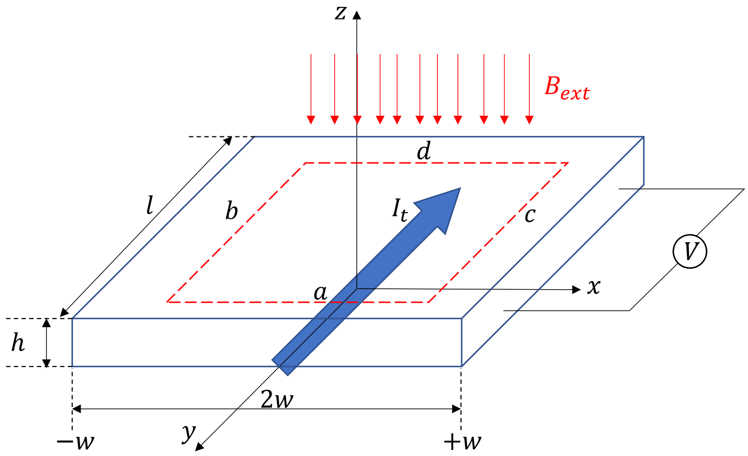

Figure 2.5.1. Schematic of the studied HTS layer experiencing both a DC and an AC external field.

Take a rectangular closed curve $abcd$ in the HTS wide surface into consideration, the voltage across it can be represented by Faraday's law:

$$\oint_{abcd} Edl = -\iint_S \frac{dB_{ext}}{dt} ds \qquad (2.5.1)$$

where S is the area formed by the closed curve $abcd$. In practice, the HTS film usually has a much longer length than its width and thickness, such that $l \gg w \gg h$. Hence, the voltage is principally determined by the y component of the electric field:

$$V = \int_b Edl = -\iint_S \frac{dB_{ext}}{dt} ds - \int_c Edl \qquad (2.5.2)$$

Since the closed loop is arbitrarily chosen, we can assume that curve c always locates at the region with zero flux movement, leading to:

$$V = \int_b Edl = -\iint_S \frac{dB_{ext}}{dt} ds \qquad (2.5.3)$$

From equation (2.5.3) it can be seen that the voltage equals to the flux changing rate in the region of the closed curve. According to the Meissner effect, the magnetic field variation will only penetrate into the HTS with a certain penetration depth p. For small amplitude of B_{ext}, the central region of HTS will not be influenced by that magnetic field variation. As a result, $V = \frac{dB}{dt} = 0$. If the transport current can occupy a flowing region $-iw < x < iw$ (i is the load ratio $I_t = iI_{c0}$) narrower than the unpenetrated region $p - w < x < w - p$, it can flow without inducing an effective voltage and hence experience zero resistance. However, if the amplitude of B_{ext} is sufficiently large, so that the unpenetrated region cannot be wider than the current flowing region, e.g., $|p - w| < |iw|$, as shown in figure 2.5.2.

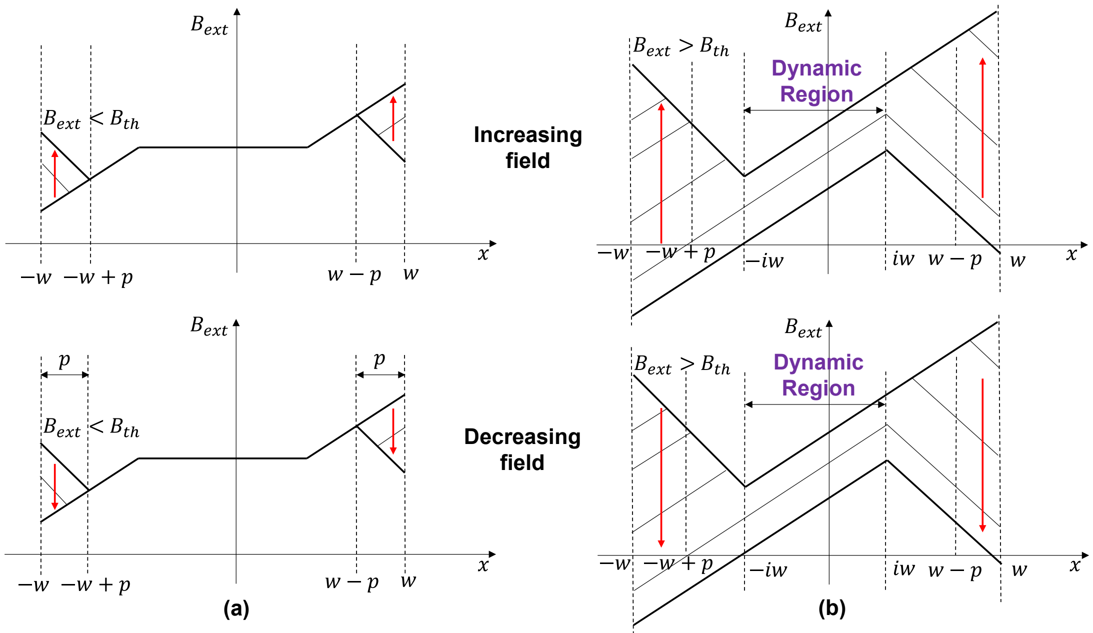

Figure 2.5.2. Magnetic field profiles inside the studied HTS layer experiencing both a DC and an AC external field. (a) Case of $B_{ext} < B_{th}$ in which the field cannot penetrate the central region defined by $-w + p < x < w - p$. (b) Case of $B_{ext} > B_{th}$, where dynamic resistance/loss occurs in the dynamic region defined by $-iw < x < iw$.

The overlap of the two regions occurs when the penetration depth equals to the current free depth, which means there is a threshold value that the external magnetic field must exceed to create an overlap region:

$$B_{th} = \frac{\mu_0}{2h}(I_{c0} - I_t) \tag{2.5.4}$$

In such conditions, the transport current I_t flows with an effective DC voltage, inducing a power dispassion in each cycle T:

$$Q = \frac{4wl}{I_{c0}} {I_t}^2 (B_{ext} - B_{th}) \tag{2.5.5}$$

From where the dynamic resistance is defined as:

$$R_{dyn} = \frac{Q}{{I_t}^2 T} = \frac{4wlf}{I_{c0}} (B_{ext} - B_{th}) \tag{2.5.6}$$

It should be noted that equation (2.5.6) is based on an assumption that the critical current density J_c is independent of the external field. If one considers the field dependence of J_c, such as equation (2.4.1), the definition of dynamic resistance remains the same, but the derivation becomes more complicated, more details can be found in [35].

2.6 AC loss

In pure DC conditions, HTS devices can mostly work without dissipative losses. However, in many practical applications, it is inevitable for the HTSCs to experience AC fields. For instance, in the generator/motor domain, the working principle is based on magnetic induction, for which AC fields are essential. In such cases, the AC loss of HTS will be caused by alternating transport currents or magnetic fields (or both). In general, depending on the AC source (transport current or external field), AC loss can be classified into transport current loss and magnetization loss. Transport current loss is caused by the carried current inside the superconductor in the absence of external magnetic fields, and magnetization loss describes the dissipation due to purely external magnetic fields without transport current. Magnetization loss consists of eddy current loss, hysteresis loss, and coupling loss. Hysteresis loss is generated by flux pinning and the loss per cycle is proportional to the area of the hysteresis loop. Coupling loss occurs due to the flowing of eddy current induced by external magnetic fields between filaments in multifilamentary conductors. Therefore, coupling loss can also be a problem for striated HTS CCs. Eddy current loss is the ohmic energy dissipation generated by the eddy current in the metal matrix. Transport current loss includes hysteresis loss and flux flow loss. Hysteresis loss occurs because the carried time-varying current provides the self-field. Flux flow loss happens due to more and more flux lines moving in the superconductor with the increase in the transport current (or the load proportion between the transport current and the self-field critical current) [36].

Let us consider a thin HTS film with the width of $2w$ and the thickness of h, as shown in figure 2.6.1 (a), having I_{c0} as the self-field critical current. When the HTS film is exposed to an AC magnetic field perpendicular to its wide surface, with the amplitude of B_{ext}, the Brandt equation can be utilised to quantify the average magnetization power loss per unit length (W/m), P_{mag}, as [37-39]:

$$P_{mag} = 4\pi\mu_0 w^2 f H_0 H_c \left\{\frac{2H_c}{H_o}\ln\left[\operatorname{csch}\left(\frac{H_0}{H_c}\right)\right] - \tanh\left(\frac{H_0}{H_c}\right)\right\} \tag{2.6.1}$$

where $H_0 = B_{ext}/\mu_0$, H_c denotes the characteristic field given by $I_{c0}/(2w\pi)$, μ_0 is the free space permeability, and f refers to the frequency of the AC field. As demonstrated in [24], the Brandt equation agrees well with the experimental data for the 12-mm-wide HTS CC.

In the absence of external magnetic fields, when the HTS thin film carries an AC current with an amplitude of I_t, according to the Norris equation, the average transport power loss per unit length (W/m), P_{trans}, can be written as [40]:

$$P_{trans} = \frac{\mu_0 f {I_{c0}}^2}{\pi}[(1-i)\ln(1-i) + (1+i)\ln(1+i) - i^2] \tag{2.6.2}$$

where i represents the load ratio, determined by $i = I_i/I_{c0}$, and f is the frequency of the AC current.

When the HTS film carries an AC transport current and simultaneously experiences an AC magnetic field, both of which share the same frequency f and the same phase, the total average power dissipation per unit length can be estimated by [41] (Formula (11) in [41] contains a typo: in the expression for P_2, the last term, 2 AB, should be a plus sign, not a minus):

$$P_{AC} = \frac{\mu_0 f {I_{c0}}^2}{4\pi}\left(\frac{b}{w}\right)(P_1 - pP_2) \tag{2.6.3}$$

$$P_1 = \alpha A \cdot \cosh^{-1}\alpha - \alpha^2 + \beta B \cdot \cosh^{-1}\beta - \beta^2 + 2 \tag{2.6.4}$$

$$P_2 = -A(\alpha + 2\beta)\cdot\cosh^{-1}\beta - B(\alpha + 2\beta)\cdot\cosh^{-1}\alpha + 2(\alpha+\beta)^2\cdot\tanh^{-1}\frac{AB}{\alpha\beta+1} + 2AB \tag{2.6.5}$$

where $b = w\sqrt{1-i^2}\sqrt{1-c^2}$, $c = \tanh[\pi B_{ext}/(\mu_0 J_{c0} h)]$, $p = \sinh(i-c)$, $\alpha = w(1+ic)/b$, $\beta = w(1-ic)/b$, $A = \sqrt{\alpha^2-1}$, $B = \sqrt{\beta^2-1}$.

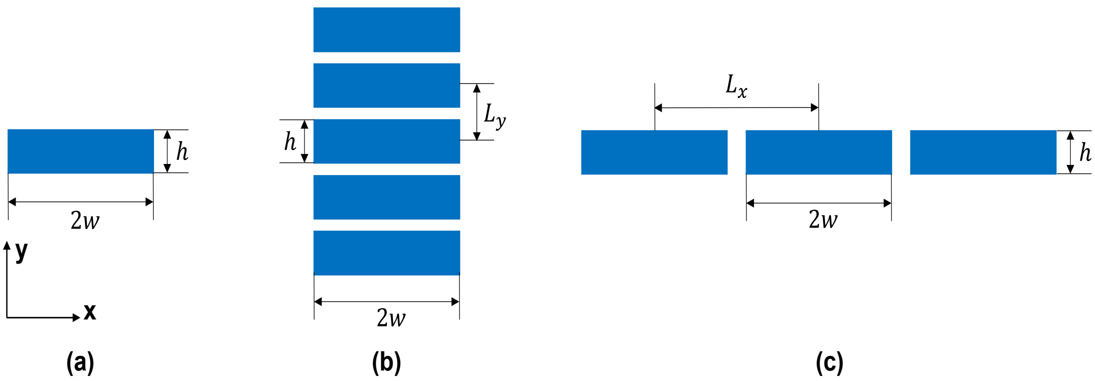

Figure 2.6.1. Cross section of the infinitely long thin HTS tape, stack, and array, each HTS layer having the width of width $2w$ and thickness of h: (a) single HTS layer, (b) stack of HTS tapes with stack periodicity L_y, (c) array of coplanar superconducting tapes with array periodicity L_x.

Additionally, the analytical techniques and formulae used to describe the transport current and magnetization losses of infinite stacks and arrays of thin tapes have been reviewed by Mikitik et al. in [42]. For an infinite stack of superconducting tapes with stack periodicity L_y, as shown in figure 2.6.1 (b), P_{trans} is given by [43]:

$$P_{trans} = \frac{\mu_0 f {I_t}^2}{\pi} \int_0^1 (1-2s) \ln \left[\frac{\cosh^2\left(\frac{\pi w}{L_y}\right)}{\cosh^2\left(\frac{\pi i s w}{L_y}\right)} - 1 \right] ds \qquad (2.6.6)$$

where I_t is the carried transport current in each tape. P_{trans} is written as [44]:

$$P_{mag} = \frac{\mu_0 f {I_{c0}}^2}{\pi} \left(\frac{L_y}{\pi w}\right)^2 {h_0}^2 \int_0^1 (1-2s) \ln \left[\frac{\sinh^2\left(\frac{\pi w}{L_y}\right)}{\cosh^2(h_0 s)} + 1 \right] ds \qquad (2.6.7)$$

where $h_0 = \pi H_0/(J_{c0} h)$.

For an infinite array of coplanar superconducting tapes with array periodicity L_x, as shown in figure 2.6.1 (c), P_{trans} and P_{nag} can be calculated by [43, 44]:

$$P_{trans} = \frac{\mu_0 f {I_t}^2}{\pi} \int_0^1 (1-2s) \ln \left[1 - \frac{\tan^2\left(\frac{\pi i s w}{L_x}\right)}{\tan^2\left(\frac{\pi w}{L_x}\right)} \right] ds \qquad (2.6.8)$$

$$P_{mag} = \frac{\mu_0 f {I_{c0}}^2}{\pi} \left(\frac{L_x}{\pi w}\right)^2 {h_0}^2 \int_0^1 (1-2s) \ln \left[1 - \frac{\sin^2\left(\frac{\pi w}{L_x}\right)}{\cosh^2(h_0 s)} \right] ds \qquad (2.6.9)$$

2.7 Introduction of flux pump

The development of superconducting technology has seen continuously increasing interests, especially in the area of clean power systems and electrification of transport with low CO_2 emission. Electric machines, as the major producer and consumer of the global electrical energy, have played a critical role in achieving zero carbon emission. The superior current carrying capacity of superconductors with zero DC loss opens the way to the next-generation electric machines characterized by much higher efficiency and power density compared to conventional machines. The persistent current mode is the optimal working condition for a superconducting magnet, and thus the energisation of superconducting field windings has become a crucial challenge to be tackled, to which HTS flux pumps have been proposed as a promising solution.

The maturation of superconducting technology has led to a wide range of industrial applications and commercial products. Magnetic resonance imagining (MRI) and nuclear magnetic resonance (NMR) machines are vital equipment in modern medical diagnosis, which usually employ superconducting magnets to provide the required magnetic fields for physical examination of states of matter [45, 46]. In the domain of motors/generators [47-53], superconductors have been attracting more and more attention since they are believed to be the optimal choice for electrification of large-size transport, such as electric aircraft, which requires the power density to be as high as possible. In the conceptual design of a hybrid-electric short-range aircraft A320 proposed by Rolls Royce and Siemens [54], a 10 MW, 7000 rpm superconducting generator employs HTS coils as the field winding and Litz wires for a two-layer distributed armature winding, which is believed to achieve a power density greater than 20 kW/kg. Another exemplary superconducting hybrid-aircraft project (being designed) adapts the radial-flux-type fully superconducting electric motors and generators [55]. In this project, the rotor winding is composed of DC racetrack HTS coils and the stator winding consists of MgB2 wires, both of which are cooled to 20–25 K by liquid hydrogen. It was estimated that these fully superconducting machines designs can achieve a power density no less than 38.1 kW/kg.

All the significant applications mentioned above rely on the superconductors to provide strong magnetic fields in an efficient way. It has been widely demonstrated that ultra-high magnetic fields can be obtained utilizing superconductors via various approaches [56-61]. Superconductor bulks have been fabricated to achieve a magnetic field of 17.24 T at 29 K using Y-Ba-Cu-O (YBCO) [62] and 17.6 T at 26 K [11], and [12] reported a trapped field of 17.7 T in a stack of superconductor tapes, all of which are an order of intensity stronger than a permanent magnet. However, the cost required for the corresponding cooling and charging system is extremely expensive and in some cases even unaffordable [63]. Advances made in the manufacture of CCs [64-66], has enabled the production of long length superconducting CCs with robust bending tolerance suitable for winding superconductor coils. Compared to bulks and tape stacks, CC coils have much better mechanical properties [67] and flexibility in terms of demagnetization and ease of maintenance [68]. These benefits make superconducting CC coils a competitive candidate for high magnetic field usage, and thus lead to a critical question: how should the superconducting coils be energised?

Technically, there are only two options for energising a coil, namely direct injection and indirect induction. By the means of direct injection, coils are connected to a power supply and energised through current leads [69]. This straightforward approach can be excruciating when the current is especially high because the current leads for transmitting very high current are extraordinarily bulky, such as that in W7-X, where 17.6 kA is required [70]. Moreover, the multistage cooling used in a Large Hardon Collider (LHC) machine dictates the current while making the current leads more complicated [71]. More importantly, the current leads physically bridge the cryostat with ambident environment at room temperatures, imposing heavy heat loads for the cooling system [72-74] and resulting in substantial additional capital and operating costs [75]. This becomes a particularly severe problem for HTS coils, for which it is challenging to self-maintain a persistent current mode due to flux creep [76], so that the current leads need to be permanently placed during the operation. In order to tackle this problem, HTS flux pumps, which can constantly drive magnetic flux into a closed superconducting loop without physical connections, have been proposed, serving as an ideal alternative to direct injection.

The flux pump device, or flux pumping effect, was originally developed for LTSCs decades ago [77-87]. The fundamental principle can be summarized as: consider two superconducting loops connected, one of which acts as a flux driver to push flux into the other, once the flux arrives the receiving loop it can be constrained within the loop given that superconductors forbid flux either entering or escaping from them. The critical step is the creation of a locally normal region in a superconductor to form the switch, providing temporary passage for the flux. It was later discovered by Coombs et al. [88-90] that the elimination of superconductivity is not necessary for HTSCs, leading to the new era of HTS flux pumps. Since then, HTS flux pumps have been widely investigated over last decade.

2.8 Low temperature superconducting flux pump

Flux pump devices were firstly proposed based on LTSCs, by using a straightforward circuit theory. As described by Van de Klundert [91, 92], the pumping procedure is illustrated in figure 2.8.1. Travelling magnetic flux enters the L1 loop with switch S1 open and approaches closed switch S2; afterwards the switch S1 is closed while S2 is opened to let the flux transfer into the L2 loop. The flux is then contained within the L2 loop, and hence the load coil is magnetized. The whole process can be periodically repeated to accumulate flux and ramp magnetization for the load coil. Owing to this cumulative effect, a small magnetic field can result in a very high charging current in the load coil. Mulder et al. reported a thermally switched flux pump in 1991, capable of generating a current of 100 kA [93]. On the foundation of this principle, various flux pumps have been proposed, and details can be found in a dedicated review for early-stage flux pumps [91].

Initially, all flux pumps that take advantage of this flux pumping effect rely on a low temperature superconducting (LTS) switch to modulate the magnetic flux. To form an LTS switch in this type of flux pump, one can either choose the magnetic or thermal approach. For the magnetic approach, as shown in figure 2.8.2, a magnetic field with its magnitude higher than the critical field H_c is applied to the LTS film to create a normal state region, which moves with the field synchronously. Alternatively, the magnetic field can be replaced by a heating source, which heats the area beneath beyond its critical temperature T_c, to create a normal state region. It is clear that either approach relies on the local elimination of superconductivity in the superconductors. However, the situation becomes quite different when it comes to HTSCs. Firstly, most HTSCs are type II superconductors, which have two critical fields H_{c1} and H_{c2} ($H_{c2} > H_{c1}$), where the upper critical field H_{c2} can be much higher than H_c of LTSCs. Therefore, it is hard to break the superconductivity of HTSCs by applying excessive magnetic fields. Similarly, driving HTSCs, which possess higher T_c, into normal state via overheating is also more difficult than that in LTSCs. It should be noted that thermal elimination of superconductivity for HTSCs is practically feasible, given that their transition temperatures are still much lower than the room temperature. Nevertheless, operating flux pumps with thermal activation, for each operation cycle, requires the HTS switch to be warmed up when the magnetic flux approaches and cooled down when the magnetic flux travels away, which severely restricts the operating frequency. In [94], Oomen et al. built a flux pump with HTS film, and heat was utilised to form the HTS switch, but the operating frequency was as low as 0.1 Hz. With such a low frequency, this kind of flux pump is not ideal for the majority of practical applications. Moreover, low frequencies can result in high ripples, as illustrated in [94] the flux ripple decreases by two orders of magnitude from 2400 to 60 ppm, when the operating frequency was increased to 50 Hz by replacing the HTS switches with MOSFETs.

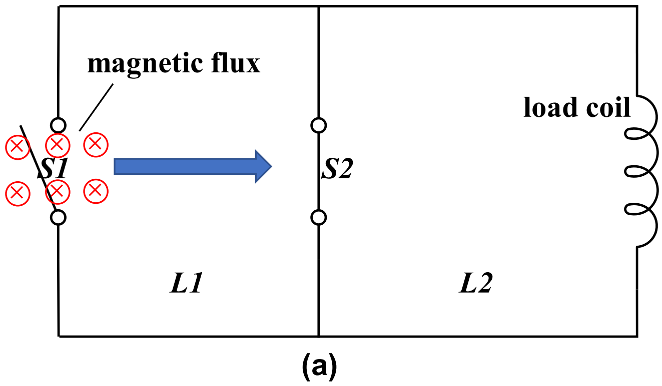

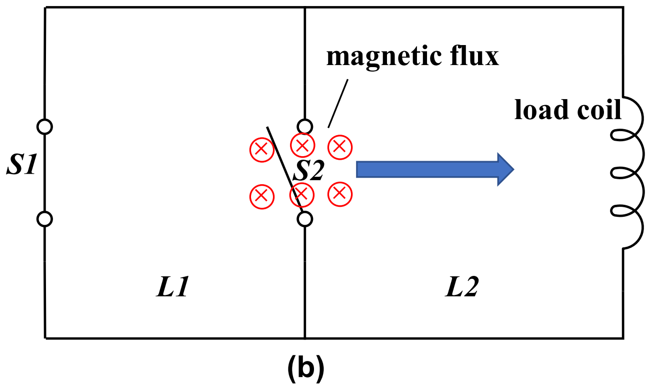

Figure 2.8.1. Illustration of flux pumping for LTSCs. Stage for (a) bringing flux into loop L1, (b) transferring flux into loop L2.

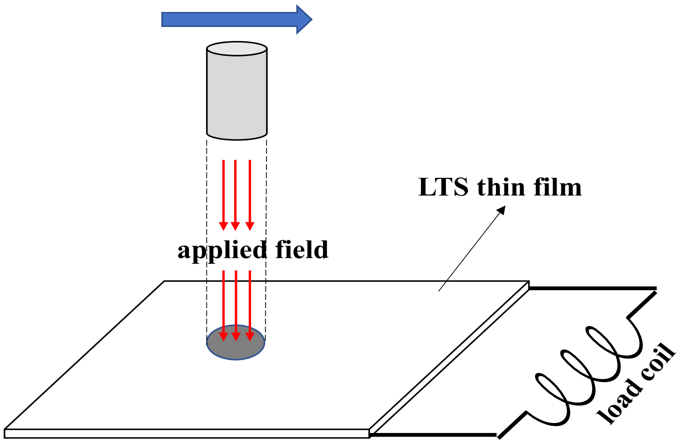

Figure 2.8.2. Illustration of magnetic switching for an LTS flux pump.

These above-mentioned issues have been critical obstacles for designing flux pumps with HTSCs. In 2007, Coombs et al. [89] built a test rig that successfully trapped a magnetic field of 0.2 T in a YBCO bulk. In their experiments, they used a thermal pulse to trigger a magnetic flux pulse travelling over the surface of an HTS sample, while the field was controlled by the change in magnetization or permeability. The significance of this experiment is that no normal regions have ever been created during the entire operation, implying that flux pumping can be achieved without breaking superconductivity for HTSCs. Following this novel discovery, tremendous efforts have been made by worldwide research groups to deeply investigate this phenomenon, leading to remarkable advancements for HTS flux pumps.

2.9 Travelling wave HTS flux pump

Inspired by the experimental tests in [89], it has been widely demonstrated that HTS flux pumps can be achieved by employing travelling magnetic waves. The generalized schematic diagram for a travelling wave HTS flux pump is illustrated in figure 2.9.1 (a), which can be modelled by the equivalent circuit in figure 2.9.1 (b). When an alternating magnetic field travels across the surface of HTSCs (typically HTS tapes), eddy currents will be induced and circulated within the superconductor. The current then results in an electric field, whose time-averaged integration over one cycle is derived to be a non-zero value. If the HTS tapes are connected to a load (usually HTS coils) to from a closed loop, then the flux pump can be considered as a DC voltage source V_{oc}, with internal resistance of R_V, charging an inductive load that has an inductance of L and resistance of R_L through resistive joints R_J. The whole system can be described by an equation:

$$V_{oc} = I(R_V + 2R_J + R_L) + L\frac{dI}{dt} \tag{2.9.1}$$

Under zero-state response, the pumped current I can be calculated as:

$$I = I_s\left(1 - e^{-\left(\frac{1}{\tau}\right)t}\right) \tag{2.9.2}$$

where I_s is the steady state current, i.e., the maximum pumped current, τ is the time constant that is determined using the following equation:

$$\tau = \frac{L}{R_V + 2R_J + R_L} \tag{2.9.3}$$

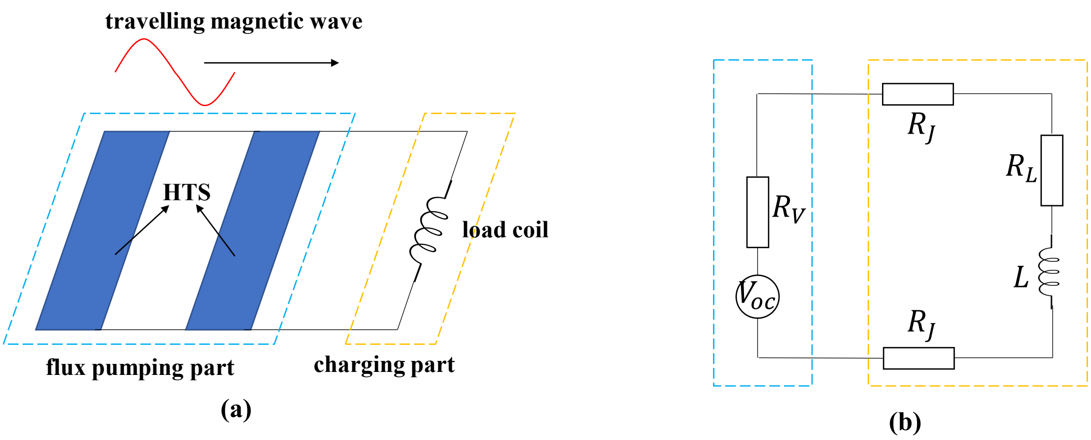

Figure 2.9.1. (a) Schematic diagram, (b) equivalent circuit for travelling wave HTS flux pump.

The most important step in operating a travelling wave HTS flux pump is to provide proper alternating magnetic fields, for which effective DC voltage can be induced. According to how the magnetic fields are provided, travelling wave flux pumps can be classified to rotary HTS flux pumps and linear HTS flux pumps.

2.9.1 Rotary HTS flux pump

HTS rotary flux pumps, or so-called HTS dynamos, firstly proposed by Hoffman et al. [95], employ one or multiple permanent magnets (PMs) mounted on a rotating disc as shown in Figure 2.9.2. The rotation of disc causes spatially varying magnetic fields and forms the travelling wave required by the flux pumps. This type of HTS flux pump has been extensively investigated, because of its simple structure and ease of operation. The basic design considerations for an HTS dynamo are the generated voltage and pumped current [96]. From Equation (2.9.1), the pumped current is directly determined by the effective DC voltage induced in the HTS tapes.

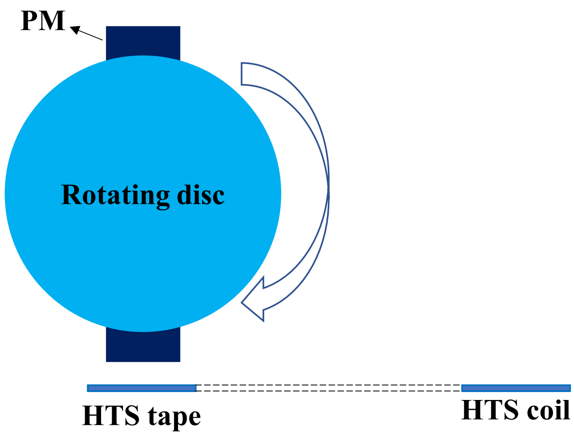

Figure 2.9.2. Cross section view of a rotary HTS flux pump equipped with two PMs.

Abundant work has been conducted to characterize the open circuit voltage for HTS dynamos, mainly credited to the research groups of the Robinson Research Institute, Victoria University of Wellington [97-100]. Inspired by the basic configuration of HTS dynamo, experiments were performed to investigate the impact of the flux gap [101], frequency (disc rotating speed) [102], tape width [103], and geometry of magnets [104] upon the open circuit voltage V_{oc}. Generally, it has been demonstrated that V_{oc} increases with the frequency and tape width but decreases with the flux gap. In terms of the magnet geometry, it was concluded in [104] that the generated voltage is insensitive to the orientation of the magnet but can be influenced by the magnet cross-section area. More precisely, the generated voltage shows a linear rise versus the frequency until a turning point usually appears around hundreds of Hz. After this turning frequency, nonlinear variation in the output voltage occurs, i.e., the slope of the voltage–frequency curve begins to decrease with frequency. This experimental observation was rather overlooked and not well explained until Zhang et al. [105, 106] proposed and demonstrated the use of a multilayer model to investigate the electromagnetic losses in HTS-coated conductors over a wide range of frequencies. It was found in [105, 106] that at frequencies higher than 100 Hz in the case of magnetization, the skin effect plays a dominant role in the determination of current distribution in an HTS CC, which results in the current drifting from the HTS layer to other non-superconducting layers, e.g., the copper stabilizers. Hence, the electric field established by the superconducting current is weakened, and thus the generated voltage experiences a progressive decrease with increasing frequencies. It is worthwhile mentioning that this is also the reason for which numerical models that only consider the HTS layer cannot manifest the nonlinear frequency response but predict a constant linear rate of increase in voltage. The generated voltage is consistently inversely proportional to the flux gap because the magnetic field experienced by the HTS tape is inversely proportional to the flux gap.

2.9.2 Linear HTS flux pump

A travelling wave HTS flux pump utilises static electromagnets rather than rotating PMs to provide the alternating magnetic fields required for generating effective DC voltage in HTS tapes. The whole device resembles the structure of a linear motor and is named as a linear HTS flux pump.

This type of HTS flux pumps has been mostly explored by the HTS group at the University of Cambridge [107-110]. Figure 2.9.3 shows a typical structure of an HTS linear flux pump. This flux pump consists of eight copper coils in four columns, in each column an HTS tape is sandwiched by an upper and lower copper coil connected in series. Each copper coil is wound around laminated iron cores and supported by an iron framework to focus the magnetic flux. The four HTS tapes are connected in parallel across the HTS coil.

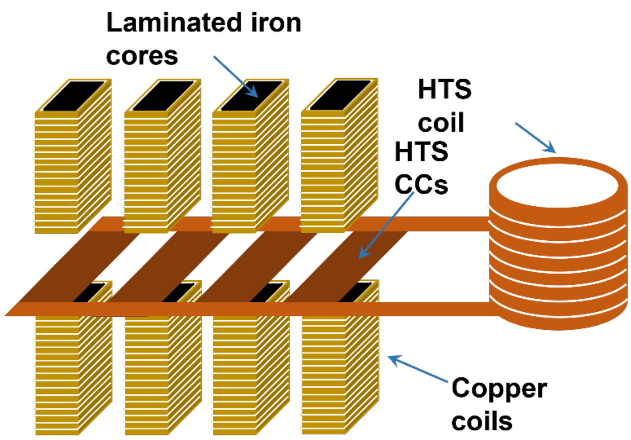

Figure 2.9.3. Schematic diagram for a linear HTS flux pump.

The linear HTS flux pump is operated by successively exciting each set of copper coils, forming a modulated field fluctuation in space that is analogue to a travelling wave. Experiments have demonstrated [108] that the pumping performance can be influenced by the frequency, amplitude, and waveform shape of the excitation current. Basically, the flux pumping is an accumulation process, where the current in the load coils is subsequently pumped up in each operation cycle. The limits are principally determined by the critical current I_c of the HTS tape rather than the magnetic field. Linear HTS flux pumps were observed to pump more or less the same current when operated at different frequencies and amplitudes, although a higher frequency and/or amplitude resulted in faster charging. For the waveform profiles, a triangular wave was demonstrated to be more effective than trapezoidal and sinusoidal waves. The authors of [107] found that a standing waveform, e.g., by exciting only one of the copper coils, can also energise the HTS load coils, which was thought to be an anomalous exception, as no travelling waves are present. In fact, this phenomenon can be explained if one considers the origin of the voltage generation in the HTS tapes, which will be clarified in detail in the following subsections.

2.9.3 Underlying physics

The travelling wave flux pump is a phenomenological subject, for which the underlying physics have been mysterious for years. Consider the flux pumping part in figure 2.9.1 (a), it is topologically identical to an AC alternator, where only AC voltage is supposed to be induced under AC fields without DC components. In 2014 [111], seven years later after the discovery of HTS flux pumping effects under travelling wave, Coombs et al. firstly gave a clue that the crucial difference between HTS travelling wave flux pumps and conventional AC alternators is likely to relate to the non-linear *E-J* characteristics, though no exhaustive explanation was given then. The first dedicated work that attempts to clarify the origin of the voltage observed in an HTS travelling wave flux pump was published by Geng et al. in 2016 [112]. They developed theoretical analysis based on a simple circuit, as shown in figure 2.9.4, that is intuitively identical to the arrangement of a linear HTS flux pump shown in figure 2.9.3, where superconducting loops can be formed by two adjacent HTS tapes.

The open circuit voltage across the HTS loop is:

$$V(t) = iR_2(t) - V_2(t) = \frac{V_1(t) + V_2(t)}{R_1(t) + R_2(t)} R_2(t) - V_2(t) \qquad (2.9.4)$$

Taking the time average derives the effective DC voltage as:

$$V_{dc} = \frac{1}{T}\int_0^T V(t)dt = \frac{1}{T}\int_0^T \frac{-\frac{d\Phi}{dt}}{R_1(t) + R_2(t)} R_2(t)dt \qquad (2.9.5)$$

where $V_1(t)$ and $V_2(t)$ represent the electromotive force induced in each HTS tape, while $R_1(t)$ and $R_2(t)$ represent their resistance accordingly. T is the cycle period of the applied field and Φ is the total flux applied to the HTS loop. To fulfil Faraday's law, $\int_0^T V_2(t)dt$ is zero. If the resistance in each HTS tape is constant throughout the operation, i.e., $\frac{R_2(t)}{R_1(t)+R_2(t)}$ equals a fixed value, the effective voltage must be zero. However, if the resistances are time varying functions, it is possible that Equation (2.9.5) can lead to a finite non-zero result, which shapes the effective DC voltage. They discussed the influence of field strength, rate of field change on the resistance, and attributed the DC voltage to the resistivity variation of type II superconductors.

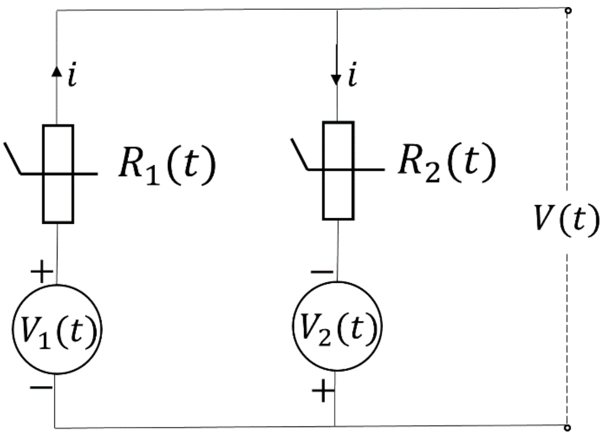

Figure 2.9.4. Electric circuit for analysing the voltage generation.

Almost at the same time, in 2016, Bumby et al. [113] published an enlightening work to explain the DC voltage origin for an HTS dynamo. In their work, the Giaver model was applied, which considers that the superconducting eddy currents "short-circuit" the high field region, e.g., the region beneath the PM during the passage of PM across the HTS tape as shown in figure 2.9.5 (a) and (b). Under this assumption, the circulating current is expected to spread over the tape, such that [113]:

$$\delta(\theta)J_{ser} = -\big(w - \delta(\theta)\big)J_{sh} \tag{2.9.6}$$

where J_{ser} is the induced average local current density in a region of the HTS tape that is directly beneath the magnet, $\delta(\theta)$ is the path width at rotor angle θ, and J_{sh} is the concomitant returning current. The flux–flow resistance in type II superconductors can be described by *E-J* power law:

$$\boldsymbol{E} = E_c \frac{\boldsymbol{J}}{J_c}\left(\frac{|\boldsymbol{J}|}{J_c}\right)^{n-1} \tag{2.9.7}$$

Hence, the resistances in each of the circulating paths can be expressed as [113]:

$$R = \frac{lE_0|\boldsymbol{J}|^{n-1}}{(w-\delta){J_c}^n} \tag{2.9.8}$$

Consider the analysis of the circuit in figure 2.9.5(c), the instantaneous representation of that effective DC voltage can be derived as [113]:

$$V(t) = \frac{-V_m(\theta)}{1+\left(\frac{\delta(\theta)}{w-\delta(\theta)}\right)^n} \tag{2.9.9}$$

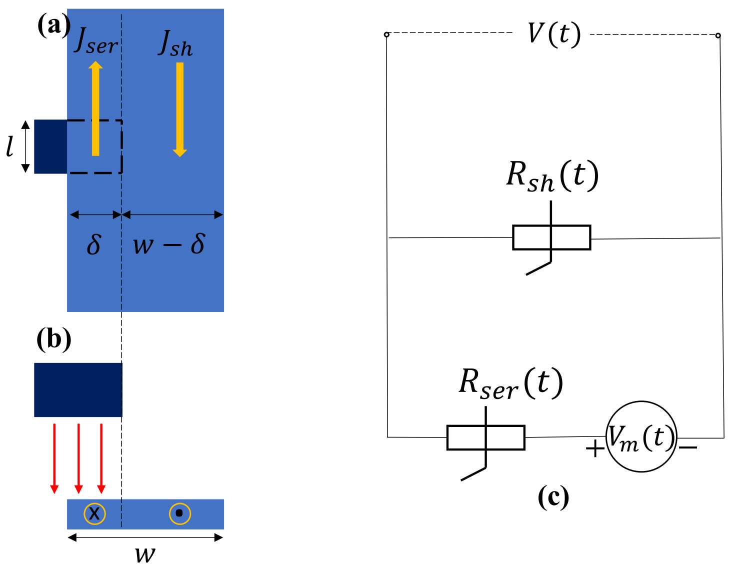

Figure 2.9.5. Schematic diagram illustrating the circulating current as the magnet rotates over the HTS tape (a) vertical view, (b) front view, (c) circuit sketch.

where J_c is the critical current density at a threshold field E_c, n is a constant coefficient related to the materials. V_m is approximated as $V_m = lvB$, with l and v representing the length and linear velocity of the magnet and B is the flux density, for the magnet passing over the tapes. Otherwise, it is always zero. This equation was able to show qualitative agreement with the experimental measurements, implying that the circulation of superconducting current seems to be the cause of the DC output voltage from an HTS dynamo. Following this work, Mataira et al. further demonstrated in [114] that the circulating superconducting current under the strong field region substantially exceeds the local critical current density and triggers a highly non-linear resistivity, leading to bizarre distortions on the induced AC waveform. As a result, the net integration of the AC waveform is no longer zero and forms an effective DC component. The same group then clearly stated that it is the non-linear resistivity and unsymmetric eddy current effect that gives rise to the DC output voltage from an HTS dynamo [115]. Thanks to that, the longstanding conundrum should have now been clarified clearly.

As an alternative to the microscopic approach presented above, Wang et al. proposed a macroscopic theory [116] to explain the DC voltage generation in an HTS travelling wave flux pump. According to their explanation, the local-field inhomogeneity, i.e., a DC biased AC waveform, causes a coupling effect between clusters of coupled vortices and the applied magnetic poles, and the coupling force drags the vortex cluster into the HTS film and hence traps flux within it, as illustrated in figure 2.9.6. The physics conceived in [116] tends to oppugn the non-linear resistivity established in [114, 115], as they stated in [117]. The focus of the debate is that a pure AC waveform cannot prompt a DC output from a travelling wave flux pump, which was not clearly studied in [114, 115]. However, the zero DC output voltage in a travelling wave HTS flux pump under pure AC fields should not be taken as evidence that challenges the theory based on the non-linear resistivity.

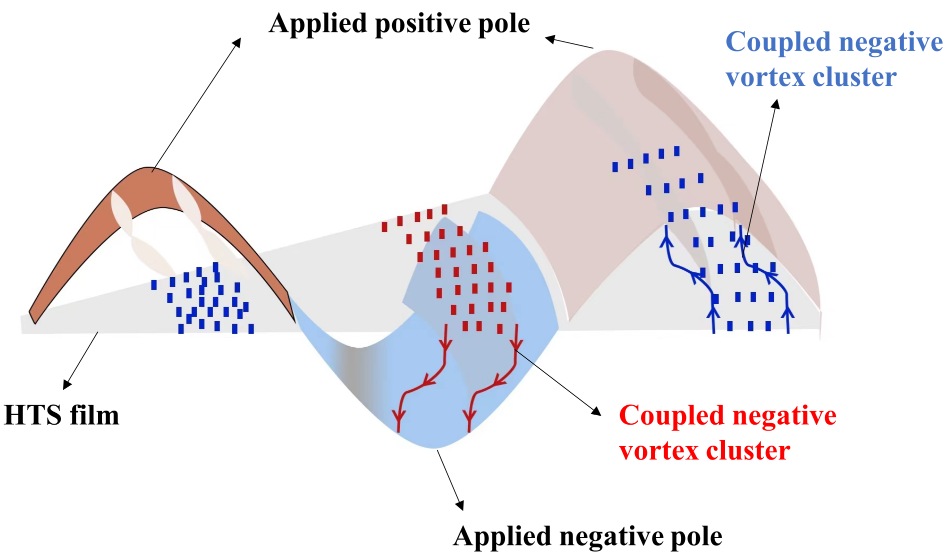

Figure 2.9.6. Coupling features including the ramping up of vortex density and misalignment between applied pole and coupled cluster. Adapted from [116].

Based on Equation (2.9.7), one can describe the net averaged DC voltage as:

$$V_{dc} = \frac{E_c}{J_c{}^n}\frac{1}{S}\frac{1}{T} l \int_0^T dt \oiint \boldsymbol{J}|\boldsymbol{J}|^{n-1} ds \tag{2.9.10}$$

For an open circuit, there must be no transport current such that:

$$\oiint \boldsymbol{J} ds = 0 \tag{2.9.11}$$

Thus, V_{dc} must be zero if $n = 1$, similar to that in a normal conductor. For $n > 1$, such as that in a superconductor with non-linear resistivity, $\boldsymbol{J}$ is spatially dependent and it can lead to a finite non-zero solution for Equation (2.9.10). Alternatively, one can also express the net averaged DC voltage directly from the Faraday's law:

$$V_{dc} = \frac{1}{T}\int_0^T dt \oiint \frac{d\boldsymbol{B}(x,y,t)}{dt} ds = \frac{1}{T}\oiint [\boldsymbol{B}(x,y,t=T) - \boldsymbol{B}(x,y,t=0)] ds \tag{2.9.12}$$

If the applied magnetic field $\boldsymbol{B}(x,y,t)$ is a pure AC waveform, then at any position it must hold that $\boldsymbol{B}(x,y,t=T) = \boldsymbol{B}(x,y,t=0)$, so V_{dc} can only be zero. Equations (2.9.10) and (2.9.12) can both hold simultaneously and agree well mathematically with each other. The physical interpretation is simply that if the applied field is pure AC and hence completely identical in the positive and negative cycles, the waveform distortion (of course still originates from the non-linear resistivity) is cancelled out during the whole periodic operation. Thus, applying a pure AC field should be considered as a special scenario instead of a counterexample of the theory built on non-linear resistivity.

2.9.4 Modelling techniques

Generally, the electromagnetic behaviours involved in operating a travelling wave HTS flux pump can be well described by Maxwell equations. Depending on the state variables selected for solving Maxwell equations, different formulations can be utilised, such as the ***H*** formulation [118-122], coupled ***H-A*** formulation [123, 124], and coupled ***T-A*** formulation [125-129]. In addition, extra techniques have been developed to simplify the solution of Maxwell equations in specific aspects, including the ***H***-formulation with shell current [114, 115, 130], segregated ***H***-formulation [131, 132], minimum electromagnetic entropy production (MEMEP) [133, 134], integral equation (IE) [135-137], volume integral equation-based equivalent circuit (VIE) [138-140], and Chebyshev polynomials-based methods [141-143]. Exhaustive details for each formulation can be found in the benchmark paper [144] published by Ainslie et al., which is strongly recommended to readers for acquiring information about HTS dynamo modelling. In addition, two remarks should be supplemented. The first one is, all models in [144] follow a classical assumption that the critical current of the HTS tape is constant. However, the critical current is sensitive to the magnetic field experienced by the HTS tapes, which has been shown to have significant impacts on the generated voltage [114]. In terms of numerical modelling, one can easily include this feature by importing the experimentally measured critical current under different fields to the model. Alternatively, one can describe the field dependence of critical current by an empirical function, equation (2.4.2):

It also should be pointed out that the models in [144] only consider the superconducting layer of an HTS tape. This approximation is valid only under low frequencies, because for relative higher frequencies (hundreds of Hz or above) the currents induced by external magnetic fields tend to be drawn away from the HTS layer to its edges due to the skin effect, which cannot be reflected by a single layer model [145]. Therefore, it is necessary to consider all layers in a coated HTS conductor, e.g., the copper stabilizers, silver overlayer as well as substrate. With the two remarks added, one should obtain a numerical model that possess the full capability to simulate the behaviour of a travelling wave HTS flux pump. Up to now, most of the modelling techniques are mainly implemented for a rotary HTS flux pump, due to its structural simplicity. As discussed before, the rotary and linear type of HTS flux pump share the same physical mechanism. The modelling techniques for HTS dynamos modelling can be confidently transferred to linear HTS flux pumps, while the only difference lies in modelling the applied field either by a remanent flux density (for PMs) or an excitation current (for electromagnets).

In addition to the widely used 2D models, Ghabeli et al. [146] proposed the first 3D model for an HTS dynamo, based on the MEMEP approach that they initially proposed for 2D HTS dynamo modelling. This model has shown good agreement with experiments as well as the 2D models. The highlight of this model is that it visualizes the screening current and electric field distribution across the HTS tape surface, which is significant as it provides evidence for the mechanism explanation based on the eddy current circulation. So far, the models discussed above usually only cover the flux pumping part shown in figure 2.9.1 (a), aiming to investigate the open circuit voltage output. In order to replicate a travelling wave HTS flux pump in full, one should also include the superconducting coils under charge. The authors of [147] modelled the full charging process for an HTS dynamo, where the load coils are simplified as a series combination of an inductor and resistor with predetermined values. To link the flux pumping part with the load coils being charged, the constraint imposed to maintain the current in HTS tapes, as previously described by Equation (2.9.11), should be amended accordingly:

$$\oiint \boldsymbol{J} ds = I_t \tag{2.9.14}$$

where I_t denotes the currents stimulated (by the induced voltage across HTS tapes) in the coils and hence also flowing through the HTS tapes as a complete circuit loop.

2.10 Transformer-rectifier HTS flux pump

HTS flux pumps can be achieved in the magnetic field driven mode, as detailed in section 2.9, while they can also be realized in the current driven mode, which are classified as transformer-rectifier HTS flux pumps. A general schematic drawing is shown in figure 2.10.1. An alternating current i_1 is induced in the secondary winding of the transformer, which is connected to the HTS bridge and coil and forms two loops in parallel. Initially, the HTS bridge short-circuits the HTS coil, and i_2 flows through loop1 only (i.e., $i_1 = i_2$). Under certain conditions, the HTS bridge can exhibit temporary resistivity; thus, breaks the short circuit and forms a rectifier. Consequently, the HTS coil can be charged by a current i_L flowing in loop2. When the HTS bridge eliminates its resistivity, the HTS coil is again short-circuited and hence flux is trapped. The flux pumping process involved here is, in essence, similar to LTS flux pumps. The difference is that the resistive region in HTSCs (analogue to the normal region in LTSCs) requires no elimination of superconductivity. Depending on how to trigger the resistivity in the HTS bridge, there are AC field switched [148-151] and self-regulating transformer-rectifier HTS flux pumps [152-154].

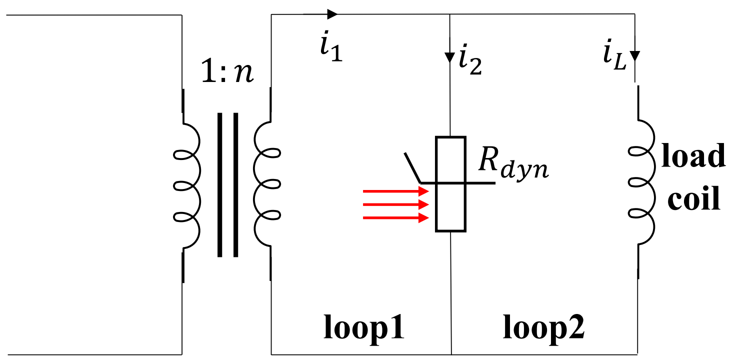

Figure 2.10.1. Circuit diagram for a transformer-rectifier HTS flux pump (red arrows denote the applied magnetic field).

2.10.1 AC field switched transformer-rectifier HTS flux pump

2.10.1.1 Topology

This type of flux pump, as shown in figure 2.10.2, was firstly demonstrated by Geng and Coombs [149]. When the HTS bridge carries a current i_2 induced in the secondary winding, an alternating magnetic field is applied perpendicularly to the surface of the HTS bridge. As long as i_2 flows in one direction in the HTS bridge with the existence of the alternating field, resistivity can be triggered.

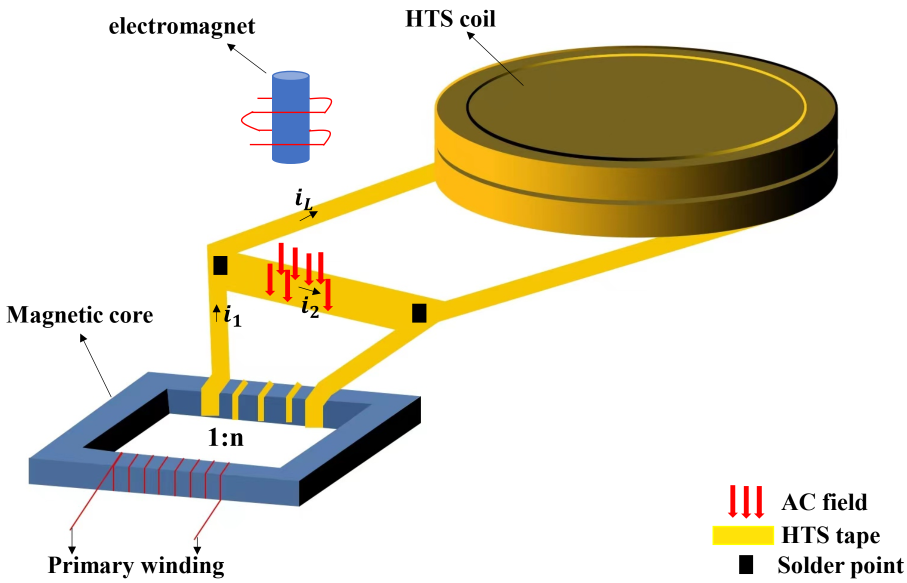

Figure 2.10.2. Structure diagram of an AC field switched transformer-rectifier HTS flux pump.

Several influential factors on the flux pumping performance were examined in the comprehensive research presented in [148], including excitation current magnitude, applied field magnitude, frequency and duration, and phase differences between current and field. Briefly, the pumping current decreases from its maximum at no phase misalignment (the transporting current is in phase with the field) to zero at 90 degrees phase difference; an increase in either the strength or frequency of the applied field leads to a continuously increasing pumped current; the duration of the applied field (i.e., how long the resistivity in the HTS bridge is maintained) has negligible impact on the pumping current. The influence of the excitation current is relatively more complicated: the pumping current increases with the excitation current magnitude up to a turning point, after which it starts to drop if the excitation current increases further, implying that there exists an optimal excitation current to maximize the pumping current. In addition, it was found in [155] that adding an actual resistance to the secondary winding can enhance the pumping current, especially when the desired current is high.

2.10.1.2 Mechanism

The working principle of an AC field switched transformer-rectifier HTS flux pump is crystal clear, since it is completely based on the well described dynamic resistance effect [35, 156, 157]. It is known that the external magnetic field B_{ext} penetrates certain distance into the superconductor from its edges. The penetration depth increases with the magnetic field. Hence, if the magnetic field is strong enough, it can penetrate the central area and create a resistive region, as previously shown in figure 2.5.2.

Under such conditions, the current flows in the central area tends to interact with the magnetic flux and cannot flow without resistivity. The formula to calculate dynamic resistance R_{dyn} was proposed in [35], which can be expressed as equation (2.5.6).

However, this linear formula cannot reflect the non-linearity of dynamic resistance. Equation (2.5.6) was then complemented by Zhang et al., in [157], where a second term was added to account for the non-linear contribution:

$$R_{dyn} = \frac{2wlf}{I_c}(B_{ext} - B_{th}) + \frac{E_c l}{I_t} i^{n+1} f_{avg}(B) \tag{2.10.1}$$

$$f_{avg}(B) = 1 + \sum_{p=0}^{\frac{n}{2}-1} \left\{ \frac{n!}{(2p+1)!\,[n-(2p+1)]!} \left(\frac{B_{ext}}{B_0}\right)^{2p+1} \frac{2^{p+1} \cdot p!}{\pi \prod_{q=0}^{2p+1}(2q+1)} + \frac{n!}{(2p+2)!\,[n-(2p+2)]!} \left(\frac{B_{ext}}{2B_0}\right)^{2p+2} \frac{(2p+2)!}{[(p+1)!]^2} \right\} \tag{2.10.2}$$

where w is the width of the superconductor, l is the length of superconductor subjected to the field, I_c is the critical current, B_{ext} and f are the amplitude and frequency of the applied field, respectively. B_{th} represents the threshold that the applied field must exceed to create the dynamic region. i is the load ratio that reflects proportions of transport current I_t to the critical current, i.e., $I_t = iI_c$. n in Equation (2.10.2) is even and in the case of an odd n, the formula has to be adapted accordingly as illustrated in [157]. It should be noted that Equation (2.5.6) was initially developed for a superconductor carrying DC current, but the HTS bridge transports an alternating current. It is still applicable here because the field is only applied when the current flows in one direction.

2.10.2 Self-regulating transformer-rectifier HTS flux pump

2.10.2.1 Topology

Following the design in figure 2.10.2, Geng et al. [158] further developed the self-regulating transformer-rectifier HTS flux pump, which are hand-in-hand with the AC field switched ones. The two prototypes share almost the same topology, whilst the only difference is whether the field generating component is included. In a self-regulating transformer-rectifier HTS flux pump, the AC magnetic field is no longer required to trigger resistivity in the HTS bridge. Alternatively, a highly asymmetric (the absolute value of positive peak is much higher than its negative peak) current is injected into the primary winding. Then, resistivity can be trigged for the HTS bridge when it conducts the positive peak current. With this approach, it eliminates the troublesome field modulation, making the whole operation solely driven by current. As a result, the operational considerations are less than that for an AC field switched HTS flux pump, principally only the magnitude and frequency of the primary current. As experimentally demonstrated in [158], unlike the AC field switched ones, where the primary current magnitude has a bilateral effect, the pumping current for a self-regulating flux pump continuously increases with the primary current. More or less the same pumping current was obtained for various primary current frequencies, but faster charging speed was observed under higher frequencies.

2.10.2.2 Mechanism

Intuitively, due to the topological similarity, the mechanism of self-regulating flux pumps is close to the AC field switched ones, but slightly different. For type II superconductors, the current and electric field relations normally can be described by the exponential *E-J* power law as Equation (2.9.7). Visualizing this equation, as shown in figure 2.10.3, one can find that if the current density exceeds a threshold value, the superconductor will enter the flux flow regime and exhibit obvious resistivity. Thus, if some parts of the secondary current waveform (e.g., the positive peak region) are greater while all the rest are smaller than the threshold, the HTS bridge can possess temporary resistivity in one cycle and hence provides the rectification effect. This is the reason why the primary current must be highly asymmetric, and the flux pump can only operate in half-wave mode.

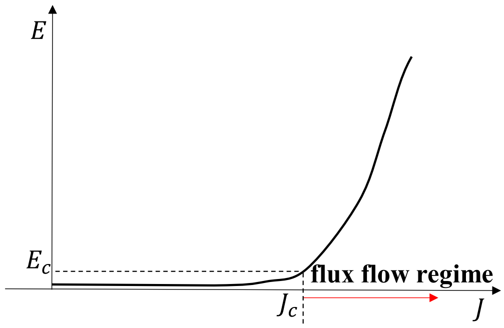

Figure 2.10.3. Visualization of the ***E-J*** relation, the red arrow means that where the flux flow regime appears after transport current exceeds the critical current density.

2.10.3 Modelling techniques

Theoretically, the methods detailed in section 2.9 for travelling wave HTS flux pumps modelling are applicable to the above two types of HTS flux pumps. Most previous work about transformer-rectifier HTS flux pumps are experimental, a good example of the modelling can be found in [159]. Based on the circuit diagram in figure 2.10.1, the transformer can be equivalently substituted by a magnetic field applied perpendicularly to loop1, which can induce a circulating screen current, accordingly. The whole system then can be simplified to three parallel HTS tapes (S_1, S_2 and S_L) connected at the terminals, which is reflected by a global constraint equation:

$$i_{S_1} + i_{S_2} + i_{S_L} = \oiint \boldsymbol{J}_{S_1} ds + \oiint \boldsymbol{J}_{S_2} ds + \oiint \boldsymbol{J}_{S_L} ds = 0 \tag{2.10.3}$$

Later, a novel modelling approach was proposed in [160]. Different from those formulation-based models aiming to solve Maxwell equations, this model completely relies on the circuit analysis for figure 2.10.1. By combining Equations (2.5.6) and (2.9.7), one can express the net output voltage across the HTS bridge as:

$$V_{out} = i_2 \frac{2wlf}{I_c} (B_{ext} - B_{th}) + E_c l \frac{{i_2}^{n-1}}{{I_c}^{n}} \tag{2.10.4}$$

which can be utilised to calculate the current in an inductive coil with fixed inductance, similar to Equation (2.9.1). This method evades sophisticated electromagnetic interactions that occur in the real operation by applying a set of approximated equations, so it is much more efficient than FEM simulations, in terms of solution time.

2.11 Other HTS flux pumps

The main categories of HTS flux pumps have been substantially detailed in section 2.9 and section 2.10; this section aims to provide readers with a wider overview of HTS flux pumps, by presenting several variants.

As mentioned earlier, Coombs et al. constructed a rig to magnetize YBCO samples [88-90]. In their experiments, they conjoined soft magnetic materials with hard ones in the flux path, as shown in figure 2.11.1. The soft magnetic materials (e.g., Prussian Blue puck) undergo a change in permeability and the hard ones (e.g., permanent magnet NdFeB) undergo changes in magnetization when their temperature changes. As a combinational effect, magnetic pulses can be generated to travel over the surface of the superconductors. Technically, the operation principles are similar to the later conceived travelling wave HTS flux pumps. This type of thermal actuated HTS flux pumps have not been further developed, due to the challenges faced in operation. However, it is of great significance since it firstly realized flux pumping for HTSCs without any break of superconductivity.

In [161-165], Bai et al. proposed a pulse-type magnetic flux pump to magnetize Bi-2223 tapes, as shown in figure 2.11.2 (a). In their design, an HTS film is placed in the middle of a set of aligned solenoids and connected to an HTS loop. By controlling the input current, the solenoids can generate specific magnetic pulses over the HTS film, after which flux can be driven into the superconducting loop. This is again very similar to the travelling wave HTS flux pumps, especially the linear ones. Nevertheless, according to their explanation, the pulses are utilised to create a local normal region in the HTS film, which makes it totally different from all HTS flux pumps discussed above but resembles an LTS flux pump. Considering their experimental configurations, the solenoids with 300 turns are energised with a current below 2.5 A with 300 turns. Such an excitation is unlikely to produce a magnetic field strong enough to break the superconductivity for HTSCs, this is essentially a variant of the travelling wave HTS flux pump.

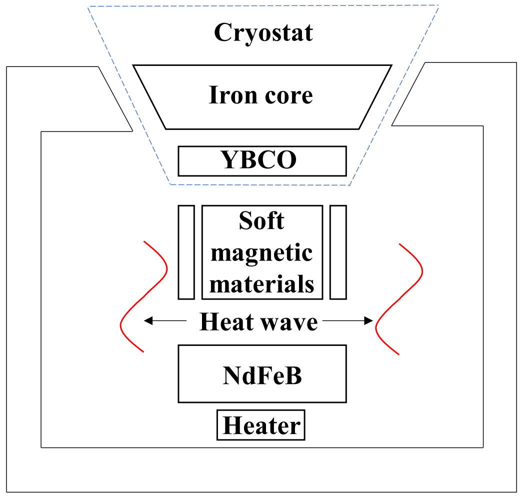

Figure 2.11.1. Illustration of the experimental set up for a thermal actuated HTS flux pump. Adapted from [88].

Refs. [166-169] claimed that they have designed a novel flux pump device to charge an HTS double pancake coil, as shown in figure 2.11.2 (b). The only acting component is the static electromagnet, and thus it is referred to as a linear HTS flux pump in [169]. However, it should be noted according to the topology, that the magnetic core directly passes through the closed superconducting loop, which intuitively forms a transformer with the superconducting loop serving as the secondary winding. From this point of view, the situation becomes tricky since the charging current can likely result from direct electromagnetic induction, rather than flux pumping. The flux pumping effect reported in [166] can be well accounted for by Faraday's law: the injected DC current in the static electromagnet has led to the occurrence of the DC magnetic flux inside the HTS loop despite a short step-variation period. It should be noted that the initial magnetic flux inside the HTS loop is zero. Given the flux conservation characteristics and nearly zero resistance of a superconducting loop, a permanent circulating DC current will be induced to force the total magnetic flux inside the HTS coil to be zero [170]. As a result, a DC current can be generated in the HTS loop.

The transformer-rectifier HTS flux pumps discussed in section 2.10 all rely on the HTS bridge to demonstrate temporary resistivity during each cycle of operation. Gawith at al. [171] proposed a double AC field switched flux pump, where an extra field is applied to part of the loop1 path in figure 2.10.1. They pointed out that for a single AC field switched transformer-rectifier HTS flux pump, the resistance in loop1 is not zero even if the HTS bridge is superconducting, because there are fixed resistances due to circuit joints and the AC loss mechanism. Adding an extra AC field switch can help modulate the resistance in loop1 and potentially improve the performance compared to the single switch case. Alternatively, except for exploiting peculiar properties of superconductors, one can replace HTS switches with electronics devices, such as MOSFETs, which demonstrates high impedance during on-state and very low impedance during off-state [94]. In addition, the critical current density of HTS materials is associated with external magnetic field. Therefore, for a self-regulating transformer HTS flux pump, one can exploit the field dependence of critical current density to reduce the threshold of flux flow regime, which has proved helpful for improving efficiency [172].

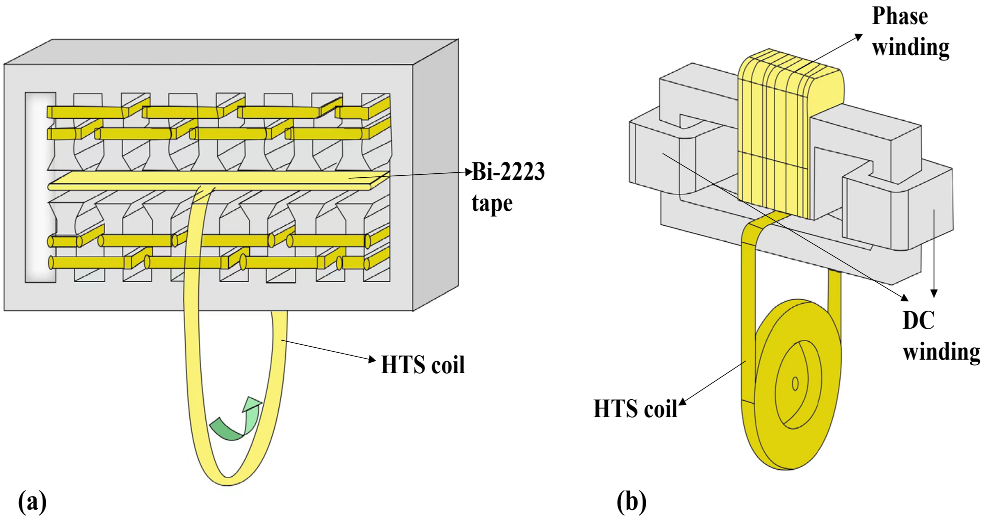

Figure 2.11.2. (a) Structure diagram of a pulse-type HTS flux pump. Adapted from [161]. (b) Experimental configuration of the linear HTS flux pump. Adapted from [166].

2.12 Discussion

Based on the above analysis, it can be concluded that the creation of a resistive region without breaking the superconductivity in the whole HTS tape is the key to achieving the DC output voltage. In other words, the non-linear dynamic resistance caused by the hysteretic and flux flow effect is the root for all types of HTS flux pumps. The functionality of all types of HTS flux pumps presented in this work is essentially achieved by the same working principle: an effective homopolar voltage is induced across a section of HTS tape, which can energise the charging loop by constantly ramping up current in it. For travelling wave HTS flux pumps, either rotating PMs or stationary electromagnets can be employed to provide the magnetic field required by the HTS tape to output a DC voltage. The core is to create highly unbalanced resistivity along the width of the HTS tape (due to the highly non-linear resistivity property), so whether the wave is "traveling" is not decisive. Applying a simple standing waveform can also lead to a measurable DC output, as long as the magnetic field is asymmetric in the time domain and spatially inhomogeneous. For transformer-rectifier HTS flux pumps, two options are available for triggering the resistivity in the HTS bridge, either by external AC magnetic fields or over-critical currents.

In terms of the fundamental physics, the two main categories (travelling wave and transformer-rectifier type) of HTS flux pumps are closely related and share common characteristics. In all cases of operating HTS flux pumps, the HTS bridge should be able to transport current greater than that carried in the load coil. This is automatically fulfilled, considering the load coil usually experiences a much higher field than the bridge. Otherwise, one would have to manually adjust the current capacity for the HTS bridge and load coil. One possible way to achieve that is to operate the HTS bridge at lower temperature than the load coil. Each of these devices requires only a small amount of supply to produce any desired level of current, while the limit is imposed by the maximum current that can be carried by the HTS load (i.e., the critical current). To scale up the pumped current level, one needs to increase the load current capacity.

Meanwhile, due to the distinctive topologies, there are critical differences between the two types of HTS flux pumps. As shown in figure 2.9.1, the entire charging process occurs in one single loop, which means that the magnetic induction and switching are tightly coupled in a traveling wave HTS flux pump. This makes it difficult to mitigate the loss, because the transport current will always need to flow through the resistive HTS path. Yet, for a transformer-rectifier HTS flux pump, as shown in figure 2.10.1, the charging current and transport current are separated. Hence, it is possible to suppress the loss, at least, by independently minimizing the off-state loss (e.g., when the applied field is removed). There is a sort of trade-off between the two types of HTS flux pumps, while the travelling wave HTS flux pump has the simplest structure and requires the least superconducting materials, the transformer-rectifier HTS flux pump possesses more flexibility and can possibly maintain lower loss.

Both of the two categories of HTS flux pumps support reversable operations. To invert the load, one can simply flip the wave propagation direction for a travelling wave HTS flux pump. By controlling whether the resistivity is triggered in the positive or negative half cycle of the secondary current, similar inversion effect can be achieved for a transformer-rectifier HTS flux pump. A comparison between different types of HTS flux pumps is presented in table 2.12.1.

Table 2.12.1. Comparison between major HTS flux pump categories.

Type	Pros	Cons	Notes
Rotary HTS flux pump	Simplest structure, easiest operation, least material consumption.	Mechanical drive is required to create relative motion between static and moving parts.	Losses are presented and difficult to mitigate due to the single loop topology.
Linear HTS flux pump	Concise configuration. The external field can be tuned easily.	Magnetic framework is required to divert flux path.	
AC field switched transformer-rectifier	The flux pumping process consists of several independent steps, thus highly flexible.	The system is sophisticated and imposes many operational considerations.	Losses are presented but can be modulated since the transport current and charging current are separated.
Self-regulating transformer-rectifier	It can operate at completely current-driven mode without any external field involved.	Potentially unstable due to the sharp ***E-J*** relation.	
Power electronics switched	Power electronics devices such as MOSFETs, IGBTs are cheap and widely available.	Commonly in power electronics devices, the on-state resistance is inevitable.	The operating frequency and output ripple are highly associated with electronics device standards.

Note: None of these HTS flux pumps need to break superconductivity during operation.

As introduced earlier, there are various modelling techniques that can be used to simulate the operation of different HTS flux pumps. Most of the methods are single or coupled formulation-based numerical models to be solved in FEM software, while some others can be computed more directly. Typical modelling approaches for major HTS flux pumps are compared in table 2.12.2. For travelling wave HTS flux pumps, especially for the rotary type, numerous FEM models have been investigated. Currently, the most efficient model for travelling wave HTS flux pumps is the Chebyshev polynomials based numerical model, which outperforms all other models in terms of the computation time. For transformer-rectifier HTS flux pump, the computational cost for FEM models can be expensive, thus models based on simplified equivalent circuit have been proposed, which can considerably reduce solution time. All models listed in this table have acceptable accuracy level, please check the corresponding references for more details.

Table 2.12.2. Typical modelling approaches for different HTS flux pumps.

Type	Model	Time [min/cycle]	Implementation
Travelling wave HTS flux pump [144]	***H-A*** formulation	2.1	COMSOL 5.5
	T-A formulation	3.9-64.6	COMSOL 5.5
	H formulation with shell current	7.9	COMSOL 5.5
	Segregated H formulation	2.6	COMSOL 5.5
	IE	5.1	COMSOL 5.5
	MEMEP	0.25	C++
	VIE	1.6	MATLAB
	Chebyshev polynomials [141]	0.05	MATLAB
Transformer-rectifier HTS flux pump	***H*** formulation [159]	>500	COMSOL 5.4
	Electrical circuit [171]	Not reported	SPICE
	Electrical circuit (one switch) [160]	~1	Simulink
	Electrical circuit (two switches) [173]	~1	Simulink

Closed loops, e.g., coils, connected to these flux pumps can be charged in a certain manner. However, the charging performance can be varied due to the specific arrangement, it is less applicable to simply characterize it in one standard. For example, the charging capacity of a flux pump is primarily determined by the critical current of the HTS tapes, thus completely different charging current can be achieved by the same type of flux pump, depending on the specifications of HTS tapes employed. Besides, the charging speed is directly influenced by the induced open circuit voltage, which is controlled by a set of parameters, e.g., the operating frequency, magnetic field strength and so on. In order to give an overview of the performance of typical flux pumps when applied to charge a closed loop, some charging test results reported in existing literature are summarised in table 2.12.3, more details regarding the specific charging process can be found in corresponding references.

Table 2.12.3. Implementation records of typical HTS flux pumps.

Type	Charge speed	Scalability	Notes
Rotary HTS flux pump	120 s	90 A	1 tape with I_c=95 A @ 77 K [103]
Linear HTS flux pump	40 s	80 A	1 tape with I_c=94 A @ 77 K [108]
AC field switched transformer-rectifier	150 s	1100 A	3 tapes with I_c=700 A @ 77 K [150]
Self-regulating transformer-rectifier	122 s	2100 A	5 tapes with I_c >500 A @ 77 K [153]

It should be pointed out that the definition of an HTS flux pump in the scope of this work is a device that can achieve flux pumping without breaking superconductivity in HTSCs at any given time during operation. In order to provide the most intuitive explanations for specific types of HTS flux pumps, the working mechanisms for typical variants of the HTS flux pump were separately introduced in Sections 3 and 4. However, we must emphasize again that the underlying physics is united, all of which point to the same principle, namely that a non-linear resistivity needs to be stimulated. More precisely, the AC-switched transformer-rectifier HTS flux pumps directly utilise the dynamic resistance that occurs when HTSCs carrying DC currents are exposed to external AC fields. The non-linear resistivity theory for travelling wave HTS flux pumps is essentially based on the *E*-*J* power law, the same as for the self-regulating transformer HTS flux pump which can be interpreted as an alternative manifestation of dynamic resistance.

2.13 Applications

As previously mentioned in the paper, HTS flux pumps provide a promising solution for efficient load energisation. One the one hand, it obviates the need for physical current leads, which not only simplifies the structural layout but also dramatically relieves the heat load imposed on the cryogenic system. On the other hand, very high current can be obtained by repeatedly applying a small field without involving expensive and bulky power supplies, saving considerable capital cost. These unique merits are exceedingly attractive in a wide range of applications, including but not limited to electrical machines, ultra-high field magnets, MRI/NMR, generally wherever high current and/or high magnetic field are demanded.

In the electrical machine domain, the rotary HTS flux pumps are considered as congenitally beneficial, because they can take advantage of the inherent motion between the rotor and stator in an electric machine to achieve flux pumping. By applying rotary HTS flux pumps to energise field windings, neither slip rings or brushes are required, which are major sources of failure in an electric machine. In [73], Sung et al. outlined the design and heat analysis of a 12 MW HTS wind power generator module employing an HTS dynamo. The results have shown that total heat loss can be maintained at 39 W when the coil supporter adopts zigzag or pole shapes. The GM cryocooler has 50 W thermal capacity for the HTS coils to be operated at a temperature under 20 K, so the application of a rotary HTS flux pump in this wind power generator demonstrates clear feasibility [174]. In [72, 175], the design was experimentally verified by fabricating Double Pancake Coils (DPCs) for the rotor poles of a 10 kW, 200 rpm wind power generator prototype. It was reported that the field windings can be energised to 1.5 T field through the injection of 85 A per pole. Research groups in Korea have proposed a structural design for a 12 MW HTS generator employing rotary HTS flux pumps in [176], where all the HTS field windings are structurally separated as shown in figure 2.13.1 (a). Each HTS module coil consists of several components, including HTS field coils, coil bobbins, bobbin supports, a heat exchanger, a flux pump, a cryostat, and a cryo-cooler. The flux pump exciters located in each module are defined as rotating and stationary parts as shown in figure 2.13.1 (b) (similar to the flux pumping part and charging part in figure 2.9.1 (a)). The rotating parts are rotated by interlocking gear teeth of the generator and flux pump exciter, while the stationary parts are included in the cryostat of the coil module to directly connect the HTS field coil with HTS stator wire. A more recent work published by Kalsi et al. [177] described a 2 MW, 25000 rpm concept design for homopolar superconducting AC machines, with rotary HTS flux pump driven field coils, for aerospace applications. The design was inspired by the General Electric's Homopolar Inductor Alternator (HIA) prototype [48], achieving a power density of ~9 kW/kg for a 5MWA, 35000 rpm machine. Machines of this type are an ideal choice for future aerospace applications, because both the AC armature and DC excitations are included within the stationary part of the machine, as shown in figure 2.13.2 (a). A solid steel rotor is magnetized by the stationary excitation winding, so that the operating speed is limited only by the mechanical stress limit of the rotor steel. The rotary HTS flux pump to be integrated with the circular coil is shown in figure 2.13.2 (b), which is capable of managing field current in the range of 188–364 A. Following the preliminary charging test of HTS coils for the rotor field winding of a 1-kW-class HTS rotating machine [178, 179], the world's first implementation of an HTS machine that employs an HTS rotary flux pump as the exciter has been reported in [180]. A maximum output power of 1779 W has been successfully obtained, with the rotating speed of 600 rpm, field current of 1.72 A, and average three phase load of 203 ohms. The excitation loss (for field current below the saturated value at 100 A) was estimated to be 1.11 W, which is approximately 91.5% less than those of the two pairs of copper current leads.

Superconducting technology has boosted MRI/NMR advancement over past decades, by the means of providing high magnetic fields that are not available from conventional magnets. MRI/NMR equipment requires the continuous production of a large homogenous field, typically 1–7 T. The state-of-the-art technology employs LTSCs, which need to cool down to liquid helium temperature 4.2 K. It is rather evident that LTSCs for current MRI/NMR technology are reaching their bottlenecks and new developments such as obtaining higher fields and reducing operational costs are in favour of HTSCs [181-184]. HTSCs not only can operate at relatively elevated temperatures (typically 100 K or above), but also are able to withstand intensive magnetic field strength, which can theoretically go up to the orders of hundreds of Tesla in magnitude. The HTS flux pump technologies, with the advantage of reliving heat load, offer additional benefits by enabling much more compact structure. The electromagnetic design of a 1.5 T REBCO magnet for dedicated MRI has been presented in [185]. By applying no-insulation linear HTS flux pump technology, the magnet was contained within a compact volume; the outer diameter and axial length are both less than 300 mm, diameter of the room-temperature bore is 200 mm. Moreover, the superconductor consumption can be greatly saved by 29.7% via employing multiple HTS flux pumps as the excitation sources. The idea of constructing a compact and mobile HTS MRI head scanner has been reported in [186], in which a half-bridge transformer-rectifier type HTS flux pump is employed to induce current in the form of triangular waves at a near DC frequency (5–10 Hz).

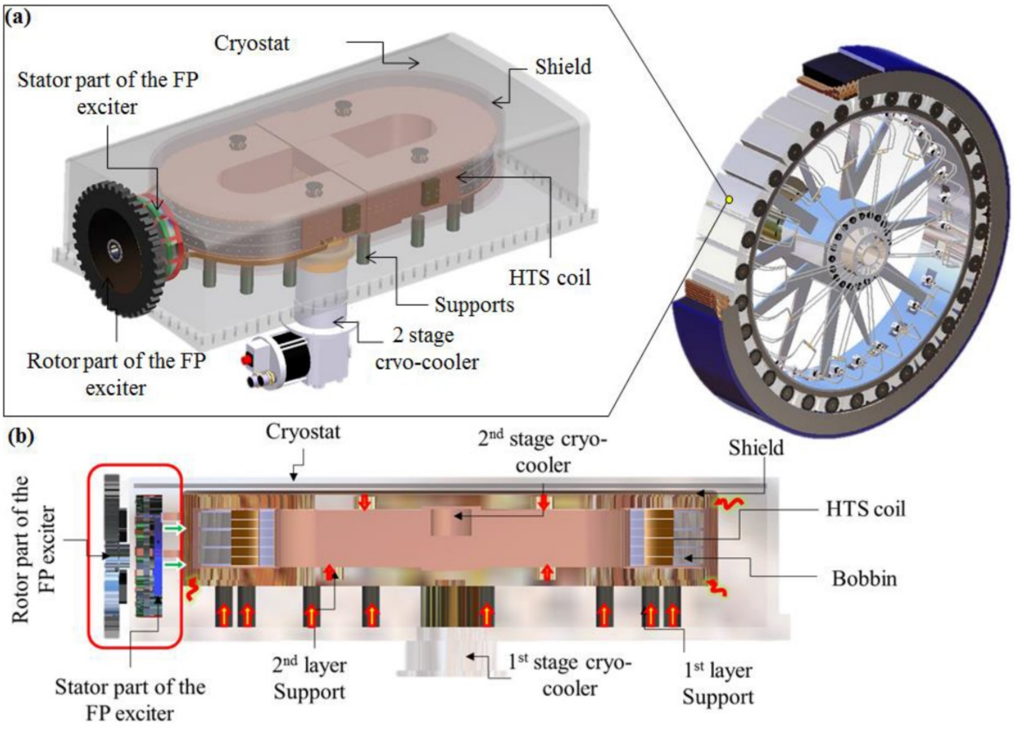

Figure 2.13.1. Configuration of the rotary HTS flux pump-based module coil. (a) overview (b) cross section view, of a separated unit of HTS field coil. Reprinted from [176].

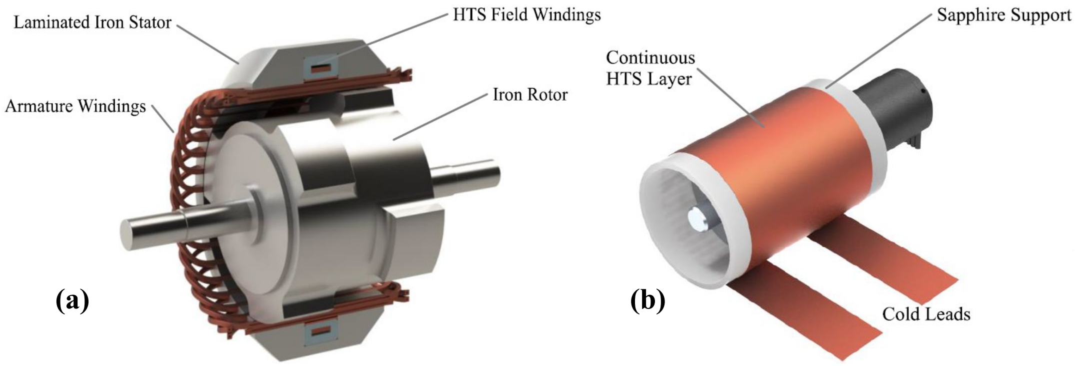

Figure 2.13.2. (a) Sectioned view of the AC homopolar motor/generator, (b) rotary HTS flux pump concept to be integrated with the field coil. Reprinted from [177].

For ultra-high field magnets required for diverse scientific and industrial uses, it has been validated that high-field copper oxide superconductor magnets can break through the top limit set by LTSCs [187]. In such cases, HTS flux pumps are also ideal candidates for providing either the background field of the direct-current hybrid magnets [188] or the desired field directly. As already discussed above, HTS flux pumps can be driven by a small magnetic field to energise the load coils, and the charging cycle can be continuously repeatedly. In other words, any desired currents, thus equivalent magnetic fields, are achievable, whilst the limitations are only imposed by the HTSCs current transport capacity and inherent losses. A quasi-persistent current of over 1.1 kA has been achieved using an AC field switched transformer-rectifier HTS flux pump, maintaining high flux injection accuracy with an overall flux ripple of less than 0.2 milli-Weber [150]. The record was broken soon afterwards when a maximum pumped current greater than 2 kA was reported in [153], utilizing a self-regulating HTS flux pump. In such a device, over 1 kA current was still achievable even with a 6.8 mm airgap incorporated into the steel transformer core. Judging from existing developments, it is promising that the HTS flux pump can play a key role in ultra-high field magnets.

2.14 Conclusions

Essentially, HTS flux pumps are enabled by the dynamic resistance caused by the hysteretic and flux flow effect. Despite remarkable progress being achieved in HTS flux pumps from different perspectives, there are some areas that are relatively overlooked and/or still challenging, some of which are highlighted here.

Most work about HTS flux pumps presented in current literature focuses on operational research and theoretical analysis, namely, how to increase the pumped current and figure out the underlying mechanism. Limited attention has been put on the losses associated with HTS flux pumps [189], which directly determine the efficiency of the flux pump system. The scenario, where conducting superconductors are exposed to external AC fields, appears in almost all HTS flux pumps, which means there must exist certain AC losses [24, 30, 190]. Especially for the AC field switched transformer-rectifier HTS flux pump, in which their working principles are essentially based on AC losses. Besides, in order to scale up the pumped current, one will need to solder multiple HTS loads together with multiple HTS bridges (switches). As a result, it is inevitable that extra heat losses due to non-zero joint resistances will be produced [150]. A recent work [191] has described the energy balance for HTS dynamos, in which it was demonstrated that due to the interactions of induced currents with rotating PMs, a significant part of the mechanical power supplied to the rotor is converted into Joule dissipation with HTSCs. If these losses are not well modulated, the HTS components may be placed at risk of quenching, which will result in failures of the whole system.

The most obvious criterion to evaluate the performance of an HTS flux pump is the output voltage (in open circuit condition) or pumping current (in closed loop condition). Ideally, we want the output to be as high as possible. However, it should be aware that the peak of the output is not the only concern. In many cases, the ripple plays a critical role. For instance, in a synchronous machine, if the excitation current in field winding is not maintained constant, the electromagnetic force generated by the external rotating field changes accordingly, which will cause output fluctuation or even fatal damage to the machine. Due to external vibrations, such as noise from the input system, ripples can be expected in any type of HTS flux pump. In particular, the self-regulating transformer-rectifier flux pump is operated in the flux flow regime (sharp *E-J* relation), where small turbulence in the current can result in very large ripples. Hence, it is necessary to integrate a reliable control system into HTS flux pumps to stabilize the output. The authors of [192, 193] proposed a proportion-integral-differential (PID) loop for a rotary HTS flux pump and [194] demonstrated a feedback circuit for a transformer-rectifier flux pump, both showing great effectiveness for smoothing the output ripple. A sensitive control system is desired for more sophisticated applications.

One of the key obstacles that hinders the advancement of the HTS flux pump is the operating cost. The HTS components, which are not cheap themselves, plus the expensive compulsory cryogenic system make the construction and operation of such devices costly. Alternatively, accurate simulation can be utilized to investigate HTS flux pump without undertaking up real experiments, saving substantial costs. The modelling of HTS flux pumps has been mainly relied on FEM models, which are extremely helpful for acquiring details about the electromagnetic behaviour involved in HTS flux pumps. However, FEM models are often time consuming, because they need to mathematically simulate the whole process to replicate the real case. Besides, FEM models require users to have abundant knowledge about the problem they are modelling. These features are absolutely not preferred from the perspective of industrial design and optimization, where the interests are capturing certain specifications that can evaluate the device performance rather than delving into the underlying physics. Currently, there are no solutions available for this issue, and the thesis will aim to fulfil this gap.

In summary, the HTS flux pump is a promising technology for contactless energisation, with higher efficiency, lower cost, and more compact size. In practical scenarios, HTS flux pumps provide general advantages for designing more flexible MRI/NMR with reduced cost. The travelling wave HTS flux pumps, especially the rotary type, show clear attractions for the next generation of electric machines, where high power density is demanded. The transformer-rectifier type of HTS flux pumps possesses considerable scale-up possibility, which is very promising for the development of ultra-high magnets. It is reasonable to expect that HTS flux pumps will become an enabling technology in various industrial sectors. In brief, all existing HTS flux pumps have been presented in detail, illustrating their design, physical mechanism, operational characteristics, as well as modelling methods. Proposals have been put forward to address potential concerns for future development. This chapter has provided an in-depth insight into the HTS flux pump technology in order to inspire further advances in the technology.

Chapter 3

Output Characteristics and FEM Simulation of Rotary HTS Flux Pumps

Rotary HTS flux pump, or so-called HTS dynamo, was firstly proposed by Hoffman et al. [95]. The HTS dynamo that utilises rotating permanent magnets to provide a time and space varied magnetic waveform and hence induce a DC biased voltage across the HTS stator wire, has drawn extensive attention, especially in the field of HTS machine design. The method of energisation of superconducting coils in electrical machines is generally assumed and few design details are provided. For stationary coils the traditional approach is to inject currents into the coils via leads which transport current from ambient temperature to the cryogenic environment. This imposes a considerable heat load upon the cryogenic system [72-74], and results in significant additional capital and operating cost [195]. For rotating coils there is the additional challenge of transfer of large DC currents across a rotating joint. The existing excitation methods, including utilization of slip rings [196] and high-frequency brushless exciters [197, 198], all increase the cost and complexity while undermine the performance [75]. Slip-ring components suffer from arc erosion at high currents [199], especially for operation at high frequency [200]. Though inductive brushless-exciters [201] provided a potential way to avoid direct electrical contact, they require rigorous power electronics operated in switched-mode to deal with large DC currents, which negatively impacts the overall power density, reliability and ease of maintenance. The simple and straightforward structure of HTS dynamos, and the benefits they offer to eliminate the brushes and slip rings, make them a very promising candidate for exciters in future HTS machines.

In order to explore more knowledge about the rotary HTS flux pumps, numerical models have been developed in this chapter. These numerical models, based on certain formulations, can simulate the operation of such devices, and replicate some of the key physics. Therefore, the simulation results can be utilised to reveal and analyse the output characteristics of rotary HTS flux pumps.

3.1 ***T-A*** model

3.1.1 Formulation description

For simplicity, the HTS dynamo can be modelled in a two-dimensional structure, as shown in figure 3.1.1. It consists of a rotating domain and a stationary domain. The rotating domain contains the rotating disc (indicated by the blue solid cycle) and the permanent magnet within it (indicated by the blue rectangle line); the space outside of the rotating disc is the stationary domain, where the HTS tape (indicated by the red rectangle) is located. In this 2D model, it is assumed that the HTS tape is infinitely long and has a thickness of 100 μm, and only the HTS layer is taken into account, which have been verified as reasonable approximations for modelling superconductor thin tapes. As discussed in the last chapter, various formulations have been implemented into commercial FEM software, e.g., COMSOL Multiphysics, for HTS modelling. Among those well verified formulations, the unique feature of coupled ***T-A*** formulation is that it simulates the superconductor as a 1D object in this 2D problem, which simplify the modelling process and relieve computation cost, and hence it was chosen to reduce the model complexity.

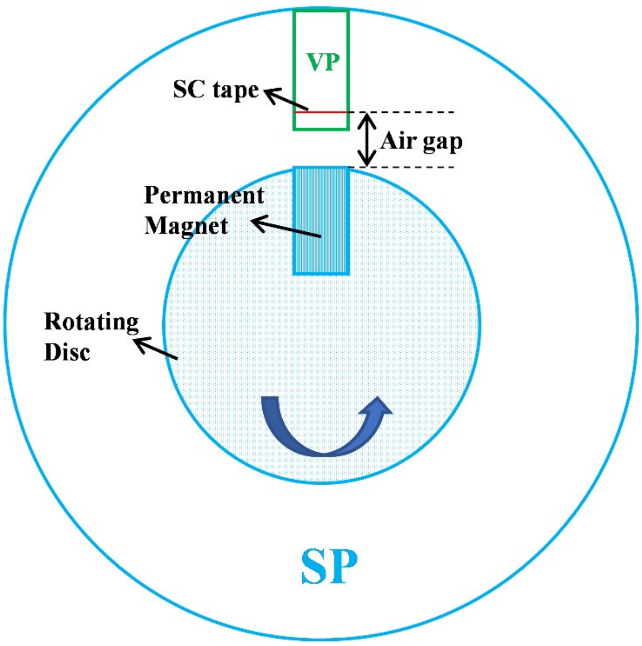

Figure 3.1.1. Schematic illustration of the basic geometry of the 2D H-formulation model used in this work, showing the modelled cross-section of the device with a 12 mm wide stator tape. Different model domains are indicated respectively, namely the magnetic vector potential (VP) region, the magnetic scalar potential (SP) region, and the T-formulation (superconductor) region. Note that the geometry is presented in the x-y plane, and the +z orientation aligns with direction that points into the plane.

The coupled ***T-A*** formulation was firstly proposed by Zhang et al. [126] and has been validated to calculate the electromagnetic characteristics of HTS tape stacks and coils made of HTSCs. As shown in figure 3.1.2, in the superconductor region, the current vector potential $\boldsymbol{T}$ is chosen as the solved variable, and the governing equations are:

$$\boldsymbol{J} = \nabla \times \boldsymbol{T} \tag{3.1.1}$$

$$\nabla \times (\rho \nabla \times \boldsymbol{T}) = -\frac{d\boldsymbol{B}}{dt} \tag{3.1.2}$$

where $\boldsymbol{J}$, $\boldsymbol{T}$, ρ and $\boldsymbol{B}$ represent the current density, current vector potential, resistivity, and magnetic flux density, respectively. For a thin HTS tape, its thickness (in the scale of micrometres) is typically much smaller than its width (in the scale of millimetres), thus one can represent the HTS tape as a line without thickness, so that the current only flows in the tangential direction ($J_y = 0$). Besides, the HTS tape is assumed infinitely long, and hence one can further claim that the current flows in the longitudinal direction only ($J_x = 0$). In such condition, equation (3.1.1) and (3.1.2) can be simplified as follows:

$$J_z = \frac{\partial(\boldsymbol{T} \cdot n_y)}{\partial x} \tag{3.1.3}$$

$$-\frac{\rho \cdot \partial(\boldsymbol{T} \cdot n_y)}{\partial_x{}^2} = -\frac{\partial B_y}{\partial t} \tag{3.1.4}$$

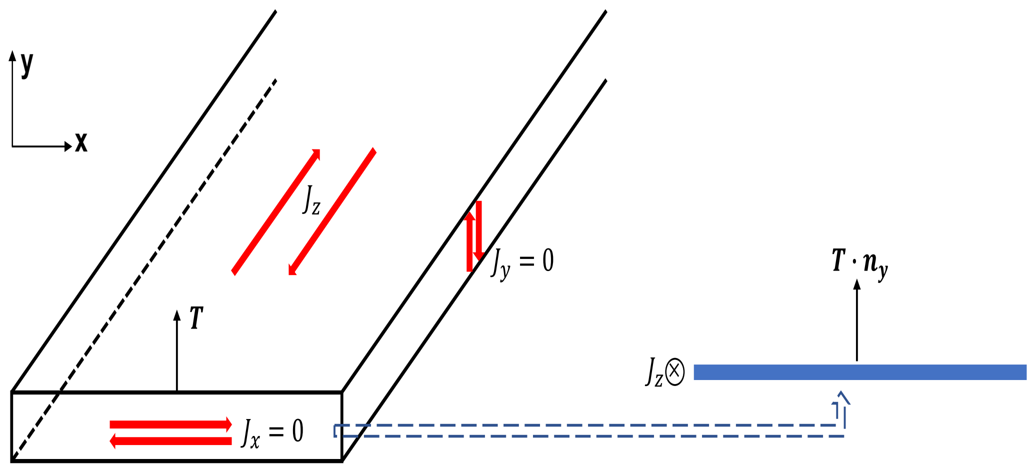

Figure 3.1.2. A schematic of a single 2G HTS layer. Note that the superconducting layer is simulated with a line that has no thickness, but the thickness of the superconducting layer is also plotted in the diagram to make it easy to understand.

For the whole space, the magnetic vector potential $\boldsymbol{A}$ is utilised to link with the distribution of sheet current density in the superconductor:

$$\nabla \times \left(\frac{1}{\mu} \nabla \times \boldsymbol{A}\right) = \boldsymbol{J} \tag{3.1.5}$$

where μ is the magnetic permeability. Equations (4.1.4) and (4.1.5) can be put together and solved, by combining following equation:

$$\boldsymbol{B} = \nabla \times \boldsymbol{A} \tag{3.1.6}$$

Meanwhile, in this configuration, effective currents can only exist in the HTS tape, which means that one can introduce the magnetic scalar potential V_m to calculate the magnetic field in the rest of space:

$$\boldsymbol{B} = \mu \nabla V_m \tag{3.1.7}$$

Following this idea, the model is divided into two regions, namely the magnetic vector potential (VP) region in close proximity to the HTS tape and the magnetic scalar (SP) potential region in the rest of the space. By replacing $\boldsymbol{A}$ with V_m, the solution time can be dramatically reduced, because the computational cost of scalar is much less compared to vector.

In addition, the *E-J* power law is employed here to represent the electrical characteristics of superconductors:

$$E_z = \rho J_z = E_c \left(\frac{J_z}{J_c(B)}\right) \left(\frac{|J_z|}{J_c(B)}\right)^{(n-1)} \tag{3.1.8}$$

where E_c and n are constant coefficient, whose values are chosen as 1×10^{-4} V/m and 20 respectively, and the critical current density $J_c(B)$ is a magnetic field dependent variable. In order to compare our results to the work presented in [114], the magnetic field dependence of the critical current density is represented by a practical interpolation function directly obtained from the experimental measurements in [114] (data are provided by our partners in the Victoria University of Wellington).

The instantaneous equivalent voltage V_{eq} is defined as:

$$V_{eq}(t) = -L \cdot \frac{1}{W_s} \int_0^{W_s} E_Z(x,t)\, dl \tag{3.1.9}$$

From where the open circuit voltage can be derived:

$$V_{oc} = \frac{1}{T}\int_{T}^{2T} V_{eq}(t)\, dt \tag{3.1.10}$$

Note that L is the active length of the dynamo, i.e., the depth of the permanent magnet. The second periodical cycle is chosen to perform the calculations, avoiding any initial transient effect that may be present in the first one.

Considering the fact that the HTS tape is open circuit, there should be no net transport current at any given time, so following constraint is imposed:

$$I(t) = \int_{0}^{W_s} J_Z(x,t)\, dl = 0 \tag{3.1.11}$$

3.1.2 Model validation

Following the modelling definitions introduced above, a numerical model was built to be solved in the commercially available FEM software COMSOL 5.5. Different state variables are chosen to solve Maxwell equations in different regions: the current vector potential $\boldsymbol{A}$ is solved only in the superconducting domain, and the magnetic scalar potential V_m is solved in the whole space. However, due to the internal software settings that forbids existence of current within any closed loop in the region that calculates V_m, $\boldsymbol{A}$ is solved in a small area with close proximity to the superconducting region. In order to verify the applicability, this model was adapted to represent the experimental set up described in [114]: a 12 mm wide ReBCO tape (Superpower SF12050F) is separated from a NdFeB magnet by an airgap of 3.7 mm. The magnet has a remanent flux density of 1.25 T and is embedded in a cylindrical disc with radius of 35 mm. The HTS dynamo is operated at low frequency 4.25 Hz. The simulations are performed under two different conditions, one takes the magnetic field dependence of critical current density $J_c(B)$ into account, while the other considers J_c as a constant. The critical current for each case is plotted in figure 3.1.3. In the case where magnetic field dependence is considered, an approximation has been made to simplify the analysis. Since the superconducting layer is represented as a 1D line in the modelling framework, there will be no magnetic field differences in the superconductor along y direction. As a result, we can presume that only the vertical component B_y of the magnetic field needs to be accounted, while the horizontal component B_x can be ignored.

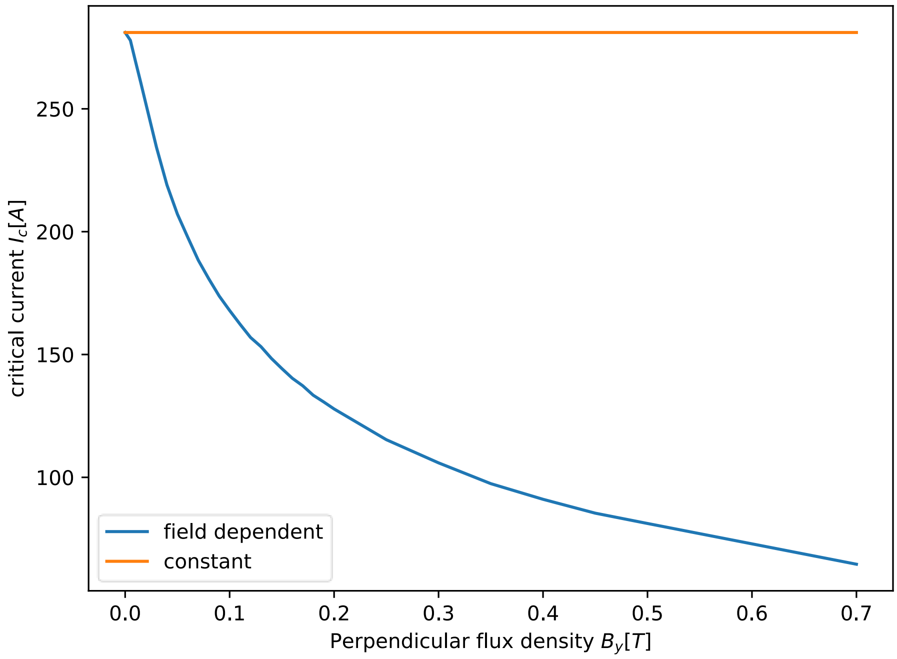

Figure 3.1.3. HTS tape critical current versus the perpendicular component of flux density.

The simulation results have been compared with data measured in experiments as shown in figure 3.1.4, in which excellent correlation can be observed. The distinct four peaks and noticeable left-to-right asymmetry observed in experiments have been reproduced qualitatively in figure 3.1.4(a), and the quantitative agreement between the experimental and simulation results from the model that takes the $J_c(B)$ dependence into account is very good in figure 3.1.4(b). With the periodic operation, the time averaged output voltage tends to converge into a stable value, which is equivalent to a DC voltage source. The up-biased open circuit voltage obtained from the model with constant critical current density can be readily understood by considering the dynamic resistance effect [106, 156, 157]. As stated in [114, 156], the open circuit voltage of an HTS dynamo originates from the actions of circulating current within the HTS tape, which can be equivalently reflected by the voltage division on the backward and forward eddy current regions, and it is the electric field generated on the forward eddy current region that essentially forms the none-zero DC output voltage (see more details in section 3.2.3). The forward region, aligned beneath the permanent magnet position, would demonstrate a significantly higher dynamic resistance if the field dependence is considered, and hence more proportions of the conserved EMF (by Faraday's law) are distributed on this region. As a combinational result, higher DC output voltage is generated eventually.

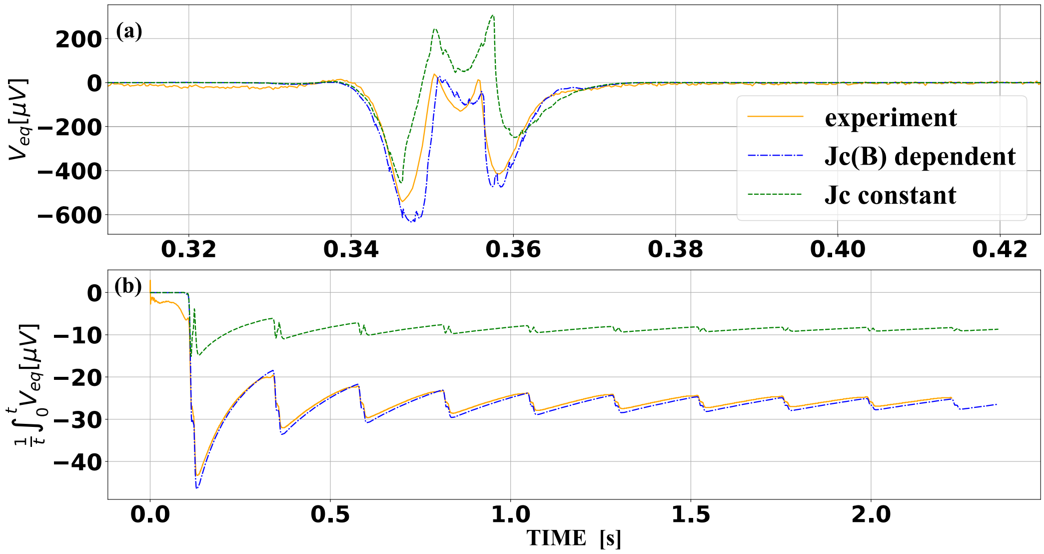

Figure 3.1.4. Instantaneous open circuit equivalent voltage waveforms for the 2nd transit of the permanent magnet past the HTS tape calculated by our model used in this work, ignoring any initial transient effects that may be present in the 1st cycle. (b) Cumulated voltage across the tape over ten cycles. The experimental results are drawn from [114].

3.2 Parameter sweep

Four groups of simulations were arranged to illustrate the relations between different parameters and the open circuit voltage of the rotary HTS flux pump, where in each group only one parameter is altered while the others remain constant.

Figure 3.2.1(a) shows the frequency response within the input range from 10 to 100 Hz, aligning within the frequency range explored in the experimental results in [102]. It is worthwhile mentioning that a perfect linear relation was observed in [102] as the frequency increased from zero until a turning point was captured at approximately 100 Hz, which can attribute to the current interactions between layers of the HTS tape [105] under high frequency. The single layer numerical model is not suitable for manifesting the multi-layer current interactions related phenomenon, hence in figure 3.2.1(a) the frequency is limited under 100 Hz to avoid this issue. Figure 3.2.1(b) and 3.2.1(c) illustrate how the output voltage varies with the air gap and the width of superconductor tape respectively, namely the open circuit output voltage decreases towards zero along the increase of air gap, and increase from zero along the increase superconductor tape width. Both of them show acceptable agreement with previous work in [101, 103], which further validates the effectiveness of this model. The impact of the remanent flux density of the permanent magnets upon the open circuit voltage is included in figure 3.2.1(d), and initial results implies it has a clear positive correlation with the open circuit voltage. In summary, within the ranges investigated in our work, it was found the open circuit voltage tends to only monotonically decrease with the air gap, whilst increasing with the other parameters. In particular, the response variable of open circuit voltage demonstrates obvious linearity with frequency, and non-linearity was observed for all the rest parameters. As for the variations of superconductor tape width, it appears that there exists an optimal point, after which its positive correlation against the open circuit voltage becomes negative, which will be discussed in more detail later.

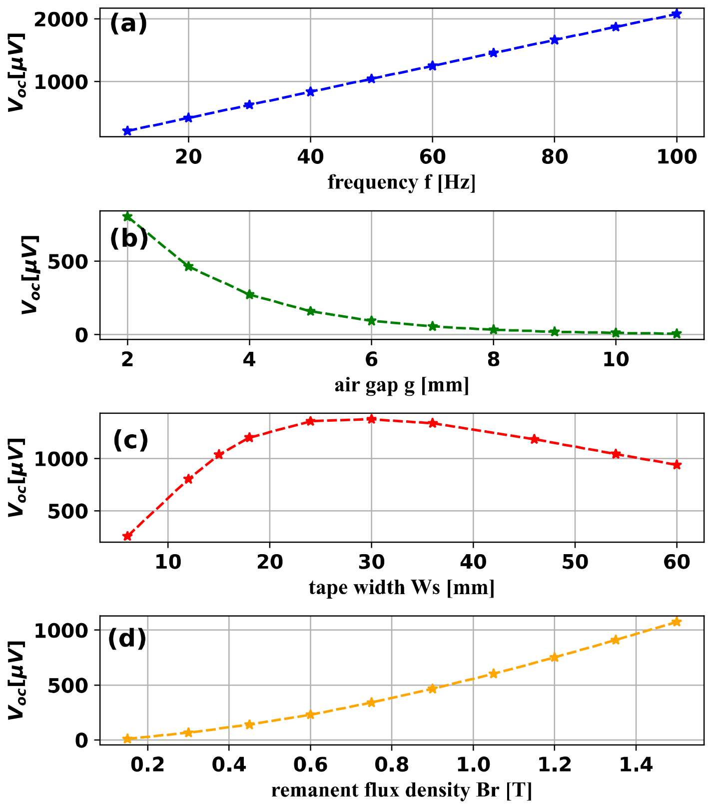

Figure 3.2.1. Calculated open circuit voltage V_{oc} versus different parameters: (a) frequency f, (b) air gap g, (c) stator width W_s, (d) remanent flux density B_r.

3.2.1 Impact of f on V_{oc}

Inspired by the observations in figure 3.2.1(a), it is reasonable to believe that the function that describes V_{oc} about frequency f can be formulated by a straight line passing through the origin under the condition where all other parameters remain the same. Hence, it leads to a critical question: does this linear relationship hold through the variation of other parameters? In order to investigate this problem, each of the other three parameters were varied under different frequencies, so that the frequency-normalized output profile V_{oc}/f can be plotted for each of the frequencies. It can be seen from figure 3.2.2 that the response level of V_{oc} against each of the other three parameters does vary under different frequencies as demonstrated by the separated solid lines, whilst the frequency-normalized output profiles collapse together as indicated by the dash lines in each subplot. Taking figure 3.2.2(a) for consideration, the curve behaviours mentioned above can happen only if the frequency acts as an independent 'amplifier' in the determination of V_{oc}, which implies that the linear relation between V_{oc} and f holds well, in regardless of the variation of superconductor tape width. The same idea also applies to the figure 3.2.2(b) and 3.2.2(c), so a simple frequency normalization can be derived in the following:

$$V_{oc}(f, g, Ws, B_r) = f \cdot \frac{V_{oc}(f,g,W_s,B_r)}{f} = f \cdot V_{oc}(g, W_s, B_r) \qquad (3.2.1)$$

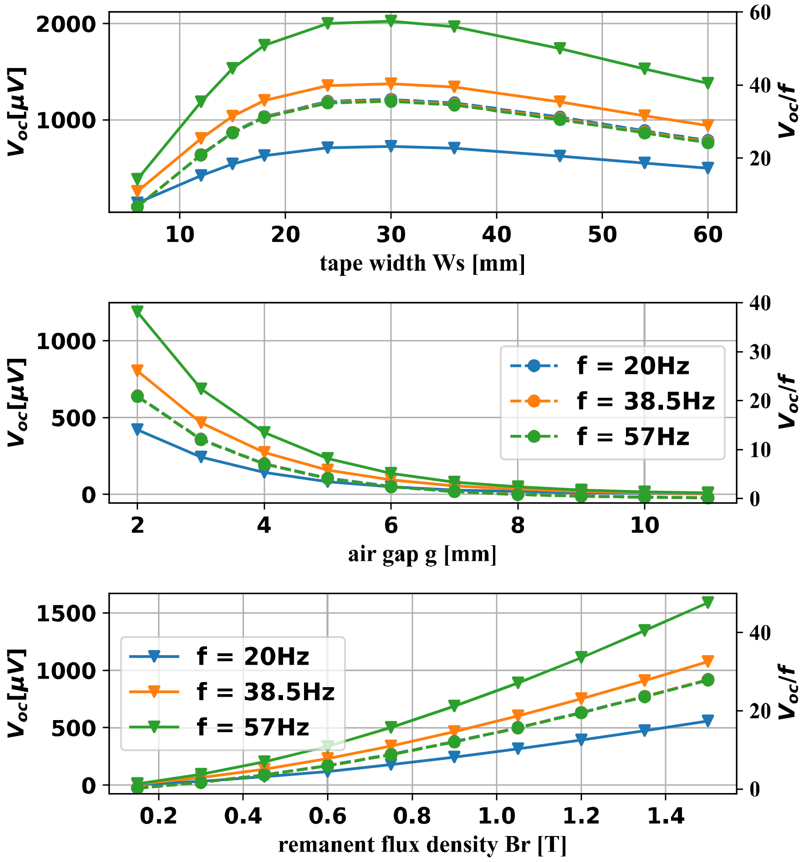

Figure 3.2.2. V_{oc} curve for each parameter under selected frequencies (solid lines are referred to the vertical axis on the left, and the vertical axis on the right are for the dash lines): (a) air gap g, (b) stator width W_s, (c) remanent flux density B_r.

3.2.2 Impact of g and B_r on V_{oc}

The consequence of adjusting the air gap g or remanent flux density B_r will be reflected by the changing of peak flux density on the surface of the tape, as well as the flux passing through it. More precisely, increasing g or decreasing B_r will lead to a smaller magnetic field seen by the tape surface, and less flux can be captured by the closed loop within the tape, e.g., if the magnet is moved away from the tape or replaced by another one with smaller remanent flux density, the tape is then effectively exposed to a smaller magnetic field, and vice versa. According to Faraday's law, the electromotive force around a closed path is equal to the negative of the rate of change of the magnetic flux enclosed by the path. Under the condition of fixed frequency, the magnetic flux traversing the tape per unit time is determined by the remanent flux density as well as air gap. Hence, the open circuit voltage V_{oc}, which is the time integration of the electromotive force, should drop according to an increase in g or decrease in W_s, due to the reduction of flux along with its changing rate. This is clearly revealed by the results in figure 3.2.1(b) and figure 3.2.1(d), where it was shown that V_{oc} drops from 800 μV with a 2 mm air gap and approaching zero after the air gap exceeds 8 mm, while V_{oc} climbs from approximately 0 to 1000 μV for values of B_r varying between 0.15 and 1.5 T. It is worthwhile mentioning that both extreme cases, where the gap distance goes to infinity and the remanent flux density reaches zero (the magnet loses magnetism) are well demonstrated in the results by confidently implying a zero output in those conditions.

3.2.3 Impact of W_s on V_{oc}

As indicated in figure 3.2.1 (c), V_{oc} increases gradually as the HTS tape width increases from 6 to 30 mm, after which it starts to decrease if W_s if further increased. This matches the experimental results presented in [103], where the *I-V* curve intercept on the x-axis firstly becomes more positive and then less positive for the tape width increasing from 6 mm to 46 mm. Yet the *I-V* curve from our model plotted in figure 3.2.3 differs from the one presented in [103], in which a straight line is interpolated for each value of tape width. In fact, in their experiments, the net transport current of the tape is constrained by the critical current of the superconducting coil connected to the tape. Thus, for the section of curve with the range of current which exceeds the critical current of the connected coils, it can only be interpolated by first few measurements where the transport current is below coil critical current. In figure 3.2.3, the limits of coil critical current have been removed so that the full profile of *I-V* curve for each tape width can be obtained. The intercept on the y-axis of each curve represents the theoretical maximum current that can be pumped if the connected coils have sufficiently enough capacity, i.e., the coils have a very large critical current. It can be seen from figure 3.2.3 *I-V* curves tend to show non-linearity for large tape width, which is in alignment with the results in [130].

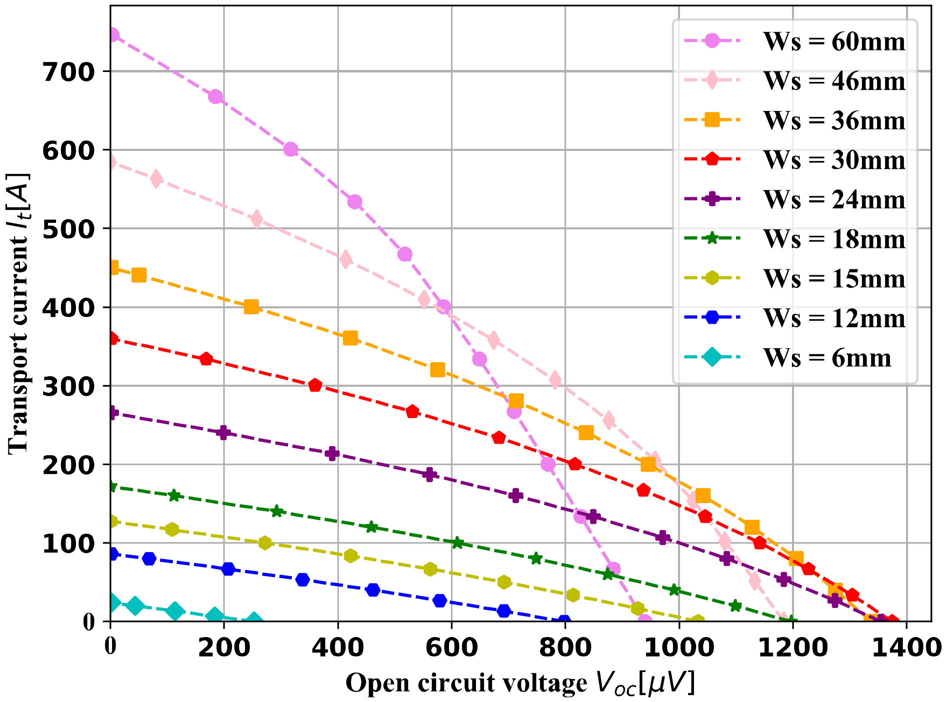

Figure 3.2.3. *I-V* curve obtained from a range of HTS tape widths.

The characteristics of this *I-V* curve can be further explored by analysing I_{sc} (the intercept of *I-V* curve on y-axis) and V_{oc} separately. It is not surprising that the short circuit current I_{sc} increases with the tape width, because wider tape tends to have higher critical current. Two f-ratios, α and β are defined to measure the proportion of the capacity of the tape occupied by the transporting current, given as:

$$\alpha = \frac{I_{sc}}{I_{c,self}} \tag{3.2.2}$$

$$\beta = \frac{I_{sc}}{I_{c,min}} \tag{3.2.2}$$

where $I_{c,self}$ denotes the critical current when the tape is not exposed to any external magnetic field, and $I_{c,min}$ refers to the minimum value of immediate critical current as the applied magnetic field varies. Figure 3.2.4(a) clearly shows that I_{sc} increases with the tape width. Figure 3.2.4(b) illustrates that I_{sc} can reach up to about 55% of the self-field critical current and 75% of the minimum critical current for a 36 mm wide tape, and then stay at this value. Moreover, if we consider the HTS dynamo as an electric circuit comprised by a voltage source with an internal resistor, then its internal resistance can be derived from the slope of the *I*-*V* curve. Due to the existence of non-linearity for some curves, a data point based differential slop has been used to calculate the resistance for each curve. Figure 3.2.4(c) plots the resistance R_{sc} and R_{oc} for each tape width when the tape is shorted (i.e., there is no voltage drop across the tape, $V_{oc} = 0$) and when the tape is isolated (i.e., the net transport current $I_t = 0$), whose values indicate the resistive properties of the tape under high and low current level. It can be seen from figure 3.2.4(c) that R_{sc} and R_{oc} both drop as the tape width increases, meaning that the wider the tape the more superconductivity can be utilised.

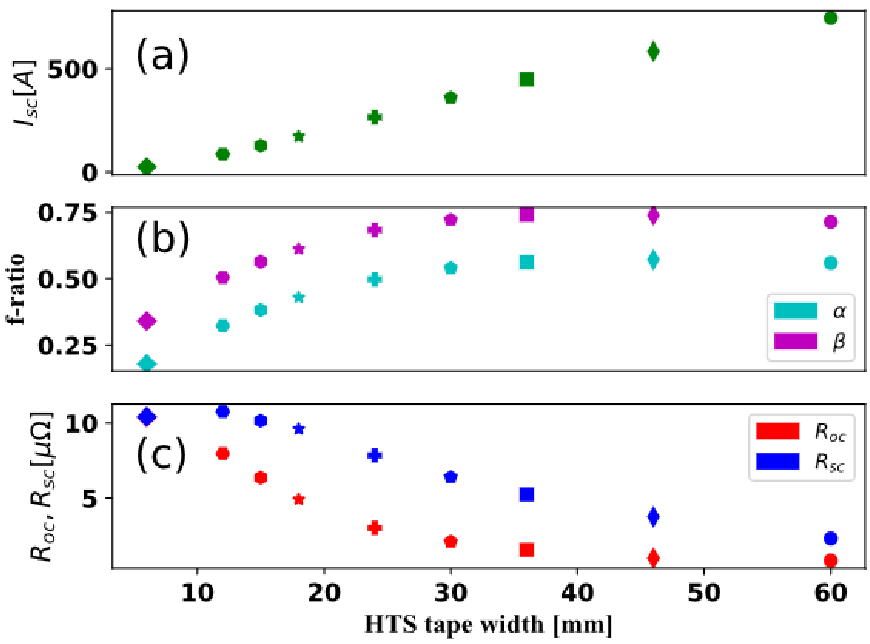

Figure 3.2.4. Derived parameters from *I*-*V* curve: (a) short circuit current I_{sc}, (b) calculated f-ratios (the values of α and β), (c) derived internal resistance in open circuit condition R_{oc} and short circuit condition R_{sc}, versus the HTS tape width.

The most noticeable feature of V_{oc} versus tape width curve is that it increases first and then decreases as the tape gets wider, which makes W_s the only parameter that has a non-monotonical relationship with V_{oc}. In order to understand why this occurs, we need to go back to the origin of V_{oc}. The uneven and nonlinear resistivity distribution of the tape can produce an asymmetric electric field induced by the eddy current under a changing magnetic field as shown in figure 3.1.4(a), which can result in a nonzero time integration and hence an averaged DC voltage output. That is to say, the distribution of instantaneous electric field E_z , or equivalently the averaged instantaneous voltage V_{eq}, has a direct impact on the determination of V_{oc}. Based on this idea, it is reasonable to deduce that the value of V_{oc} can be roughly reflected by the magnitude of the first peak of V_{eq} curve.

As stated in equation (3.1.9), at each instant V_{eq} is calculated by averaging the integration of the electric field along the tape, and it is the net remanent integration of the negative electric field that determines the final value of V_{eq}. Thus, we will need to know how the electric field is distributed along the tape to investigate the formation of V_{eq}. The distribution profiles have been captured for selected tape width in figure 3.2.5 when the first peak appears. It can be seen from figure 3.2.5(a)-(c) that the integration over the range of negative electric field (such as the region marked as N_2 in figure 3.2.5(b)) increases significantly as the tape becomes wider, which contributes to a larger value of V_{eq}. As illustrated from figure 3.2.5(d)-(f), once the tape reaches a certain width, the integration for electric field in region N_2 remains approximately constant, and further width increasement will only raise the integration over the range of positive electric field (such as the region marked as N_1 in figure 3.2.5(b)). Consequently, a fixed integration over the negative region will be cancelled more and more by an increasing integration over the positive region, leading to a small V_{eq} as a combinational effect. This smaller V_{eq} peak value implies that less V_{oc} is obtainable through the time integration of V_{eq} over the whole cycle, which explains why V_{oc} can be promoted by the tape width but suppressed if the tape becomes too wide. It should be pointed out, the definition of 'too wide' here is restricted by the sole variation of tape width, but the effects described above can be also influenced by the geometry of the device, e.g., the air gap between the magnet and tape, the dimension of the magnet itself and even the radius of the rotary disc. More comprehensive analysis is required to fully investigate the bilateral effect of the HTS tape width on output voltage and complete the definition of 'too wide' by cooperating all relevant parameters, which is beyond the scope of this chapter and can be addressed in the future.

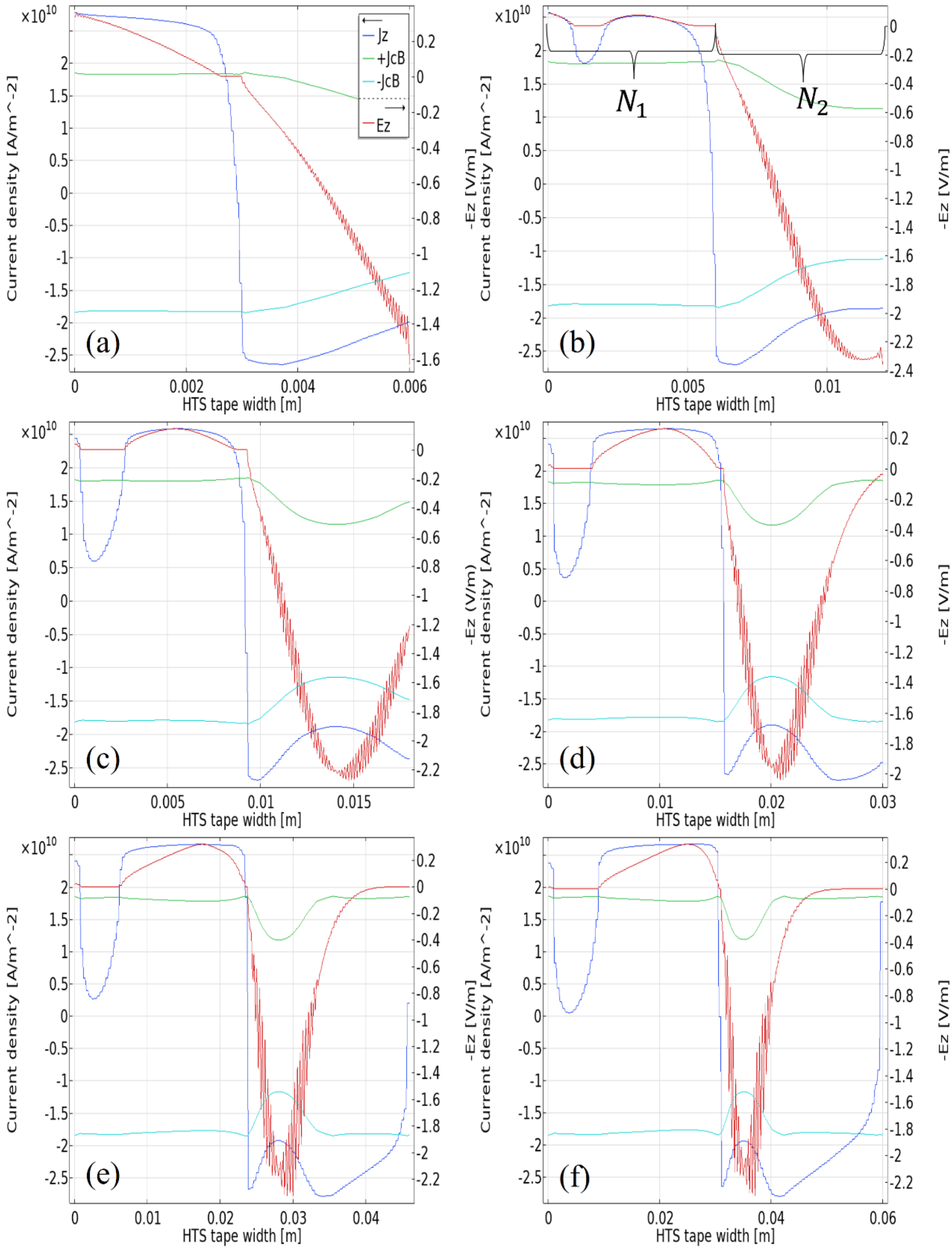

Figure 3.2.5. The current and electric field distribution at the moment of first peak of V_{eq} for selected HTS tapes (with the width of 6, 12, 18, 30, 46, 60 mm respectively).

3.3 ***H-A*** model

The ***T-A*** model only considers the superconducting layer and simplifies the superconductor tape as a straight line without thickness. With such an assumption, the model can save substantial computation cost. However, in practice, superconductor tapes are normally CCs that comprise several layers, i.e., the copper layers, stabilizer layer. Therefore, instead of passing through only the superconducting layer, currents can flow in all those layers. In [105], Zhang et al. found that under high frequencies, currents tend to be drifted away from the superconducting layer to the copper layers. Equivalently saying, with high frequencies, currents in a superconductor tape will not be dominated by the superconducting layer but more distributed in other structural layers. Hence, the ***T-A*** model, which ignores the multilayer structure of the superconductor tape, is not suitable for scenarios with high frequencies. It should be note that the original ***T-A*** formulation proposed in [126] has been extended to thick conductors so that large coils with different coupling scenarios between turns can be considered [128]. However, implementing ***T-A*** formulation requires to impose constraints of the projection of current potential ***T*** on the boundary of the superconductor, which can be less straightforward if the superconductor has an arbitrary geometry. As an alternative, ***H-A*** formulation can be utilised to avoid above issues. In addition, according to the benchmark problem [144], ***H-A*** formulation-based models also outperform ***T-A*** models in terms of the computation cost.

3.3.1 Formulation description

The coupled ***H-A*** formulation was proposed by Brambilla et al. [123], for modelling superconducting machines. The implementation of ***H-A*** formulation aims to model a small region with close proximity to the superconductor with ***H*** formulation, and anywhere else is modelled by the magnetic vector ***A***.

In the region where ***H*** formulation is implemented, the solved variables are the components of the magnetic field strength ***H***, and the governing equations are derived from Ampere's and Faraday's laws:

$$\nabla \times \boldsymbol{H} = \boldsymbol{J} \tag{3.3.1}$$

$$\nabla \times \boldsymbol{E} = -\frac{\partial \boldsymbol{B}}{\partial t} \tag{3.3.2}$$

Equation (3.3.1) and (3.3.2) and the constitutive relation $\boldsymbol{B} = \mu \boldsymbol{H}$ are combined with the *E-J* power law, equation (3.1.8).

In the region where ***A*** formulation is implemented, the solved variables are the components of the magnetic vector potential ***A***, and the governing equations are:

$$\boldsymbol{B} = \nabla \times \boldsymbol{A} \tag{3.3.3}$$

$$\boldsymbol{E} = -\frac{\partial \boldsymbol{A}}{\partial t} \tag{3.3.4}$$

It is clear that equation (3.3.3) together with (3.3.4) automatically fulfil equation (3.3.2) and the magnetic flux conservation law:

$$\nabla \times \boldsymbol{B} = 0 \tag{3.3.5}$$

For which equation (3.3.1), Ampere's law, can be then solved.

Similar to that as introduced in subsection 3.1.1, the model can be further simplified by restricting the region that directly solves the vector fields associated with Maxwell equations to a small region around the current carrying subdomain, i.e., the part of $\boldsymbol{H}$ formulation subdomain that surroundings the superconductor, as illustrated in figure 3.3.1. By doing so, most of the modelling space can be solved by utilizing the magnetic scalar potential V_m following equation (3.1.7). The continuity between $\boldsymbol{A}$ and V_m are achieved by imposing following constraint equations:

$$\boldsymbol{n}_1 \times \boldsymbol{H}_A = \boldsymbol{n}_1 \times \boldsymbol{H}_A = \boldsymbol{n}_1 \times (-\nabla V_m) \tag{3.3.6}$$

$$\boldsymbol{n}_2 \cdot \boldsymbol{B}_{Vm} = \boldsymbol{n}_2 \cdot \boldsymbol{B}_A = \boldsymbol{n}_2 \cdot \nabla \times \boldsymbol{A} \tag{3.3.7}$$

where $\boldsymbol{n}_1$ and $\boldsymbol{n}_2$ are the surface normal vectors in antiparallel. In the commercial software COMSOL Multiphysics, equation (3.3.6) and (3.3.7) are taken as weak contributions, which can be interpreted as a surface current density:

$$\boldsymbol{J}_s = -\boldsymbol{n} \times \boldsymbol{H} \tag{3.3.8}$$

and magnetic surface charge density, respectively:

$$\sigma_m = \boldsymbol{n} \cdot \boldsymbol{B} \tag{3.3.9}$$

In addition, the $\boldsymbol{H}$ formulation and $\boldsymbol{A}$ formulation has to be coupled effectively, which is conventionally achieved by defining the tangential component of the magnetic field H_t in the two formulations. In the $\boldsymbol{A}$ formulation region, we define:

$$H_t^{(A)} = t_x \cdot \frac{1}{\mu}\frac{\partial A_z}{\partial y} - t_y \cdot \frac{1}{\mu}\frac{\partial A_z}{\partial x} \tag{3.3.10}$$

In the $\boldsymbol{H}$ formulation region, we define:

$$H_t^{(H)} = t_x \cdot H_x + t_y \cdot H_y \tag{3.3.11}$$

Since the model is constructed as a two-dimensional framework, above two equations are defined with two dimensions. Directly setting equation (3.3.10) equal to equation (3.3.11) has been proved ineffective to couple the two formulations in [124]. Alternatively, one can include the ***H*** formulation $H_t^{(H)}$ as a source in the boundary condition imposed on the ***A*** formulation part and take the ***A*** formulation E_z as a source in the boundary condition imposed on the ***A*** formulation part. This is accomplished by entering expressions to the weak form of the problem. To add $H_t^{(H)}$ and E_z as sources, test functions are required to ensure that the source terms equal to zero everywhere except for the specified boundary in which they are imposed.

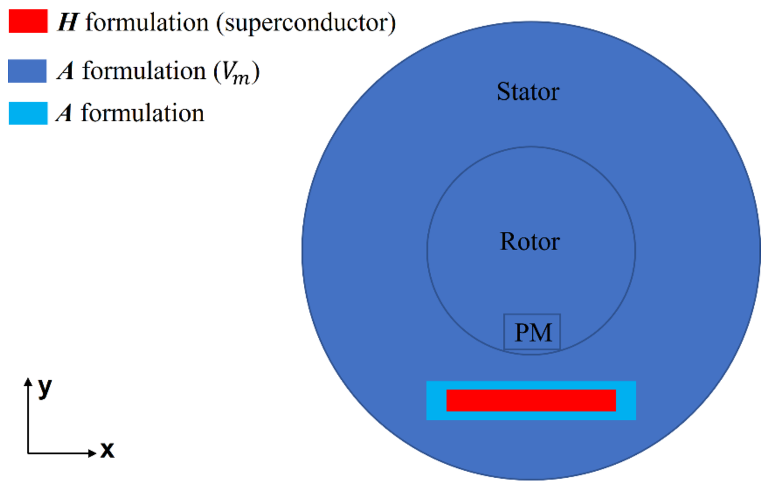

Figure 3.3.1. An illustration of the hybrid formulation division.

In the ***H*** formulation, following weak form contribution is imposed:

$$E_z \cdot test\left(H_t^{(H)}\right) \tag{3.3.12}$$

In the ***A*** formulation, following weak form contribution is imposed:

$$H_t^{(H)} \cdot test(E_z) \tag{3.3.13}$$

3.3.2 Multilayer structure

In this work, the modelled HTS tape comprises two copper layers at the up and bottom of the tape, which are adjacent to a silver stabilizer layer and a substrate layer, respectively, and the HTS layer is sandwiched in the middle. The thickness of each layer is 20 μm, 2 μm, 1 μm, 50 μm and 20 μm, as illustrated in figure 3.3.2. The resistivity of the copper layer, silver stabilizer layer and substrate are set to be 1.667 $e^{-8}\ \Omega\cdot m$, 1.59 $e^{-8}\ \Omega\cdot m$ and 1.25 $e^{-6}\ \Omega\cdot m$, respectively.

The *E-J* power law, equation (3.1.8) is employed to represent the electrical characteristics of the HTS layer. The $J_c(B)$ dependence is described by an empirical function, equation (2.4.2). Fitting the experimental measurement results (data are provided by our partners in the Victoria University of Wellington) to the empirical function, as shown in figure 3.3.3, the values of constant parameters J_{c0}, B_0, k and α are determined to be 23.583 $e^9\ A/m^2$, 169.4 mT, 0.1538 and 1.022, respectively.

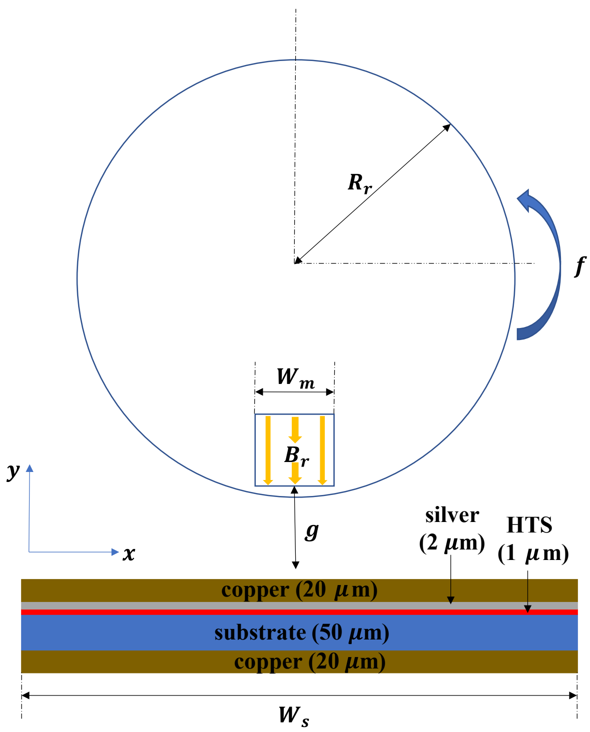

Figure 3.3.2. Cross section schematic for the multilayer structure adapted in the model.

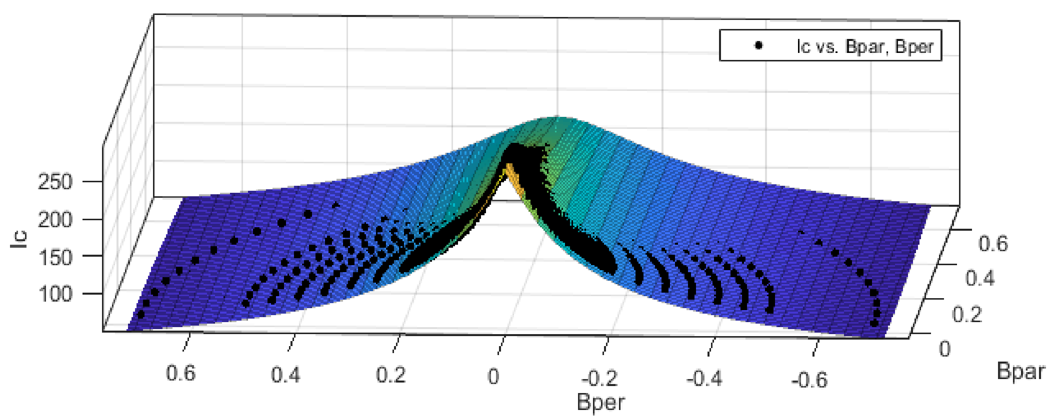

Figure 3.3.3. Data fitting of $J_c(B)$ dependence.

With this modelling framework, the HTS tape is no longer represented by a straight line, but in the shape of a rectangle. To derive the instantaneous voltage, we need to integrate the electric field over the cross-section area, so the definition of V_{eq} ,equation (3.1.9) should be amended as following:

$$V_{eq}(t) = -L \cdot \frac{1}{S} \iint E_Z(x, y, t) ds \tag{3.3.14}$$

where S represents the cross-section area of the HTS tape.

The definition of the open circuit voltage V_{oc} remains the same as equation (3.1.10), which is still the time average over one complete operation cycle. In order to ensure that there is no net transport current in the HTS tape at any given time, following constraint equation is imposed:

$$I(t) = \iint J_Z(x, y, t) ds = 0 \tag{3.3.15}$$

3.3.3 Model validation

Based on the modelling definitions introduced above, a numerical model was built to be solved in the commercially available FEM software COMSOL 5.5. To verify the applicability of this model, again it was adapted to represent the experimental set up described in [114]: a 12 mm wide REBCO tape (Superpower SF12050F) is separated from a NdFeB magnet by an airgap of 3.7 mm. The magnet has a remanent flux density of 1.25 T and is embedded in a cylindrical disc with radius of 35 mm. The HTS dynamo is operated at low frequency 4.25 Hz. The comparison results between the instantaneous voltage obtained from the ***H-A*** formulation-based model and the experiments are plotted in figure 3.3.4. As it can be seen, the waveforms show excellent coincidence with each other. Besides, the open circuit voltage based on equation (3.1.10) calculated from the corresponding waveform is 27.51 μV and 27.57 μV, respectively, confirming the effectiveness of this model.

Meanwhile, since the main aim of developing this ***H-A*** formulation-based model is to replicate the non-linear frequency response with high frequencies. Hence, it is necessary to investigate the how the open circuit voltage varies within a relatively wide range of frequencies by utilizing the proposed model. As a comparison, the V_{oc} results, for the frequency increasing from 0 to 1000 Hz, obtained from the simulations via the ***H-A*** formulation-based model and the previously developed ***T-A*** formulation-based model are plotted in figure 3.3.5. It is clear from the plot that, with the ***T-A*** model, the voltage-frequency curve (the green one) is a straight line, which implies that V_{oc} consistently increases with the frequency linearly. However, with the ***H-A*** model, the voltage-frequency curve (the blue one) resembles a parabolic curve, which has a decreasing slope with the increase of frequency. This phenomenon proves that the ***H-A*** formulation based model developed here can well reflect the non-linear frequency response as experimentally observed in [102].

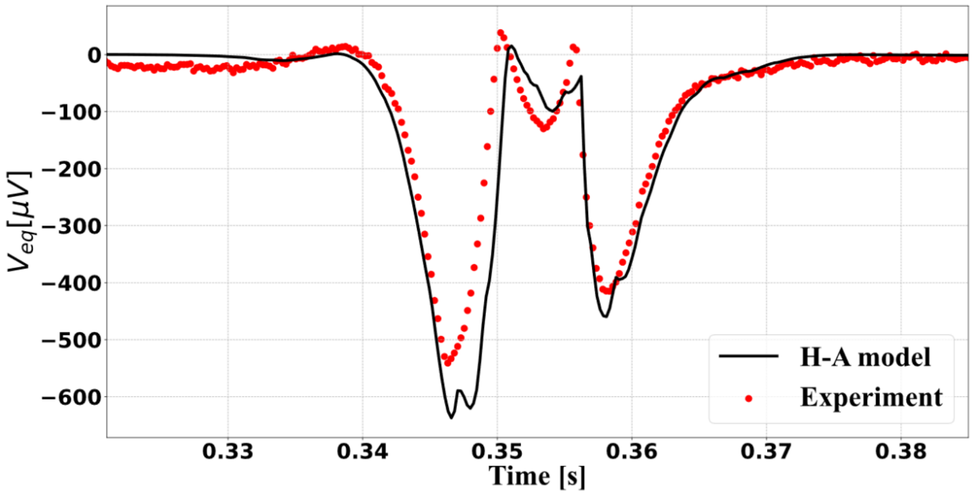

Figure 3.3.4. Time dependent equivalent voltage waveforms for the PM past the HTS tape in the 2nd cycle, ignoring any initial transient effects.

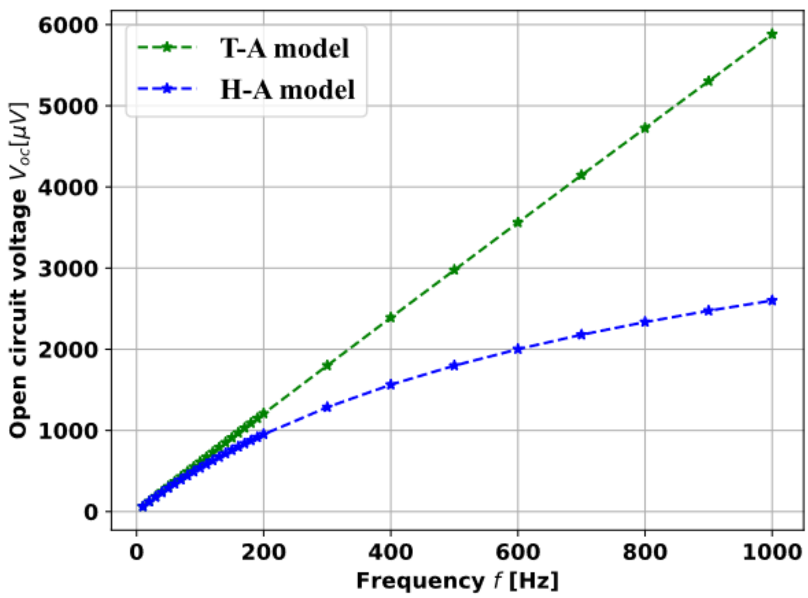

Figure 3.3.5. The frequency response with the ***T-A*** formulation-based model and the ***H-A*** formulation-based model.

3.4 Discussions

It should be noted that the FEM simulation model utilised in this work has adopted the radial flux geometry, in which the superconductor tape and permanent magnet surfaces are flat such that the airgap between the magnet and tape varies as the magnet rotates. This radial flux arrangement has been investigated in a number of previous studies [95, 101, 104, 111, 114, 147]. Alternatively, the superconductor tape and magnet could be curved so that their surfaces are strictly parallel resulting in a constant airgap between the tape and magnet, but still in a radial flux configuration. Such an arrangement has been used in [130]. In an axial flux arrangement, the permanent magnet with a flat surface can be mounted on a rotating disc that is parallel to the flat surface of the superconductor tape, such that the airgap is uniform during the operation. Figure 3.4.1 illustrates these different configurations.

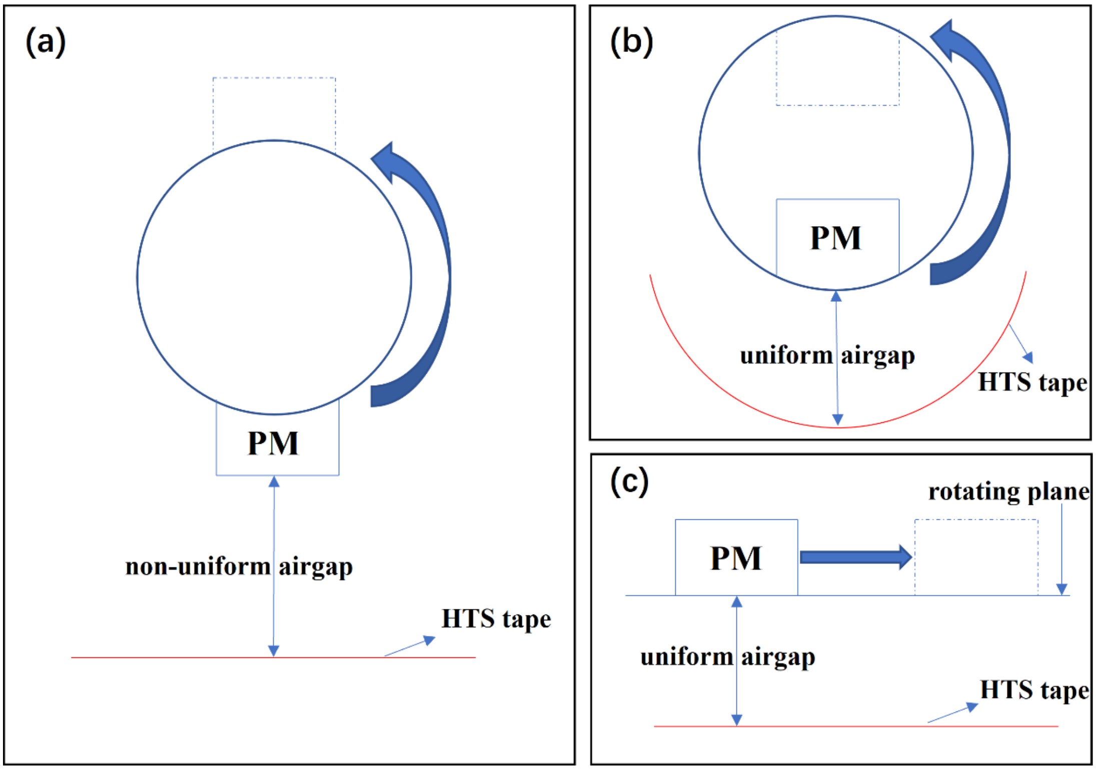

Figure 3.4.1. Cross-section schematic diagrams for different HTS dynamo configurations. (a) redial flux configuration with flat tape and PM surface, (b) radial flux arrangement with curved tape and PM surface, (c) axial flux arrangement with flat tape and PM surface.

The use of flat surfaces in a radial flux configuration resulting in a non-uniform air gap accounts for the difference in the results obtained in this work compared to those in [130], in which the air gap is uniform. As can be seen from subsection 3.2.3, the open circuit voltage V_{oc} tends to increase versus the superconductor tape width W_s

until it reaches an optimal value, after which it starts to decrease. However, it was found in [130], where the uniform air gap configuration was modelled, that V_{oc} would increase with W_s at the beginning, and it gradually saturates to a maximum value, which implies that the HTS dynamo with the uniform air gap configuration will not experience the bilateral width effect discovered in this work. Besides, the results presented in figure 3.2.4 shows that the maximum short circuit current I_{sc} that can be possibly pumped will increase with the superconductor tape width and then saturate at 75% of the minimum critical current $I_{c,min}$ of the tape, whilst in [130] this proportion can reach 100%. The reason for the distinct superconductor tape width response can be attributed to whether the air gap has been maintained constant or not, though future work is required to further explore this phenomenon and provide a clearer explanation for the underlying physics.

3.5 Conclusions

In this chapter, a 2D ***T-A*** formulation-based FEM model has been constructed to simulate the HTS dynamo, which was validated with experimental results in [114]. The difference between the results from a constant J_c model and a field dependent $J_c(B)$ model has been explained by considering the dynamic resistance. It is pointed out that the $J_c(B)$ dependence tends to increase the dynamic resistance for the superconductor tape region beneath the permanent magnet, where the forward eddy current flows, and elimination of such dependence, e.g., assume constant J_c, will cause less of the conserved EMF to be distributed to the forward eddy current region and consequently result in a smaller open circuit voltage, from which we demonstrate the importance of considering field dependence of J_c in such models. Based on this numerical model, a comprehensive sensitivity analysis of the open circuit voltage V_{oc} has been conducted, considering the impacts of the operating frequency f, air gap g, superconductor tape width W_s and remanent flux density of the permanent magnet B_r. The individual effect of each parameter on the open circuit voltage has been investigated, in particular, it was found that the superconductor tape width W_s has a bilateral impact on V_{oc}, and this is because the integration over the negative electric field saturates when the tape becomes wide enough, yet further increasing the tape width will still raise the integration over the positive electric field to offset the integration over the negative electric field that essentially forms V_{oc}. Lastly, an ***H-A*** formulation based numerical has been built to simulate the HTS dynamo with considering the coated structure of the HTS tape. By utilizing this numerical model, the non-linear frequency response, which cannot be replicated by the ***T***-***A*** formulation-based model, has been successfully demonstrated. This phenomenon can be considered as a proof that the non-linear frequency response of the HTS dynamo is due to the current interactions with different layers of the HTS tape, which highlights the importance of considering the full structure of the HTS tape when the HTS dynamo is operated with high frequencies.

Chapter 4

Artificial Intelligence based Modelling of Rotary HTS Flux Pumps

As mentioned in previous chapters, HTS dynamo is a typical variant of travelling wave flux pump, which has been introduced in detail in the last chapter. The flux pumping effects in HTS dynamos have been investigated experimentally for different influential design parameters, such as the air-gap distance [101], the operating frequency [102], the width of the stator wire [103] and the geometry of the magnet [104], and typical curves for output characteristics have been obtained. Both qualitative and quantitative analysis [113-115, 130, 132, 146, 202] have been done previously for the output characteristics of HTS dynamo, but little attention has been paid to integrate all design parameters together and then derive a model that can capture the output characteristics in a fast and accurate manner. Although experiments and FEM simulations are capable of extracting essential information for quantitative analysis, the frequent change of a variety of parameters is costly in terms of time due to the complexity of models and experimental arrangements. In order to address this challenge, artificial intelligence techniques have been applied to an engineering formulation to quantify the relationship between the open circuit voltage V_{oc}, versus a set of design parameters within a rational range.

4.1 Machine learning regression model

Regression is a popular method for data processing, which is found to be very effective in exploring the underlying relations between a set of predictor variables and corresponding response variables. The aim of regression analysis is to predict outputs by feeding relevant inputs, which can be achieved either by parametric regression or non-parametric regression. Parametric regression is the process to describe the correlations among all inputs and outputs by mathematical expressions, and a typical model for a polynomial regression can be expressed as:

$$\widehat{y^i} = \alpha + \beta_1 x_1^i + \beta_2 x_2^i + \cdots + \beta_n x_n^i + \epsilon^i \tag{4.1.1}$$

Note that α is the intercept to describe a constant factor that can be inherently included in the expression, β_n is the coefficient for n^{th} independent predictor variable x_n, ϵ^i is the random error for i_{th} observation, and y is the pre-defined response variable. In most cases, parametric regression is preferred, because it gives intuitive hints about what roles each of the input plays in determining the output and provides full details about the numerical relations. Nevertheless, parametric regression is valid only if the investigated data correlations can be well described by explicit formulations. When the underlying relations among a set of input and output data involves highly complex and tedious mathematical transformation, it is challenging and inefficient to obtain analytical formulations. Fortunately, modern artificial intelligence-based approach enables non-parametric regression, which is the process to summarize the key features about outputs dependence on the inputs in certain manner that can be understood by computers, and hence the predictions of outputs by feeding relevant inputs is achieved without deriving explicit expressions.

From above, it has been shown that parametric regression is not suitable for relating the predict variable V_{oc} to the four parameters investigated here, namely the frequency f, air gap g, superconductor tape width W_s and magnet remanent flux density B_r. As a result, non-parametric regression will be conducted by some of the popular artificial intelligence-based methods via Python Scikit-learn 5.1 environment [203], including the multi-layer perception neural network (MLP), support vector machine (SVM), Gaussian process regression (GPR), decision tree (DT) and k-nearest neighbours (KNNs). The adapted Nash-Sutcliffe model efficiency coefficient (NSE) is employed to evaluate the goodness-of-fit, and the other top three most popular metrics [204], namely the root mean squared error (RMSE), mean absolute error (MAE) and mean absolute percentage error (MAPE) are included as complementary statistics to assess the regression results from different aspects. These numerical criteria are centred on prediction error, whose values can be interpreted mathematically and translated to the effectiveness of a certain regression model. For example, the best possible score for NSE is 1, which implies that the regression model reaches the highest correctness level so that any unseen observations can be predicted with full confidence, i.e., no errors. In addition, graphical criterion proposed in [205] have been implemented, such as prediction distributions versus observations and the prediction rate curves, to illustrate more complex aspects of the relationship between the models and data, from which the most effective one can be selected.

$$NSE = 1 - \frac{\sum_{i=1}^{n}(y_i - \hat{y}_i)^2}{\sum_{i=1}^{n}(y_i - \bar{y})^2} \tag{4.1.2}$$

$$RMSE = \sqrt{\frac{1}{n}\sum_{i=1}^{n}\left(y_i - \hat{y}_i\right)^2} \tag{4.1.3}$$

$$MAE = \frac{1}{n}\sum_{i=1}^{n}\left|y_i - \hat{y}_i\right| \tag{4.1.4}$$

$$MAPE = \frac{100}{n}\sum_{i=1}^{n}\left|\frac{y_i - \hat{y}_i}{y_i}\right| \tag{4.1.5}$$

Although HTS dynamo can now be simulated by various numerical models via FEM programs, including the ***T-A*** formulation-based model proposed in previous sections, which enable us to obtain considerable knowledge of the physical mechanism that takes place during the operation. Yet in terms of industrial design, the ultimate goal is to make use of the functionality of certain devices. As for HTS dynamo, it is expected to be utilised as an energisation source that can pump current into load coils and hence form an HTS magnet. From this point of view, it is the averaged output DC voltage V_{oc} that matters. There is no doubt that V_{oc} can be measured from experiments, which yet are often time-consuming and expensive. Valid FEM simulations are considered to be a promising substitution for setting up real experiments to get comprehensive results in less time and saved cost. However, these FEM models can sometimes require relatively long time for solution (hours or even days), and the applicability is also limited by user knowledge and accessibility to a sophisticated FEM program, which is not guaranteed. Artificial intelligence methods are powerful tools to accurately model certain data behaviour, which have been recently involved in solving applied superconductivity problems [206]. For instance, artificial neural network (ANN) has been utilised in [207-210] to estimate the calculation of AC losses in specific superconductor systems and aid the design of superconductor facilities. As an alternative, we have explored the feasibility of constructing a statistical model, which can give accurate V_{oc} values according to the given controllable parameters within seconds, and hence provides primary guidance for the design of such devices in practical applications.

1,000 sets of different parameters, in which each of them lies in a rational range (see figure 3.2.1) for a practical design process, have been randomly chosen and simulated by the ***H-A*** model described above to derive V_{oc} for each set of parameters. As suggested in equation (3.2.1), all output voltage variations that are solely affected by frequency can be easily quantified by a simple normalization calculation, so we have precluded the frequency parameter f in following investigations, e.g., all parameter settings share the same value of frequency (50 Hz), in order to simplify the modelling work. According to the conventional 8-2 rule, data samples are evenly divided into five folders for cross validation, in which four folders will be utilised as the training group and keep the remaining one as the testing group for each validation.

4.1.1 MLP model

MLP is a supervised neural network model that learns the function mapping $R_i \rightarrow R_o$, where the subscript i denotes the dimension of input dataset and o signifies the dimension of output data set. A typical neural network comprises three layers at least: the input layer, hidden layer and output layer, as shown in figure 4.1.1. The number of neurons in the input layer and output layer are predefined by the features of given problem, namely the number of predictor and independent variables. It is the process that takes place in the hidden layers links the output layer to the input layer, where each neuron takes values from the previous layers and conducts a weighted summation by a transformation with specific activation function. Considering the model is expected to predict the open circuit voltage, which is a continuous variable. The identity function:

$$f(x) = x \tag{4.1.6}$$

is adopted as the activation function in the output layer to receive results from the last hidden layer, and the squared error with regularization is utilised as the loss function:

$$Loss(\hat{y}, y, \boldsymbol{\omega}) = \frac{1}{2}||\hat{y} - y||_2^2 + \frac{\alpha}{2}||\boldsymbol{\omega}||_2^2 \tag{4.1.7}$$

where $\hat{y}$ signifies the predicted values, $\boldsymbol{\omega}$ is the weight coefficient matrix and α is a non-negative hyperparameter that puts penalty on the complexity of the models, and hence supress overfitting. Based on this loss function, certain solvers are appointed to update the weight coefficients in hidden layers. For instance, the stochastic gradient descent (SGD) algorithm derives new parameter values using the gradient of loss function with respect to the parameter that needs to be updated:

$$w' = w - \eta\left(\frac{\partial Loss}{\partial \boldsymbol{\omega}} + \alpha\frac{\partial R(\boldsymbol{\omega})}{\partial \boldsymbol{\omega}}\right) \tag{4.1.8}$$

where η represents the training rate that controls the step size of parameter updating. Note that $Loss$ and $R(\boldsymbol{\omega})$ here is first and second term of equation (4.1.7). Besides, there are other solvers in the Scikit-learn environment. Adaptive moment estimation (Adam) is also a stochastic optimizer, similar to SGD, but it is capable of making use of adaptive estimates of lower-order moments to adjust the amount to update parameters [211]. Limited-memory Broyden-Fletcher-Goldfarb-Shanno (L-BFGS) is an optimization algorithm as a member of the quasi-Newton methods family. This algorithm aims to minimize $u(x)$ over unconstrained values of the real vector x with u as a differentiable scalar function [212]. Using either algorithm, the parameter updating process will stop if it reaches a predefined maximum number of iterations, or when the improvement in loss is below a certain threshold.

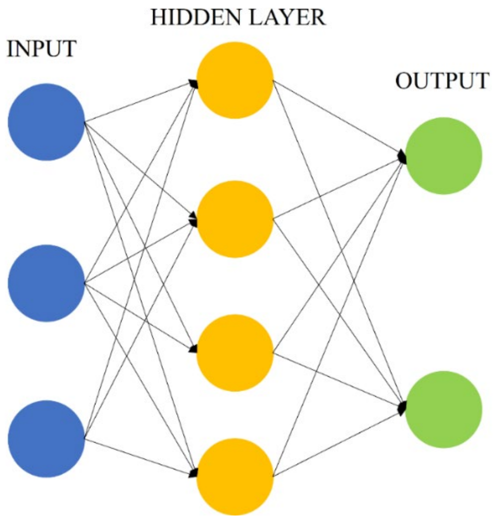

Figure 4.1.1. Schematic diagram of the structure of a MLP network.

In this MLP model, there are several tuning parameters that have direct impacts on the regression performance, including the number of layers and neurons in each layer, activation function, weight coefficients update solver, learning rate as well as the maximum number of iterations that controls the termination of the regression if it fails to converge to the specific tolerance. In order to figure out the best parameter settings, a grid search was performed over possible choices. The determination of the hidden layer size to be tested remains the critical step to perform the grid search, as it needs manual declaration. Following the basis that the least hidden layer should be used to save the training time and model complexity [213], only one hidden layer is considered. On the other hand, it is stated in [214] that the number of hidden layer neurons should be less than twice of the number of hidden neurons in the input layer, hence the number of neurons is set from 1 to 7. The searching space of the optimisation solvers comprises SGD, Adam and L-BFGS. In terms of the activation function, available choices are set to be the identity function, the rectified linear unit (ReLU) function $f(x) = \max(0, x)$, the hyperbolic tan function $f(x) = \tanh x$, and the logistic sigmoid function $f(x) = 1/(1 + \exp(-x))$. Therefore, in total $7 \times 3 \times 4 = 84$ combinations of parameter settings have been tested, from which the one with the highest NSE score can be selected as the best MLP model.

Table 4.1.1. Parameter setting for the best MLP model.

Hidden layer size	Activation function	Weight coefficents solver
1*6	Tanh	Adam

Table 4.1.2. Cross validation metrics for the best MLP model.

RMSE	MAE	MAPE	NSE
58.56	39.73	9447.38	0.975268

Note that the maximum iteration limitation for each model setting has been adjusted carefully to provide enough space to reach a convergence. As can be seen from table 4.1.1 and 4.1.2, the MLP model that has the hyperbolic tan function, Adam weight coefficients update solver and one hidden layer with six neurons performs the best. A further increase of the hidden layer size can possibly enhance the model performance, yet the model complexity and consequently the solution time increase exponentially with the size of hidden layers. Considering the already obtained prediction accuracy, it is reasonable to utilise the existing model as the optimal one.

4.1.2 GPR model

In the field of non-parametric regression, GPR is considered as a highly effective approach because it can provide a framework to approximate sophisticate nonlinear functions with probabilistic estimates. The description of a Gaussian process can be simplified as a distribution over a set of functions, as shown in figure 4.1.2. There are many possible functions that can connect given data (red points), as indicated by the light purple shadow area, which obeys Gaussian distribution. Among all the functions, there is a function that has the highest possibility (the deep blue line).

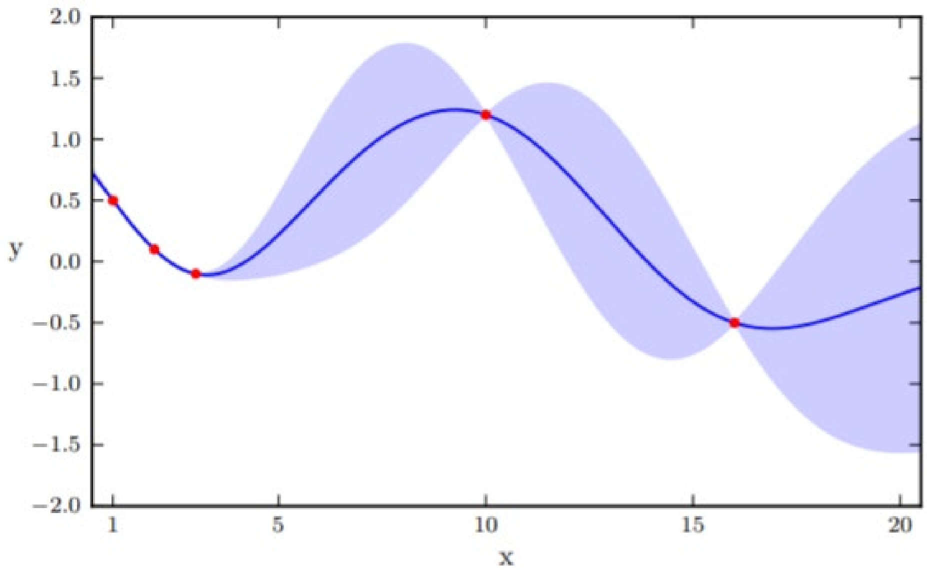

Figure 4.1.2. A simplified Illustration for the GPR.

More precisely, given a finite set of N inputs $X = \{\boldsymbol{x}_1, \boldsymbol{x}_2, \cdots \boldsymbol{x}_N\}$, $\boldsymbol{x}_N \in R^d$, a Gaussian process is defined as a collection of random variables $\{f(\boldsymbol{x}) | \boldsymbol{x} \in X\}$ such that the collection $f(\boldsymbol{x}_1), f(\boldsymbol{x}_2), \cdots, f(\boldsymbol{x}_N)$ has a joint multivariate Gaussian distribution [215]. A Gaussian process is completely and uniquely defined by its mean and kernel (or called 'covariance') functions.

A Gaussian process with mean function $m(\boldsymbol{x})$ and a covariance function $k(\boldsymbol{x}, \boldsymbol{x}')$ provides the prediction $\boldsymbol{f} = [f(\boldsymbol{x}_1), f(\boldsymbol{x}_2), \cdots, f(\boldsymbol{x}_N)]^{\mathrm{T}}$ as a random variable, which is referred to as a prior for the Gaussian process, such that:

$$p(\boldsymbol{f}|X) = \mathcal{N}\big(\boldsymbol{f}; m(X), k(X, X)\big) \tag{4.1.9}$$

where $k(X, X)$ denotes the matrix with elements $\big[k\big(\boldsymbol{x}_i, \boldsymbol{x}_j\big)\big]_{1 \le i,j \le N}$ and $m(X)$ denotes the vector $[m(\boldsymbol{x}_1), m(\boldsymbol{x}_1), \cdots, m(\boldsymbol{x}_N)]^{\mathrm{T}}$. With the mean vector $\mathbf{m}$ and covariance matrix K being known, the multivariate normal probability distribution $\mathcal{N}(\boldsymbol{f}; \mathbf{m}, K)$ can be expressed as:

$$\mathcal{N}(\boldsymbol{f};\mathbf{m},K)=\frac{1}{(2\pi)^{\frac{N}{2}}\left|K^{\frac{1}{2}}\right|}\exp\left(-\frac{1}{2}(\boldsymbol{f}-\mathbf{m})^{\mathrm{T}}K^{-1}(\boldsymbol{f}-\mathbf{m})\right) \tag{4.1.10}$$

If we assume that the noise σ (i.e., error) between the actual observations $\boldsymbol{y}=[y(\boldsymbol{x}_1),y(\boldsymbol{x}_1),\cdots,y(\boldsymbol{x}_N)]^{\mathrm{T}}$ collected from the set of inputs $X=\{\boldsymbol{x}_1,\boldsymbol{x}_2,\cdots\boldsymbol{x}_N\}$ and the Gaussian process prediction $\boldsymbol{f}$ satisfies the Gaussian distribution, then the probability of observing data $\boldsymbol{y}$ based on equation (4.1.9), which is referred as the Gaussian likelihood, can be calculated as:

$$p(\boldsymbol{y}|X,\boldsymbol{f})=\mathcal{N}(\boldsymbol{f},\sigma^2 I_N) \tag{4.1.11}$$

where I_N represents the $N\times N$ identity matrix.

Denoting the hyperparameters, which depend on the covariance kernel function, as $\boldsymbol{\theta}$. Apparently, both the prior and Gaussian likelihood have dependence on $\boldsymbol{\theta}$, for which we write their dependence as $p(\boldsymbol{f}|X,\boldsymbol{\theta})$ and $p(\boldsymbol{y}|X,\boldsymbol{f},\boldsymbol{\theta})$, respectively.

The marginal likelihood is given by:

$$p(\boldsymbol{y}|X,\boldsymbol{\theta})=\int p(\boldsymbol{y}|X,\boldsymbol{f},\boldsymbol{\theta})p(\boldsymbol{f}|X,\boldsymbol{\theta})d\boldsymbol{f} \tag{4.1.12}$$

Assume the prior has a zero mean, i.e., $m(X)\equiv 0$. The log-marginal-likelihood for a Gaussian process can then be written as:

$$\begin{aligned}log\,p(\boldsymbol{y}|X,\boldsymbol{\theta})=-\frac{1}{2}\boldsymbol{y}^T(K(X,X)+\sigma^2 I_N)^{-1}\boldsymbol{y}\\-\frac{1}{2}log|K(X,X)+\sigma^2 I_N|-\frac{N}{2}log\,2\pi\end{aligned} \tag{4.1.13}$$

Equation (4.1.13) is now a function of the hyperparameters $\boldsymbol{\theta}$, which can be optimized to produce the most likely values of the hyperparameters, by the means of maximum likelihood estimation (MLE).

After the hyperparameters have been chosen, the posterior of the Gaussian process can be given according to Bayes rule:

$$p(\boldsymbol{f}|X,\boldsymbol{y},\boldsymbol{\theta})=\frac{p(\boldsymbol{f}|X,\boldsymbol{\theta})p(\boldsymbol{y}|X,\boldsymbol{f},\boldsymbol{\theta})}{p(\boldsymbol{y}|X,\boldsymbol{\theta})} \tag{4.1.14}$$

Hence, given the $\boldsymbol{\theta}$ dependence included prior $p(\boldsymbol{f}|X,\boldsymbol{\theta})$ and the Gaussian likelihood

$p(\boldsymbol{y}|X,\boldsymbol{f},\boldsymbol{\theta})$, the GPR prediction f^* at a new data point $\boldsymbol{x}^*$ now can be calculated as:

$$p(f^*|\mathbf{y},X,\mathbf{x}^*,\boldsymbol{\theta}) = \mathcal{N}\begin{pmatrix} k(\mathbf{x}^*,X)(k(\mathrm{X},X)+\sigma^2 I_N)^{-1}\mathbf{y}, k(\mathbf{x}^*,X) \\ -k(\mathbf{x}^*,\mathbf{x}^*)(k(\mathbf{x}^*,X)+\sigma^2 I_N)^{-1}[k(\mathbf{x}^*,X)]^{\mathrm{T}} \end{pmatrix} \quad (4.1.15)$$

By now, it is clear that the kernel function is involved in every mathematical derivation in the GPR model, so the choice of kernel functions has significant impacts on the model performance. In this work, we have tested some of the most commonly used kernel functions as introduced in follows:

The radial-basis function (RBF), or so-called squared exponential kernel:

$$k(\boldsymbol{x}_i,\boldsymbol{x}_j) = \exp\left(-\frac{1}{2l^2}d(\boldsymbol{x}_i,\boldsymbol{x}_j)^2\right) \quad (4.1.16)$$

where l is a length-scale parameter and $d(\cdot,\cdot)$ is the Euclidean distance.

The Matérn kernel:

$$k(\boldsymbol{x}_i,\boldsymbol{x}_j) = \frac{1}{\Gamma(v)2^{v-1}}\left(\frac{\sqrt{2v}}{l}d(\boldsymbol{x}_i,\boldsymbol{x}_j)\right)^v K_v\left(\frac{\sqrt{2v}}{l}d(\boldsymbol{x}_i,\boldsymbol{x}_j)\right) \quad (4.1.17)$$

where $\Gamma(\cdot)$ is a modified Bessel function, $K_v(\cdot)$ is the gamma function and v is an additional parameter that controls the smoothness of the resulting function. With v approaching infinity, the Matérn kernel becoming the same to the RBF kernel.

In particular, with $v=\frac{3}{2}$:

$$k(\boldsymbol{x}_i,\boldsymbol{x}_j) = \left(1+\frac{\sqrt{3}}{l}d(\boldsymbol{x}_i,\boldsymbol{x}_j)\right)\exp\left(-\frac{\sqrt{3}}{l}d(\boldsymbol{x}_i,\boldsymbol{x}_j)\right) \quad (4.1.18)$$

and with $v=\frac{5}{2}$:

$$k(\boldsymbol{x}_i,\boldsymbol{x}_j) = \left(1+\frac{\sqrt{5}}{l}d(\boldsymbol{x}_i,\boldsymbol{x}_j)+\frac{5}{3l}d(\boldsymbol{x}_i,\boldsymbol{x}_j)^2\right)\exp\left(-\frac{\sqrt{5}}{l}d(\boldsymbol{x}_i,\boldsymbol{x}_j)\right) \quad (4.1.19)$$

are popular templates for setting a Matérn kernel [216], which are not infinitely differentiable (as assumed by the RBF kernel), but once ($v=\frac{3}{2}$) or twice differentiable ($v=\frac{3}{2}$).

The rational quadratic kernel:

$$k(\boldsymbol{x}_i, \boldsymbol{x}_j) = \left(1 + \frac{d(\boldsymbol{x}_i, \boldsymbol{x}_j)^2}{2\alpha l^2}\right)^{-\alpha} \tag{4.1.20}$$

where α is a scale mixture parameter.

The dot-product kernel:

$$k(\boldsymbol{x}_i, \boldsymbol{x}_j) = \delta^2 + \boldsymbol{x}_i \cdot \boldsymbol{x}_j \tag{4.1.21}$$

where δ^2 is a parameter that controls the homogeny of the function.

It should be noted different choices of kernel will result in different hyperparameters to be tunned during the training process, and the length-scale parameter l is a vector that has the same dimension as the input variable. For example, if the input has d features, i.e., $\boldsymbol{x}_i$ has d components, the RBF kernel can be written as:

$$k(\boldsymbol{x}_i, \boldsymbol{x}_j) = \exp\left(-\frac{1}{2l^2}\sum_{h=1}^{d}\left(\frac{{\boldsymbol{x}_i}^h - {\boldsymbol{x}_j}^h}{l_h}\right)^2\right) \tag{4.1.22}$$

Since the MLE may have multiple local optima, how many times the optimizer (the fmin-l-bfgs-b algorithm is utilised as the optimizer in this work) is allowed to repeatedly start can also have impacts on the model performance. Hence, the number of optimisations is treated as one of the parameters that need to be searched, in the range of 1 to 50 with a step size of 5.

Table 4.1.3. Parameter setting for the best GPR model.

Kernal function	μ	Number of optimisations
Matérn	2.5	20

Table 4.1.4. Cross validation metrics for the best GPR model.

RMSE	MAE	MAPE	NSE
2.68	1.25	0.0684	0.999949

Among the GPR models that have been tested with different kernel functions and number of optimisations, as shown in table 4.1.3 and 4.1.4, it is found that the model that has the Matérn kernel with $v = \frac{5}{2}$ and 20 runs of hyperparameter optimisations achieves the highest NSE score. It should be pointed out that GPR models are highly dependent on the choice of kernel function, and it is possible to combine different existing functions and hence form a new one or even manually construct a novel kernel function, which may further enhance the model performance. Nevertheless, this requires significant mathematical work and computation resources, so it is a good start point to look at the established popular kernel functions.

4.1.3 SVM model

The original proposed SVM has seen successful applications in classification problem because the core idea of SVM is to locate a hyperplane $y = \langle \boldsymbol{\omega}, \boldsymbol{x} \rangle + b$, where $\langle \cdot, \cdot \rangle$ represents dot product, which can divide the data domain into two subdomains. In two-dimensional problem, the hyperplane becomes a straight line, as shown in figure 4.1.3. Each of the subdomain only contains data samples that share the same certain feature, which perfectly suits the purposed of classification problem. The closest samples in each side of the hyperplane are the support vectors, which form the safety margin around the hyperplane and hence leads to an explicit mathematical object: minimizing the margin space. Similar idea can be adapted to handle regression problems, by considering the outputs now as continuous values, instead of finite discrete values. Given the data inputs, most regression methods aim to find a function $y = f(\boldsymbol{x})$ that can predict the dependent variables as close to the real observations as possible. While SVM regression declares an allowable error rate ε to tolerate all predictions with the deviations from the real observations less than ε. Instead of focusing on actual residuals at each data point, all predictions are accepted as long as they remain within the safety margin, which is now the space around the hyperplane and bounded by the declared error rate ε. The object of this regression process is now to ensure the flatness of the hyperplane, or alternatively speaking the coefficient vector $\boldsymbol{\omega}^{\mathrm{T}}$ must be constrained to restrict its impacts on the regression results in order to generalize the model, which can be formulated as follows [217]:

$$MIN \frac{1}{2} \|\boldsymbol{\omega}\|_2^2 \tag{4.1.23}$$

$$s.t. \begin{cases} y_i - \langle \boldsymbol{\omega}, \boldsymbol{x}_i \rangle - b \leq \varepsilon \\ \langle \boldsymbol{\omega}, \boldsymbol{x}_i \rangle + b - y_i \leq \varepsilon \end{cases} \tag{4.1.24}$$

Equation (4.3.24) is based on a tacit assumption that there exists a function $f(\boldsymbol{x})$, which is capable of describing all data samples within the precision of ε. In order to fairly take every data sample into consideration when equation (4.1.24) cannot be consistently satisfied, one can introduce the slack variable ξ and ξ^*, which effectively releases the error rate so that all data samples can be potentially included in the safety margin. Meanwhile, data that lies beyond the original margin bounds are undesired, so a coefficient C is necessary to impose penalties on such data points to minimize their contributions. Consequently, we can arrive at following objective equations:

$$MIN\ \frac{1}{2}\|\boldsymbol{\omega}\|_2^2 + C\sum_{i=1}^{N}(\xi_i + \xi_i^*) \tag{4.1.25}$$

$$s.t. \begin{cases} y_i - \langle \boldsymbol{\omega}, \boldsymbol{x_i} \rangle - b \leq \varepsilon + \xi_i \\ \langle \boldsymbol{\omega}, \boldsymbol{x_i} \rangle + b - y_i \leq \varepsilon + \xi_i^* \\ \xi_i, \xi_i^* \geq 0 \end{cases} \tag{4.1.26}$$

It should be noted that although the implementation of SVM is based on the condition that the data samples can be linearly classified, it is still applicable to non-linear problems. This is because nonlinearly dividable data samples $\boldsymbol{x}_\mathbf{i}$ in low dimensions can be transformed to higher dimensions $\varphi(\boldsymbol{x}_\mathbf{i})$ via a proper transformation function $\varphi()$, in which the data samples can become linearly separatable.

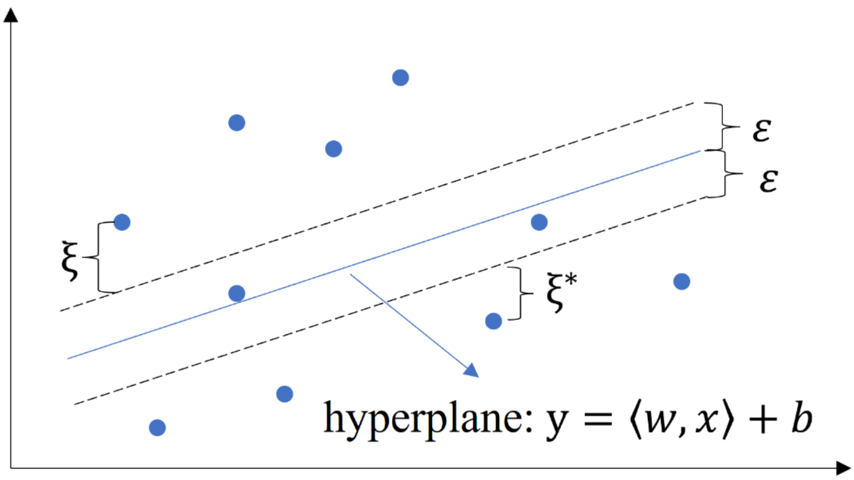

Figure 4.1.3. Illustration of SVM algorithm.

The dual problem is now:

$$MIN\frac{1}{2}(\alpha - \alpha^*)^{\mathrm{T}}Q(\alpha - \alpha^*) + \varepsilon e^T(\alpha - \alpha^*) - y(\alpha - \alpha^*) \tag{4.1.27}$$

$$s.t.\ \begin{cases} e^T(\alpha - \alpha^*) = 0 \\ 0 \leq \alpha_i, \alpha_i^* \leq C \end{cases} \tag{4.1.28}$$

where e is the vector of all ones, and Q is an $N \times N$ positive semidefinite matrix with $Q_{i,j} \equiv K(\boldsymbol{x}_i, \boldsymbol{x}_j) = \varphi(\boldsymbol{x}_\mathrm{i})^{\mathrm{T}}\varphi(\boldsymbol{x}_\mathrm{j})$ as the kernel. α and α^* are the Lagrange multipliers.

Based on which the prediction on at a new point $\boldsymbol{x}_n$ is given by:

$$\sum_{\mathrm{i}=1}^{\mathrm{N}}(a_\mathrm{i} - a_\mathrm{i}^*)K(\boldsymbol{x}_n, \boldsymbol{x}_i) + b \tag{4.1.29}$$

Similar to the GPR models, SVM models also employ kernel functions to complete the regression process. According to the availability in the Scikit-learn environment [203], we have tested the following four kernel functions.

The linear kernel function:

$$K(\boldsymbol{x}_i, \boldsymbol{x}_j) = \langle \boldsymbol{x}_i, \boldsymbol{x}_j \rangle \tag{4.1.30}$$

The polynomial kernel function:

$$K(\boldsymbol{x}_i, \boldsymbol{x}_j) = \left(\gamma\langle \boldsymbol{x}_i, \boldsymbol{x}_j \rangle + r\right)^d \tag{4.1.31}$$

The sigmoid kernel function:

$$K(\boldsymbol{x}_i, \boldsymbol{x}_j) = \tanh\left(\gamma\langle \boldsymbol{x}_i, \boldsymbol{x}_j \rangle + r\right) \tag{4.1.32}$$

The RBF function as introduced in equation (4.1.16). Note that γ, r and d in above three functions are coefficient parameters, which are considered as the corresponding hyperparameters and will be optimized during the training process. Again, other kernel functions are potentially applicable, but these well-established kernel functions are tested to avoid the complexity of deep optimisation. Compared with GPR models, SVM models have extra flexibility because they not only rely on the choice of kernel functions, but also the precession level ε and the penalty coefficient C. Generally, small absolute value of ε and large value of C are quired to obtain accurate predictions, i.e., the ideally best SVM models should be achieved when ε is close to zero and C goes to infinity. However, it is much more difficult to reach a convergence in such extreme conditions. We have arranged randomized search for values of ε and C within the bounds of 10^{-5} to 1 and 1 to 10^5 respectively, and compared the performance of SVM models with different kernel functions as described above. As shown in table 4.1.5 and 4.1.6, the RBF kernel function with the precession level and penalty coefficient set to be 3.237613×10^{-5} and 87472 respectively, demonstrates remarkable capability of predicting the outputs from given inputs with minor errors.

Table 4.1.5. Parameter setting for the best SVM model.

Kernal function	Precesion level	Penalty coefficient
RBF	3.237613e-5	87472

Table 4.1.6. Cross validation metrics for the best SVM model.

RMSE	MAE	MAPE	NSE
3.07	1.51	0.0743	0.999936

4.1.4 DT model

Similar to the SVM algorithm, the DT algorithm was also born for classification problem. The main principle is to divide the data samples into smaller subsets by certain threshold criteria subsequently until decisions can be made on each data sample with enough accuracy. The finalized structure of a DT model resembles a top-down tree constitutes of a root, certain amount of branch of nodes and leaves. Similar principle can be also applied to regression problems by replacing the category labels with continuous values, i.e., the output voltage. The critical step in DT regression is to select proper threshold criteria, which must ensure every split of the data samples pushes the model closer to the optimal one with higher prediction accuracy. Let us consider there are N_m samples at node m, represented by Q_m. A possible split $\theta(j, t_m)$, where j is the feature dimension of the subset and t_m is the threshold value, can partition Q_m into the left subset Q_m^{left} and right subset Q_m^{right}:

$$Q_m^{left}(\theta) = \{(\boldsymbol{x}, y)|x_j \leq t_m\} \tag{4.1.33}$$

$$Q_m^{right}(\theta) = Q_m \backslash\backslash Q_m^{left}(\theta) \tag{4.1.34}$$

Then the quality of this split $M(Q_m, \theta)$ can be evaluated by employing an impurity function $P()$, which should be specified according to the tasks to be solved:

$$M(Q_m, \theta) = \frac{N_m^{left}}{N_m} P\left(Q_m^{left}(\theta)\right) + \frac{N_m^{right}}{N_m} P\left(Q_m^{right}(\theta)\right) \tag{4.1.35}$$

Based on equation (4.1.35), the best split parameter $\theta^*(j, t_m)$ can be derived by minimising the impurity and the process recurse for subsets $Q_m^{left}(\theta)$ and $Q_m^{right}(\theta)$ as shown in figure 4.1.4, until pre-defined termination requirement is satisfied. Normally, the recursion can be controlled by specifying the maximum numbers of recursions and/or minimum number of data samples in a subset. In this work, the minimum number of data samples in a subset is set to be 2, meaning if any subset contains 2 or less data samples then it will not be divided further. The number of maximum number of recursions is determined by a grid search, ranging from 5 to 200.

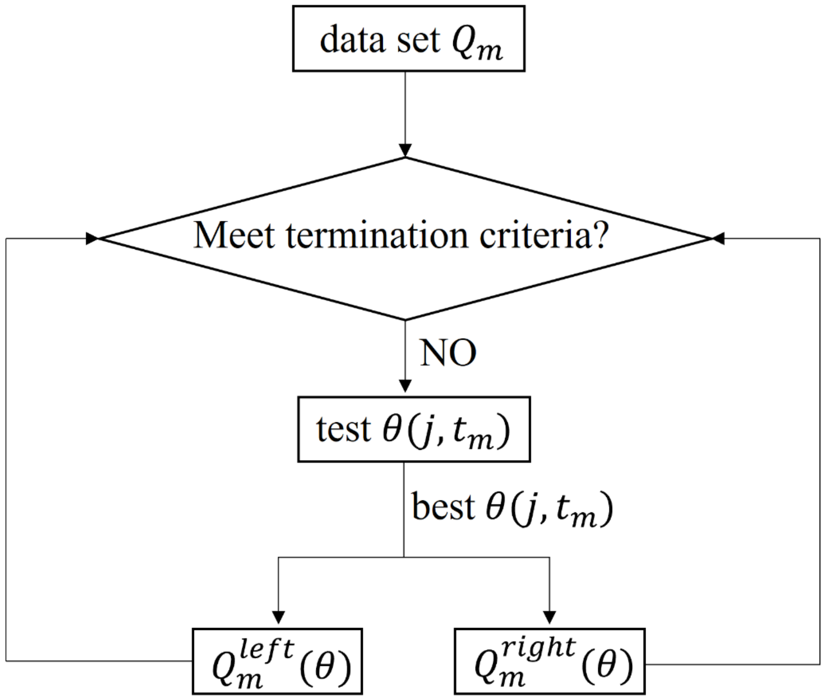

Figure 4.1.4. The block diagram for the logic of constructing a DT model.

From the regression point of view, the object is to minimize the residuals between predictions and observations. Therefore, any metrics that measure the residuals level can be utilised as the impurity function to be optimized at each split. Here, we have teste three common criteria for regression problem, namely the mean squared error (MSE), Friedman-mean square error (F-MSE) [218] and MAE.

The equation of MSE is given by:

$$MSE = \frac{1}{n}\sum_{i=1}^{n}(y_i - \bar{y})^2 \tag{4.1.36}$$

whose calculation is completely based on the data samples in the target subset, i.e., either $Q_m^{left}(\theta)$ or $Q_m^{right}(\theta)$. While F-MSE takes contributions from both subsets into consideration, which is formulated as:

$$F\text{-}MSE = \frac{n_{left} * n_{right}}{n_{left} + n_{right}} \left(\bar{y}_{left} - \bar{y}_{right}\right)^2 \qquad (4.1.37)$$

As can be seen for table 4.1.7 and 4.1.8, the DT model that has the maximum depth of 10 and F-MSE threshold criterion achieves the highest NSE score and demonstrates the best prediction performance.

Table 4.1.7. Parameter setting for the best DT model.

Threshold criterion	Maximum depth
F-MSE	10

Table 4.1.8. Cross validation metrics for the best DT model.

RMSE	MAE	MAPE	NSE
79.07	49.28	0.5356	0.957424

4.1.5 KNN model

Up to now, the models aforementioned all implement supervised machine learning process that relies on a specific objective function in those models, such as the loss function in MLP models and the log-marginal-likelihood function in GPR models These objective functions essentially convert the regression to an optimization problem of such a function. In contrast, KNN models do not count on an objective function to transform the regression problem to a function optimisation process. Instead, KNN models strictly relates the dependent variables to their corresponding inputs through an intuitive convention: data samples that have similar values of the dependent variables should also have similar values of the independent variables. Based on this straightforward principle, given the input for a new data point, the output for that point can be predicted by following logic: first finding out k data points in the data set, which have the shortest distance to the inquired data point, and then simply averaging the outputs of these points, as shown in figure 4.1.4.

As a result, how to calculate the distance between two data samples and find the k closest data samples are the most important steps in constructing KNN models. Commonly, one can calculate the Euclidean distance between the inquired data point and every data sample in the dataset, from where the k closest data samples can be determined by sorting out all the distances, which is referred to the brute-force search. In this approach, given N data samples with D dimensions, the computational complexity scales as $O[DN^2]$. Thus, the computational complexity will increase exponentially with the number of data samples. In order to address the inefficiency of brute-force search with large number of data samples, K-D tree search has been developed [219]. The basic idea of such an approach is that if point A is very far away from point B, and point B is very close to point C, then it is clear that point A is also very far away from point C without having to calculate the distance between them explicitly. By constructing a K-D tree, the number of distance computations can be dramatically reduced. However, it is less effective to construct a K-D tree structure in high dimensions. Therefore, the ball tree search has been further developed to handle data samples that have many feature dimensions. In this work, we have tested all three of the search algorithms with the value of k ranges from 1 to 50.

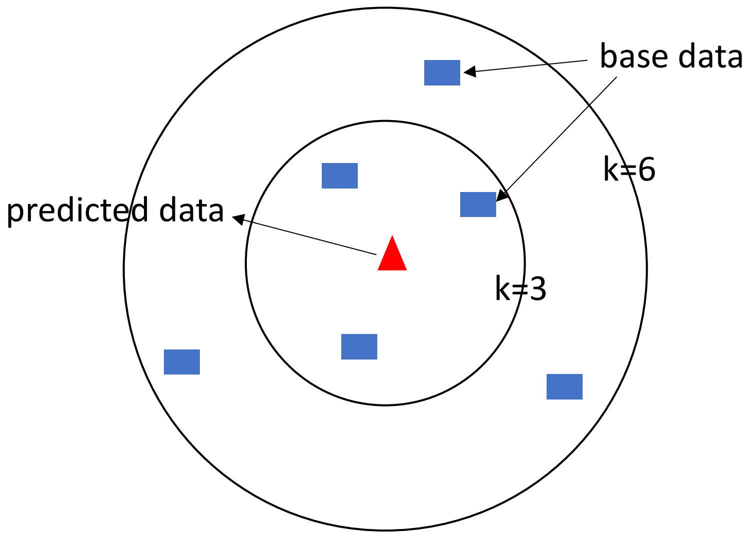

Figure 4.1.4. Illustration for the KNN regression.

As it can be seen from table 4.1.9, the best KNN model is obtained by utilizing the ball tree search approach to estimate new predictions by choosing 6 the closest points, and the across validation metrics are shown in table 4.1.10.

Table 4.1.9. Parameter setting for the best KNN model.

Search algorithm	Number of cloest points
Ball tree	6

Table 4.1.10. Cross validation metrics for the best KNN model.

RMSE	MAE	MAPE	NSE
60.40	35.74	0.5627	0.975355

4.1.6 Model selection

Regression models based on five different machine learning techniques have been primarily tested under various settings, and each of them has also been evaluated by the numerical metrics introduced in equation (4.1.2) to (4.1.5), to judge the goodness of such a model in predicting the HTS output voltage according to the four design parameters. Yet, numerical criteria just show the general aspect of a model, which may not be enough in practice. As stated earlier, in order to illustrate the broader and more sophisticated aspects of the relationships between models and data, graphical criteria are indispensable. Let us define the samples with relative prediction errors below a given level as effective-predicted samples, and we can evaluate the predicting effectiveness of different models by the proportions of the effective-predicted samples with respect to the relative prediction error, which is referred as prediction rate. In order to achieve this, we define $\delta_i = \left|\frac{y_i - \hat{y_i}}{y_i}\right|$ and then plot the additive rate of n samples, i.e., from 0 to 1 by step of $1/n$ with respect to the sorted δ_i from zero to the maximum relative error. The prediction rate curve of a model is obtained by joining those points. The ratio of effective-predicted samples can be accessed from vertical axis as relative error being the horizontal axis. The introduction of this graph allows us to examine more details about the performance of each model. The area between the prediction rate curve and the vertical axis, which aggregates the relative errors, provides a linkage to the numerical criteria as formerly discussed. In general, a model can be considered good if this area is smaller, and it is visually easy to compare models with this plot. Based on the results from subsection 4.1.1 to 4.1.5, the best candidate from each model group is chosen to plot its prediction rate curve.

As shown in figure 4.1.5, the prediction rate curves for MLP, DT and KNN models lie completely below those for GPR and SVM models, which means that for any given error level, less samples can be effectively predicted by MLP, DT and KNN models than the others. Besides, the prediction rate curve of MLP, DT and KNN models cover a much wider range of errors than that of GPR and SVM models, indicating that they have worse error containing ability. For instance, the maximum relative error generated by MLP, DT and KNN models are around 154%, 123% and 80%, respectively, and this strengthens the conclusion that MLP, DT and KNN models are not effective in providing stable and trustable predictions (Note that the actual V_{oc} values of those samples being predicted range from 0 to 1971 μV). As for the GPR and SVM models, though they both demonstrates good capability of maintaining the relative errors well below 12%. Meanwhile, the curve of SVM model almost consistently grows beneath that of GPR model, which can be interpreted as: more samples can be accurately predicted by GPR model than SVM model given a certain threshold error level. It is true that the capability of producing minor error predictions is not significantly different between the GPR and SVM model, yet their solution time are relatively distinct. The SVM model requires more than 2 minutes to be solved, while the GPR model only takes few seconds, which is ten times less. Therefore, it is reasonable to select the GPR model as the optimal candidate to model the HTS dynamo output voltage, not only for its excellent accuracy but also due to the promise of saving considerable solution cost.

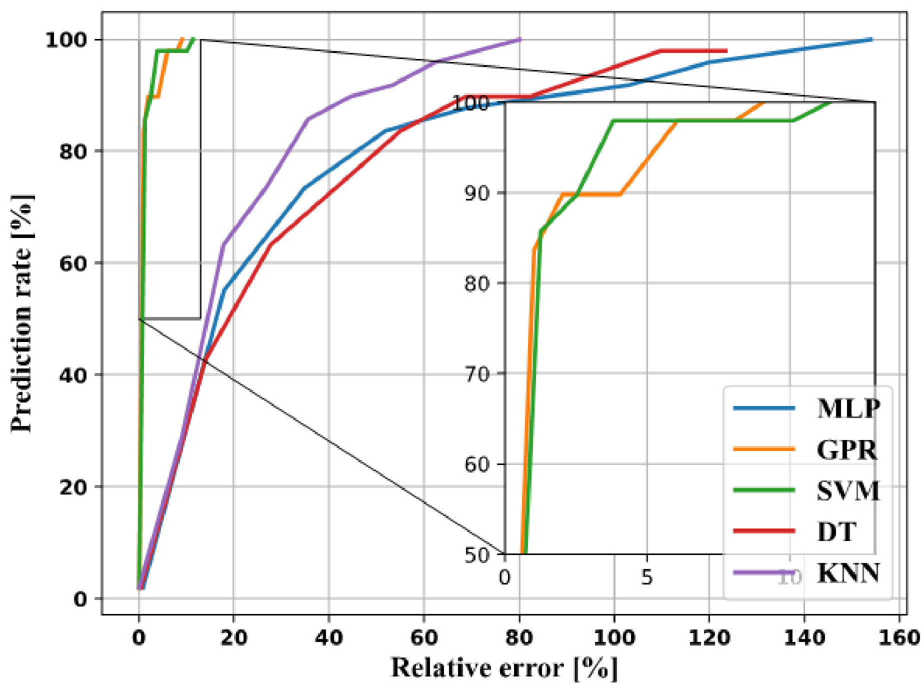

Figure 4.1.5. The curve plot of prediction rate versus relative error

To further verify the effectiveness of the GPR model, this model was utilised to reproduce figure 3.2.1 by feeding three sets of parameters (except for the frequency f) as inputs and extracts the values of predicted V_{oc} as outputs. The results are presented in figure 4.1.6(a), where the V_{oc} values of blue dots come from real FEM simulations, i.e., those plotted in figure 3.2.1, and the red dots include V_{oc} values predicted by the GPR model. It is clear that the output voltage dependences versus all the three design parameters are well described by the predictions, more precisely, V_{oc} drops with the increase of air gap (from 1st to 10th run), V_{oc} firstly increases then decreases over the increases of HTS tape width (from 11th to 20th run), and V_{oc} climbs with the increase of the remanent flux density of the permanent magnet (from 21st to 30th run). As further illustrated in figure 4.1.6(b), the average error rate for all predictions is 2.98%, which demonstrates the accuracy of this model. It should be noted that there are several predictions that have noticeable errors, such as the 21st, 22nd runs, which are corresponding to extreme conditions, e.g., B_r equals to 0.15 T and 0.3 T. Under such extreme circumstances, very weak output voltage is expected and hence those small values are highly sensitive to any mismatch. However, in practice B_r is commonly around 1 T or above, so that the incompetence of this GPR model for predicting output voltage in extreme conditions will not undermine its goodness of performance in general. As a result, it can be concluded that this GPR model is capable of predicting accurate output characteristics for HTS rotary flux pumps.

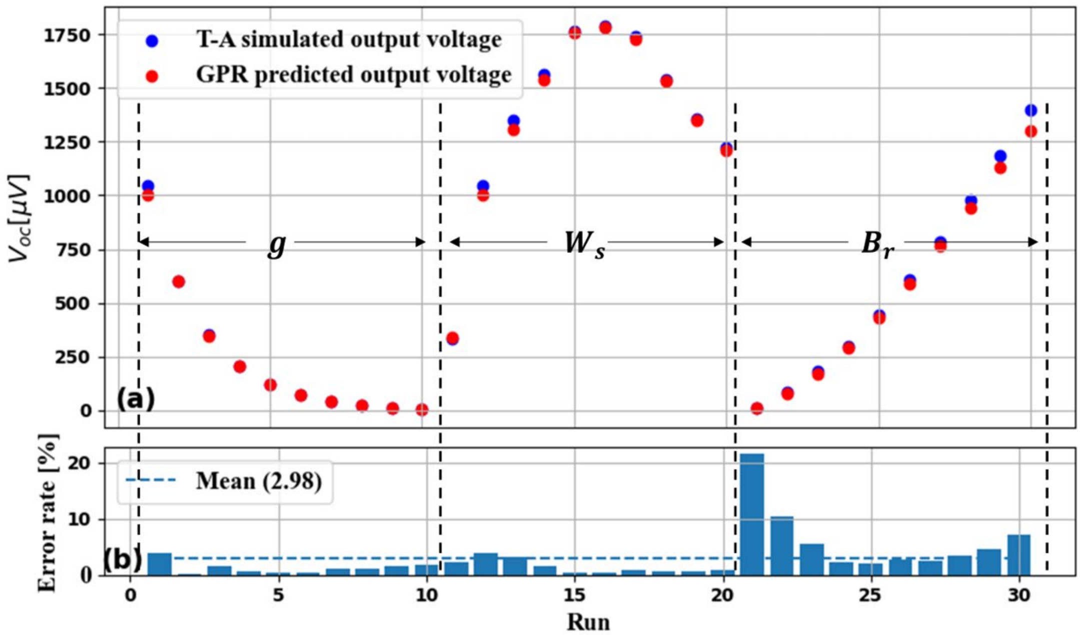

Figure 4.1.6. Reproduced results of figure 4.2.1 by our GPR model.

4.2 Sensitivity analysis

It has so far been revealed that how the operating frequency f, air gap g, superconductor tape width W_s and remanent flux density of the permanent magnet B_r influence the HTS dynamo output voltage V_{oc}, after which a GPR based statistical model has been proposed to accurately predict V_{oc} by feeding these design parameters as inputs. However, to what extent does each parameter impact the output voltage still remains unclear. In order to fulfil the aim of this work, which is to provide comprehensive guidance for HTS rotary flux pump design, the sensitivity of each parameter is further explored through an analysis of variance (ANOVA). As before, the operating frequency f is excluded from the analysis list to reduce the workload. As a result, the number of second order interaction terms is reduced from C_4^2 to C_3^2, namely $g * W_s$, $g * B_r$ and $W_s * B_r$. We have set the values of each parameter to three levels, because the relation between V_{oc} and W_s is not monotonic so that at least three values are required to represent the variation trend, which comprises of both the increasing and decreasing parts. The orthogonal tables are believed to effectively reduce the cost of experimental schedules and mathematical calculations, by the means of only considering the representative values of each parameter in a proper way. The $L_{27}(313)$ Taguchi array has been adapted to include the three parameters and their corresponding interaction terms, as shown in table 4.2.1. The ANOVA results are represented in table 4.2.2, which interprets each of variable via F-test and the statistical hypotheses (under a 95% confidence level) test. It is shown that all three parameters are significant as their F-values are far greater than the criterion $F_{0.05}(2{,}8) = 4.46$. The remanent flux density of permanent magnet seems to be the prior dominant factor for determining the output voltage, and the importance of air gap is slightly lower while the importance of superconductor tape width is dramatically less with only 40% of the F-value for the remanent flux density of permanent magnet. As for the interaction terms, it is believed that the interactions between g and B_r are very significant as its F-value supresses the criterion $F_{0.05}(4{,}8) = 3.84$. Meanwhile, the other two interaction terms are relatively significant, because their F-values are located between the criterion interval $F_{0.05}(4{,}8) = 3.84$ and $F_{0.1}(4{,}8) = 2.81$. In a summary, the importance ranking for each parameter is: $B_r > g > W_s$, and all the second order interaction effects between them are found to be influential as well. This implies that the individual effect of each parameter should be considered first during the design and optimisation of HTS rotary flux pumps, whist the designer should be aware of the existence of interaction effects since they possess unignorable influences upon the output characteristics.

Table 4.2.1. Adapted L27 (313) Taguchi array. Note that the letter A, B and C in the table represent the level of variable value, e.g. A means the smallest, B means the medium and C means the highest.

No.	g/mm	W_s/mm	g*W_s	g*W_s	B_r/T	g*B_r	g*B_r	W_s*B_r	W_s*B_r	V_{oc}/ μV
1	2(A)	6(A)	A	A	0.2(A)	A	A	A	A	4.70
2	2(A)	6(A)	A	A	0.8(B)	B	B	B	B	135.40
3	2(A)	6(A)	A	A	1.4(C)	C	C	C	C	409.04
4	2(A)	30(B)	B	B	0.2(A)	A	A	B	C	39.98
5	2(A)	30(B)	B	B	0.8(B)	B	B	C	A	919.87
6	2(A)	30(B)	B	B	1.4(C)	C	C	A	B	2079.66
7	2(A)	54(C)	C	C	0.2(A)	A	A	C	B	6.92
8	2(A)	54(C)	C	C	0.8(B)	B	B	A	C	646.72
9	2(A)	54(C)	C	C	1.4(C)	C	C	B	A	1591.87
10	6(B)	6(A)	B	C	0.2(A)	B	C	A	A	0.08
11	6(B)	6(A)	B	C	0.8(B)	C	A	B	B	6.77
12	6(B)	6(A)	B	C	1.4(C)	A	B	C	C	29.41
13	6(B)	30(B)	C	A	0.2(A)	B	C	B	C	0.33
14	6(B)	30(B)	C	A	0.8(B)	C	A	C	A	209.69
15	6(B)	30(B)	C	A	1.4(C)	A	B	A	B	621.11
16	6(B)	54(C)	A	B	0.2(A)	B	C	C	B	0
17	6(B)	54(C)	A	B	0.8(B)	C	A	A	C	183.83
18	6(B)	54(C)	A	B	1.4(C)	A	B	B	A	672.00
19	10(C)	6(A)	C	B	0.2(A)	C	B	A	A	0
20	10(C)	6(A)	C	B	0.8(B)	A	C	B	B	0.43
21	10(C)	6(A)	C	B	1.4(C)	B	A	C	C	2.53
22	10(C)	30(B)	A	C	0.2(A)	C	B	B	C	0
23	10(C)	30(B)	A	C	0.8(B)	A	C	C	A	29.77
24	10(C)	30(B)	A	C	1.4(C)	B	A	A	B	169.70
25	10(C)	54(C)	B	A	0.2(A)	C	B	C	B	0
26	10(C)	54(C)	B	A	0.8(B)	A	C	A	C	30.14

Table 4.2.2. ANOVA results.

Source	Degree of freedom	F -value	p-value
g	2	23.668	0.000437
W_s	2	10.136	0.006
B_r	2	25.342	0.000345
$g * W_s$	4	3.261	0.073
$W_s * B_r$	4	3.835	0.050
$B_r * g$	4	8.039	0.007

Please note that the F-value and p-value are the results for 'F-test' and 'statistical hypothesis testing', respectively. Simply speaking, the p-value tells how likely the response variable is correlated with independent variables. For example, this 'statistical hypothesis testing' here is conducted under a 95% confidence level, so if the p-value of a certain independent variable is smaller than (1-95%=0.05), then it is 95% correct to declare that the variable is correlated with the response variable. The 'F-test' shows directly how significantly each of the independent variable plays in determining the response variable, whose value can reflect the significance of each variable.

4.3 Semi-deep learning neural network

The numerical models, including the ***T-A*** formulation-based model utilised in the last chapter and the ***H-A*** formulation-based model developed in the last section, are widely used to solve superconductivity problems, which can solve Maxwell equations combined with required physical laws and conditions through FEM simulations. It is well-recognized that FEM simulations can simulate the physical process involved, offering an efficient and low-cost alternative to experimental work. However, the utilization of FEM simulations is subjected to professional knowledge about the target problem, which requires abundant user interactions, and the efficiency deserves further improvement. Such as approach does not lend itself to the industrial design and optimization, where the focus is put on certain specifications that can reflect the performance of the device rather than the underlying physics.

In above sections, we proved the feasibility of applying common machine-learning techniques to capture the output characteristics of an HTS dynamo in a fast and accurate manner [220], which treats each of the design parameters as independent inputs and V_{oc} as output and link them together by a determined mathematical model. The model proposed in [220] is however limited by only considering the three previously considered design parameters, namely the air gap g, HTS tape width W_s and the remanent flux density B_r of the PM. In order to break through those limitations and expand our findings further, in this we aimed to take extra parameters, including the non-linear high frequency f response, rotor radius R_r and magnet width W_m, into account. With all key design considerations of an HTS dynamo being covered, the newly proposed model is believed to be capable of efficiently describing the output behaviour of HTS dynamo at full scale.

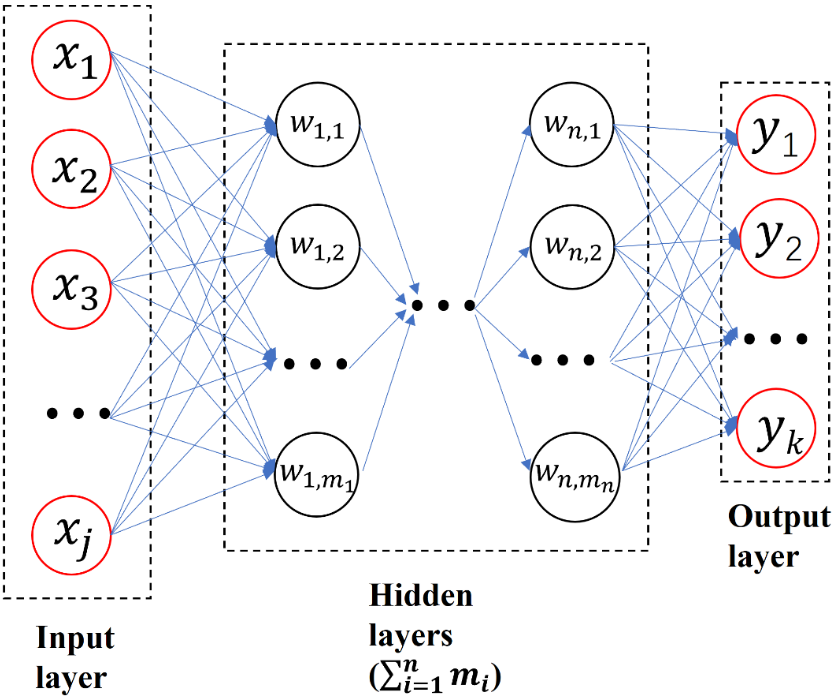

Figure 4.3.1. Structure of a full-connected MLP neural network.

Deep learning is a neural network based artificial intelligence method, which can represent unknown relations among a set of data samples in the form of a statistical model. MLP is the most widely used neural network, consisting of the input layer, output layer and hidden layer(s). Figure 4.3.1 shows a full-connected neural network, which has n hidden layers with m_i $(i = 1, \cdots, n)$ neurons in each of them. Neurons in each layer are connected through certain activation functions, so that the given input and output can be linked together. For the problem concerned here, the number of neurons in the input layer and output layer are to be six and one, respectively, in accordance with the six design parameters and one voltage output for an HTS dynamo. Given the relationships between the output and each of inputs can be highly nonlinear, the rectified linear unit (ReLU) function, which possesses the superior ability to characterize the complex nonlinearity of the model and smoothen gradient propagation during the training, is employed as the activation function [221]:

$$ReLU(x) = \max(0, \boldsymbol{w}^T\boldsymbol{x} + b) \tag{4.3.1}$$

where $\boldsymbol{w}^T$ denotes the weight coefficients matrix and b signifies the bias coefficients. The main purpose of the model is to predict the voltage, which can be considered as a regression task to predict a continuous variable, and hence the squared L2 norm is adopted as the loss criterion:

$$l(x, y) = \{l_1, \cdots, l_N\},\ \ l_N = (x_n - y_n)^2 \tag{4.3.2}$$

Based on this loss function, Adam is applied as the optimisation solver to update weight coefficients matrix in equation (4.3.8) as follows [211]:

$$g_t = \nabla_\theta f_t(\theta_{t-1}) \tag{4.3.3}$$

$$m_t = \beta_1 m_{t-1} + (1 - \beta_1)g_t \tag{4.3.4}$$

$$v_t = \beta_2 v_{t-1} + (1 - \beta_2)g_t^2 \tag{4.3.5}$$

$$\widehat{m_t} = \frac{m_t}{1 - \beta_1^t} \tag{4.3.6}$$

$$\widehat{v_t} = \frac{v_t}{1 - \beta_2^t} \tag{4.3.7}$$

$$\theta_t = \theta_{t-1} - \frac{\alpha \widehat{m_t}}{\sqrt{\widehat{v_t}} + \epsilon} \tag{4.3.8}$$

where f_t is the objective function and θ_t represents the parameters to be updated, while α, β and ϵ are set to be constant values as 0.001, 0.9 and 10^{-8}, respectively. In order to make the trained neural network has a more generalized performance, the k-fold cross validation scheme is taken. As demonstrated in figure 4.3.2, the data set is divided into k mini sets. The training processes repeat k times, in each time one of the k mini sets is taken as the train set and the rest $k - 1$ mini sets are taken as the validation set, subsequently. After the cross validation is completed, the average adapted NSE is calculated to evaluate the performance of the trained model:

$$NSE = \frac{1}{k}\sum_{t=1}^{k}\left[1 - \frac{\sum_{i=1}^{p}(y_i - \hat{y}_i)^2}{\sum_{i=1}^{p}(y_i - \bar{y})^2}\right] \tag{4.3.9}$$

where k is the number of mini-sets (set to be 10), p is the number of data samples, $\bar{y}$ represents the average output, y_i and $\hat{y}_i$ indicate the observed and predicted output, respectively. The best NSE score that can be achieved is 1, which means that the model can predict all data samples perfectly with no errors. Otherwise, the closer the NSE score is to 1, the better accuracy the model will have. We have previously implemented the MLP with one hidden layer to predict the output characteristics for an HTS dynamo based on three input design parameters, in section 4.1. In this section, we take advantage of the deep learning approach enhanced by graphics processing unit (GPU) acceleration to investigate more complicated neural networks, then put forward an improved model, which can rapidly and accurately capture the output characteristics for HTS dynamo with all design parameters now included.

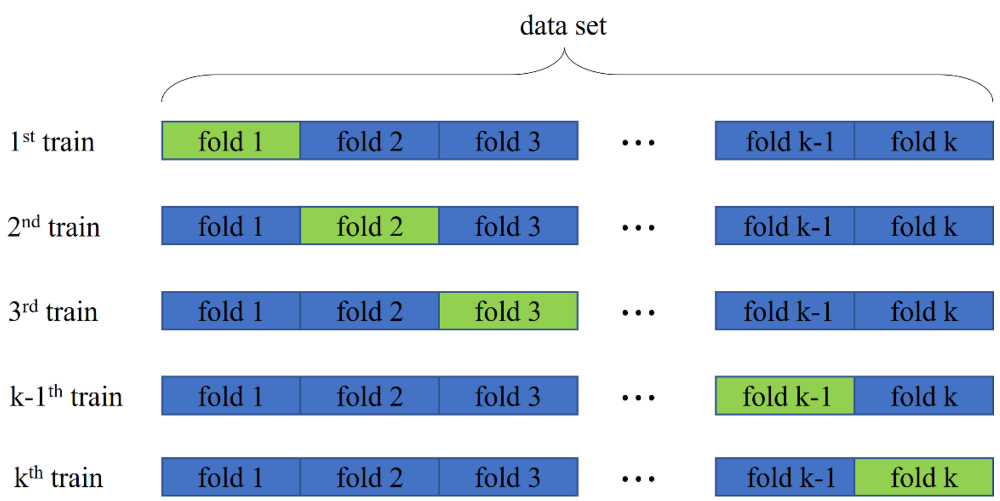

Figure 4.3.2. Illustration of the k-fold cross validation, the fold in green contains the data samples for the train set and the fold in blue contains the data samples for the validation set.

Each set of data required by the DNN training requires seven values, with six values for specifying the input design parameters and one for specifying the output open circuit voltage. In order to make the input data more effective and representative, two data schemes were chosen. The first one divides the value range (see the ranges in figure 3.2.1) for each parameter into 1000 small intervals, which essentially forms a dense data map that improves the resolution of the prediction model. The second one divides the value range for each parameter into 50 relatively large intervals, which allows more room for different parameter combinations with limited data samples, so that it is easier for the model to learn the general behaviour from the data samples. In each scheme, 4,000 data samples are generated, so totally 8,000 data samples are fed to the DNN models.

The input values propagate through the hidden layers simultaneously until they reach the output layer, so it is important that the values for each input neuron are closely comparable, otherwise the input neuron with a significantly higher value will dominate the training process and lead to poor performance for the model to predict the output when taking other input neurons into account. Therefore, the values for each input neuron were normalised into unit scale by the following transformation:

$$x_t = \frac{x - x_{min}}{x_{max} - x_{min}} \tag{4.3.10}$$

Though it is commonly believed that the output values will not have impacts on the quality of the trained model, it should be noted that the output values in this study represent the open circuit voltage from an HTS dynamo, which can vary between zero to thousands of micro-volts. In order to avoid any convergence difficulties due to the wide fluctuation of values, the logarithm for the output values is taken to constrain them in a narrow domain as follows:

$$y_t = \log(y + 1) \tag{4.3.11}$$

4.3.1 Topology determination

In terms of constructing a MLP type neural network, there are several influential factors, or so-called hyperparameters that have significant impact on the performance of the derived model. Some of these hyperparameters can be intuitively set according to the nature of the problem, such as the number of neurons in the input and output layer, and some of the others can follow the general rules of practice published in existing literature, such as the choice of proper activation function and loss function. However, exact guidelines about how to determine the structure of hidden layers are still lacking [222]. Researchers have put tremendous efforts in trying to provide a solution for this issue, including the Akaike's Criterion [223], Inverse test method [224] and some customized methods to find the optimal architecture for the neural network. Yet those methods are developed for specific problems, and it is hard to simply apply them to a new situation. In this work, we determined the neural network topology based on previous work and our understanding of this specific problem.

Theoretically, hidden layers greater than one can describe any arbitrary functions with arbitrary boundaries. Nevertheless, more hidden layers do not necessarily guarantee a better performance of the model. Besides, the increase of hidden layers will expand the model complexity and result in lower efficiency since more computation resources are required to solve the problem. Choldum et al. have stated in [225] that the number of hidden layers in the neural network can be determined according to the amin components suggested by the principal components analysis. In our case, the six input variables are pre-selected design parameters, which are independent to each other, and no correlations exist among them. Hence, it is reasonable to limit the hidden layers for the neural network below six. As for the number of neurons in the hidden layers, it also needs careful attention. On the one hand, insufficient neurons will make the model incapable of learning the underlying relations from the data set, which is often referred as to as 'under fitting'. On the other hand, excessive neurons will cause 'over fitting', where the model gets stuck in local optima and fails to learn the general behaviour from the data set. Considering the suggestions in [213, 226, 227], and the computing resources available, a randomized grid search was performed to test the number of neurons in each hidden layer ranging from 4 to 1024. A series of experiments with different DNN topologies were then conducted, and the quality of those models were evaluated using their NSE scores, equation (4.3.9). The best topology that achieved the highest NSE score for each number of hidden layers has been selected to be presented in table 4.3.1.

Table 4.3.1. NSE scores for different DNN model topologies.

Number of neurons in each layer						NSE
1	2	3	4	5	6	
1020	NA	NA	NA	NA	NA	0.99601
808	292	NA	NA	NA	NA	0.99932
636	376	444	NA	NA	NA	0.99927
432	820	328	836	NA	NA	0.99908
400	816	856	348	400	NA	0.99910
968	328	160	696	128	92	0.99907

Table 4.3.1 shows that the best training performance was achieved by the DNN model with 2 hidden layers, where there are 808 and 292 neurons in the first and second hidden layer, respectively. Yet a high NSE score does not necessarily mean

that the model must have a good quality, because the data set prepared to train the model is limited. In order to ensure that the model has a generalized prediction capability, the best trained DNN model was selected to predict a new set of data samples that are not covered in any of the train and validation set. As shown in figure 4.3.3, all the predictions denoted by the red points locate in close proximity of the perfect match line, indicating very good performance of this model in the general case. The relative error in percentage for each prediction is plotted in figure 4.3.4, from where it can be seen that the maximum error for two predictions is 12% out all (183) tested samples, while most of the predictions have an error rate less than 2% and the average error rate is maintained at 2.06%. Figure 4.3.5 shows these prediction errors in more detail by dividing all the test samples into different intervals in terms of their proportions to the maximum value. It can be observed that high error rates are easier to occur for small predicted values, e.g. the 0~10% interval, which can be readily understood because small values are more vulnerable to the error measurement under relative criteria. Even including those outliers (identified by the black cycles in figure 4.3.5), the average error rate (marked by the green triangles in figure 4.3.5) for predictions in every interval are well below 3%. Besides, the demand for designing and optimizing HTS dynamo type of devices, in most cases, is to maximize the output voltage, for which we believe the applicability and effectiveness of this model will not be undermined.

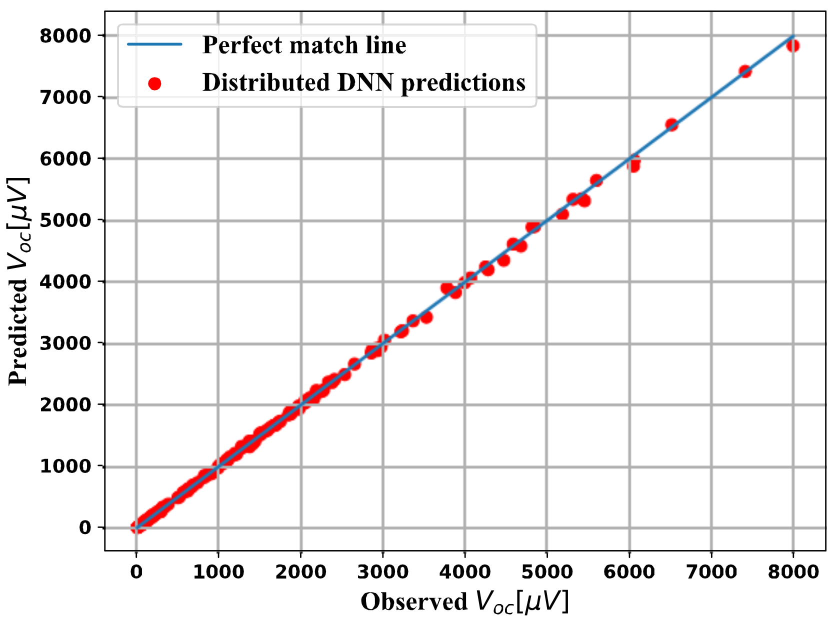

Figure 4.3.3. Predictions for the test samples by the selected best DNN model.

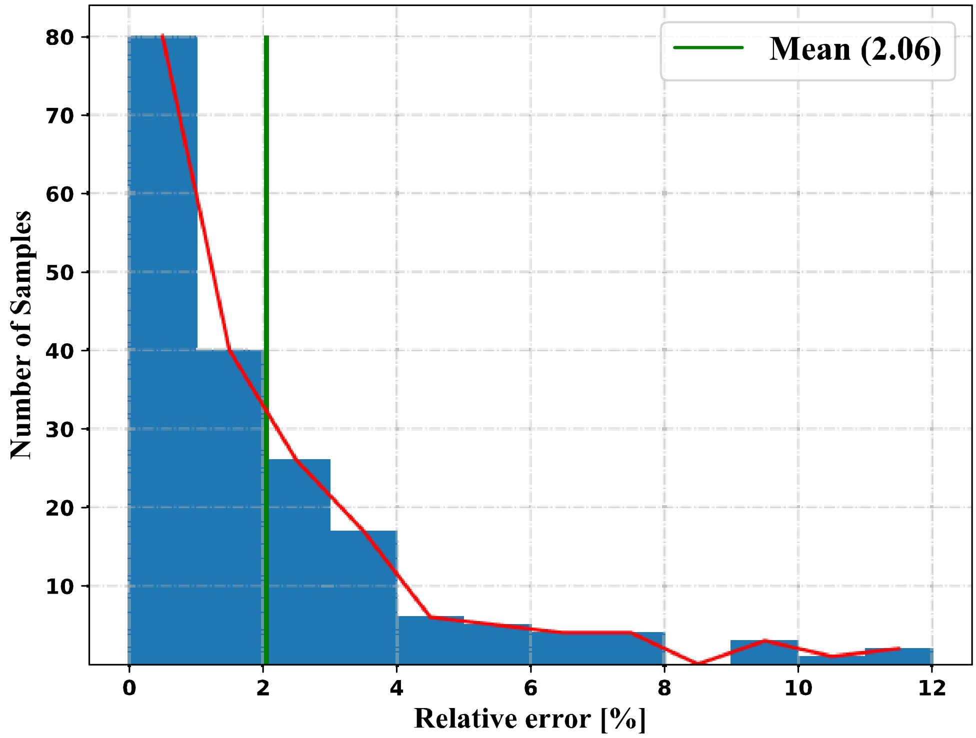

Figure 4.3.4. Histogram plot for the relative errors of predicted voltage. The red line connects the medium relative error in each sample group, and the green line identifies the mean value of the relative errors for all data samples.

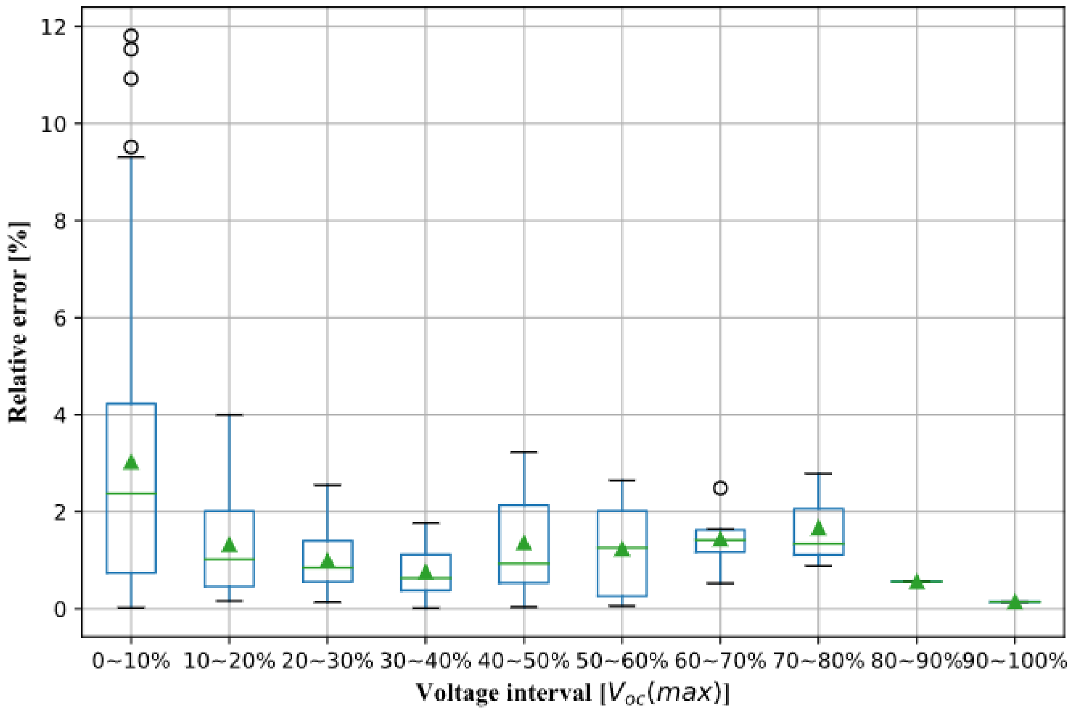

Figure 4.3.5. Box plot of the relative errors for predicted voltage grouped by different intervals (proportions to the maximum prediction).

4.3.2 Parameter grouping

As a demonstration of the proposed model, we utilised the model to illustrate the output characteristics of each of the six parameters. Since it is not practical to visualize all the parameters in one single plot, the six parameters were manually classified into three groups. Firstly, both the frequency and the rotor radius determine how long the HTS tape will experience the effective field provided by the rotating magnet in one complete cycle, so they are grouped together as the 'duration group'. Secondly, the magnetic field experience by the HTS tape is directly controlled by the air gap and the PM remanent flux density, and so form the 'field group'. Lastly, the authors of [103] have pointed out that the HTS tape width relative to the PM width can make a difference on the output voltage by affecting some critical features, e.g., whether the applied field can be considered homogenous. Therefore, we have grouped the tape and PM width together as the 'width group'. As it can be seen from figure 4.3.6(a), the smooth curved surface implies that the frequency response of the HTS dynamo tends to become non-linear when the frequency increases gradually (the turning point occurs at approximately 100 Hz), which is in accordance with the observation in [132]. In addition, the rotor radius response also shows what is expected: the output voltage decreases when the rotor gets larger. This is because a lager rotor will reduce the time interval during which the HTS is exposed to the effective PM magnetic field, which is essentially equivalent to a decrease in frequency. From figure 4.3.6(b) it can be observed that the peak output voltage can be achieved by having the smallest air gap and the largest remanent flux density at the same time. The saddle shape in figure 4.3.6(c) reflects the bilateral effects of the HTS tape width on the output voltage, namely the fact that the voltage increases with HTS tape width up to a certain point, after which it starts to decrease. Meanwhile, the PM width also plays a critical role on the output voltage, which increases monotonically with the PM width within the investigated range.

4.3.3 Optimal tape width

Combining previous studies in chapter 3 and the work demonstrated in subsection 4.3.2, it is concluded that the individual impact of all design parameters on the output voltage can be described by a monotonic function, except for the HTS tape width. Since the existence of an optimal HTS tape width for the HTS dynamo to obtain maximum output voltage has been proven, it is worthwhile knowing whether the optimal width is influenced by other parameters. Based on the proposed DNN model, it is convenient to arrange a series of parameter sweeps for each of the other five parameters by varying the HTS tape width, from which the optimal HTS tape width for different configurations can be identified. According to the results shown in figure 4.3.7, altering any of the parameters will change the optimal width correspondingly. An increase in PM remanent flux density and PM width both result in a considerably wider HTS tape required to obtain higher output voltage. The rotor radius has a relatively weak influence on the optimal HTS tape, while its impact on the output voltage is also not significant as can be seen from figure 4.3.6(a), so it is reasonable to ignore the rotor radius. In particular, the optimal HTS tape width tends to decrease for small airgap and high operating frequency. Meanwhile, either a decrease in the air gap or an increase in the operating frequency can help level up the output voltage. This observation can lead to a useful HTS dynamo design rule, namely that the device should be operated under small air gap and high frequency (up to 200 Hz), because less HTS tape is required while obtaining higher output voltage.

As aforementioned, the width ratio of the PM and the HTS tape is a key factor that can influence the output voltage for an HTS dynamo. In order to explore this factor in more detail, we define the 'width ration' W_{rt} as:

$$W_{rt} = \frac{W_s}{W_m} \tag{4.3.12}$$

The output characteristics predicted by our DNN model for different W_{rt} comparison is presented in figure 4.3.8. Each of the solid lines with a distinct colour represents the PM width response under a specific width ratio, and it is clear that increasing the PM width increases the output voltage if the width ratio is kept constant. However, for W_{rt} greater than 6, the intersections between different lines imply that increasing the width ratio cannot guarantee that the voltage will also increase. This result proves the existence of the bilateral effect of the HTS tape width again, and implies that the HTS tape width and the PM width should be considered separately while employing the width ratio between them is not sufficient to summarize their individual impacts in one variable. Moreover, figure 4.3.8 also provides a possible solution to avoid the limitation of the bilateral effect of the HTS tape width for HTS dynamo design, which is to increase the PM width further, so that the optimal HTS tape width can be effectively extended.

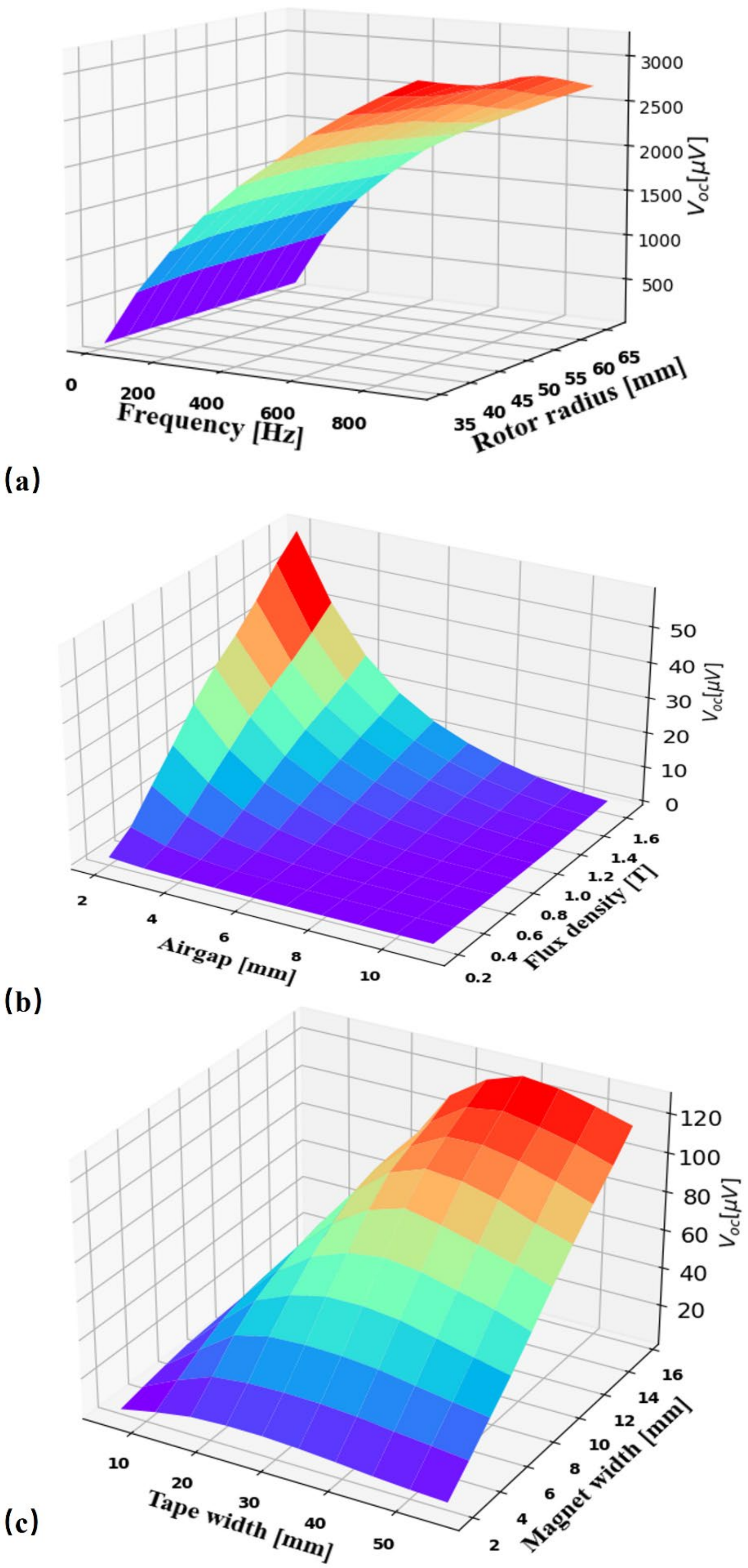

Figure 4.3.6. Surface plots for different parameter groups. (a) 'duration group', (b) 'field group', (c) 'width group'.

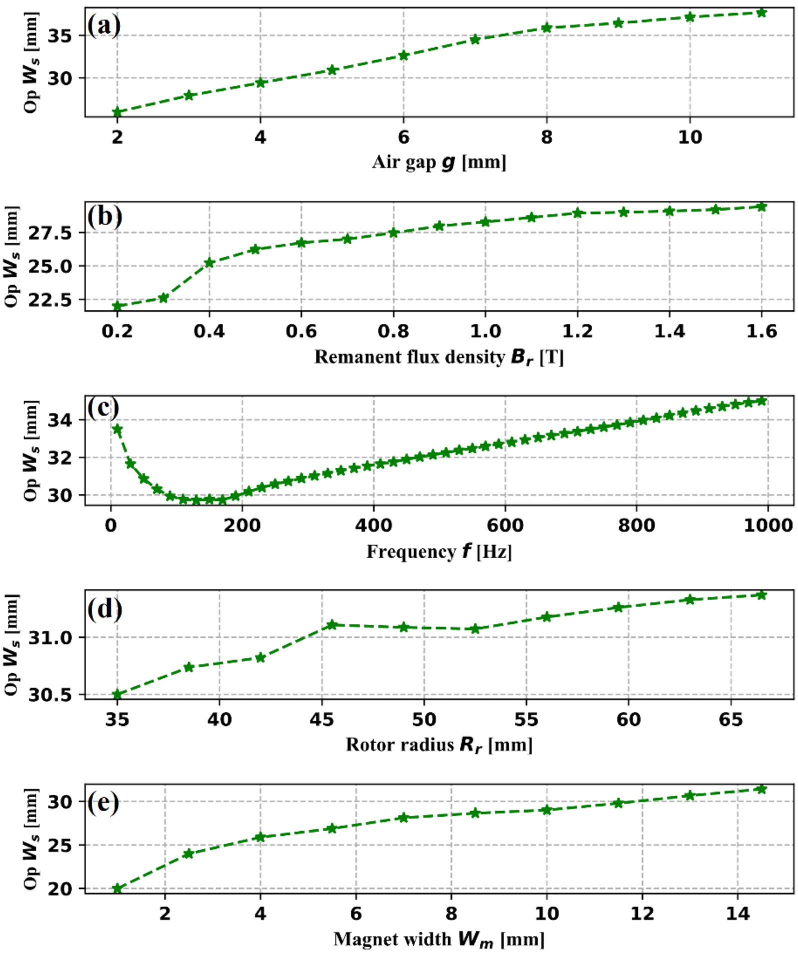

Figure 4.3.7. Optimal HTS tape width for different parameter settings.

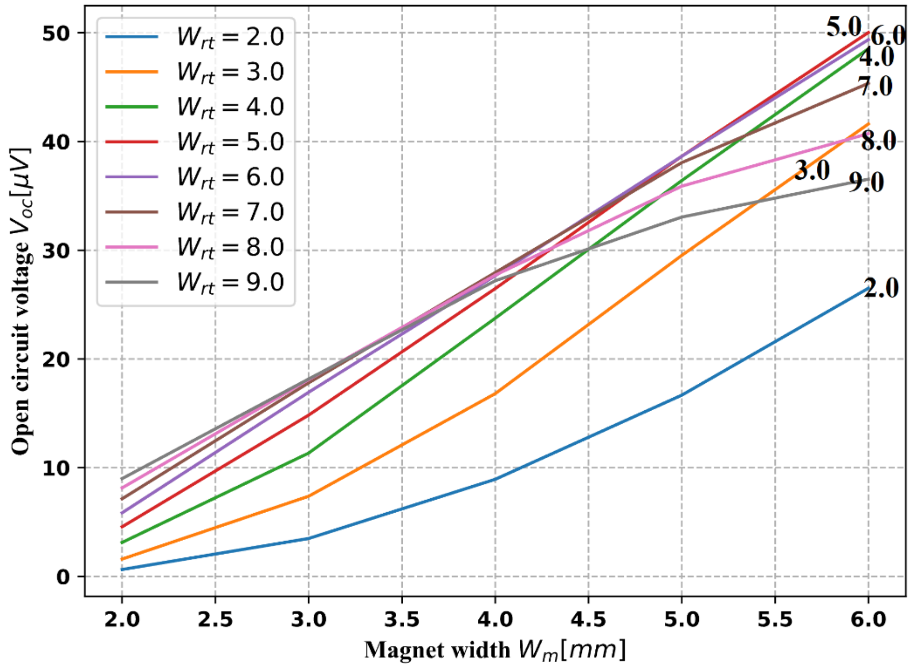

Figure 4.3.8. Voltage characteristics versus PM width with various width ratio.

4.3.4 Case study

The DNN model proposed in this chapter can bring direct benefits to those who want to obtain the output voltage for arbitrary configurations. When it comes to another typical design scenario, where the desired output voltage is specified but the design parameters are to be determined, this model also can be utilised as a powerful design tool to provide recommended parameters, according to the given specifications. As a demonstration of this useful function, several design conditions are assumed to perform a case study. In case 1, there are no manual constraints on any of the design parameters, which means that the model is allowed to provide possible recommendations in the full default range for each of the parameters. In case 2, the air gap is restricted between 3 to 5 mm. In case 3, the tape width must be less than 36 mm. In case 4, the frequency is restricted under 200 Hz while the PM width is restricted between to 2 to 12 mm. In case 5, the remanent flux density can only be 1.2 T. For all cases described above, the desired output voltage is set to be 260 μV. It should be noted that there may exist various parameter combinations, which can result in the same output voltage. Hence, for each of the assumed design conditions, one set of the recommended design parameters is selected to run through the base numerical model (the ***H-A*** formulation-based FEM model) to validate its correctness. The results are presented in table 4.3.2, where the correctness is defined as C_t:

$$C_t = 1 - \frac{|V_{simu} - V_{exp}|}{V_{exp}} \tag{4.3.13}$$

where V_{exp} identifies the desired voltage, V_{simu} identifies the output voltage calculated from the numerical simulations by setting the recommended parameters.

Table 4.3.2. Recommended parameters for each pre-defined case.

	g/mm	W_s/mm	B_r/T	f/Hz	R_r/mm	W_m/mm	C_t
Case 1	9.5	46	1.23	750.25	35	4.75	96.77%
Case 2	5	60	0.85	250.75	52.5	4.75	98.91%
Case 3	4.5	4	1.23	500.5	43.75	8.5	91.22%
Case 4	7	32	0.85	50.75	35	12	97.54%
Case 5	4.5	4	1.2	500.5	43.75	12.25	96.48%

It can be seen from table 4.3.2 that an HTS dynamo with the recommended parameters for each case is capable of generating an output voltage that is close to the expected value, which demonstrates that the proposed model can provide fast guidance under specific design considerations by listing reliable parameter recommendations.

4.4 Conclusions

In this chapter, the feasibility of constructing statistical models as a substitution for FEM models has been proved by utilizing a GPR regression model to reproduce the output characteristic curves for three design parameters of the HTS dynamo, namely the air gap g, HTS tape width W_s, the remanent flux density B_r of the PM, which has an average accuracy as high as 97%. Afterwards, a complete DNN model has been proposed, which is capable of predicting the open circuit voltage of an HTS dynamo, by additionally taking the values of the rotating speed of the magnet R_s (operating frequency f), rotor radius R_r and magnet width W_m as inputs, with an average accuracy of 97.94%. Such a statistical model allows fast tests on the open circuit voltage of an HTS dynamo under different configurations, from where the optimal HTS tape width for various parameter settings has been explored. It was found that it is beneficial to operate the HTS dynamo with a small air gap and high frequency, because higher output voltage can be obtained while less HTS tape is required. Meanwhile, increasing the magnet width can help effectively extend the optimal HTS tape width, which can serve as a solution to avoid the bilateral effect of the HTS tape width. In addition, the DNN model can not only generate predictions for the output voltage, but also can be utilised to produce the values for each design parameter by specifying the output voltage. Based on the DNN model, an executable application has been developed, which is believed to be a powerful design tool to facilitate the design and optimization of HTS dynamo devices (see Appendix).

Chapter 5

Investigation and Statistical Models of the Stationary Wave HTS Flux Pumps

In simple words, an HTS flux pump is the sort of device which can inject current into a closed loop without physical contact. The HTS dynamo investigated in chapter 3 employs a rotating magnet to provide a travelling magnetic waveform to trigger the dynamic resistance in the HTS tape, and hence enable the energisation. Alternatively, the travelling waveform can be also generated by static electromagnets. By subsequentially controlling the current fed into each electromagnet, an effective travelling wave is produced to achieve the flux pumping. Such devices are referred to the linear HTS flux pump, as introduced in chapter 2, and have been experimentally tested in [107]. In this chapter, we have shown that travelling wave is not necessary. Instead, a pure stationary magnetic waveform, i.e., an electromagnet with single-phase excitation, is sufficient for achieving flux pumping as long as the HTS tape is not symmetric with respect to the electromagnet. Based on this discovery, a series of investigations has been conducted to explore the output characteristics of the stationary wave HTS flux pump.

5.1 Modelling framework

The physical structure of a stationary HTS flux pump is presented in figure 5.1.1. In terms of geometry, it is very similar to the structure of the HTS linear flux pump, as shown in figure 2.9.3. An HTS linear flux pump consists of several copper solenoids wound on iron cores, which are injected separately by currents with different phases to form the required travelling magnetic waveform. Since a stationary magnetic field can be easily produced by a simple electromagnet, the structure of a stationary wave HTS flux pump can be further simplified by employing only one copper solenoid.

In essence, the operation principle of the stationary wave HTS flux pump is almost the same as that of the HTS dynamo. Hence, theoretically, the modelling techniques introduced in chapter 3 can be conveniently applied to build a numerical model for the stationary HTS flux pump. The biggest difference is that the PM, in the model of an HTS dynamo, should be replaced by an electromagnet. However, it was found in our modelling experiences that either with the ***T-A*** or ***H-A*** formulation, convergence problems can be caused by integrating the modelling of the electromagnet and HTS tape together, which makes it challenging to construct a numerical model for a stationary wave flux pump in a conventional manner. Therefore, an alternative approach has been taken to represent the electromagnet.

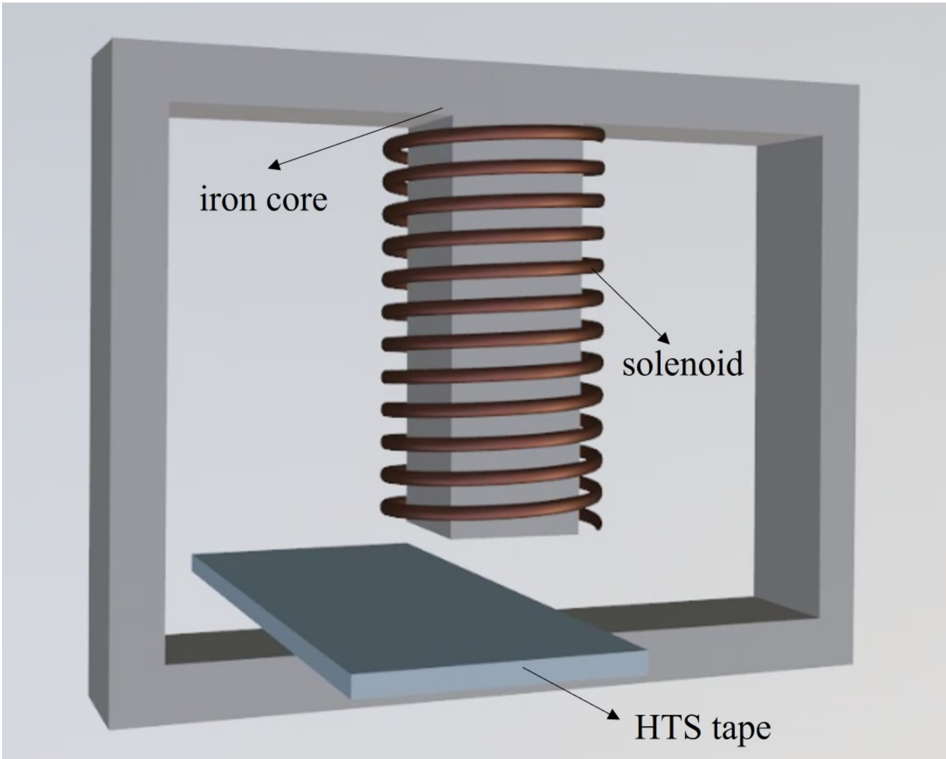

Figure 5.1.1. Illustration of the structure of a stationary wave HTS flux pump.

Consider a transporting current I, then the magnetic flux density at point P, as shown in figure 5.1.2, generated by a current unit Idl can be described by Biot-Savart law [228]:

$$d\vec{B} = \frac{\mu_0}{4\pi}\frac{Idl \times \vec{r}}{r^3} = \frac{\mu_0}{4\pi}\frac{Idl \sin\theta}{r^3} \tag{5.1.1}$$

where r is the distance between point P and the current unit and θ is the angle between the direction of the current unit and the direction point from point P to the current unit. From where it can be seen, in a static system, the generated magnetic field can be directly controlled by modulating the current fed into the solenoids. Thus, the magnetic field for an electromagnet can be approximately depicted as a function of the current fed into the solenoids:

$$B = I \cdot constantA \tag{5.1.2}$$

where $constantA$ is a coefficient that is irrelevant to the current I. When it comes to the PM, whose magnetic field can be depicted as a function of its remanent flux density:

$$B = B_r \cdot constantB \tag{5.1.3}$$

where $constantB$ is a coefficient that is irrelevant to the remanent flux density B_r.

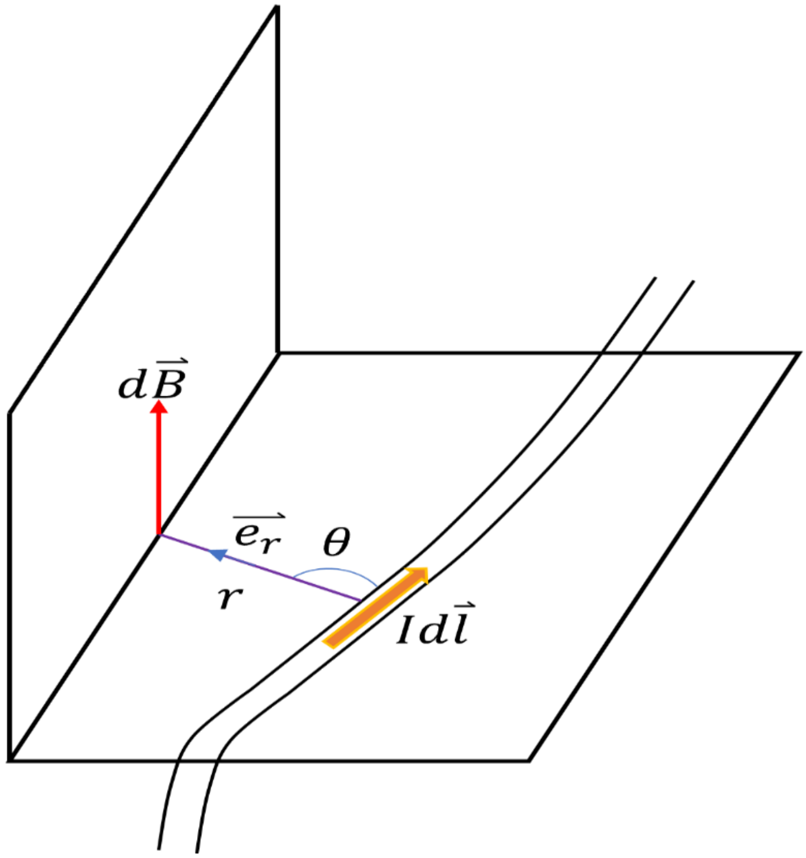

Figure 5.1.2. Illustration of Biot-Savart law.

Comparing equation (5.1.2) and equation (5.1.3), it can be found that the magnetic field of a PM and an electromagnet can be equivalent. For instance, let us consider an electromagnet energised by a sinusoidal current $I(t) = \sin t$. Then the corresponding magnetic of the electromagnet can be roughly equivalent by a PM with a sinusoidal remanent flux density $B_r(t) = \sin t \, constantC$, by maintaining $constantC = constantA/constantB$. It should be pointed out that it is common to energise the electromagnet with variable currents, i.e., one can apply proper electronic devices to inject arbitrary currents to the solenoids, but the remanent flux density is one of the inherent properties of the PM, which cannot be altered arbitrarily in practice. However, in terms of modelling, it is feasible to represent the remanent flux density of a PM as a predefined function rather than a constant. In other words, the discussion presented here simply introduces a comprise for the modelling, but not corresponds to the actual scenario in reality. Since the electromagnet can now be modelled as a PM, it is reasonable to follow one of the modelling procedures introduced in chapter 3. As discussed in that chapter, the ***H-A*** formulation is more suitable for manifesting the current interactions in HTS tapes under high frequencies, and more efficient compared with ***T-A*** formulation. In this chapter, the ***H-A*** formulation has been utilised to build the numerical model for the stationary HTS flux pump. The full coated structure is considered for the HTS tape, which comprises two copper layers, a silver stabilizer layer and a substrate layer, as introduced in subsection 3.3.2. Hence, the output voltage is defined by equation (3.3.14) with the constraint of equation (3.3.15).

In order to verify the assumption that the magnetic field of an electromagnet can be equivalently achieved by modelling a PM, two separate models have been constructed. One of them models the conventional structure of an electromagnet, as shown in figure 5.1.3(a), where 40 turns copper coils are wound on the magnetic core and injected with a current with the amplitude of 5 A and frequency of 5 Hz, $I(t) = 5\sin(10\pi t)$, while the other one models a static PM with a time-varying remanent flux density $B_r(t) = 0.24\sin(10\pi t)$, as shown in figure 5.1.3 (b). Probes have been put on several points on the HTS tape to measure the magnetic flux density in each of the two models. Note that the material of the iron core utilises the silicon steel NGO 50PN1300 available in the COMSOL built-in packages, and the magnetization is modelled based on its B-H curve, so the effect of magnetic hysteresis loop is ignored. The magnetic flux density norm at each point of the probes for the two models are presented in figure 5.1.4(a) and (b) respectively It can be seen that the magnetic field in the PM model and electromagnet model both demonstrate the shape of standard sinusoidal waveforms, and the flux density decreases from the probes on left to right as expected. The magnitudes of each plot also show excellent agreement with each other, implying that the electromagnet can be effectively modelled as a PM.

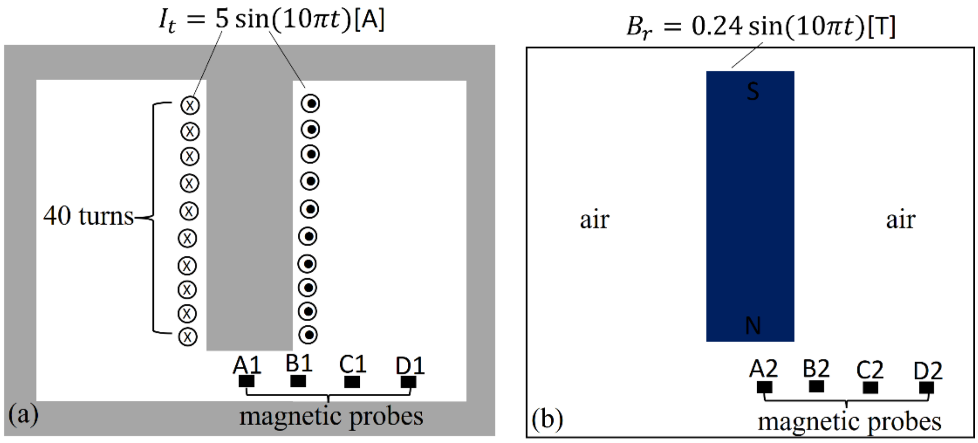

Figure 5.1.3. Illustration of the (a) model of electromagnet with alternating excitation current, and (b) model of PM with alternating remanent flux density.

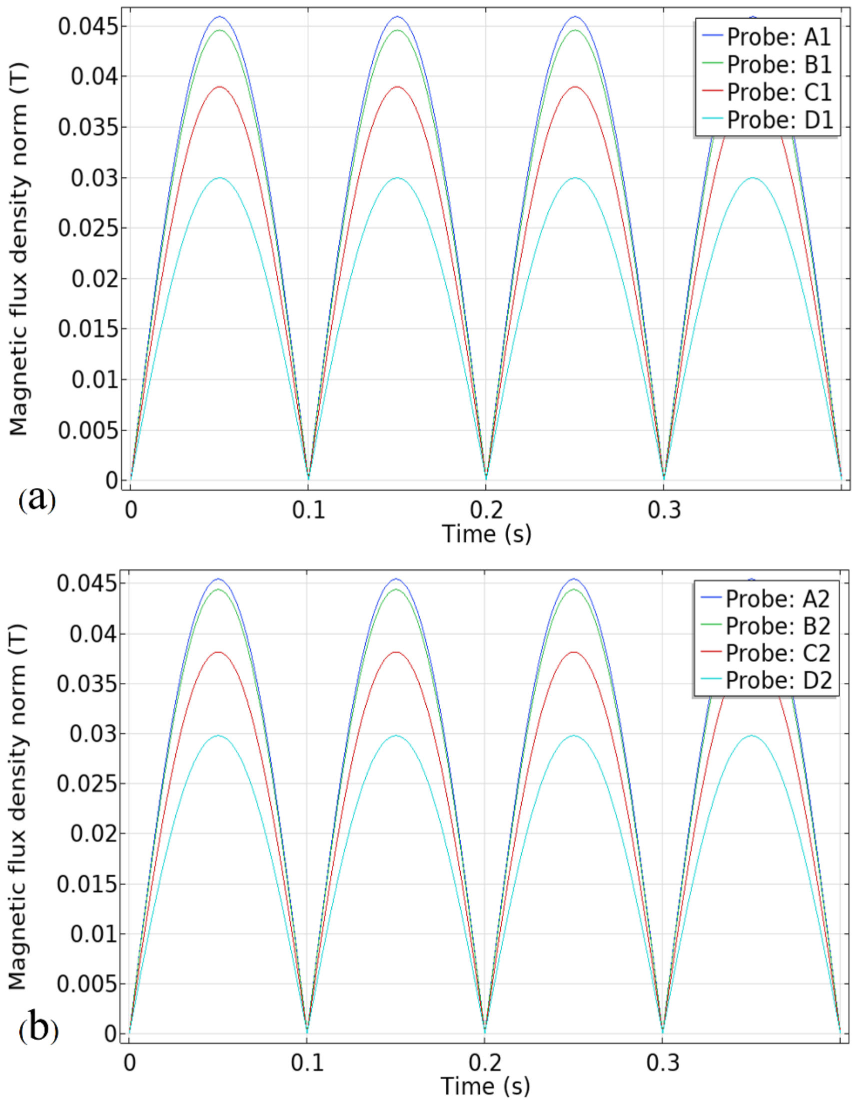

Figure 5.1.4. The magnetic flux density for (a) probes of A1, B1, C1 and D1 in the electromagnet model, (b) probes of A2, B2, C2 and D2 in the PM model.

5.2 Output characteristics

In order to investigate the performance of such a stationary waveform HTS flux pump, a numerical model has been developed based on the modelling framework introduced above. Considering the main usage of HTS flux pump is to provide excitation to different applications in practice, the open circuit voltage across the HTS tape, which acts as the excitation source, is chosen as the criteria to evaluate its performance. Through various FEM simulations, the characteristics of open circuit voltage versus a set of controllable parameters, including the misalignment distance M_d, air gap g, peak flux density B_a and waveform profile of applied magnetic field, operating frequency f, HTS tape width W_s and copper solenoid width W_{so} have been studied. The geometric parameters are illustrated in figure 5.2.1.

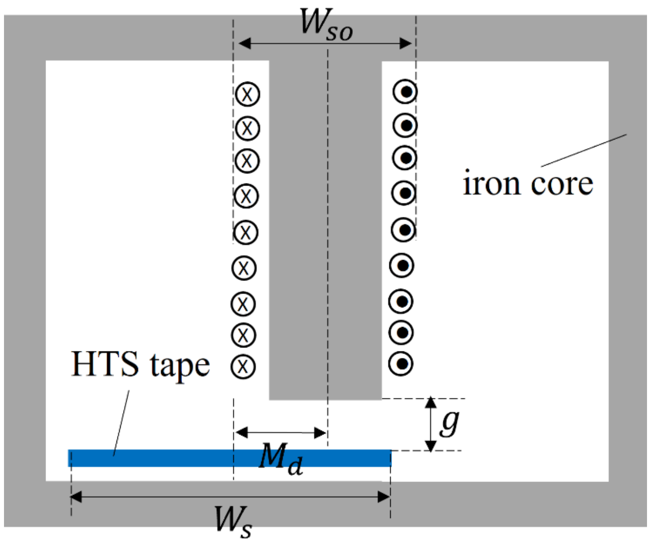

Figure 5.2.1. Illustration of the geometric parameters.

5.2.1 Misalignment distance

As shown in figure 5.2.1, the misalignment distance M_d is defined as the distance between the central axis of the electromagnet and HTS tape, such that $M_d = 0$ means that the electromagnet is symmetry with respect to the HTS tape. The open circuit voltages at different misalignment distances with various waveform profiles of the applied magnetic field are plotted in figure 5.2.2. It can be seen that there is no voltage output when the electromagnet is symmetry with respect to the HTS tape ($M_d = 0$). Increasing the misalignment distance, e.g., moving the HTS tape horizontally to the left or right, can raise the open circuit voltage to a maximum, after which the voltage gradually decreases back to zero. The effect of different waveform profiles of the applied magnetic field has also been investigated here. According to figure 5.2.2, the voltage curves are almost the same for triangular waveform and trapezoidal waveform with a duty ratio t_c of 0.2, e.g., the constant period accounts for 20% of one complete cycle, so that the falling period and rising period, which have been set to be equal, account for 40% each. Hence, a triangular waveform is equivalent to a trapezoidal waveform with a duty ratio of zero. It has been shown that increasing the duty ratio of a trapezoidal waveform decreases the obtained open circuit voltage. Among the tested waveforms, it was found that sinusoidal waveform can result in the maximum output voltage at any misalignment distance. Therefore, a sinusoidal waveform with a misalignment distance of 2.5 mm is utilised in the following subsections. It should be noted that while investigating the impact of misalignment distance and waveform profile, all other parameters are fixed. More precisely, the frequency, air gap, peak flux density, HTS tape width and copper solenoid width are set to be 500 Hz, 3.75 mm, 1.85 T, 12 mm and 6 mm, respectively. Unless explicitly specified, the same setting is applied to all simulations in the rest of this chapter.

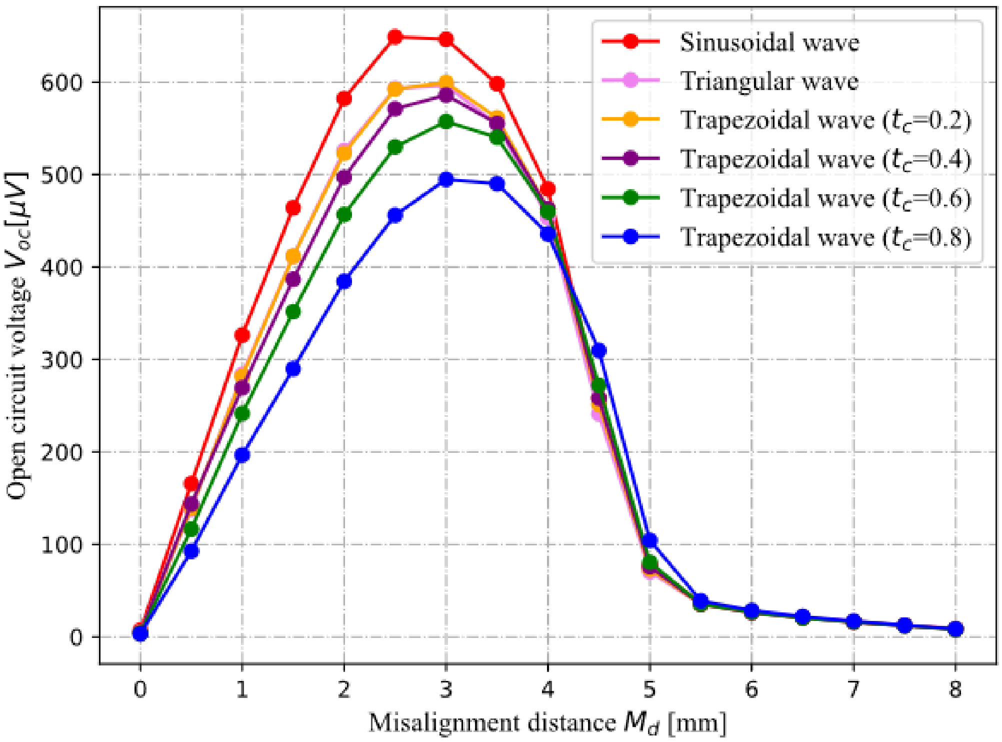

Figure 5.2.2. Open circuit voltage at different misalignment distances for various magnetic field waveforms.

5.2.2 Air gap

The open circuit voltage obtained at different air gaps is plotted in figure 5.2.3, from where it can be seen that output voltage decreases from 900 μV at the minimum air gap of 2 mm to almost 0 μV at 10 mm, with the shape of a convex function, e.g., a decreasing absolute slope. It was also found that if the misalignment distance is zero, the output voltage remains zero in spite of the variation of air gap.

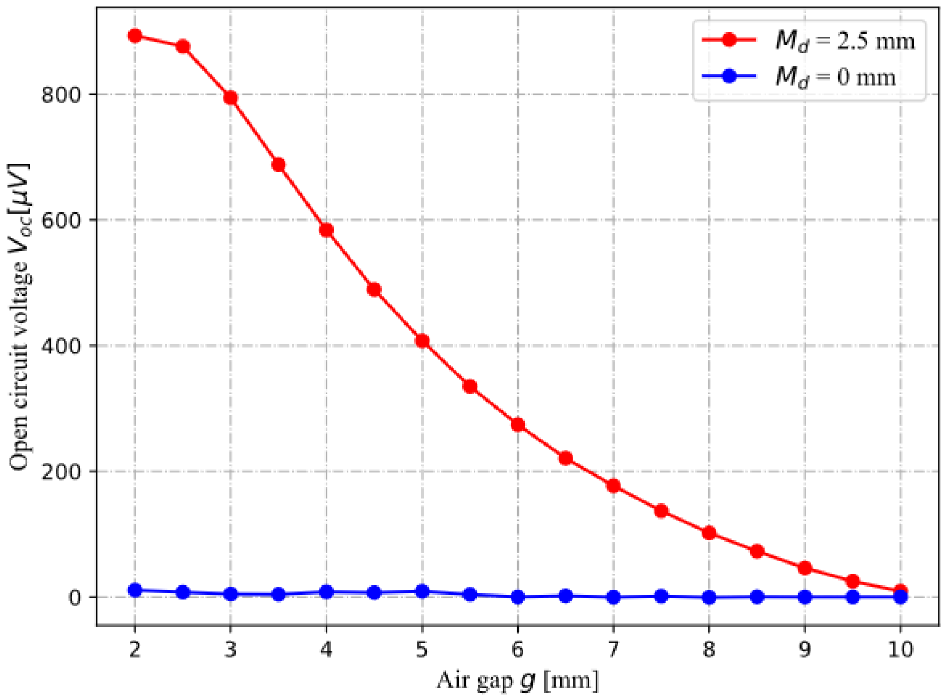

Figure 5.2.3. Open circuit voltage versus air gap at 2.5 mm (red curve) and 0 mm (blue curve) misalignment distance.

5.2.3 Peak flux density

Since the applied magnetic field is a sinusoidal waveform, the peak value of the magnetic flux density was chosen as the criteria to investigate the impact of the intensity of applied magnetic fields. As shown in figure 5.2.4, the output voltage is positively correlated to the peak flux density of the applied magnetic field, namely the voltage increases with the peak flux density. The curve of voltage versus peak flux density demonstrates strong non-linearity with a decreasing slope. Increasing the peak flux density from 1 T to roughly about 3 T can dramatically raise the output voltage, then the voltage seems to saturate at the flux density of 4 T, after which the output voltage is irrelevant to the peak flux density and keeps, more or less, constant. For a stationary wave HTS flux pump employing electromagnet, which consists of copper solenoids and iron cores, as the source of the magnetic field, such a voltage saturation effect can be expected. It is because iron cores are ferromagnetic materials, which will transfer into the magnetic saturation state and produce approximately a constant magnetic flux density, if the excitation of copper solenoids, controlled by the amplitude of injected currents and number of turns, goes beyond a certain point. Hence, the magnetic saturation of iron cores can eventually turn to the saturation of output voltage. However, that is not the case for the results presented here. It should be pointed out that, as discussed in section 5.1, instead of utilizing copper solenoids with iron cores, the electromagnet is modelled as a PM with alternating remanent flux density, so the magnetic saturation of iron cores is essentially ignored and the abscissa in figure 5.2.4 directly represents the magnetic field applied to the HTS tape. Therefore, it can be deduced from figure 5.2.4 that the output voltage cannot be promoted unlimitedly by increasing the applied magnetic field. This is in contrast to that of an HTS dynamo, since it has been revealed in figure 3.2.1(d) that the output voltage can consistently increase with the magnetic field (remanent flux density), and it seems that it will not experience the voltage saturation observed here. Again, it was also found that if the misalignment distance is zero, the output voltage remains zero in spite of the variation of peak flux density of applied fields.

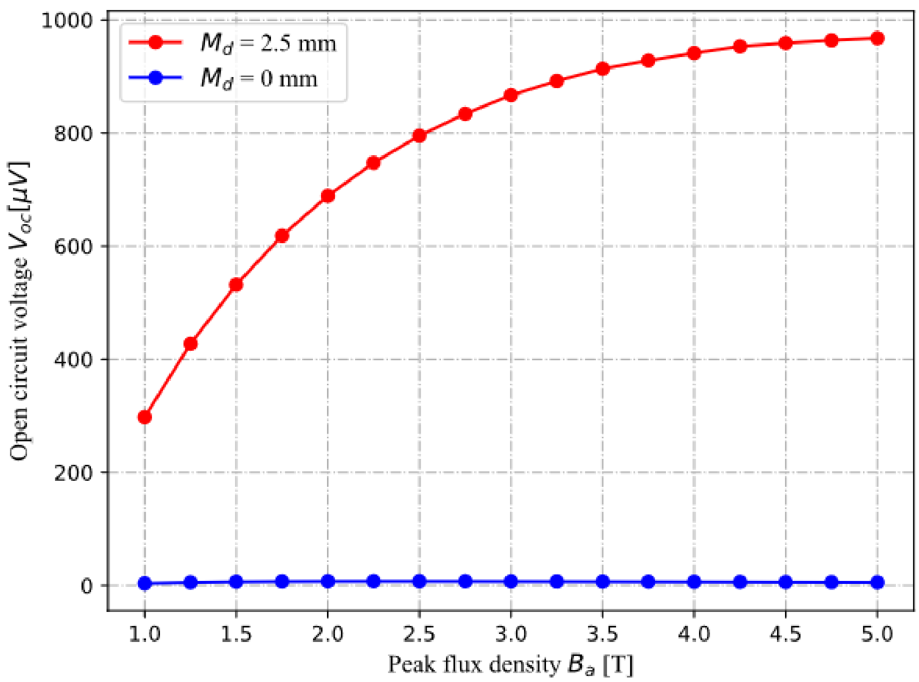

Figure 5.2.4. Open circuit voltage versus peak flux density at 2.5 mm (red curve) and 0 mm (blue curve) misalignment distance.

5.2.4 Frequency

The frequency response, in the range of 0 to 1000 Hz, of the stationary wave HTS flux pump is plotted in figure 5.2.5. It can be seen the output voltage consistently increases with the frequency in the investigated range. Besides, the relationship between the voltage and frequency behaves almost linearly, which is in contrast to that of an HTS dynamo. As previously illustrated in figure 3.2.1(a), the output voltage of an HTS dynamo linearly increases with the operating frequency up to a certain point (roughly at 100 Hz), after which nonlinearity appears.

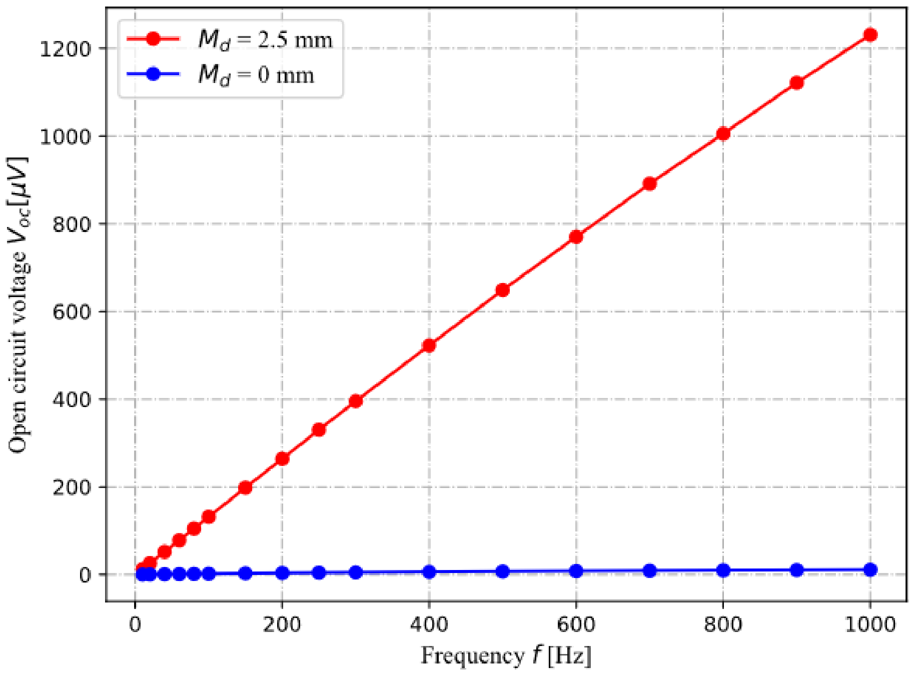

Figure 5.2.5. Open circuit voltage versus frequency at 2.5 mm (red curve) and 0 mm (blue curve) misalignment distance.

This distinct frequency response can be attributed to the nature of the applied magnetic field in each scenario. For the HTS dynamo, the HTS tape is exposed to a strong magnetic field when it is close to the PM, e.g., right beneath the PM. For the majority of a rotating cycle, the HTS tape is far away from the PM, and hence experiences a very weak magnetic field. Consequently, the magnetic field applied to the HTS tape in an HTS dynamo, in the time domain, resembles a sharp pulse, which corresponds to an effectively higher frequency than the actual operating frequency. For the stationary wave HTS flux pump, the frequency of the applied magnetic field is exactly the same as the frequency. Since the reason for the nonlinear frequency response is the current interaction between different layers of the HTS tape, it is possible that the nonlinearity can also be observed in the stationary HTS flux pump, at very high frequencies. However, considering HTS flux pump will possibly not be operated at extraordinarily high frequencies, the results in figure 5.2.5 may indicate that the stationary wave HTS flux pump is more positively sensitive to the operating frequency by suppressing the nonlinear response, at least in the kilo Hz level. Meanwhile, it was also found that the output voltage remains zero in spite of the variation of operating frequency if the misalignment distance is zero.

5.2.5 Tape width

Based on the experiences from investigations about HTS dynamo, it is expected that the output voltage is dependent on the width of HTS tape. As shown in figure 5.2.6, the output voltage firstly increases, and then decreases with the HTS tape width, which implies that the HTS tape width demonstrates a bilateral effect on the open circuit voltage, similar to what has been found for an HTS dynamo in chapter 3. However, for the stationary wave HTS flux pump, the output voltage tends to reach the maximum at a relatively much smaller width, about 16 mm. Increasing the HTS tape width beyond this point dramatically suppresses the voltage output, meaning that relatively narrow HTS tape is more suitable for the stationary HTS flux pump. Besides, if the misalignment distance is zero, the output voltage remains zero, no matter how wide the HTS tape is.

5.2.6 Solenoid width

Lastly, the impact of solenoid width, i.e., the diameter of the copper coil plus the width of the inserted iron core, on the output voltage is investigated. As illustrated in figure 5.2.7, the voltage-width curve shows a typical parabolic shape, whose peak appears at the solenoid width being approximately 7 mm. Thus, making the inserted iron core wider or narrower will result in a smaller output voltage. This is different from that of an HTS dynamo, as previously illustrated in figure 3.2.1, increasing the PM width will raise the output voltage to an approximate saturation value.

Similar to that has been revealed for other parameters, as presented above, regardless of the solenoid width, the output voltage remains zero, if the misalignment distance is zero.

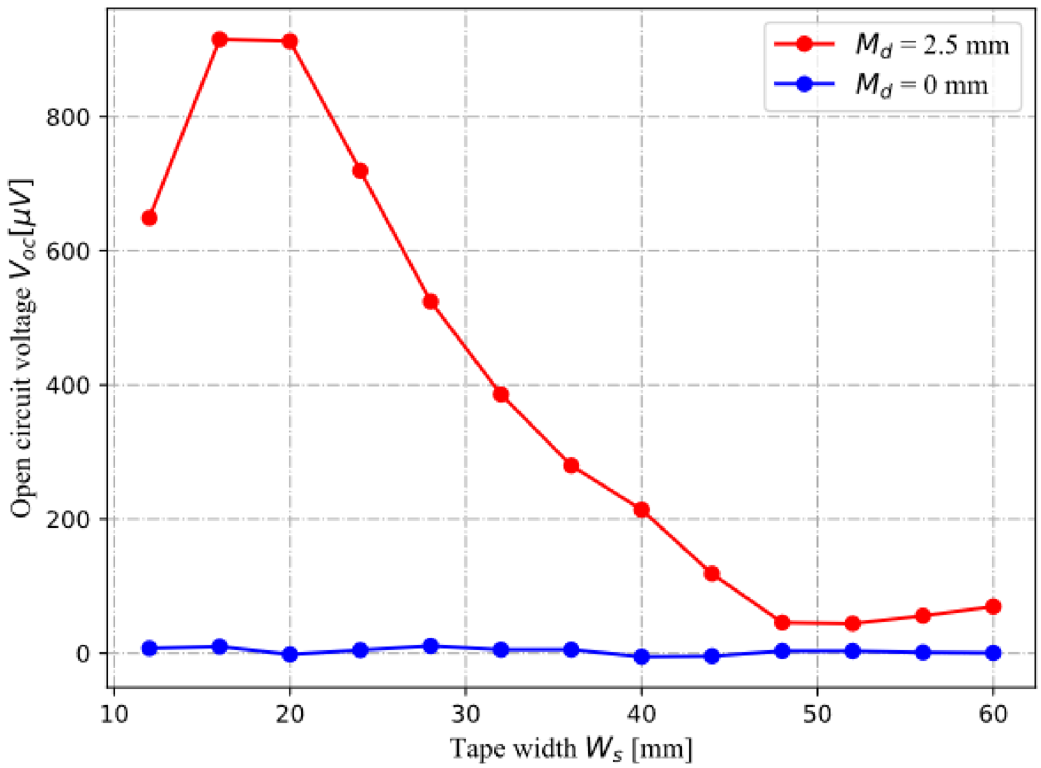

Figure 5.2.6. Open circuit voltage versus HTS tape width at 2.5 mm (red curve) and 0 mm (blue curve) misalignment distance.

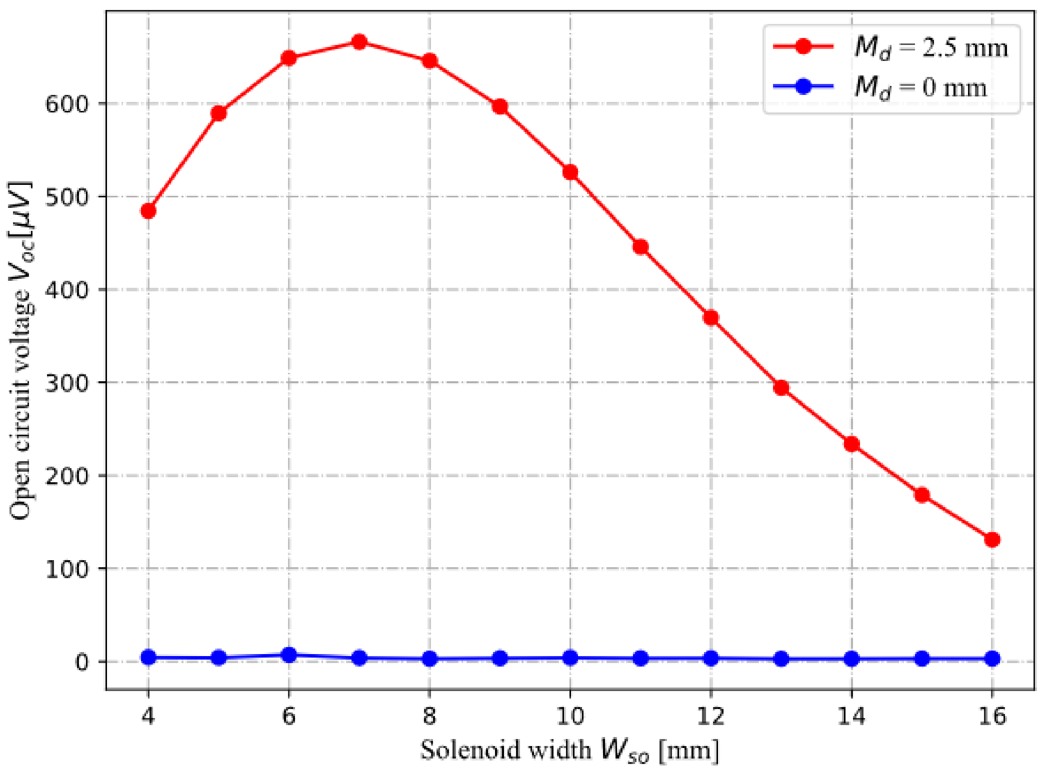

Figure 5.2.7. Open circuit voltage versus solenoid width at 2.5 mm (red curve) and 0 mm (blue curve) misalignment distance.

5.3 Discussions

According to the results presented in the last section, the most noticeable feature of the output characteristics of the stationary wave HTS flux pump is that no net DC output voltage can be generated if the misalignment distance is zero regardless of any other parameters, which means that misalignment is the prerequisite for the stationary wave HTS flux pump to produce an effective DC output voltage. In order to explore this phenomenon in more detail, the equivalent voltage across the HTS tape, as defined in equation (3.3.14), for the flux pump operated at a misalignment distance of 2.5 mm and 0 mm, is plotted in figure 5.3.1. As it can be seen, in the case of 0 mm misalignment distance, the equivalent voltage is roughly zero at every moment in one complete cycle, whose integration over time must also be zero, corresponding to a net zero DC output voltage. In contrast, in the case of 2.5 mm misalignment distance, the equivalent voltage profile resembles a distorted sinusoidal waveform, but there is a huge difference between the absolute value of positive and negative peak, which can result in a non-zero time integration over one complete cycle, and hence produce an effective net DC output voltage. The distinct profile can be understood from the operating mechanism of the HTS flux pump.

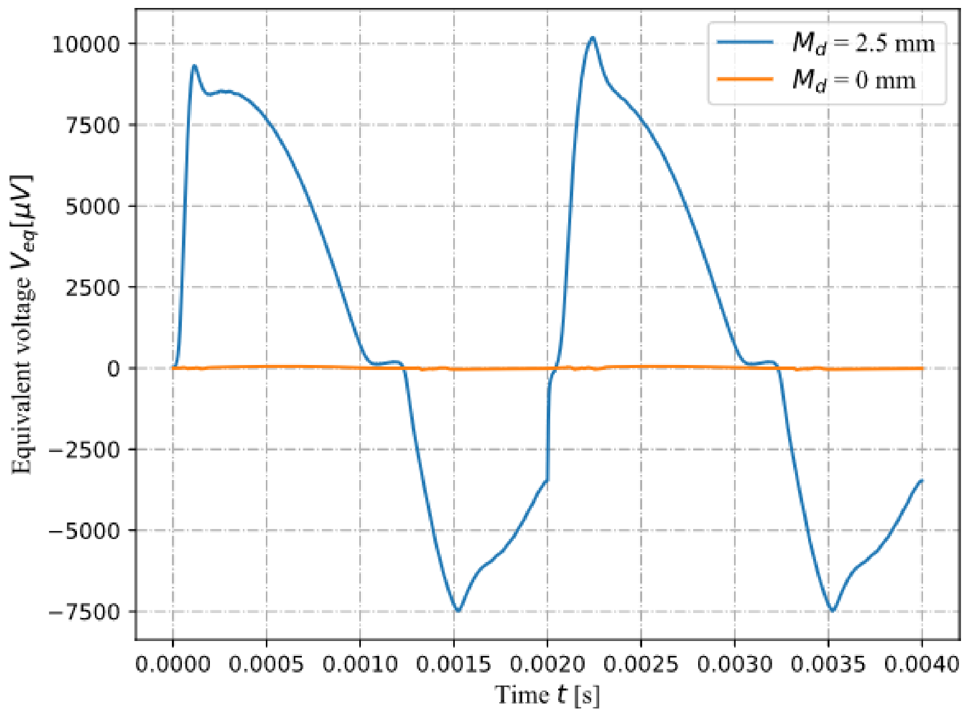

Figure 5.3.1. The time dependent equivalent voltage across the HTS tape at 2.5 mm (blue curve) and 0 mm (orange curve) misalignment distance.

As discussed in previous chapters, the voltage of such an HTS flux pump, either the HTS dynamo (travelling wave) or the stationary wave HTS flux pump, originates from the circulating currents flowing within the HTS tape. Assume the circulating currents are evenly distributed along the HTS tape width, e.g., the left half tape is occupied by the forward current and the right half tape is occupied by the backward current. The magnetic field experienced by each half tape can be approximately evaluated by the distance between the middle point of each half tape and the solenoid. If the misalignment distance is zero, in which case the HTS tape is symmetric to the solenoid, as well as the applied magnetic field. Then, it is obvious that, at any instant, each half tape experiences exactly the same magnetic field, since $r_1 = r_2$, as shown in figure 5.3.2(a). According to the $Jc(\boldsymbol{B})$ dependence, each half tape should exhibit the same resistivity given they are exposed to the same magnetic field. Hence, the electric field established in the forward current region should be the same as that in the backward region. The two electric fields can perfectly cancel each other out, leading to a net zero integration over the width of the HTS tape. If the misalignment is 2.5 mm (or any other values), the right half tape will experience a different magnetic field with respect to the left half tape, since $r_1 \neq r_2$ as shown in figure 5.3.2(b).

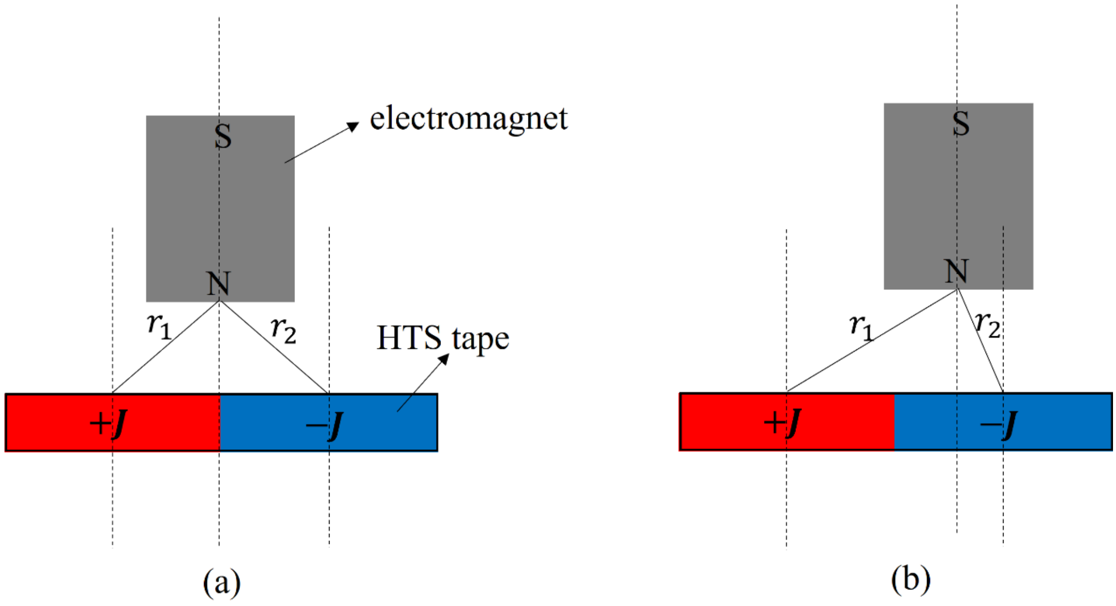

Figure 5.3.2. 2D illustration of the framework of a stationary wave HTS flux pump (a) zero M_d ($r_1 = r_2$), (b) 2.5 mm M_d ($r_1 > r_2$).

Due to the $Jc(\boldsymbol{B})$ dependence, the right half tape will demonstrate a resistivity that is different from the left half tape. Therefore, the electric field established in the forward current region and backward current region are not the same and cannot fully cancel each other. As a result, a net DC voltage across the HTS tape can be obtained.

Though it is now clear that there must be a misalignment distance for the stationary HTS flux pump to generate an effective DC output voltage, it also should be noted that the misalignment distance cannot be irrationally big. For example, in the extreme case where M_d goes infinite, i.e., the HTS tape is far away from the electromagnet, it can be expected that no output voltage will be generated, since the magnetic field allied to the HTS tape can be considered ignorable. Thus, a proper misalignment distance is essential for the stationary HTS flux pump to produce an optimal voltage output. Under the evenly distributed current assumption, the final derived DC voltage is determined by the difference between the resistivity, equivalently the magnetic field owing to the $Jc(\boldsymbol{B})$ dependence, on the left half (backward current region) and right half (forward current region) HTS tape. It is clear that the portion of HTS tape that is right beneath the electromagnet will experience the possibly highest magnetic field, so the difference between the resistivity on the backward current region and forward current region can be maximized, if the electromagnet completely locates in one of the two regions. To increase the misalignment distance from zero, one can either horizontally move the HTS tape to the right or left direction. Considering the HTS tape is moved to the right direction, as the reference. Under such condition, it is reasonable to deduce that the maximum output voltage can be obtained, when the HTS tape is moved to a position, where the electromagnet is vertically embraced by the right half tape, as shown in figure 5.3.3.

To fulfil this condition, the distance that the HTS tape needs to be moved is equal to half of the solenoid width. As it can be seen from figure 5.2.2, the maximum output voltage is obtained roughly at a misalignment distance of 2.5 mm, which is very close to half of the solenoid width (6 mm). In order to further verify this hypothesis, the output voltage at different misalignment distances for various solenoid widths is calculated, as shown in figure 5.3.4. The maximum output voltage for a 6 mm, 10 mm, 14 mm solenoid width is obtained at a misalignment distance of 2.5 mm, 3 mm, and 4 mm, respectively. In each case, the misalignment distance required for obtaining the maximum output voltage is not exactly equal to half of the solenoid width. This can be resulted from the fact that the circulating currents are no longer evenly distributed along the width of the HTS tape, and the more the tape is moved towards each side, the more the circulating currents are different from the even distribution. However, it can be told from figure 5.3.4 that the misalignment distance required for obtaining the maximum output voltage is positively related to the solenoid width, and smaller than half of the solenoid width. Thus, half of the solenoid width can be considered as the limit to maximize the output voltage from a stationary wave HTS flux pump.

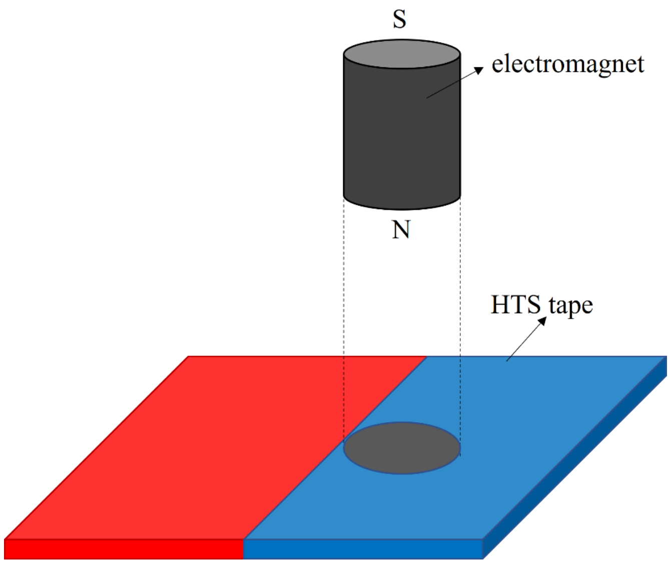

Figure 5.3.3. An illustration of the case where the electromagnet is vertically embraced by half of the HTS tape.

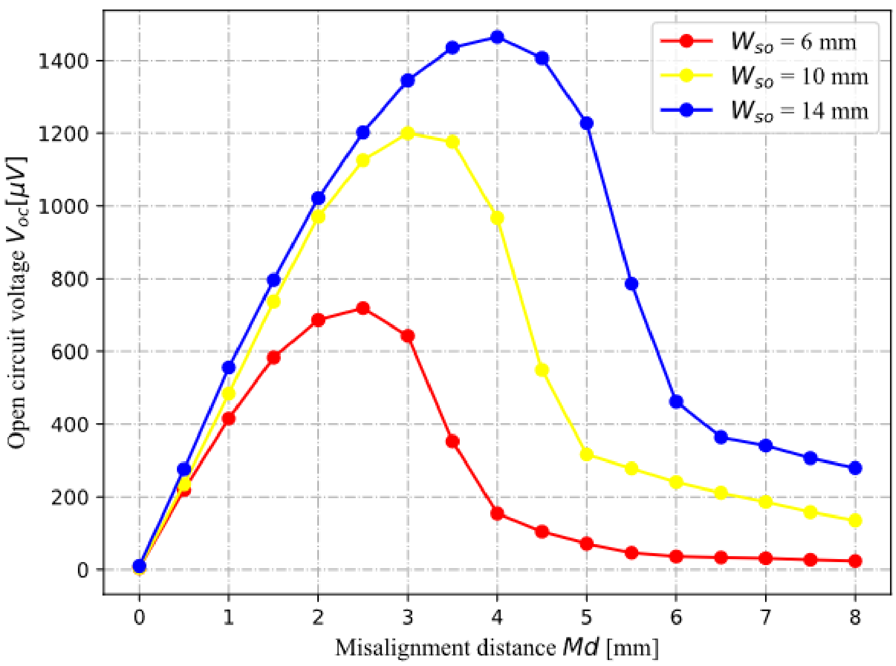

Figure 5.3.4. Open circuit voltage versus misalignment distance at different solenoid width.

5.4 Origin of the output voltage

The misalignment distance M_d, as defined in figure 5.2.1, is the distance between the central axis of the electromagnet and HTS tape. This is the decisive factor for whether or not the stationary wave HTS flux pump can generate an effective DC output voltage, because if $M_d = 0$, the open circuit voltage remains zero despite variations of other parameters. In section 5.3, this phenomenon has been discussed regarding the $J_c(B)$ dependence. Since the resistivity of HTS tape is highly sensitive to the magnetic field, the resistivity along the tape is directly influenced by the magnetic field applied to the tape surface, which is controlled by the relative position of the electromagnet and HTS tape. However, it should be noted that this is only one of the possible reasons, which assumes the circulating currents are evenly distributed and does not consider the non-linear resistivity of HTS tapes.

In fact, non-linear resistivity is one of the intrinsic properties of HTS materials, and it is described by the ***E-J*** power law in the numerical models. The essential impact of the ***E-J*** power can be interpreted as the resistivity of HTS tapes being closely dependent on the flowing currents. Thus, if different parts of the HTS tape are occupied by distinguished currents, then distinct resistivities will be demonstrated on different regions of the HTS tape. It can be found in the existing literature that the non-linear resistivity has been attributed to the cause of open circuit voltage for travelling wave HTS flux pumps. To explicitly explore the effect of such a non-linear resistivity, the circulating current distribution within the tape must be considered.

The current distributions in the HTS tape, for a stationary wave HTS flux pump with a misalignment distance of 0 mm (see subsection 5.2.1 for the settings for other parameters), at 1/8, 1/4, 5/8 and 3/4 of one cycle of the applied magnetic field are shown in figure 5.4.1. As can be seen, the circulating currents are centralized in the HTS layer (please refer to figure 3.3.2 for the demonstration of different layers of the HTS tape) and evenly distributed along the width of the tape, and they are consistently symmetric with respect to the centre of the tape (as denoted by the dashed black line in the figure). Under the condition of a zero-misalignment distance, it is obvious that the applied magnetic field must also be symmetric with respect to the centre of the tape. As a result, each half of the HTS will possess equal resistivity. Hence, the electric field established on the forward current region and backward current region will cancel out, which means that no voltage can be generated across the HTS tape. Figure 5.4.2 shows the current distributions for a stationary wave HTS flux pump with a misalignment distance of 0 mm, at 1/8, 1/4, 5/8 and 3/4 of one cycle of the applied magnetic field. As indicated by figure 5.4.2 (b) to (d), the circulating currents are no longer symmetric with respect to the centre of the tape.

Let the average forward and backward current density be J_1 and J_2, respectively. Denote the width occupied by each region (forward or backward current) as w_1 and w_2, respectively. The following equation must hold in open circuit conditions:

$$J_1 w_1 + J_2 w_2 = 0 \tag{5.4.1}$$

According to ***E-J*** power law, the electric field across the HTS tape resulting from the circulating currents is determined by (ignoring $J_c(B)$ dependence):

$$w_1 \left(\frac{|J_1|}{J_c}\right)^n - w_2 \left(\frac{|J_2|}{J_c}\right)^n \tag{5.4.2}$$

If the misalignment distance is 0 mm, the circulating currents are evenly distributed along the tape width, such that $w_1 = w_2$, which guarantees $J_1 = -J_2$. In this case, equation (5.4.2) must equal to zero. Nevertheless, if the misalignment distance is not zero, the situation becomes quite different.

For example, let $w_1 = 2w_2$, then $J_2 = -2J_1$. Equation (5.4.2) can only be equal to zero if $n = 1$, i.e., for normal conductors. For HTS conductors, n usually takes a value around 20. In other words, following equation (5.4.2), the circulating currents shown in figure 5.4.2 can cause a biased electric field across the HTS tape, and hence generate an effective DC output voltage. It should be noted that equation (5.4.2), originating from ***E-J*** power law, does not rely on the field dependence of critical current density, which implies that the non-linear resistivity alone can be sufficient to achieve flux pumping by inducing a net DC voltage across the HTS tape.

In order to verify the correctness of the hypothesis, FEM simulations have been conducted to calculate the open circuit voltage of a stationary HTS flux pump, by assuming a constant critical current density. As shown in figure 5.4.3, the equivalent voltage across the HTS tape under constant J_c condition is similar to that with $J_c(B)$ dependence considered. Meanwhile, the magnitude of the equivalent voltage with constant J_c is suppressed, which corresponds to a 63 μV time-averaged output voltage.

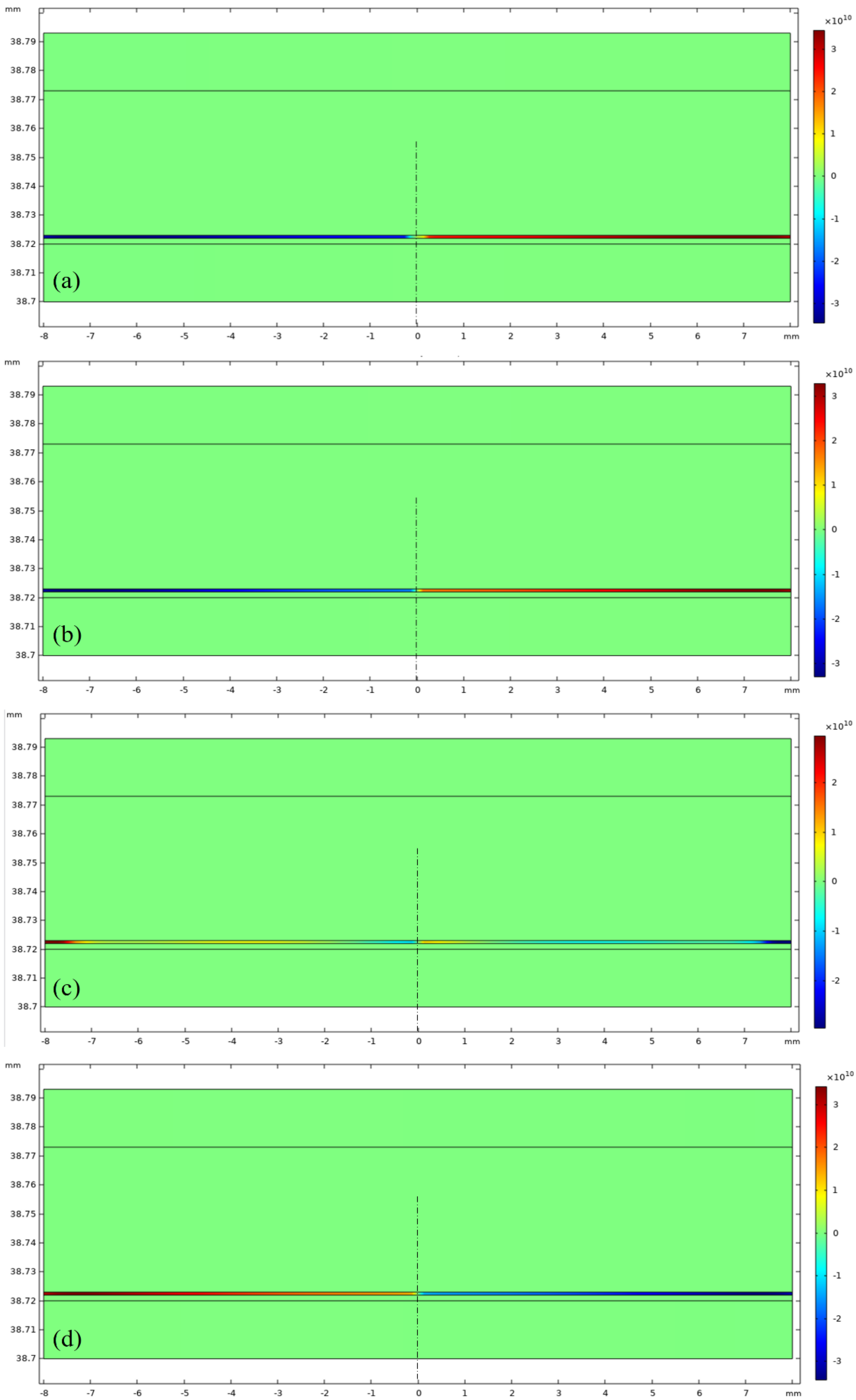

Figure 5.4.1. The current distribution in the HTS tape for a stationary HTS flux pump with $M_d = 0$ mm, at (a) 1/8, (b) 1/4, (c) 5/8, (d) 3/4 of one cycle of the applied magnetic field.

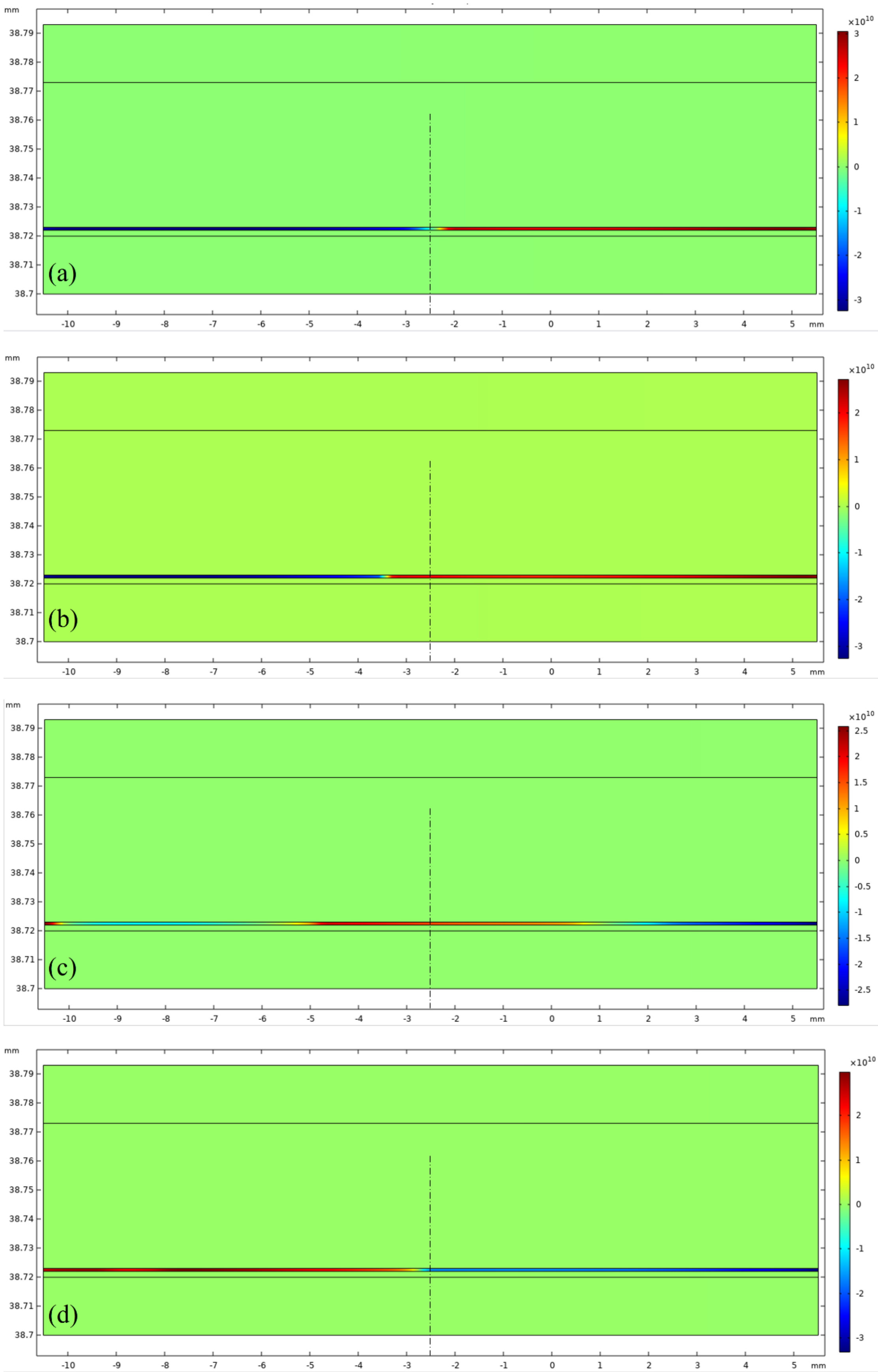

Figure 5.4.2. The current distribution in the HTS tape for a stationary HTS flux pump with $M_d = 2.5$ mm, at (a) 1/8, (b) 1/4, (c) 5/8, (d) 3/4 of one cycle of the applied magnetic field.

Though it is much smaller compared with the 915 μV output voltage with $J_c(B)$ dependence considered, the results clearly demonstrate that non-linear resistivity is enough to produce an effective DC output voltage, which can be dramatically enhanced by the dependence of critical current density on the magnetic field.

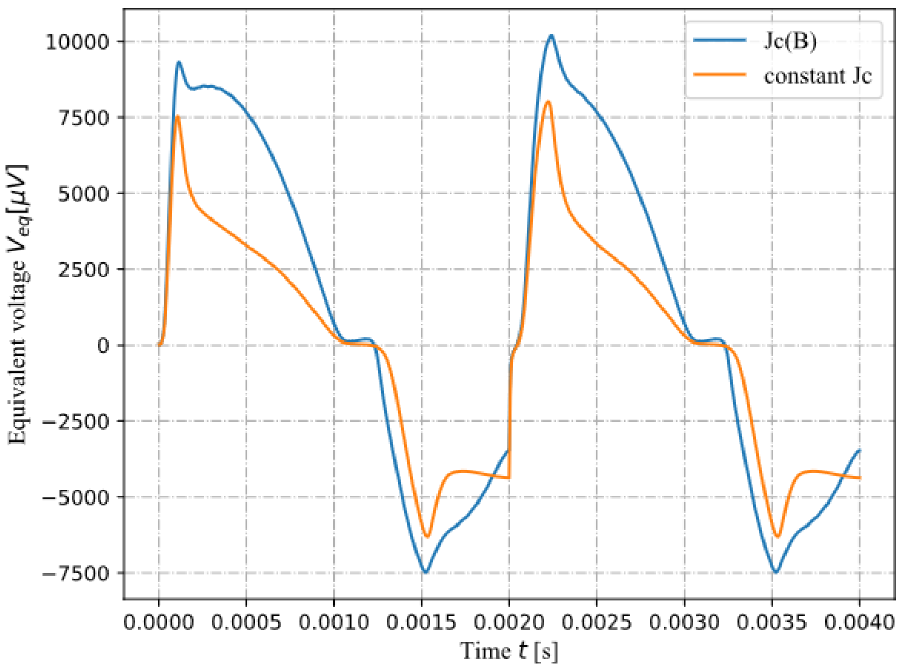

Figure 5.4.3. The time dependent equivalent voltage across the HTS tape considering $J_c(B)$ dependence (blue curve) and constant J_c (orange curve).

5.5 Field modulation

As it can be seen from figure 5.3.1 and figure 5.4.3, during one cycle of the applied magnetic field, the waveform of induced voltage across the HTS tape consists of the positive part and the negative part. More precisely, take the first cycle, for example, the equivalent voltage is positive from 0 s to 0.001 s, and then becomes negative from 0.001 s to 0.002 s. It is the unbalance between the integral of positive voltage and negative voltage that enables this type of flux pump produces an effective DC voltage, and hence charge the rest of the circuit if a closed loop is formed. It should be noted that HTS flux pump is normally employed with superconducting coils, which can be considered as an inductive load. For an inductive load, the terminal voltage is not directly correlated to the current flowing direction. Instead, the voltage controls the changing rate of the current, i.e., $V = L\frac{di}{dt}$, which means it is possible for the current to preserve its flowing direction even if the terminal voltage changes its sign.

Therefore, such an alternating voltage is still capable of charging the load unidirectionally, depending on the sign of net voltage over one complete cycle.

As discussed above, the charging performance is essentially controlled by the net voltage, which is determined by the sum of positive and negative voltage. However, it should be pointed out that, as shown in figure 5.4.3, the valid charging, i.e., increasing the flowing current, only takes place in the first half cycle, from 0 s to 0.001 s. In fact, in the second half cycle from 0.001 s to 0.002 s, the negative voltage will result in a discharging effect if connected to the inductive load. From this perspective, the charging performance can be dramatically enhanced, if one can get rid of the discharging part. That to say, the negative voltage should be avoided, so that the positive voltage can be fully exploited, and thus the load can be consistently charged.

Since the applied magnetic field is a half-sinusoidal waveform, it can be noticed that the positive equivalent voltage occurs during the rising period of applied magnetic fields, and the negative voltage appears during the falling period of applied magnetic fields. Hence, it can be expected that by applying only the rising period of applied magnetic fields, only positive voltage will be induced across the HTS tape. In order to test the feasibility of such an approach, FEM simulations have been conducted, in which the applied magnetic fields are modulated to be either one-quarter sinusoidal waveform, or the sum of two- or three-quarter sinusoidal waveforms, as shown in figure 5.5.1. The equivalent voltage across the HTS tape is plotted in figure 5.5.2, from where it can be seen that only positive voltage presents, as expected. With the applied magnetic field being one-quarter sinusoidal waveform, the corresponding open circuit voltage is 3058.9 μV, which is three times higher than the half wave case (915 μV). Besides, by subsequently applying additional the same quarter sinusoidal magnetic field, the purely positive equivalent voltage can be periodically generated, which means the flux pumping effect can be superposed.

The results above demonstrate that it is possible to enhance the output voltage of a stationary wave HTS flux pump by properly modulating the applied magnetic fields, i.e., preserving only the rising part of a sinusoidal waveform and remaining at its peak value. With such an approach, it is expected that the charging performance can be dramatically increased by containing a purely positive equivalent voltage across the HTS tape, and hence taking full advantage of the flux pumping effect. However, it should be noted that since the applied magnetic fields are no longer periodic, the stationary wave HTS flux pumps cannot be operated periodically. Unlike the travelling wave HTS flux pumps and the stationary wave HTS flux pumps with a cyclic magnetic field, which can be easily operated in a periodic mode and gradually accumulate flux in the charging loop, the modulated stationary wave HTS flux pumps tend to finish the charging with a one-off process. Even though, it does not mean that the modulated stationary wave HTS flux pumps are not applicable when the desired charging cannot be finished at one time. For the cases where multi-phase charging is required, one can employ extra magnetic fields, as shown in figure 5.5.1, to add more charging cycles. Theoretically, by applying adequate magnetic fields, i.e., employing multiple electromagnets, the modulated stationary wave HTS flux pumps also possess the capability of generating any desired field with an accumulation process. Though implementing this approach is not as intuitive as those periodic mode supported HTS flux pumps, such as rotating magnets for a rotary HTS flux pump, it is still feasible in practice.

Meanwhile, the work presented in section 5.2 can also be helpful for exploring the output performance of a modulated stationary wave HTS flux pump. For example, it is reasonable to deduce that the open circuit voltage can be increased by either increasing the operating frequency or decreasing the air gap. For a short summary, the field modulation provides a useful method to increase the output voltage for a stationary wave HTS flux pump, and substantially accelerate the load charging.

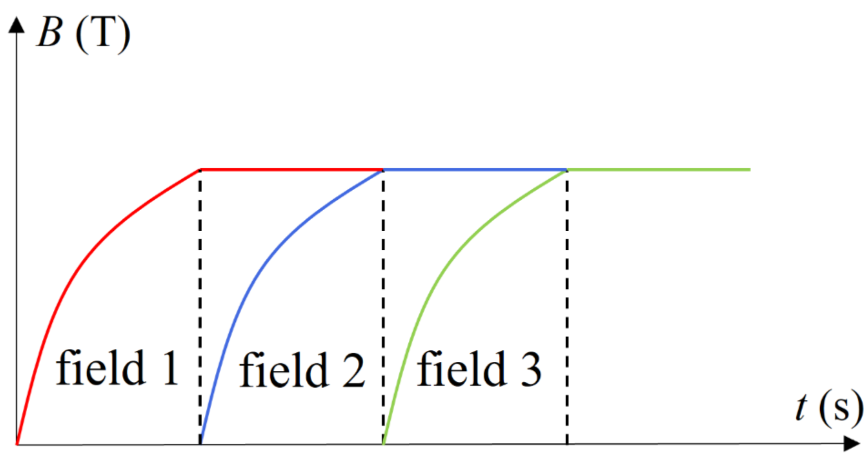

Figure 5.5.1. Illustration of the waveform profiles of applied magnetic fields.

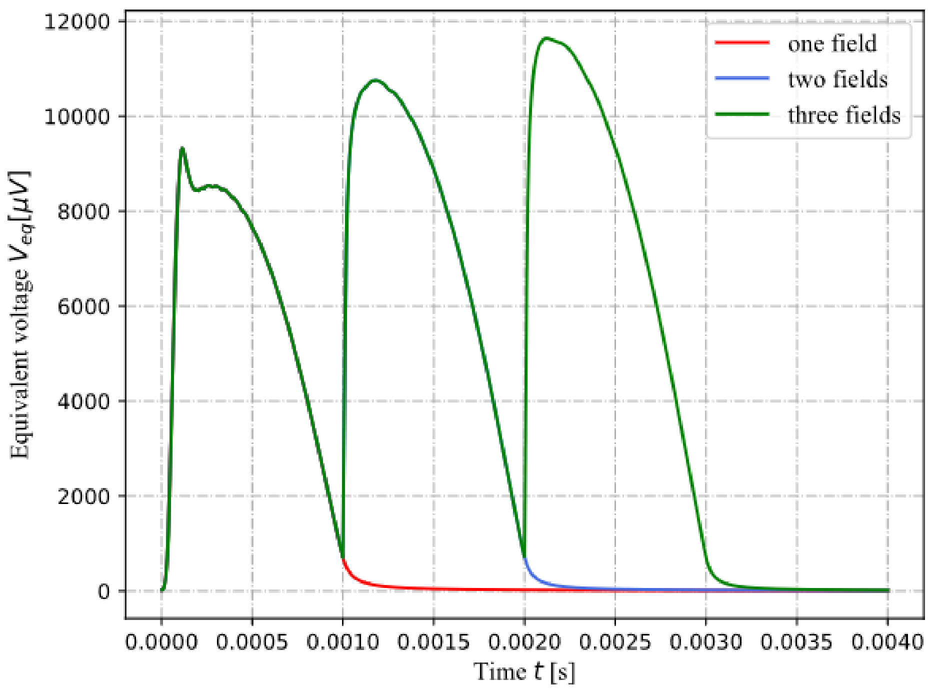

Figure 5.5.2. Equivalent voltage with various applied magnetic fields, parts of the one field condition (red curve) and two fields condition (blue curve) overlap each other and are sheltered by the three fields condition (green curve).

Meanwhile, the work presented in section 5.2 can also be helpful for exploring the output performance of a modulated stationary wave HTS flux pump. For example, it is reasonable to deduce that the open circuit voltage can be increased by either increasing the operating frequency or decreasing the air gap. For a short summary, the field modulation provides a useful method to increase the output voltage for a stationary wave HTS flux pump, and substantially accelerate the load charging.

5.6 Dynamic resistance

When alternating magnetic fields are applied to HTSCs with transporting currents, measurable resistivity will be induced, which is often termed as dynamic resistance. This resistance can be influenced by either the external environments, such as the transporting current and applied magnetic field, or the inherent properties, such as the n-value of the HTSCs. For HTS flux pumps under open-circuit conditions, the dynamic resistance, resulting from circulating currents with external magnetic fields, is important to understand their mechanism and operation.

The dynamic resistance ρ_d in the HTS layer along the tape width at different moments in one cycle, under the condition of 0 mm and 2.5 mm misalignment distance, are plotted in figure 5.6.1 and figure 5.6.2, respectively. As it can be seen, in either case, the is varying resistance in the HTS layer. The resistivity induced in the HTS layer, in the level of $10^{-10}\ \Omega \cdot m$, is in orders smaller than the resistivity in other layers, in the range of $10^{-6}\ \Omega \cdot m \sim 10^{-8}\ \Omega \cdot m$. Since electric current always tends to find a path with the lowest resistivity, this explains why the circulating currents mainly flow in the HTS layer, as illustrated in figure 5.4.1 and figure 5.4.2.

It has been demonstrated that in the case of 0 mm misalignment distance, no flux pumping effect can be observed. However, figure 5.6.1 shows that there is still noticeable dynamic resistance in the HTS layer, though the resistivity is completely symmetric along the tape width. As discussed previously, the circulating currents, in this case, are also symmetric along the tape. Therefore, the positive electric field and negative electric field will cancel each other, and result in a zero-output voltage across the HTS tape, as a combinational effect.

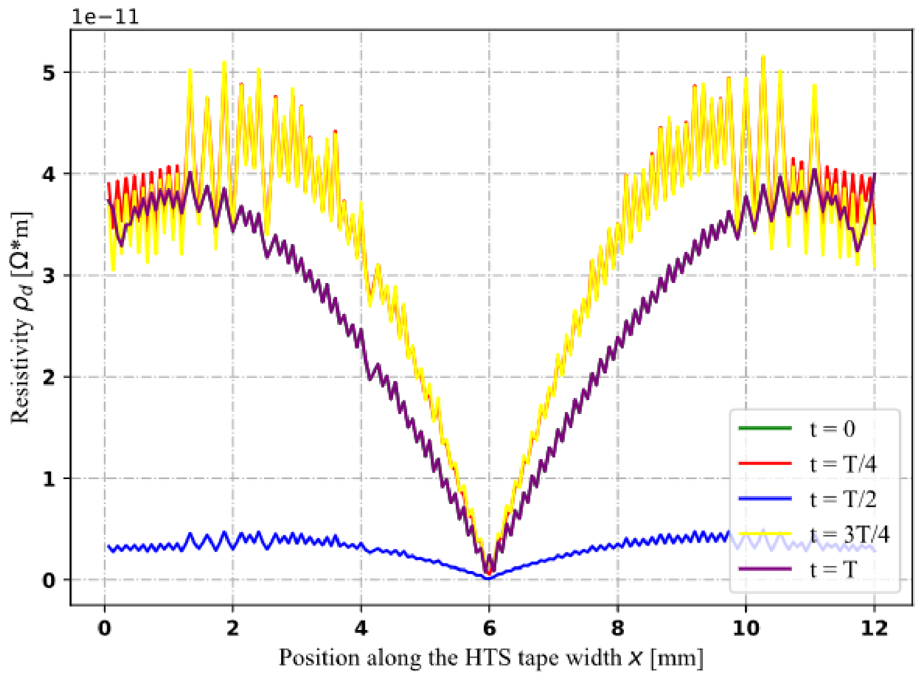

Figure 5.6.1. HTS layer resistivity along the tape width (0 mm misalignment distance).

Results in figure 5.6.2 demonstrate that if there is a certain misalignment distance between the electromagnet and HTS tape, the dynamic resistance becomes consistently asymmetric along the tape width. In this specific case, the dynamic resistance in the right part of the HTS tape, e.g., from 6 mm to 12 mm, is dramatically higher than that in the left part. This can be understood as the right part of the HTS tape is closer to the electromagnet, which tends to exhibit a higher resistance, considering $J_c(B)$ dependence. It is the asymmetry that makes it possible for the circulating currents to produce an unbalanced positive and negative electric field, and hence generate a net DC voltage output across the HTS tape. Since the dynamic resistance is time and space dependent, one can define its effective value as:

$$R_{eff} = \frac{L}{S} \cdot \frac{1}{T} \int dt \frac{1}{S} \iint \rho_d(x, y, t) ds \tag{5.6.1}$$

where S represents the cross section area of the HTS layer.

Considering flux pumping is caused by the dynamic resistance, it is worthwhile investigating how its effective value is influenced by the design parameters, namely the misalignment distance M_d, air gap g, peak flux density B_p, frequency f, HTS tape width W_s and copper solenoid width W_{so}. The references for each parameter are set to be 2.5mm, 500 Hz, 3.75 mm, 1.85 T, 12 mm and 6 mm.

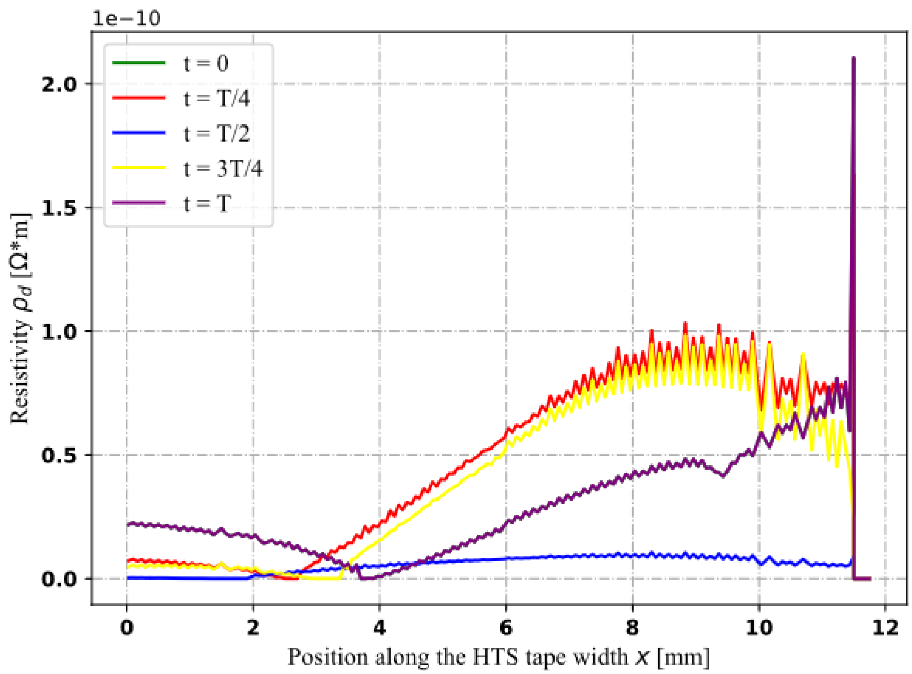

Figure 5.6.2. HTS layer resistivity along the tape width (2.5 mm misalignment distance).

5.6.1 Impact of M_d on R_{eff}

The dependence of the effective resistance of HTS tape on misalignment distance is shown in figure 5.6.3, from where it can be seen that the effective resistance contains its peak value with the misalignment distance in the range of 0~2 mm.

Moving the electromagnet away from the HTS tape further gradually decreases the resistance, which can be understood by noticing that the magnetic field applied on the HTS tape is weakened with an increasing misalignment distance.

Compared to figure 5.2.2, a significant difference is that there are no extreme points in the curve. Considering the definition of output voltage, its magnitude is determined by the difference between the positive and negative electric fields. Since the resistivity is isotropic over the HTS tape, the effective resistance is essentially derived by summing up the resistance on the positive and negative circulating currents regions. Under open circuit conditions, the positive current must be equal to the negative current to achieve a net zero transport current. To maintain resistance constant while increasing the voltage output, for M_d in 0~1.5 mm, it can be deduced that the resistance in the negative current region (depending on the sign of output voltage) is increased, but the resistance in the positive current region is decreased.

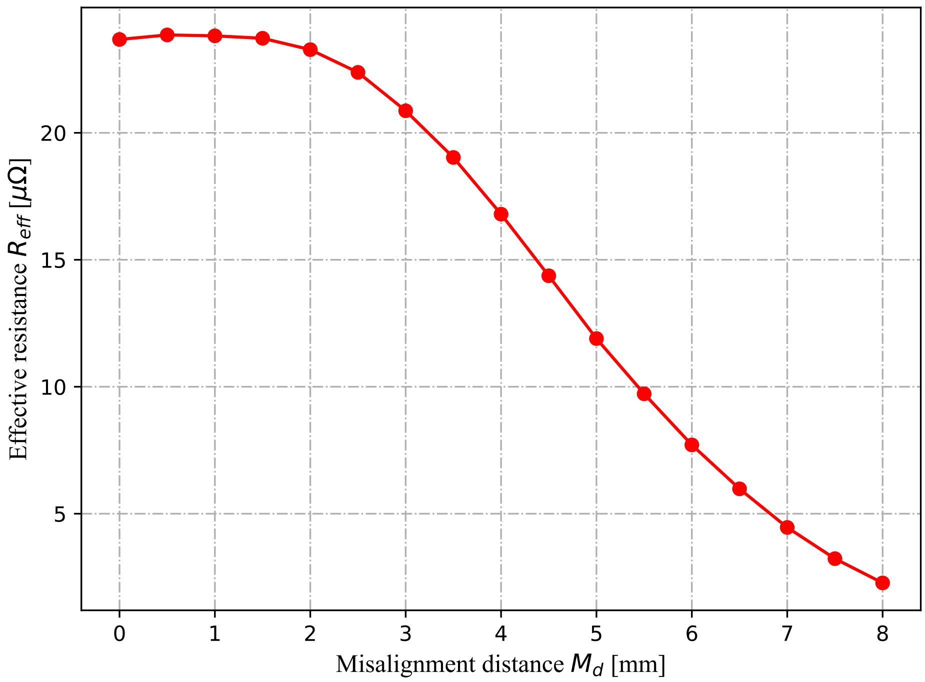

Figure 5.6.3. Effective resistance R_{eff} versus misalignment distance M_d.

5.6.2 Impact of g on R_{eff}

As shown in figure 5.6.4, the effective resistance is inversely proportional to the air gap. This phenomenon can be well understood by considering the $J_c(B)$ dependence. Increasing the air gap will decrease the flux density applied on the surface of the HTS tape, so that the critical current density of the tape will increase. Then, based on the ***E-J*** power law, the resistivity tends to decrease accordingly.

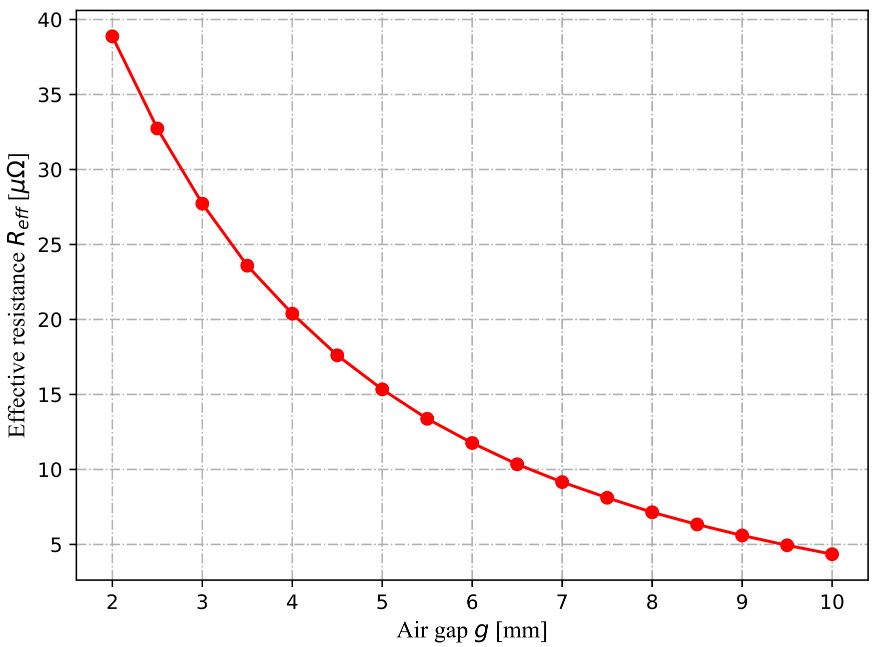

Figure 5.6.4. Effective resistance R_{eff} versus air gap g.

5.6.3 Impact of B_p on R_{eff}

Similar to varying the air gap, changing the applied peak flux density directly determines the magnetic field experienced by the HTS tape. Due to the $J_c(B)$ dependence, increasing flux density will result in a smaller critical current density in the HTS tape. As a result, the dynamic resistance increases, as shown in figure 5.6.5.

5.6.4 Impact of f on R_{eff}

In terms of the dependence of effective resistance on operating frequency, figure 5.6.6 demonstrates a roughly linear relationship between them. It should be noted that the frequency is irrelevant to the magnitude of flux density, and hence should have no impact on the critical current density by taking the $J_c(B)$ dependence into account. Nevertheless, the frequency represents the changing rate of the flux density, which, based on electromagnetic induction, can affect the induced circulating currents in the HTS tape. Learning from the definition of E-J power law, the resistivity of the HTS tape is not only influenced by the flux density, but also the flowing current itself, which can explain the variation of effective resistance with frequency.

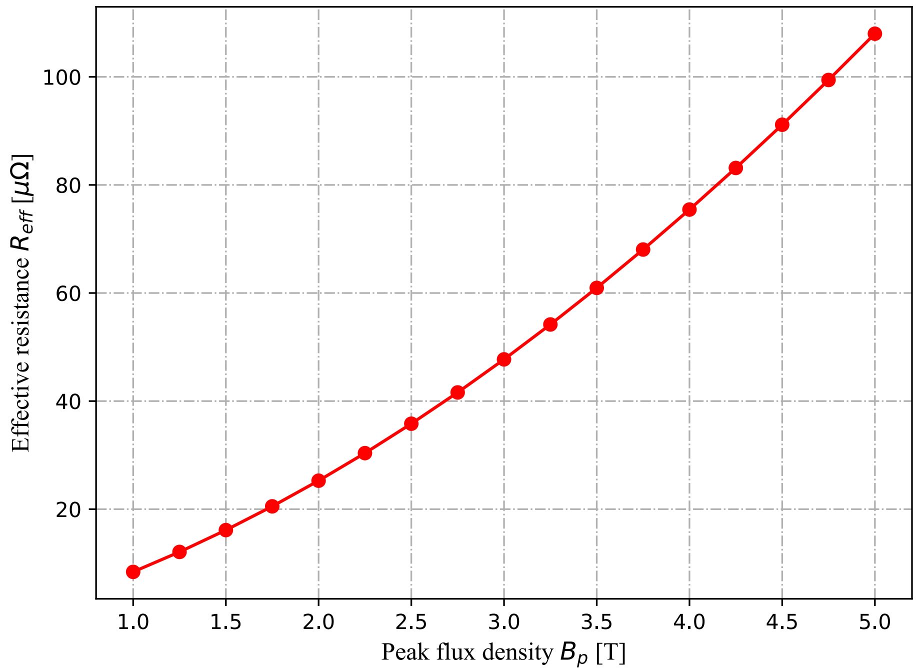

Figure 5.6.5. Effective resistance R_{eff} versus peak flux density B_p.

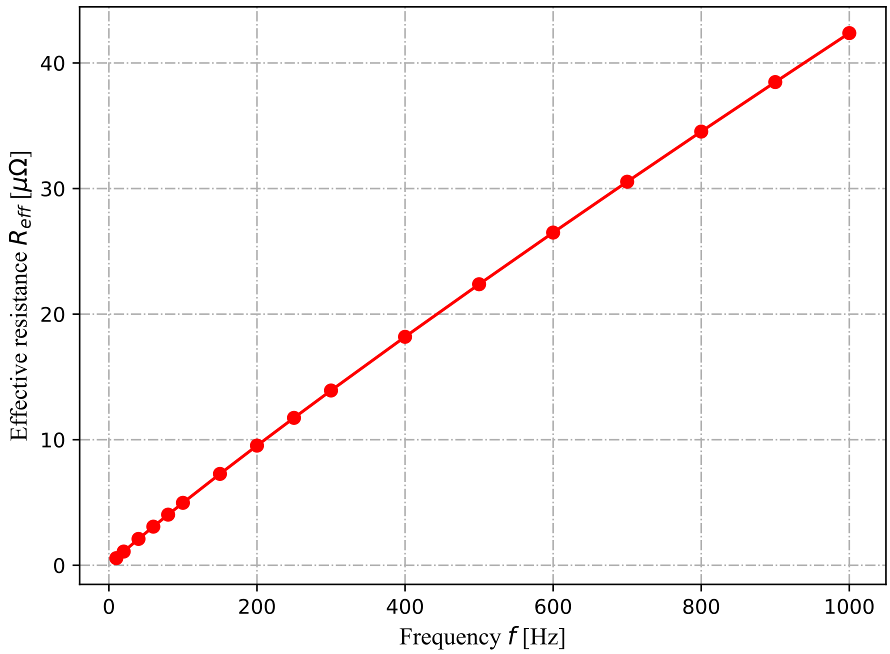

Figure 5.6.6. Effective resistance R_{eff} versus operating frequency f.

5.6.5 Impact of W_s on R_{eff}

As illustrated in figure 5.6.7, increasing the width of HTS tape consistently decreases its effective dynamic resistance. It should be pointed out that figure 5.2.6 has demonstrated that the output voltage is yet not in such an inversely proportional relation to the tape width. In contrast, the output voltage firstly increases to reach a peak value, after which it starts to decrease with the HTS tape width. This again implies that the output voltage is though originates from, but not solely determined by the dynamic resistance. Since the net output voltage is a combinational effect of the positive and negative circulating currents, it is possible for this voltage to exhibit different variations from the overall resistance of the tape.

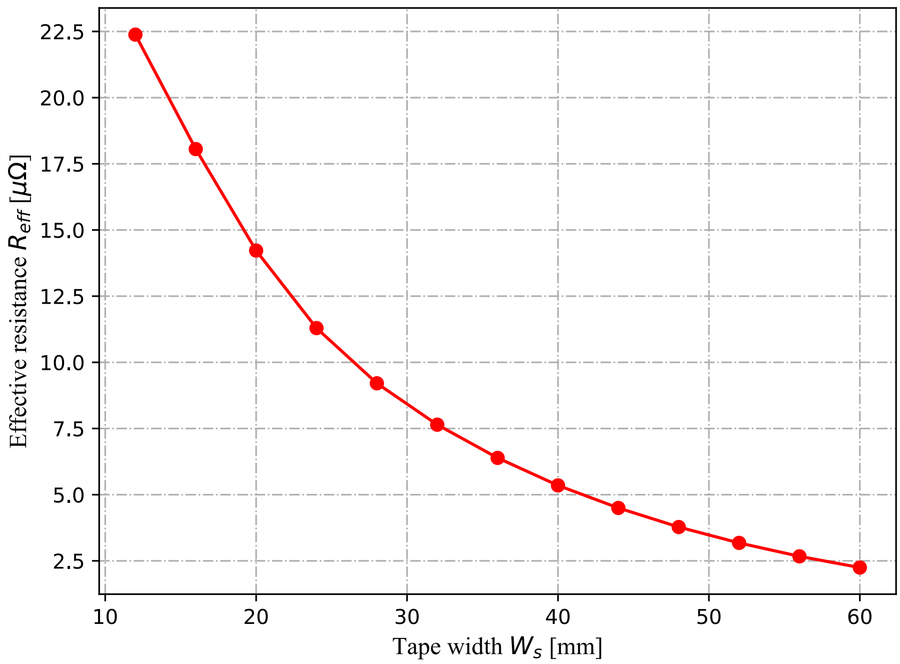

Figure 5.6.7. Effective resistance R_{eff} versus HTS tape width W_s.

5.6.6 Impact of W_{so} on R_{eff}

For the framework of the proposed stationary wave HTS flux pump, the width of the solenoid controls the effective source area of the magnetic field. For instance, increasing the solenoid width means more proportions of the HTS tape are placed beneath the electromagnet, which experience a stronger magnetic field. Therefore, more proportions of the HTS tape have a lower critical current density, and hence higher dynamic resistance, as shown in figure 5.6.8. However, it has been revealed in figure 5.2.7 that there is an optimal solenoid width to maximize the output voltage. Once the solenoid width exceeds the optimal value, it can cause the output voltage to decrease. Considering this effect, it is important that a proper solenoid width should be selected in the design and operation of a stationary HTS flux pump, because making the solenoid width unnecessarily wide can not only decrease the output voltage, but also result in extra losses owning to higher resistance.

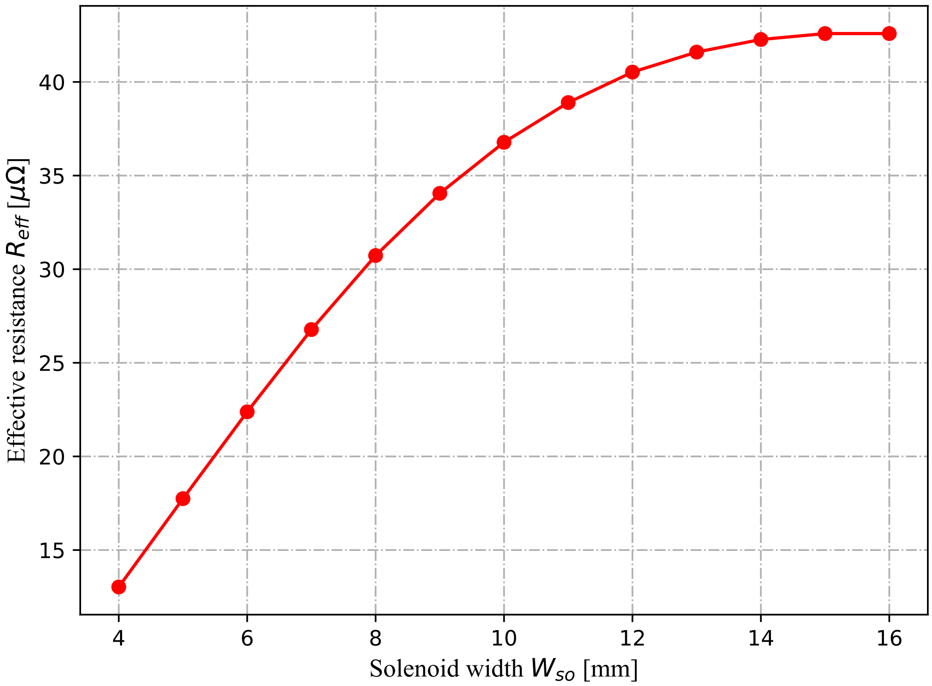

Figure 5.6.8. Effective resistance R_{eff} versus solenoid width W_{so}.

5.7 Machine learning modelling

It has now been revealed that the effective dynamic resistance of a stationary HTS flux pump is clearly influenced by each of the four geometric parameters, as defined in figure 5.2.1, and the two operating parameters, peak flux density and frequency of applied magnetic fields. In the last chapter, the individual dependence of the open circuit voltage on each of these design parameters has already been demonstrated. That is to say, there should be certain functions to describe how the open circuit voltage and effective dynamic resistance are correlated with these design parameters. Knowing this correlation, through feasible approaches, can be helpful to facilitate the design and optimization of such a stationary HTS flux pump. Earlier, it has been discussed that arranging experimental tests can be impractical due to the expensive costs. As a traditional alternative, FEM simulations are useful to replicate the operation of HTS flux pumps without setting experimental tests. However, solving FEM models can be time consuming and makes them inefficient when it comes to frequently changing model parameters, let alone the complicated construction process and professional knowledge can also be significant barriers for designers.

To address these challenges, machine-learning based approaches have been proposed in the last chapter, which have proved to be extremely beneficial for the design of rotary HTS flux pumps. Inspired by those successful experiences, it is worthwhile to implement similar ideas for stationary waveform HTS flux pumps, in order to obtain statistical models that can predict the open circuit voltage and effective dynamic resistance in an accurate and efficient manner.

5.7.1 Open circuit voltage prediction

Compared with rotary HTS flux pumps, the proposed stationary waveform HTS flux pumps also possess the same amount of, i.e., six design parameters. Except for the air gap g, operating frequency f and HTS tape width W_s, which are directly involved in both types of HTS flux pumps, there are several different design parameters that have close physical meanings. The peak flux density B_a and copper solenoid width W_{so}, for a stationary waveform HTS flux pump, are equivalent to the remanence flux density B_r and magnet width W_m, for a rotary HTS flux pump, respectively. One significant difference is that there is no rotor radius R_r for a stationary waveform HTS flux pump, since it does not require the rotating disc, yet another new parameter, the misalignment distance M_a, is introduced to reflect the relative position of the HTS tape with respect to the copper solenoid.

From the perspective of obtaining the open circuit voltage of a stationary waveform HTS flux pump while integrating all the six design parameters, it is equivalent to a regression problem that links six independent (input) variables to one dependent (output) variable. Intuitively, the task is identical to constructing a statistical model for capturing the output voltage for rotary HTS flux pumps, as presented in Chapter 4. Hence, the deep learning-based neural network (DNN) is utilised, and a similar procedure is followed to fulfil the goal of predicting the open circuit voltage.

Firstly, based on the built numerical models, 5000 sets of data samples that include different design parameter combinations have been generated and extracted through FEM simulations. To form these parameter combinations, values for each design parameter have been randomly chosen in a fixed range (see figure 5.6.3 to figure 5.6.8). Then, various DNN topologies with different hidden layers and neurons in each layer have been tested. The performance of tested DNN topologies was evaluated by comparing their NSE scores, which is a criterion to measure how much the predicted values deviated from the actual values. The best NSE score that can be possibly achieved is 1, which means all predictions are exactly matched to their corresponding observations. Table 5.7.1 shows the best NSE scores obtained for different DNN topologies with 1 to 6 hidden layers, from where it can be seen that the highest NSE score increases with the number of hidden layers up to 3. Overall, the best training performance was realized by the DNN model with 3 hidden layers, with 111, 222 and 333 neurons in the first, second and third hidden layer, respectively. As discussed before, since the data space used to train those DNN models is limited, the selected optimal model with the highest NSE score may not guarantee that it must have desired prediction capability. Therefore, new data samples that are not covered in the original training and validation step are generated and fed into the selected model to verify its generalized effectiveness. The workflow is summarized in figure 5.7.1, and more details can be found in Chapter 4.

Table 5.7.1. NSE scores for different DNN model topologies (V_{oc} prediction).

Number of neurons in each layer						NSE
1	2	3	4	5	6	
1020	NA	NA	NA	NA	NA	0.93987
808	292	NA	NA	NA	NA	0.96251
636	376	444	NA	NA	NA	0.96665
432	820	328	836	NA	NA	0.96357
544	252	924	508	76	NA	0.96158
672	348	56	844	836	156	0.95881

As illustrated in figure 5.7.2, within the extra data samples prepared for testing the generalized prediction capability of the selected model, all predictions (denoted by red dots) are in close proximity to the blue diagonal, which indicates the excellent accuracy of this model. In order to examine the prediction performance in more depth, the relative error in percentage for each prediction is plotted in figure 5.7.3. As can be seen, the maximum error reaches about 40%, but only for very few predictions. Most of the predictions have an error rate less than 5%, and the average error rate is maintained at 7.41%. More precisely, by dividing all test samples into different intervals in terms of their proportions to the maximum value, one can further explore these predictions. According to figure 5.7.4, test samples in intervals close to the left end of the x-axis tend to have higher error rates, which can be understood by considering the fact that those test samples are corresponding to small values, and hence they are more sensitive to errors measured in percentage. Even so, including outliers identified by the black cycles in figure 5.7.4, the average error rates marked by the green triangles in figure 5.7.4 for predictions in each interval are well below 10%.

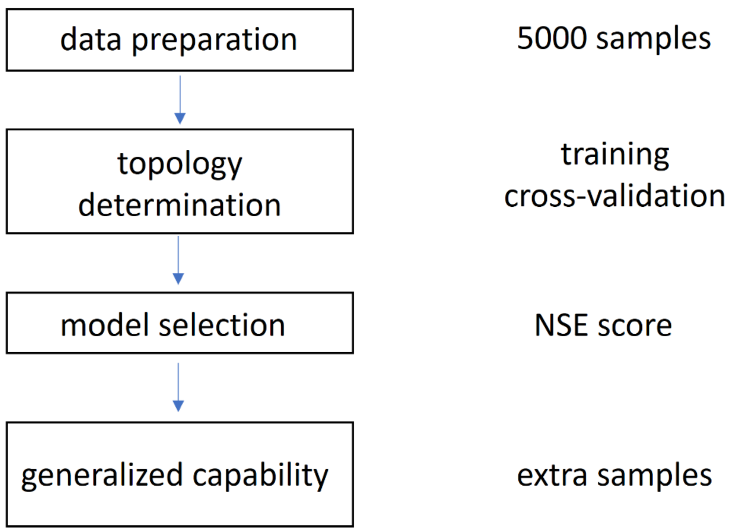

Figure 5.7.1. Diagram of the procedure for deriving the prediction model.

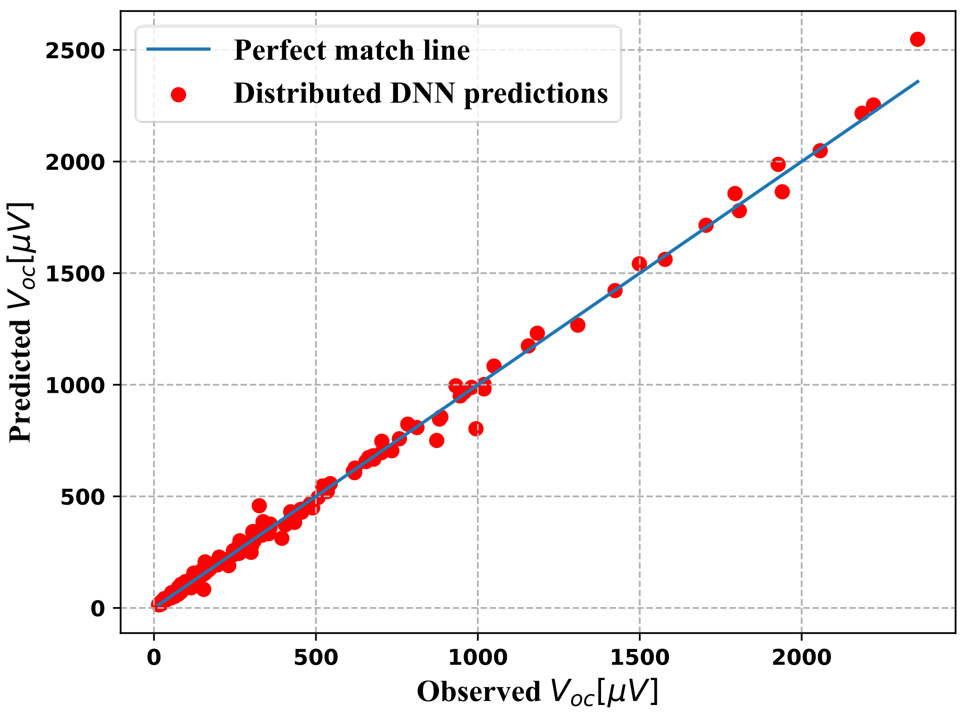

Figure 5.7.2. Open circuit voltage for test data samples predicted from the selected best DNN model against observed values.

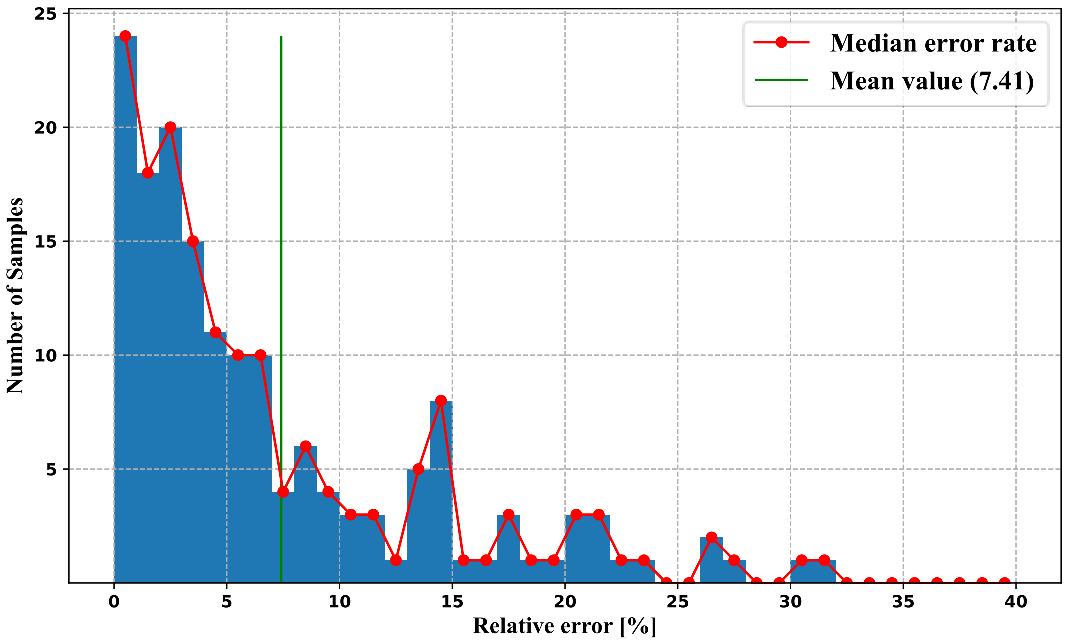

Figure 5.7.3. Histogram plot for the relative errors of predicted voltage. The red line connects the medium relative error in each sample group, and the green line identifies the mean value of the relative errors for all data samples.

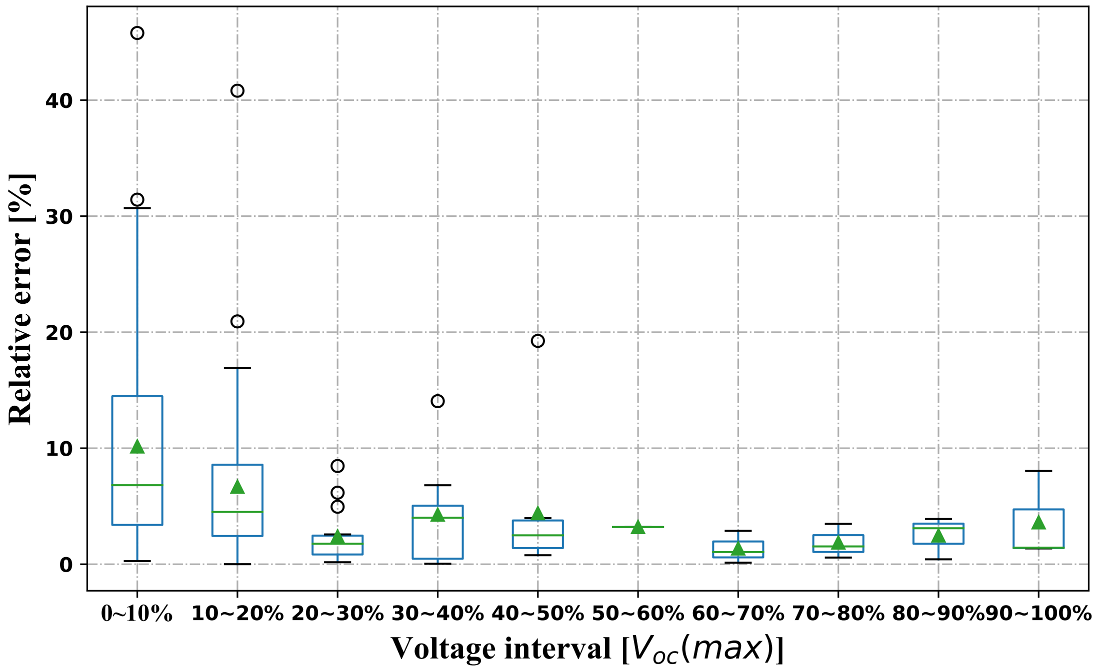

Figure 5.7.4. Box plot of the relative errors for predicted voltage grouped by intervals with different proportions to the maximum prediction value. Black cycles indicate outliers and green triangles signify the average value in each interval.

5.7.2 Effective resistance prediction

In section 5.6, the effective dynamic resistance R_{eff} has been introduced to calculate the value of the inherent resistance during the flux pumping process for a stationary wave HTS flux pump. The dynamic resistance has been demonstrated to be the root of the non-zero time-averaged output voltage, and it exits in regardless of the open circuit voltage, i.e., there can be a measurable dynamic resistance even if the open circuit voltage is zero. Quantifying the dynamic resistance is of great significance because it provides an indicator to appraise the inherent losses that can be caused by the circulating currents flowing with HTS tapes.

Similar to the open circuit voltage, R_{eff} is also a complex variable that depends on a series of factors. From the operation point of view, the effective dynamic resistance is clearly influenced by every pre-defined design parameter, as presented in figures 5.6.3 to 5.6.8. In order to estimate the value of the effective dynamic resistance based on given design parameters, the proposed machine-learning techniques have been applied to extract the correlations between the output (effective dynamic resistance) and inputs (design parameters) by the means of a statistical model.

The path to deriving the prediction model follows the same procedure as introduced in section 5.7.1, which mainly consists of data preparation and training, model selection and evaluation. Under such a routine, the results of the best NSE scores obtained for different DNN topologies with 1 to 6 hidden layers are listed in table 5.7.2. Judging from NSE scores, the best DNN topology turns out to be a three-layer structure with 860, 124 and 972 neurons in the first, second and third layer, respectively. Based on this determined topology, extra data samples that are not covered in the original training and validation step are generated to verify its generalized effectiveness.

Table 5.7.2. NSE scores for different DNN model topologies (R_{eff} prediction).

Number of neurons in each layer						NSE
1	2	3	4	5	6	
760	NA	NA	NA	NA	NA	0.99489
500	972	NA	NA	NA	NA	0.99840
860	124	972	NA	NA	NA	0.99867
412	180	36	256	NA	NA	0.99803
276	992	60	316	656	NA	0.99815
472	312	68	64	144	656	0.99774

The effective dynamic resistance of extra test samples and their estimated values predicted by the selected DNN model are plotted in figure 5.7.5, from where it can be seen that all red points align well with the blue diagonal line, meaning that for each test data sample the predicted effective dynamic resistance precisely match its actual value. Figure 5.7.6 further explores the accuracy of each prediction by examining the error rates in percentage, which shows that predictions for more than 100 test samples (out of 180 in total) have an error rate lower than 1%, and few predictions possess relatively higher error rates up to around 10%. On the whole, the average error rate for all predictions is 1.4%. As has been done for the open circuit voltage, test samples can be divided into groups based on their proportions to the maximum effective dynamic resistance. Figure 5.7.7 illustrates the error rate distribution in 10 intervals, with a step of 10% increasement from zero to the maximum. In the first interval, which corresponds to test samples that have small resistance, there are several outliers with relatively higher error rates, including the highest error rate 14%. This is understandable because minor values are more vulnerable to errors measured in percentage. The average error rate in each interval, with all outliers included, is contained well below 2%.

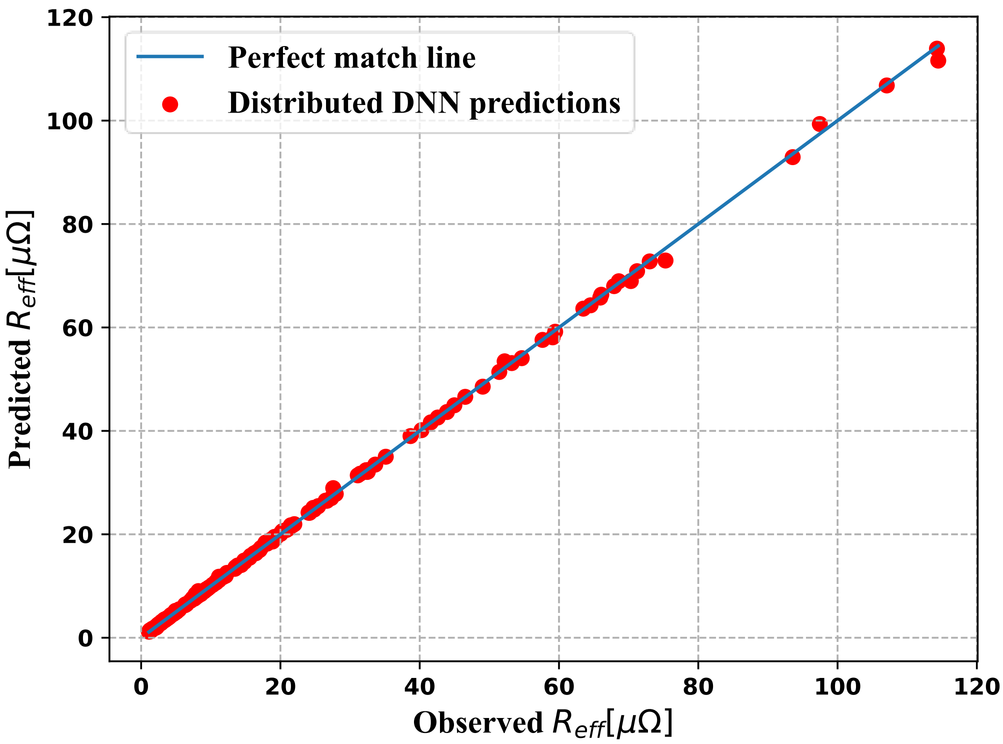

Figure 5.7.5. Effective dynamic resistance for test data samples predicted from the selected best DNN model against observed values.

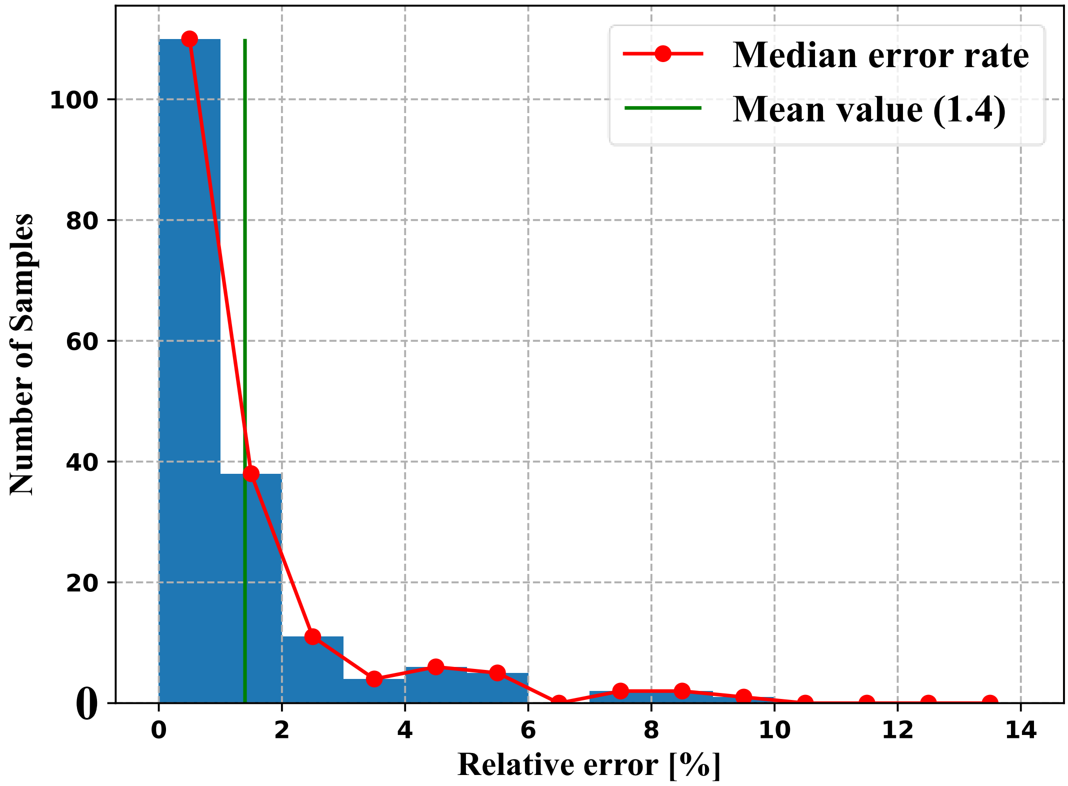

Figure 5.7.6. Histogram plot for the relative errors of predicted effective dynamic resistance. The red line connects the medium relative error in each sample group, and the green line identifies the mean value of the relative errors for all data samples.

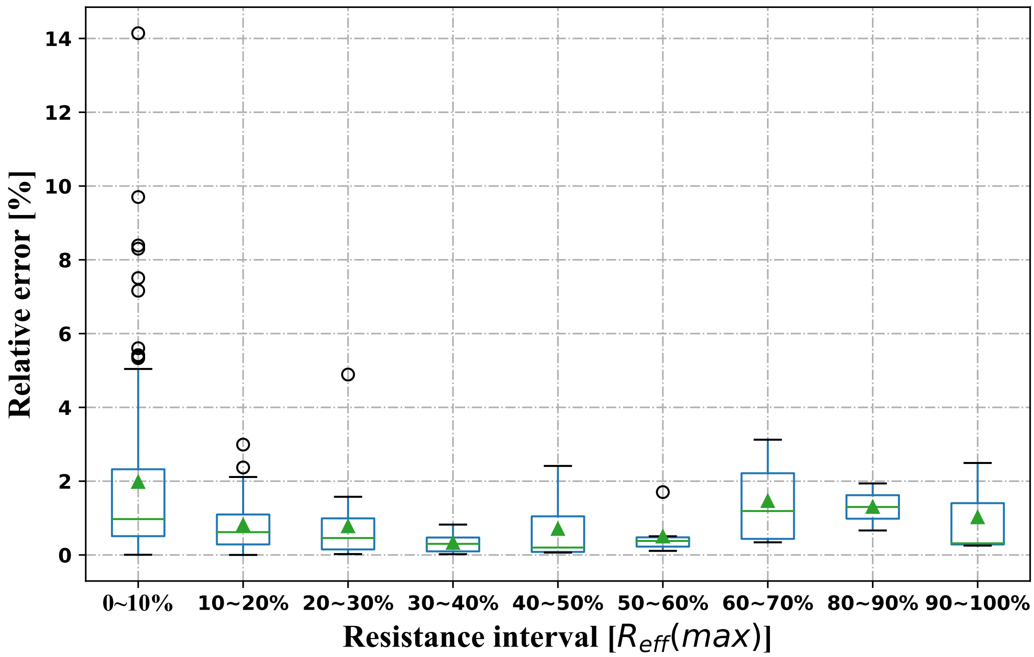

Figure 5.7.7. Box plot of the relative errors for predicted effective dynamic resistance grouped by intervals with different proportions to the maximum prediction value. Black cycles indicate outliers and green triangles signify the average value in each interval.

5.8 Conclusions

In this chapter, a novel HTS flux pump has been developed. This type of flux pump utilised only one solenoid injected by a single-phase excitation, which, to distinguish from those travelling waveform HTS flux pumps, is term as stationary wave HTS flux pump. It has been demonstrated that this type of flux pump can produce remarkable open circuit voltage, and the output characteristics for a set of controllable parameters have been investigated. The origin of the open circuit voltage for stationary waveform HTS flux pumps has been discussed. It has been demonstrated that the asymmetry of the resistivity trigged in HTS tapes is the fundamental requirement for such a non-zero time-averaged DC voltage, while the $J_c(B)$ dependence is not necessary but can dramatically prompt the generated voltage. Following the disclosure of the voltage origin, a possible method has been proposed to increase the output voltage by the means of subsequently applying multiple external magnetic fields. This phenomenon further demonstrates that flux pumping is an accumulative process, which implies that theoretically a desirable high level of field can be achieved by very small fields.

Besides, the dynamic resistance has been investigated, and its dependences on each of the six pre-defined design parameters have been explored. The machine learning modelling approaches proposed in former chapters have been re-applied to derive statistical models to predict the open circuit voltage and effective dynamic resistance, which successfully achieved an excellent accuracy of 92.59% and 98.6%, respectively, with respect to the values calculated by FEM simulations.

Chapter 6

Conclusions and Future Work

6.1 Thesis summary

An HTS flux pump enables current injection into a closed superconducting coil wirelessly and provides continuous compensation to offset current decay, avoiding excessive cryogenic losses and sophisticated power electronics facilities. The purpose of this PhD project is to conduct throughout research on HTS flux pumps and bring more insight into their principles. More importantly, this project pays particular attention to the scenario of industrial applications, which in other words is to find practical approaches in substitution to traditional experimental tests and numerical simulations that can not only benefit general research purposes, but also facilitate the design and optimisation process of such devices.

Over the past decades, HTS flux pumps have been extensively investigated. To figure out the current status and where the gap exists, the latest achievements and up-to-date progress have been reviewed. Details about the two most representative types, namely the travelling wave HTS flux pump and switched transformer-rectifier HTS flux pump, have been elaborated, regarding their working principles, underlying mechanisms, and modelling techniques. In addition, other variants in existing literature have also been introduced. The features of distinct HST flux pumps have been indicated, and their outlooks on practical applications have been discussed.

In order to investigate the operation of rotary HTS flux pumps, an effective numerical model based on ***T*-*A*** formulation has been built. This model has been validated by comparing its calculated voltage waveform with experimental measurements, where an excellent agreement was observed. During the model validation, it was found that there was a significant difference between the model with a constant J_c and one with the $J_c(B)$, which has been attributed to the changes of dynamic resistance on two conditions. Through FEM simulations, the characteristics of open circuit voltage against the air gap, HTS tape width, operating frequency and remanent flux density of the PM have been illustrated. Within the investigated range, the positive linear correlation between the output voltage and operating frequency holds consistent in despite of the variation of other parameters. Decreasing the air gap or increasing the remanent flux density can continuously raise the output voltage, in a curved manner. Instead of being monotonic, it was found that the output voltage tends to increase up to a certain value and then dwindle with the HTS tape width, which has been discussed by examining the electric field distribution in the HTS tape with different widths. Afterwards, the ***T*-*A*** formulation based numerical model was replaced by an updated ***H*-*A*** formulation-based model. Rather than taking the classical approximation to assume the HTS tape as a single line without thickness as in the old one, the new model considers the full structure of HTS tape, which includes the copper layer, silver layer, HTS layer as well as substrate layer. The multi-layer model has clearly demonstrated the non-linear frequency response at high frequencies (hundreds to kHz level), which was caused by the interactions between different layers of the HTS tape.

To address the research question identified in the Introduction (Chapter 1), 1,000 sets of data samples have been generated and extracted from the ***T*-*A*** model firstly, which contain various parameter combinations (those investigated in Chapter 4) with corresponding output voltage. For simplicity, due to the straightforward linear correlation, the frequency was considered as a constant multiplier and exempted from the variable list. These data samples have been utilised to train regression models by applying the most popular machine learning algorithms in Scikit-learn framework, which includes MLP, GPR, SVM, DT and KNN. The performance of each algorithm has been evaluated and compared, after which a highly accurate and reliable GPR model, being capable of replicating the results from numerical models within seconds, was proposed. Afterwards, an ANOVA was conducted to reveal the significance of each parameter on the output voltage, from the statistical perspective. Following the successful demonstration of the feasibility of applying machine learning techniques to capture the output characteristics of rotary HTS flux pumps, further work has been conducted to propose a more complete and powerful design tool. The ***T*-*A*** numerical model was then utilised to generate 8,000 sets of data samples, in which each half of them were extracted from a pre-defined data acquisition scheme. In this case, every data sample contains three extra design parameters, namely the operating frequency, rotor radius and the width of PM. In total, the six parameters were included to cover all the key design parameters. Since more parameters were considered and hence more data samples were prepared, the deep-learning techniques, which can take advantage of GPU to accelerate model computation, were adopted. Numerous tests have been conducted via the Pytorch framework, after which a DNN model with two hidden layers, being capable of predicting the output voltage while integrating all design parameters with an average accuracy of 98% with respect to the numerical simulation results, was proposed. This statistical model has been utilised to visualize the output characteristics of a rotary HTS flux pump and quantify the optimal HTS tape width for various configurations. Besides, an executable application with an operable interface has been developed specifically as a user-friendly tool to facilitate the design and optimization of such devices. This design tool possesses powerful functionalities not only because it can accurately estimate the output voltage for any given design parameters, but also because it can provide possible choices for the values of design parameters by specifying the desirable voltage.

Evolved from the basic principles of rotary HTS flux pumps, the concept of replacing the rotating magnets with static electromagnets to achieve flux pumping has been proposed and verified. The idea was based on the fact that the employment of PM in a rotary HTS flux pump is to provide a varying magnitude field seen by the HTS tape, which was caused by the spatial movement of PM. Equivalently, a similar situation can be created by utilizing a current-driven electromagnet placed at a fixed position, whose field can be controlled by the excitation current. A numerical model based on ***H-A*** formulation has been built, from whose results it has been demonstrated that a measurable voltage can be generated across the HTS tape. Since the applied field in this case was only varying in the time domain, which resembles a stationary wave, this type of device was terms as a stationary wave HTS flux pump. Six parameters, including the air gap, HTS tape width, operating frequency, peak field, width of the copper solenoid as well as the misalignment distance, have been defined to investigate the output characteristics of such a stationary wave HTS flux pump. Each parameter was shown to be influential to the output voltage, and in particular, a non-zero misalignment distance was demonstrated to be an essential requirement for obtaining an effective output voltage regardless of other parameters.

To further explore the newly proposed stationary wave HTS flux pump, the formation of the open circuit voltage has been examined in more depth. It was illustrated that if the electromagnet was placed at the position, where its central line was aligned with that of the HTS tape, the circulating currents in the HTS tape is completely symmetric with respect to the central line, and hence the net voltage across the tape can only be zero. This was because under such circumstances, exactly the same magnetic field was experienced by each half of the HTS tape, which means that the same dynamic resistance would be induced accordingly. This also implied that the origin of the output voltage came from the unregular distribution of the dynamic resistance, and hence the circulating currents within the HTS tape. The impact of each parameter on the effective dynamic resistance has been investigated, which can be a primary indicator to access the inherent losses. The previously proposed machine learning techniques have been adapted and reapplied, based on which statistical models were put forward to predict both the open circuit voltage and effective dynamic resistance of a stationary wave flux pump. Along with the obtained statistical models as another set of design tools, it has also been confirmed that the innovatively applied machine learning techniques were highly extendable to a wide range of scenarios for practical applications.

To conclude, the tasks presented in this thesis deepened the understanding of HST flux pump technologies, and brought in novel approaches to facilitate the design and optimisation of such devices. It is expected that the work and outcomes of this thesis can be beneficial to the research community in relevant fields.

6.2 Future work

This project has investigated the output characteristics of rotary HTS flux pumps with a set of design parameters and come up with statistical models as alternatives to the traditional numerical models. The innovatively developed machine learning modelling techniques have been applied to the newly proposed stationary wave HTS flux pumps, which proved to be effective and useful. Stepping on the project, extra work can be done in the future to break through some of the limitations endogenous to the delivered accomplishments and achieve further improvements.

To begin with, the fundamental numerical models built in this project were 2D, which assumed infinite length of the HTS tape. Though this is a classical approximation and the results have been validated with experimental measurements, utilizing 3D models that take the real structure into account can be helpful for revealing more sophisticated physics during the operation of HTS flux pumps.

Next, the investigations made in this project mainly focused on the output voltage in open circuit conditions, which was considered as a significant criterion for evaluating the performance of HTS flux pumps. Nevertheless, in real cases HTS flux pumps should be operated with an external circuit to form a closed loop. It is suggested to replicate the full charging cycle by integrating associated load components, and the output characteristics could be further explored.

Thirdly, to fulfil the aim of developing design tools for HTS flux pumps, statistical models have been proposed based on certain machine learning techniques. Various algorithms have been tested and tuned during the research, including the typical CPU based MLP, GPR, SVM, DT and KNN models, as well as the GPU accelerated DNN models. Besides these classical algorithms, there are other algorithms that may provide better results, which are yet to be explored. Meanwhile, the statistical models proposed in this project were selected by an acceptable level of accuracy rate subjected to the standard of industrial applications, which allows a certain space for further improvements. For instance, in terms of the prediction capability, the proposed models were shown to generate relatively higher error rates when the outputs are small values. Though, in the case of this thesis, it is understandable that small values are more vulnerable to relative errors and HTS flux pumps are typically required to generate higher output, it is still worthwhile trying to increase the overall accuracy of the statistical models by adjusting and optimizing the algorithms themselves, which is beyond the scope of this thesis but can be done in the future.

Last but not least, the feasibility of applying machine learning techniques was firstly verified by proposing statistical models to predict the output voltage of a rotary HTS flux pump, and its effectiveness was double-confirmed by obtaining statistical models to predict the output voltage and effective dynamic resistance of a stationary wave HTS flux pumps. The work has shed light on proposing convenient and powerful design tools with such approaches, and it is encouraging to implement the concept into a wider range of scenarios and achieve more benefits.

Appendix

Executable Application

Inspired by our work presented in section 4.3 and in order to facilitate the design and optimization of the HTS dynamo, we have developed a toolbox, in the form of an executable application for the Windows system, that can predict the open circuit voltage by feeding the values of required design parameters, and vice versa. This application is specifically developed for the HTS dynamo that has the radial flux configuration with flat HTS tape. As shown in figure A.1, 6 parameters are selected to describe the performance of the HTS dynamo, namely the air gap g, HTS tape width W_s, the remanent flux density B_r of the PM, the rotating speed of the magnet R_s (operating frequency f), rotor radius R_r and magnet width W_m. In practice, it is obvious that each of the parameters can only have values in a rational range. Hence, the valid domain for each parameter is set to be 2~12 mm, 4~60 mm, 0.1~1.6 T, 60~60000 rpm (1~1000 Hz), 35~70 mm, 1~16 mm, respectively, in this application.

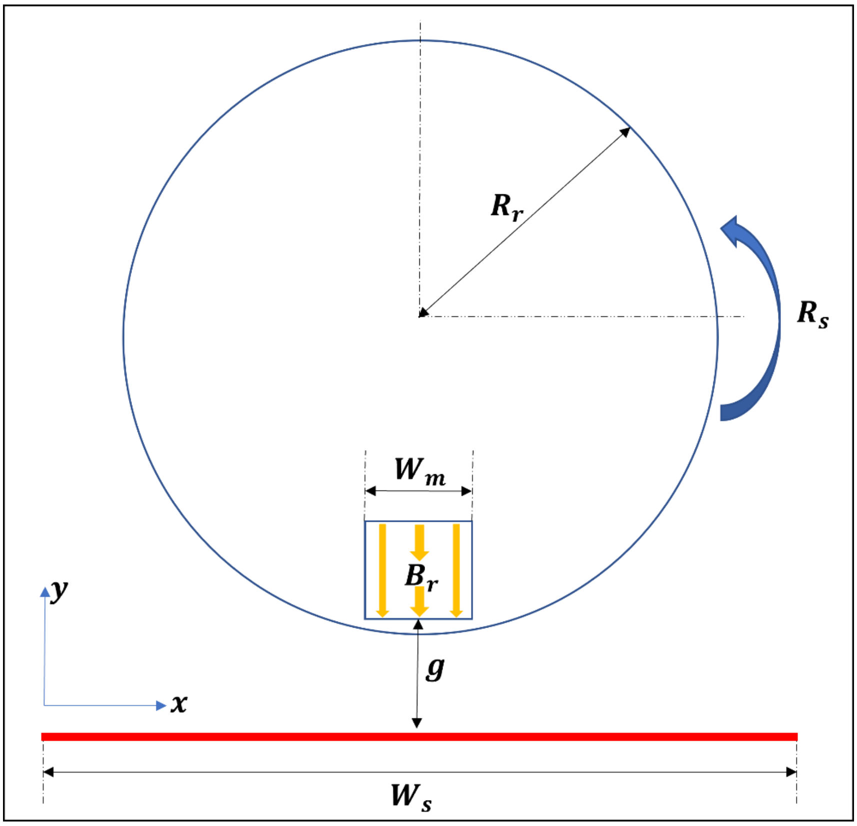

Figure A.1. Schematic diagram for the HTS dynamo prototype.

‘Get V_{oc}’ function

The fundamental usage of this application is to assist researchers design and optimize their HTS dynamo devices by accurately capturing the output characteristics against a collection of design parameters in a quick manner. As shown in figure A.2, the ‘Get V_{oc}’ pushbutton allows users to get an estimation of V_{oc} for their HTS dynamo devices after they specify each of the design parameters. Besides, this function also demonstrates the bilateral width effect by automatically plotting the curve of V_{oc} versus W_s alongside the V_{oc} estimation. This plot shows how the output voltage is expected to vary versus the variation of HTS tape width, i.e., all the design parameters are fixed except for the HTS tape width, which can help users to identify the optimal HTS tape width for any given configuration.

Figure A.2. User interface of the 'Get V_{oc}' function.

‘Get Design Parameters’ function

In the practical design process, engineers could come across a situation where they want their HTS dynamo devices to generate a certain voltage, but they are not sure about how to set up each of the design parameters. If this is the case, the ‘Get Design Parameters’ pushbutton can be extremely helpful since it can provide possible design parameters according to the specified voltage, which can serve as a good starting point to initialize the design.

To implement this function, the ‘Desire Voltage’, as shown in figure A.3, is the only input that must be manually specified. Though any positive value is acceptable for defining the voltage, errors can be raised if the specified value is not rational in terms of representing the voltage output from an HTS dynamo, e.g., millions level, which cannot be possibly achieved. It should be noted that it is very likely that the specified voltage can be obtained from more than one unique parameter setting, hence an Excel file will be generated to store all the possible parameter settings.

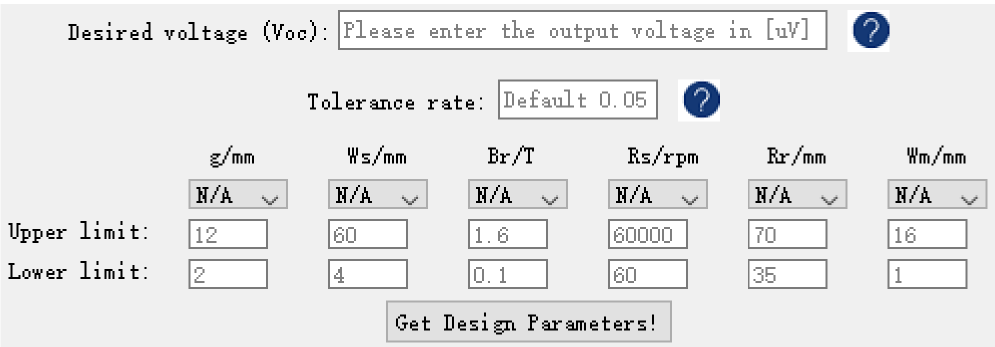

Figure A.3. User interface of the 'Get Design Parameters' function.

There are several optimal settings in this function to help the users refine and customize their design. The users can manually set the ‘Tolerance rate’, which controls the maximum mismatch (in percentage) between the voltage expected from the recommended parameters and the user desired voltage. For example, if 100 μV is specified as the desired voltage and the tolerance is set to 0.05 (by default), then the HTS dynamo with the recommended parameters is expected to output a voltage in the range of 95~105 μV. By default, each of the recommended parameters will locate in the valid domain as stated above, but the users are allowed to manually set the lower and upper limits for each of the design parameters. For instance, if the ‘Lower limit’ and ‘Upper limit’ for the air gap are set to be 4 mm and 6 mm, respectively, then the recommended parameters will end up having an air gap between 4~6 mm. Furthermore, the users can fix any of the parameters by setting the 'Lower limit' and 'Upper limit' both equal to a specific value. Meanwhile, a dropdown menu is provided for each parameter, where the most typical values can be easily found and chosen.

Discussions

The predefined valid domain for each parameter has been chosen carefully, for which it is believed to cover the common design demand of an HTS dynamo in most situations, so the users are not encouraged to break any of the predefined valid domains. In the 'Get V_{oc}' function, the input value for each of the design parameters must strictly lie in the valid domain as defined above, in order to guarantee the users with results as accurate and reliable as possible. However, considering that the aim of the 'Get Design Parameters' function is to provide rough and quick guide for the users to initialize their potential designs, both the lower and upper limits are allowed to break the predefined valid domain limits, and thus fully unlock this function with possible trade-off in accuracy. The judgement of whether this trade-off is worthwhile is left to the users, who know their own design requirements best.

Mathematically, predicting the output voltage by specifying the input design parameters and providing design parameters by specifying the output voltage are inverse problems. Nevertheless, it should be noted that both the 'Get V_{oc}' and 'Get Design Parameters' functions rely on the same principle of the DNN model, which is to predict the output voltage by giving the input design parameters. The 'Get Design Parameters' function is achieved by the following procedure: firstly, a certain number of input parameters will be selected based on the conditions set by the users, and fed into the DNN model, after which the output voltage of each set of input parameters will be computed and compared with the desired voltage; then, the parameters with an output voltage that is close enough, defined by the tolerance rate, to the desired voltage will be reserved and produced as the recommended parameters.

It was found in our experiments that parameters in the 'Extreme Conflict Scenario' will likely trigger relatively large errors. The 'Extreme Conflict Scenario' is defined as: given one set of parameters, there are two (or more) parameters that are close to the edge of their valid domain and expected to have converse impacts on the output voltage. This is an example of the ‘Extreme Conflict Scenario’: the air gap is set to be 2 mm (the minimum value in the valid domain of air gap), which is expected to result in a very high output voltage; while the width of the magnet is set to be 1 mm (the minimum value in the valid domain of magnet width), which is expected to result in a very low output voltage. Careful attention is advised, if users are dealing with parameters in the ‘Extreme Conflict Scenario’ with this application.

The application with all its associated files has been made public in [229], and can be freely downloaded and accessed there.

Reference

[1] IEA. "World Energy Balances 2022," https://www.iea.org/data-and-statistics/data-product/world-energy-balances.

[2] M. D. Aminu, S. A. Nabavi, C. A. Rochelle *et al.*, “A review of developments in carbon dioxide storage,” *Applied Energy,* vol. 208, pp. 1389-1419, 2017.

[3] Z. Zhang, S.-Y. Pan, H. Li *et al.*, “Recent advances in carbon dioxide utilization,” *Renewable and sustainable energy reviews,* vol. 125, pp. 109799, 2020.

[4] V. Grewe, A. Gangoli Rao, T. Grönstedt *et al.*, “Evaluating the climate impact of aviation emission scenarios towards the Paris agreement including COVID-19 effects,” *Nature Communications,* vol. 12, no. 1, pp. 3841, 2021.

[5] A. Krein, and G. Williams, “Flightpath 2050: Europe’s vision for aeronautics,” *Innovation for Sustainable Aviation in a Global Environment: Proceedings of the Sixth European Aeronautics Days, Madrid,* vol. 30, 2012.

[6] J. K. Nøland, M. Leandro, J. A. Suul *et al.*, “High-power machines and starter-generator topologies for more electric aircraft: A technology outlook,” *IEEE access,* vol. 8, pp. 130104-130123, 2020.

[7] A. W. Schäfer, S. R. Barrett, K. Doyme *et al.*, “Technological, economic and environmental prospects of all-electric aircraft,” *Nature Energy,* vol. 4, no. 2, pp. 160-166, 2019.

[8] IEA. "Wind Electricity," https://www.iea.org/reports/wind-electricity.

[9] H. Chen, Y. Zuo, K. Chau *et al.*, “Modern electric machines and drives for wind power generation: A review of opportunities and challenges,” *IET Renewable Power Generation,* vol. 15, no. 9, pp. 1864-1887, 2021.

[10] M. Tinkham, *Introduction to superconductivity*: Courier Corporation, 2004.

[11] J. H. Durrell, A. R. Dennis, J. Jaroszynski *et al.*, “A trapped field of 17.6 T in melt-processed, bulk Gd-Ba-Cu-O reinforced with shrink-fit steel,” *Superconductor Science and Technology,* vol. 27, no. 8, pp. 082001, 2014.

[12] A. Patel, A. Baskys, T. Mitchell-Williams *et al.*, “A trapped field of 17.7 T in a stack of high temperature superconducting tape,” *Superconductor Science and Technology,* vol. 31, no. 9, pp. 09LT01, 2018.

[13] A. Patel, V. Climente-Alarcon, A. Baskys *et al.*, "Design considerations for fully superconducting synchronous motors aimed at future electric aircraft." pp. 1-6.

[14] D. Dew-Hughes, “Model for flux creep in high Tc superconductors,” *Cryogenics,* vol. 28, no. 10, pp. 674-677, 1988.

[15] D. Van Delft, and P. Kes, “The discovery of superconductivity,” *Physics Today,* vol. 63, no. 9, pp. 38-43, 2010.

[16] J. C. Gallop, *SQUIDs, the Josephson effects and superconducting electronics*: CRC Press, 2017.

[17] M. Van Camp, O. Francis, and T. Lecocq, “Recording Belgium's Gravitational History,” *Eos*, 2017.

[18] M. Van Camp, O. de Viron, A. Watlet *et al.*, “Geophysics from terrestrial time‐variable gravity measurements,” *Reviews of Geophysics,* vol. 55, no. 4, pp. 938-992, 2017.

[19] W. Meissner, and R. Ochsenfeld, “Ein neuer effekt bei eintritt der supraleitfähigkeit,” *Naturwissenschaften,* vol. 21, no. 44, pp. 787-788, 1933.

[20] L. N. Cooper, “Bound electron pairs in a degenerate Fermi gas,” *Physical Review,* vol. 104, no. 4, pp. 1189, 1956.

[21] J. R. Clem, R. Huebener, and D. Gallus, “Gibbs free-energy barrier against irreversible magnetic flux entry into a superconductor,” *Journal of Low Temperature Physics,* vol. 12, pp. 449-477, 1973.

[22] J. G. Bednorz, and K. A. Müller, “Possible highT c superconductivity in the Ba− La− Cu− O system,” *Zeitschrift für Physik B Condensed Matter,* vol. 64, no. 2, pp. 189-193, 1986.

[23] Wikipedia, "Timeline of Superconductivity from 1900 to 2015," p. https://en.wikipedia.org/wiki/File:Timeline_of_Superconductivity_from_1900_to_2015.svg#metadata.

[24] H. Zhang, Z. Wen, F. Grilli *et al.*, “Alternating current loss of superconductors applied to superconducting electrical machines,” *Energies,* vol. 14, no. 8, pp. 2234, 2021.

[25] A. A. Abrikosov, “On the magnetic properties of superconductors of the second group,” *Soviet Physics-JETP,* vol. 5, pp. 1174-1182, 1957.
[26] C. P. Bean, “Magnetization of hard superconductors,” *Physical review letters,* vol. 8, no. 6, pp. 250, 1962.
[27] C. P. Bean, “Magnetization of high-field superconductors,” *Reviews of modern physics,* vol. 36, no. 1, pp. 31, 1964.
[28] Y. Kim, C. Hempstead, and A. Strnad, “Critical persistent currents in hard superconductors,” *Physical Review Letters,* vol. 9, no. 7, pp. 306, 1962.
[29] Y. Kim, C. Hempstead, and A. Strnad, “Magnetization and critical supercurrents,” *Physical Review,* vol. 129, no. 2, pp. 528, 1963.
[30] F. Grilli, E. Pardo, A. Stenvall *et al.*, “Computation of losses in HTS under the action of varying magnetic fields and currents,” *IEEE Transactions on Applied Superconductivity,* vol. 24, no. 1, pp. 78-110, 2013.
[31] W. K. Chan, P. J. Masson, C. Luongo *et al.*, “Three-dimensional micrometer-scale modeling of quenching in high-aspect-ratio YBa2Cu3O7-δ coated conductor tapes—part I: model development and validation,” *IEEE Transactions on Applied Superconductivity,* vol. 20, no. 6, pp. 2370, 2010.
[32] W. K. Chan, and J. Schwartz, “A Hierarchical Three-Dimensional Multiscale Electro–Magneto–Thermal Model of Quenching in $\hbox {REBa} _ {2}\hbox {Cu} _ {3}\hbox {O} _ {7-\delta} $ Coated-Conductor-Based Coils,” *IEEE transactions on applied superconductivity,* vol. 22, no. 5, pp. 4706010-4706010, 2012.
[33] H. Fujishiro, and T. Naito, “Simulation of temperature and magnetic field distribution in superconducting bulk during pulsed field magnetization,” *Superconductor Science and Technology,* vol. 23, no. 10, pp. 105021, 2010.
[34] P. Gao, W.-K. Chan, X. Wang *et al.*, “Stress, strain and electromechanical analyses of (RE) Ba2Cu3Ox conductors using three-dimensional/two-dimensional mixed-dimensional modeling: fabrication, cooling and tensile behavior,” *Superconductor Science and Technology,* vol. 33, no. 4, pp. 044015, 2020.
[35] M. Oomen, J. Rieger, M. Leghissa *et al.*, “Dynamic resistance in a slab-like superconductor with Jc (B) dependence,” *Superconductor science and technology,* vol. 12, no. 6, pp. 382, 1999.
[36] M. D. Ainslie, “Transport AC loss in high temperature superconducting coils,” University of Cambridge, 2012.
[37] E. H. Brandt, and M. Indenbom, “Type-II-superconductor strip with current in a perpendicular magnetic field,” *Physical review B,* vol. 48, no. 17, pp. 12893, 1993.
[38] M. Halse, “AC face field losses in a type II superconductor,” *Journal of Physics D: Applied Physics,* vol. 3, no. 5, pp. 717, 1970.
[39] E. Zeldov, J. R. Clem, M. McElfresh *et al.*, “Magnetization and transport currents in thin superconducting films,” *Physical Review B,* vol. 49, no. 14, pp. 9802, 1994.
[40] W. Norris, “Calculation of hysteresis losses in hard superconductors carrying ac: isolated conductors and edges of thin sheets,” *Journal of Physics D: Applied Physics,* vol. 3, no. 4, pp. 489, 1970.
[41] S. Farinon, P. Fabbricatore, F. Grilli *et al.*, “Applicability of the adaptive resistivity method to describe the critical state of complex superconducting systems,” *Journal of superconductivity and novel magnetism,* vol. 25, no. 7, pp. 2343-2350, 2012.
[42] G. P. Mikitik, Y. Mawatari, A. T. Wan *et al.*, “Analytical methods and formulas for modeling high temperature superconductors,” *IEEE Transactions on Applied Superconductivity,* vol. 23, no. 2, pp. 8001920-8001920, 2013.
[43] Y. Mawatari, “Critical state of superconducting strip array systems in perpendicular magnetic fields,” *IEEE transactions on applied superconductivity,* vol. 7, no. 2, pp. 1216-1219, 1997.
[44] Y. Mawatari, “Critical state of periodically arranged superconducting-strip lines in perpendicular fields,” *Physical Review B,* vol. 54, no. 18, pp. 13215, 1996.
[45] H. Weijers, U. Trociewitz, W. Markiewicz *et al.*, “High field magnets with HTS conductors,” *IEEE transactions on applied superconductivity,* vol. 20, no. 3, pp. 576-582, 2010.
[46] S. Hahn, D. K. Park, J. Voccio *et al.*, “No-Insulation (NI) HTS Inserts for $> $1 GHz LTS/HTS NMR Magnets,” *IEEE transactions on applied superconductivity,* vol. 22, no. 3, pp. 4302405-4302405, 2011.

[47] A. B. Abrahamsen, N. Mijatovic, E. Seiler *et al.*, "Superconducting wind turbine generators," *Superconductor Science and Technology,* vol. 23, no. 3, pp. 034019, 2010.

[48] K. Sivasubramaniam, T. Zhang, M. Lokhandwalla *et al.*, "Development of a high speed HTS generator for airborne applications," *IEEE Transactions on applied superconductivity,* vol. 19, no. 3, pp. 1656-1661, 2009.

[49] M. Miki, S. Tokura, H. Hayakawa *et al.*, "Development of a synchronous motor with Gd–Ba–Cu–O bulk superconductors as pole-field magnets for propulsion system," *Superconductor Science and Technology,* vol. 19, no. 7, pp. S494, 2006.

[50] K. Umemoto, K. Aizawa, M. Yokoyama *et al.*, "Development of 1 MW-class HTS motor for podded ship propulsion system." p. 032060.

[51] W. Nick, M. Frank, G. Klaus *et al.*, "Operational experience with the world's first 3600 rpm 4 MVA generator at Siemens," *IEEE transactions on applied superconductivity,* vol. 17, no. 2, pp. 2030-2033, 2007.

[52] H.-J. Sung, G.-H. Kim, K. Kim *et al.*, "Practical design of a 10 MW superconducting wind power generator considering weight issue," *IEEE transactions on applied superconductivity,* vol. 23, no. 3, pp. 5201805-5201805, 2013.

[53] H.-J. Sung, G.-H. Kim, K. Kim *et al.*, "Design and comparative analysis of 10 MW class superconducting wind power generators according to different types of superconducting wires," *Physica C: Superconductivity,* vol. 494, pp. 255-261, 2013.

[54] M. Filipenko, L. Kühn, T. Gleixner *et al.*, "Concept design of a high power superconducting generator for future hybrid-electric aircraft," *Superconductor Science and Technology,* vol. 33, no. 5, pp. 054002, 2020.

[55] M. Boll, M. Corduan, S. Biser *et al.*, "A holistic system approach for short range passenger aircraft with cryogenic propulsion system," *Superconductor Science and Technology,* vol. 33, no. 4, pp. 044014, 2020.

[56] Y. Lvovsky, E. W. Stautner, and T. Zhang, "Novel technologies and configurations of superconducting magnets for MRI," *Superconductor Science and Technology,* vol. 26, no. 9, pp. 093001, 2013.

[57] V. Corato, T. Bagni, M. Biancolini *et al.*, "Progress in the design of the superconducting magnets for the EU DEMO," *Fusion engineering and design,* vol. 136, pp. 1597-1604, 2018.

[58] M. Zhang, W. Yuan, D. K. Hilton *et al.*, "Study of second-generation high-temperature superconducting magnets: the self-field screening effect," *Superconductor Science and Technology,* vol. 27, no. 9, pp. 095010, 2014.

[59] H. Khodzhibagiyan, N. Agapov, P. Akishin *et al.*, "Superconducting magnets for the NICA accelerator collider complex," *IEEE transactions on applied superconductivity,* vol. 24, no. 3, pp. 1-4, 2013.

[60] L. Rossi, "Superconducting magnets for the LHC main lattice," *IEEE transactions on applied superconductivity,* vol. 14, no. 2, pp. 153-158, 2004.

[61] K. Yokoyama, T. Oka, H. Okada *et al.*, "Solid-liquid magnetic separation using bulk superconducting magnets," *IEEE Transactions on applied superconductivity,* vol. 13, no. 2, pp. 1592-1595, 2003.

[62] M. Tomita, and M. Murakami, "High-temperature superconductor bulk magnets that can trap magnetic fields of over 17 tesla at 29 K," *Nature,* vol. 421, no. 6922, pp. 517-520, 2003.

[63] J. Toth, and S. Bole, "Design, construction, and first testing of a 41.5 T all-resistive magnet at the NHMFL in Tallahassee," *IEEE Transactions on Applied Superconductivity,* vol. 28, no. 3, pp. 1-4, 2017.

[64] Y. Iijima, N. Kaneko, S. Hanyu *et al.*, "Development of IBAD/PLD process for long length Y-123 conductors in Fujikura," *Physica C: Superconductivity and its applications,* vol. 445, pp. 509-514, 2006.

[65] H. C. Freyhardt, "YBaCuO and REBaCuO HTS for applications," *International journal of applied ceramic technology,* vol. 4, no. 3, pp. 203-216, 2007.

[66] Y. Shiohara, M. Yoshizumi, T. Izumi *et al.*, "Present status and future prospect of coated conductor development and its application in Japan," *Superconductor Science and Technology,* vol. 21, no. 3, pp. 034002, 2008.

[67] M. Sugano, K. Osamura, W. Prusseit *et al.*, "Reversible strain dependence of critical current in 100 A class coated conductors," *IEEE transactions on applied superconductivity,* vol. 15, no. 2, pp. 3581-3584, 2005.

[68] J.-H. Lee, H. Lee, J.-W. Lee *et al.*, "RCE-DR, a novel process for coated conductor fabrication with high performance," *Superconductor Science and Technology,* vol. 27, no. 4, pp. 044018, 2014.
[69] A. Ballarino, "Current leads, links and buses," *arXiv preprint arXiv:1501.07166*, 2015.
[70] L. Wegener, "Status of Wendelstein 7-X construction," *Fusion Engineering and Design,* vol. 84, no. 2-6, pp. 106-112, 2009.
[71] A. Ballarino, "Current leads for the LHC magnet system," *IEEE transactions on applied superconductivity,* vol. 12, no. 1, pp. 1275-1280, 2002.
[72] C. W. Bumby, R. A. Badcock, H.-J. Sung *et al.*, "Development of a brushless HTS exciter for a 10 kW HTS synchronous generator," *Superconductor Science and Technology,* vol. 29, no. 2, pp. 024008, 2016.
[73] H. Sung, R. Badcock, Z. Jiang *et al.*, "Design and heat load analysis of a 12 MW HTS wind power generator module employing a brushless HTS exciter," *IEEE Transactions on Applied Superconductivity,* vol. 26, no. 4, pp. 1-4, 2016.
[74] H. Jeon, J. Lee, S. Han *et al.*, "Methods for increasing the saturation current and charging speed of a rotary HTS flux-pump to charge the field coil of a synchronous motor," *IEEE Transactions on Applied Superconductivity,* vol. 28, no. 3, pp. 1-5, 2018.
[75] S. S. Kalsi, *Applications of high temperature superconductors to electric power equipment*: John Wiley & Sons, 2011.
[76] M. Feigel'man, V. Geshkenbein, and V. Vinokur, "Flux creep and current relaxation in high-T c superconductors," *Physical Review B,* vol. 43, no. 7, pp. 6263, 1991.
[77] A. F. Hildebrandt, H. Wahlquist, and D. D. Elleman, "Configurations of superconducting shells required for near critical uniform magnetic fields," *Journal of Applied Physics,* vol. 33, no. 5, pp. 1798-1800, 1962.
[78] A. F. Hildebrandt, D. D. Elleman, F. C. Whitmore *et al.*, "Some Experimental Consequences of Flux Conservation within Multiply‐Connected Superconductors," *Journal of Applied Physics,* vol. 33, no. 7, pp. 2375-2377, 1962.
[79] H. Van Beelen, M. AJPT Arnold, H. Sypkens *et al.*, "A 25 000 gauss, 175 amperes Nb-25% Zr wire magnet fed by a flux pump," *Physics letters,* vol. 7, no. 3, 1963.
[80] A. Rose-Innes, "A superconducting magnetic flux compressor," *Cryogenics,* vol. 13, no. 2, pp. 103-105, 1973.
[81] J. Van Suchtelen, J. Volger, and D. Van Houwelingen, "The principle and performance of a superconducting dynamo," *Cryogenics,* vol. 5, no. 5, pp. 256-266, 1965.
[82] H. Van Beelen, J. V. B. Houckgeest, R. D. B. Ouboter *et al.*, "Remarks on a moving-flux experiment in superconducting sheets," *Physica,* vol. 36, no. 1, pp. 107-117, 1967.
[83] D. Atherton, "High‐Efficiency Superconducting Homopolar dc Generators," *Journal of Applied Physics,* vol. 39, no. 6, pp. 2639-2639, 1968.
[84] H. Van Beelen, M. De Langen, and C. Kerkdijk, "Comments on the efficiency of flux pumping into superconducting circuits," *Physica,* vol. 42, no. 2, pp. 265-276, 1969.
[85] J. Purcell, and E. Payne, "Superconducting rectifiers," *Advances in Cryogenic Engineering*, pp. 149-153: Springer, 1961.
[86] C. Hempstead, Y. Kim, and A. Strnad, "Inductive behavior of superconducting magnets," *Journal of Applied Physics,* vol. 34, no. 11, pp. 3226-3236, 1963.
[87] T. Buchhold, "Superconductive power supply and its application for electrical flux pumping," *Cryogenics,* vol. 4, no. 4, pp. 212-217, 1964.
[88] T. Coombs, Z. Hong, Y. Yan *et al.*, "The next generation of superconducting permanent magnets: The flux pumping method," *IEEE transactions on applied superconductivity,* vol. 19, no. 3, pp. 2169-2173, 2009.
[89] T. Coombs, Z. Hong, and X. Zhu, "A thermally actuated superconducting flux pump," *Physica C: Superconductivity,* vol. 468, no. 3, pp. 153-159, 2008.
[90] Y. Yan, Q. Li, and T. Coombs, "Thermally actuated magnetization flux pump in single-grain YBCO bulk," *Superconductor Science and Technology,* vol. 22, no. 10, pp. 105011, 2009.
[91] L. Van de Klundert, and H. H. ten Kate, "Fully superconducting rectifiers and fluxpumps Part 1: Realized methods for pumping flux," *Cryogenics,* vol. 21, no. 4, pp. 195-206, 1981.

[92] L. van de Klundert, and H. ten Kate, "On fully superconducting rectifiers and fluxpumps. A review. Part 2: Commutation modes, characteristics and switches," *Cryogenics,* vol. 21, no. 5, pp. 267-277, 1981.

[93] G. Mulder, H. Ten Kate, H. Krooshoop *et al.*, "Development of a thermally switched superconducting rectifier for 100 kA," *IEEE transactions on magnetics,* vol. 27, no. 2, pp. 2333-2336, 1991.

[94] M. P. Oomen, M. Leghissa, G. Ries *et al.*, "HTS flux pump for cryogen-free HTS magnets," *IEEE transactions on applied superconductivity,* vol. 15, no. 2, pp. 1465-1468, 2005.

[95] C. Hoffmann, D. Pooke, and A. D. Caplin, "Flux pump for HTS magnets," *IEEE transactions on applied superconductivity,* vol. 21, no. 3, pp. 1628-1631, 2010.

[96] C. Hoffmann, R. Walsh, E. Karrer-Mueller *et al.*, "Design parameters for an HTS flux pump," *Physics Procedia,* vol. 36, pp. 1324-1329, 2012.

[97] C. W. Bumby, A. E. Pantoja, H.-J. Sung *et al.*, "Through-wall excitation of a magnet coil by an external-rotor HTS flux pump," *IEEE Transactions on Applied Superconductivity,* vol. 26, no. 4, pp. 1-5, 2016.

[98] J. G. Storey, A. E. Pantoja, Z. Jiang *et al.*, "Impact of annular yoke geometry on performance of a dynamo-type HTS flux pump," *IEEE Transactions on Applied Superconductivity,* vol. 28, no. 3, pp. 1-6, 2018.

[99] A. E. Pantoja, J. G. Storey, R. A. Badcock *et al.*, "Output during continuous frequency ramping of a dynamo-type HTS flux pump," *IEEE Transactions on Applied Superconductivity,* vol. 28, no. 3, pp. 1-5, 2018.

[100] J. G. Storey, A. E. Pantoja, Z. Jiang *et al.*, "Optimizing rotor speed and geometry for an externally mounted HTS dynamo," *IEEE Transactions on Applied Superconductivity,* vol. 29, no. 5, pp. 1-5, 2019.

[101] Z. Jiang, C. W. Bumby, R. A. Badcock *et al.*, "Impact of flux gap upon dynamic resistance of a rotating HTS flux pump," *Superconductor Science and Technology,* vol. 28, no. 11, pp. 115008, 2015.

[102] C. W. Bumby, S. Phang, A. E. Pantoja *et al.*, "Frequency dependent behavior of a dynamo-type HTS flux pump," *IEEE Transactions on Applied Superconductivity,* vol. 27, no. 4, pp. 1-5, 2016.

[103] A. E. Pantoja, Z. Jiang, R. A. Badcock *et al.*, "Impact of stator wire width on output of a dynamo-type HTS flux pump," *IEEE Transactions on Applied Superconductivity,* vol. 26, no. 8, pp. 1-8, 2016.

[104] R. A. Badcock, S. Phang, A. E. Pantoja *et al.*, "Impact of magnet geometry on output of a dynamo-type HTS flux pump," *IEEE Transactions on Applied Superconductivity,* vol. 27, no. 4, pp. 1-5, 2016.

[105] H. Zhang, M. Yao, K. Kails *et al.*, "Modelling of electromagnetic loss in HTS coated conductors over a wide frequency band," *Superconductor Science and Technology,* vol. 33, no. 2, pp. 025004, 2020.

[106] H. Zhang, H. Chen, Z. Jiang *et al.*, "A full-range formulation for dynamic loss of high-temperature superconductor coated conductors," *Superconductor Science and Technology,* vol. 33, no. 5, pp. 05LT01, 2020.

[107] L. Fu, K. Matsuda, and T. Coombs, "Linear flux pump device applied to HTS magnets: further characteristics on wave profile, number of poles, and control of saturated current," *IEEE Transactions on Applied Superconductivity,* vol. 26, no. 3, pp. 1-4, 2016.

[108] L. Fu, K. Matsuda, T. Lecrevisse *et al.*, "A flux pumping method applied to the magnetization of YBCO superconducting coils: frequency, amplitude and waveform characteristics," *Superconductor Science and Technology,* vol. 29, no. 4, pp. 04LT01, 2016.

[109] L. Fu, K. Matsuda, M. Baghdadi *et al.*, "Linear flux pump device applied to high temperature superconducting (HTS) magnets," *IEEE Transactions on Applied Superconductivity,* vol. 25, no. 3, pp. 1-4, 2015.

[110] L. Fu, K. Matsuda, B. Shen *et al.*, "Charging an HTS Coil: Flux Pump With an HTS Square Bridge," *IEEE Transactions on Applied Superconductivity,* vol. 31, no. 8, pp. 1-5, 2021.

[111] T. Coombs, J.-F. Fagnard, and K. Matsuda, "Magnetization of 2-G coils and artificial bulks," *IEEE Transactions on Applied Superconductivity,* vol. 24, no. 5, pp. 1-5, 2014.

[112] J. Geng, K. Matsuda, L. Fu *et al.*, "Origin of dc voltage in type II superconducting flux pumps: field, field rate of change, and current density dependence of resistivity," *Journal of Physics D: Applied Physics,* vol. 49, no. 11, pp. 11LT01, 2016.

[113] C. Bumby, Z. Jiang, J. Storey *et al.*, "Anomalous open-circuit voltage from a high-T c superconducting dynamo," *Applied Physics Letters,* vol. 108, no. 12, pp. 122601, 2016.

[114] R. Mataira, M. Ainslie, R. Badcock *et al.*, "Origin of the DC output voltage from a high-Tc superconducting dynamo," *Applied Physics Letters,* vol. 114, no. 16, pp. 162601, 2019.

[115] R. Mataira, M. Ainslie, A. Pantoja *et al.*, "Mechanism of the high-T c superconducting dynamo: models and experiment," *Physical Review Applied,* vol. 14, no. 2, pp. 024012, 2020.

[116] W. Wang, and T. Coombs, "Macroscopic magnetic coupling effect: The physical origination of a high-temperature superconducting flux pump," *Physical Review Applied,* vol. 9, no. 4, pp. 044022, 2018.

[117] J. Wei, W. Wang, Z. Yang *et al.*, "Build Charging Database of Linear-Motor Type Flux Pump and Analyze the Influence of DC-Bias Field Using Fixed Step Size Search Algorithm," *IEEE Transactions on Applied Superconductivity,* vol. 31, no. 8, pp. 1-5, 2021.

[118] K. Kajikawa, T. Hayashi, R. Yoshida *et al.*, "Numerical evaluation of AC losses in HTS wires with 2D FEM formulated by self magnetic field," *IEEE transactions on applied superconductivity,* vol. 13, no. 2, pp. 3630-3633, 2003.

[119] Z. Hong, A. Campbell, and T. Coombs, "Numerical solution of critical state in superconductivity by finite element software," *Superconductor Science and Technology,* vol. 19, no. 12, pp. 1246, 2006.

[120] R. Brambilla, F. Grilli, and L. Martini, "Development of an edge-element model for AC loss computation of high-temperature superconductors," *Superconductor Science and Technology,* vol. 20, no. 1, pp. 16, 2006.

[121] M. D. Ainslie, W. Yuan, Z. Hong *et al.*, "Modeling and electrical measurement of transport AC loss in HTS-based superconducting coils for electric machines," *IEEE transactions on applied superconductivity,* vol. 21, no. 3, pp. 3265-3268, 2010.

[122] M. D. Ainslie, T. J. Flack, and A. M. Campbell, "Calculating transport AC losses in stacks of high temperature superconductor coated conductors with magnetic substrates using FEM," *Physica C: Superconductivity,* vol. 472, no. 1, pp. 50-56, 2012.

[123] R. Brambilla, F. Grilli, L. Martini *et al.*, "A finite-element method framework for modeling rotating machines with superconducting windings," *IEEE Transactions on Applied Superconductivity,* vol. 28, no. 5, pp. 1-11, 2018.

[124] B. M. O. Santos, F. J. M. Dias, F. Sass *et al.*, "Simulation of superconducting machine with stacks of coated conductors using hybrid ah formulation," *IEEE Transactions on Applied Superconductivity,* vol. 30, no. 6, pp. 1-9, 2020.

[125] F. Liang, S. Venuturumilli, H. Zhang *et al.*, "A finite element model for simulating second generation high temperature superconducting coils/stacks with large number of turns," *Journal of Applied Physics,* vol. 122, no. 4, pp. 043903, 2017.

[126] H. Zhang, M. Zhang, and W. Yuan, "An efficient 3D finite element method model based on the T–A formulation for superconducting coated conductors," *Superconductor Science and Technology,* vol. 30, no. 2, pp. 024005, 2016.

[127] E. Berrospe-Juarez, V. M. Zermeño, F. Trillaud *et al.*, "Real-time simulation of large-scale HTS systems: Multi-scale and homogeneous models using the T–A formulation," *Superconductor Science and Technology,* vol. 32, no. 6, pp. 065003, 2019.

[128] F. Grilli, E. Pardo, A. Morandi *et al.*, "Electromagnetic modeling of superconductors with commercial software: Possibilities with two vector potential-based formulations," *IEEE Transactions on Applied Superconductivity,* vol. 31, no. 1, pp. 1-9, 2020.

[129] T. Benkel, M. Lao, Y. Liu *et al.*, "T–A-formulation to model electrical machines with HTS coated conductor coils," *IEEE Transactions on Applied Superconductivity,* vol. 30, no. 6, pp. 1-7, 2020.

[130] R. Mataira, M. D. Ainslie, R. Badcock *et al.*, "Modeling of Stator Versus Magnet Width Effects in High-$ T_c $ Superconducting Dynamos," *IEEE Transactions on Applied Superconductivity,* vol. 30, no. 4, pp. 1-6, 2020.

[131] L. Quéval, K. Liu, W. Yang *et al.*, "Superconducting magnetic bearings simulation using an H-formulation finite element model," *Superconductor Science and Technology,* vol. 31, no. 8, pp. 084001, 2018.

[132] M. D. Ainslie, L. Quéval, R. C. Mataira *et al.*, “Modelling the frequency dependence of the open-circuit voltage of a high-T c superconducting dynamo,” *IEEE Transactions on Applied Superconductivity,* vol. 31, no. 5, pp. 1-7, 2021.

[133] E. Pardo, J. Šouc, and L. Frolek, “Electromagnetic modelling of superconductors with a smooth current–voltage relation: variational principle and coils from a few turns to large magnets,” *Superconductor Science and Technology,* vol. 28, no. 4, pp. 044003, 2015.

[134] E. Pardo, and M. Kapolka, “3D computation of non-linear eddy currents: Variational method and superconducting cubic bulk,” *Journal of Computational Physics,* vol. 344, pp. 339-363, 2017.

[135] R. Brambilla, F. Grilli, L. Martini *et al.*, “Integral equations for the current density in thin conductors and their solution by the finite-element method,” *Superconductor Science and Technology,* vol. 21, no. 10, pp. 105008, 2008.

[136] F. Grilli, R. Brambilla, L. F. Martini *et al.*, “Current density distribution in multiple YBCO coated conductors by coupled integral equations,” *IEEE Transactions on applied superconductivity,* vol. 19, no. 3, pp. 2859-2862, 2009.

[137] R. Brambilla, F. Grilli, D. N. Nguyen *et al.*, “AC losses in thin superconductors: the integral equation method applied to stacks and windings,” *Superconductor Science and Technology,* vol. 22, no. 7, pp. 075018, 2009.

[138] A. Morandi, M. Fabbri, P. L. Ribani *et al.*, “The measurement and modeling of the levitation force between single-grain YBCO bulk superconductors and permanent magnets,” *IEEE Transactions on Applied Superconductivity,* vol. 28, no. 5, pp. 1-10, 2018.

[139] M. Fabbri, M. Forzan, S. Lupi *et al.*, “Experimental and numerical analysis of DC induction heating of aluminum billets,” *IEEE Transactions on Magnetics,* vol. 45, no. 1, pp. 192-200, 2009.

[140] E. Perini, G. Giunchi, M. Geri *et al.*, “Experimental and Numerical Investigation of the Levitation Force Between Bulk Permanent Magnet and ${\rm MgB} _ {2} $ Disk,” *IEEE transactions on applied superconductivity,* vol. 19, no. 3, pp. 2124-2128, 2009.

[141] L. Prigozhin, and V. Sokolovsky, “Fast solution of the superconducting dynamo benchmark problem,” *Superconductor Science and Technology,* vol. 34, no. 6, pp. 065006, 2021.

[142] L. Prigozhin, and V. Sokolovsky, “Two-dimensional model of a high-T c superconducting dynamo,” *IEEE Transactions on Applied Superconductivity,* vol. 31, no. 3, pp. 1-7, 2021.

[143] V. Sokolovsky, L. Prigozhin, and A. B. Kozyrev, “Chebyshev spectral method for superconductivity problems,” *Superconductor Science and Technology,* vol. 33, no. 8, pp. 085008, 2020.

[144] M. Ainslie, F. Grilli, L. Quéval *et al.*, “A new benchmark problem for electromagnetic modelling of superconductors: the high-T c superconducting dynamo,” *Superconductor Science and Technology,* vol. 33, no. 10, pp. 105009, 2020.

[145] H. Zhang, P. Machura, K. Kails *et al.*, “Dynamic loss and magnetization loss of HTS coated conductors, stacks, and coils for high-speed synchronous machines,” *Superconductor Science and Technology,* vol. 33, no. 8, pp. 084008, 2020.

[146] A. Ghabeli, E. Pardo, and M. Kapolka, “3D modeling of a superconducting dynamo-type flux pump,” *Scientific Reports,* vol. 11, no. 1, pp. 1-12, 2021.

[147] A. Ghabeli, M. Ainslie, E. Pardo *et al.*, “Modeling the charging process of a coil by an HTS dynamo-type flux pump,” *Superconductor Science and Technology,* vol. 34, no. 8, pp. 084002, 2021.

[148] J. Geng, K. Matsuda, L. Fu *et al.*, “Operational research on a high-Tc rectifier-type superconducting flux pump,” *Superconductor Science and Technology,* vol. 29, no. 3, pp. 035015, 2016.

[149] J. Geng, and T. Coombs, “Mechanism of a high-Tc superconducting flux pump: Using alternating magnetic field to trigger flux flow,” *Applied Physics Letters,* vol. 107, no. 14, pp. 142601, 2015.

[150] J. Geng, T. Painter, P. Long *et al.*, “A kilo-ampere level HTS flux pump,” *Superconductor Science and Technology,* vol. 32, no. 7, pp. 074004, 2019.

[151] H. Zhang, J. Geng, and T. Coombs, “Magnetizing high-Tc superconducting coated conductor stacks using a transformer–rectifier flux pumping method,” *Superconductor Science and Technology,* vol. 31, no. 10, pp. 105007, 2018.

[152] P. Zhou, G. Ma, Y. Deng *et al.*, "A contactless self-regulating HTS flux pump," *IEEE Transactions on Applied Superconductivity,* vol. 30, no. 4, pp. 1-6, 2020.

[153] J. Geng, C. W. Bumby, and R. A. Badcock, "Maximising the current output from a self-switching kA-class rectifier flux pump," *Superconductor Science and Technology,* vol. 33, no. 4, pp. 045005, 2020.

[154] Y. Zhai, P. Zhou, J. Li *et al.*, "Performance Investigation of Contactless Self-Regulating HTS Flux Pump," *IEEE Transactions on Applied Superconductivity,* vol. 31, no. 5, pp. 1-5, 2021.

[155] C. Li, J. Geng, B. Shen *et al.*, "Investigation on the transformer-rectifier flux pump for high field magnets," *IEEE Transactions on Applied Superconductivity,* vol. 29, no. 5, pp. 1-5, 2019.

[156] Z. Jiang, K. Hamilton, N. Amemiya *et al.*, "Dynamic resistance of a high-Tc superconducting flux pump," *Applied Physics Letters,* vol. 105, no. 11, pp. 112601, 2014.

[157] H. Zhang, C. Hao, Y. Xin *et al.*, "Demarcation currents and corner field for dynamic resistance of HTS-coated conductors," *IEEE Transactions on Applied Superconductivity,* vol. 30, no. 8, pp. 1-5, 2020.

[158] J. Geng, and T. Coombs, "An HTS flux pump operated by directly driving a superconductor into flux flow region in the E–J curve," *Superconductor Science and Technology,* vol. 29, no. 9, pp. 095004, 2016.

[159] J. Geng, and T. A. Coombs, "Modeling methodology for a HTS flux pump using a 2D H-formulation," *Superconductor Science and Technology,* vol. 31, no. 12, pp. 125015, 2018.

[160] C. Li, J. Yang, B. Shen *et al.*, "A HTS flux pump simulation methodology based on the electrical circuit," *IEEE Transactions on Applied Superconductivity,* vol. 30, no. 4, pp. 1-5, 2020.

[161] Z. Bai, S. Ding, C. Li *et al.*, "A newly developed pulse-type microampere magnetic flux pump," *IEEE Transactions on Applied Superconductivity,* vol. 20, no. 3, pp. 1667-1670, 2010.

[162] Z. Bai, G. Yan, C. Wu *et al.*, "A novel high temperature superconducting magnetic flux pump for MRI magnets," *Cryogenics,* vol. 50, no. 10, pp. 688-692, 2010.

[163] Z. Bai, C. Chen, Y. Wu *et al.*, "Effect of various pulse wave forms for pulse-type magnetic flux pump," *Cryogenics,* vol. 51, no. 9, pp. 530-533, 2011.

[164] Z. Bai, C. Ma, C. Chen *et al.*, "Study on the excitation of a Bi-2223 small superconducting coil by a pulse-type magnetic flux pump," *IEEE Transactions on Applied Superconductivity,* vol. 27, no. 2, pp. 1-5, 2017.

[165] Z. Bai, X. Cui, and C. Ma, "Characteristics of Pumping Current in a YBCO Coil by a Pulse-Type Magnetic Flux Pump," *IEEE Transactions on Applied Superconductivity,* vol. 31, no. 4, pp. 1-6, 2021.

[166] W. Wang, Y. Lei, S. Huang *et al.*, "Charging 2G HTS double pancake coils with a wireless superconducting DC p ower supply for persistent current operation," *IEEE Transactions on Applied Superconductivity,* vol. 28, no. 3, pp. 1-4, 2018.

[167] Y. Zhang, W. Wang, H. Ye *et al.*, "Compact linear-motor type flux pumps with different wavelengths for high-temperature superconducting magnets," *IEEE Transactions on Applied Superconductivity,* vol. 30, no. 4, pp. 1-5, 2020.

[168] H. Ye, W. Wang, Y. Zhang *et al.*, "Measuring the output voltage of a linear-motor type flux pump with an insulated HTS coil," *IEEE Transactions on Applied Superconductivity,* vol. 30, no. 4, pp. 1-5, 2020.

[169] H. Ye, W. Wang, Y. Zhang *et al.*, "A Linear-Motor Type HTS Flux Pump With Pumped Current Exceeding 640 A," *IEEE Transactions on Applied Superconductivity,* vol. 31, no. 8, pp. 1-5, 2021.

[170] H. Zhang, T. Yang, W. Li *et al.*, "Origin of the anomalous electromechanical interaction between a moving magnetic dipole and a closed superconducting loop," *Superconductor Science and Technology,* vol. 35, no. 4, pp. 045009, 2022.

[171] J. Gawith, J. Geng, C. Li *et al.*, "A half-bridge HTS transformer–rectifier flux pump with two AC field-controlled switches," *Superconductor Science and Technology,* vol. 31, no. 8, pp. 085002, 2018.

[172] B. Leuw, J. Geng, J. H. Rice *et al.*, "A half-wave superconducting transformer-rectifier flux pump using J c (B) switches," *Superconductor Science and Technology,* vol. 35, no. 3, pp. 035009, 2022.

[173] I. Patel, A. Shah, Y. Öztürk *et al.*, "MATLAB implementation of an HTS transformer-rectifier flux pump using HTS dynamic voltage switches," *IEEE Transactions on Applied Superconductivity,* vol. 32, no. 4, pp. 1-4, 2021.

[174] H.-J. Sung, B.-S. Go, Z. Jiang *et al.*, “Heat loss analysis-based design of a 12 MW wind power generator module having an HTS flux pump exciter,” *Physica C: Superconductivity and its applications,* vol. 530, pp. 133-137, 2016.

[175] H.-J. Sung, B.-S. Go, H. Park *et al.*, “Design, fabrication, and analysis of HTS coils for a 10-kW wind power generator employing a brushless exciter,” *IEEE Transactions on Applied Superconductivity,* vol. 27, no. 4, pp. 1-5, 2017.

[176] O. Tuvdensuren, H. Sung, B. Go *et al.*, "Structural design and heat load analysis of a flux pump-based HTS module coil for a large-scale wind power generator." p. 012084.

[177] S. Kalsi, R. Badcock, K. Hamilton *et al.*, "Homopolar superconducting AC machines, with HTS dynamo driven field coils, for aerospace applications." p. 012028.

[178] J. H. Kim, H. L. Quach, C.-J. Boo *et al.*, “Fabrication and charging test of HTS field windings using HTS contactless rotary excitation device,” *IEEE Transactions on Applied Superconductivity,* vol. 29, no. 5, pp. 1-7, 2019.

[179] J. H. Kim, C. J. Hyeon, H. L. Quach *et al.*, “Design, analysis, and fabrication of salient field-pole for a 1-kW-class HTS rotating machine,” *Cryogenics,* vol. 97, pp. 126-132, 2019.

[180] J. H. Kim, Y. S. Chae, H. L. Quach *et al.*, “Fabrication and performance testing of a 1-kW-class high-temperature superconducting generator with a high-temperature superconducting contactless field exciter*,” *Superconductor Science and Technology,* vol. 33, no. 9, pp. 095003, 2020.

[181] B. J. Parkinson, R. Slade, M. J. Mallett *et al.*, “Development of a cryogen free 1.5 T YBCO HTS magnet for MRI,” *IEEE transactions on applied superconductivity,* vol. 23, no. 3, pp. 4400405-4400405, 2012.

[182] Y. Terao, O. Ozaki, C. Ichihara *et al.*, “Newly designed 3 T MRI magnet wound with Bi-2223 tape conductors,” *IEEE transactions on applied superconductivity,* vol. 23, no. 3, pp. 4400904-4400904, 2013.

[183] B. Parkinson, K. Bouloukakis, and R. Slade, “A compact 3 T all HTS cryogen-free MRI system,” *Superconductor Science and Technology,* vol. 30, no. 12, pp. 125009, 2017.

[184] S. Yokoyama, H. Miura, T. Matsuda *et al.*, “Design and cooling properties of high stable field REBCO superconducting magnet for MRI,” *IEEE Transactions on Applied Superconductivity,* vol. 30, no. 4, pp. 1-4, 2020.

[185] X. Wang, W. Wang, Y. Lei *et al.*, “Electromagnetic design of 1.5 T no-insulation REBCO coil system charged by multiflux pumps for dedicated MRI,” *IEEE Transactions on Applied Superconductivity,* vol. 29, no. 5, pp. 1-5, 2019.

[186] Y. Öztürk, B. Shen, R. Williams *et al.*, “Current status in building a compact and mobile HTS MRI instrument,” *IEEE Transactions on Applied Superconductivity,* vol. 31, no. 5, pp. 1-5, 2021.

[187] S. Hahn, K. Kim, K. Kim *et al.*, “45.5-tesla direct-current magnetic field generated with a high-temperature superconducting magnet,” *Nature,* vol. 570, no. 7762, pp. 496-499, 2019.

[188] J. R. Miller, “The NHMFL 45-T hybrid magnet system: past, present, and future,” *IEEE transactions on applied superconductivity,* vol. 13, no. 2, pp. 1385-1390, 2003.

[189] K. Hamilton, R. Mataira, J. Geng *et al.*, “Practical estimation of HTS dynamo losses,” *IEEE Transactions on Applied Superconductivity,* vol. 30, no. 4, pp. 1-5, 2020.

[190] H. Zhang, M. Yao, Z. Jiang *et al.*, “Dependence of dynamic loss on critical current and n-value of HTS coated conductors,” *IEEE Transactions on Applied Superconductivity,* vol. 29, no. 8, pp. 1-7, 2019.

[191] A. Morandi, G. Russo, M. Fabbri *et al.*, “Energy balance, efficiency and operational limits of the dynamo type flux pump,” *Superconductor Science and Technology*, 2022.

[192] R. M. Walsh, R. Slade, D. Pooke *et al.*, “Characterization of current stability in an HTS NMR system energized by an HTS flux pump,” *IEEE transactions on applied superconductivity,* vol. 24, no. 3, pp. 1-5, 2013.

[193] H. Jeon, J. Lee, S. Han *et al.*, “PID control of an electromagnet-based rotary HTS flux pump for maintaining constant field in HTS synchronous motors,” *IEEE Transactions on Applied Superconductivity,* vol. 28, no. 4, pp. 1-5, 2018.

[194] J. Geng, B. Wang, M. Baghdadi *et al.*, “Feedback control of a rectifier type HTS flux pump: Stabilizing load current with minimized losses,” *IEEE Transactions on Applied Superconductivity,* vol. 27, no. 4, pp. 1-4, 2017.

[195] T. Coombs, “Superconducting flux pumps,” *Journal of Applied Physics,* vol. 125, no. 23, pp. 230902, 2019.

[196] D. Alley, L. Hagen, D. Kuhlmann-Wilsdorf *et al.*, “Automated apparatus for long-term testing of electrical brushes,” *IEEE transactions on components, hybrids, and manufacturing technology,* vol. 14, no. 1, pp. 31-36, 1991.
[197] G. Snitchler, B. Gamble, and S. S. Kalsi, “The performance of a 5 MW high temperature superconductor ship propulsion motor,” *IEEE Transactions on Applied Superconductivity,* vol. 15, no. 2, pp. 2206-2209, 2005.
[198] V. Ruuskanen, M. Niemelä, J. Pyrhönen *et al.*, “Modelling the brushless excitation system for a synchronous machine,” *IET electric power applications,* vol. 3, no. 3, pp. 231-239, 2009.
[199] D. K. Lawson, and T. Dow, “The sparking and wear of high current density electrical brushes,” *Wear,* vol. 102, no. 1-2, pp. 105-125, 1985.
[200] T. Dow, and J. Kannel, “Thermomechanical effects in high current density electrical slip rings,” *Wear,* vol. 79, no. 1, pp. 93-105, 1982.
[201] D. Littler, *Turbines, Generators and Associated Plant: Incorporating Modern Power System Practice*: Elsevier, 2013.
[202] A. Ghabeli, and E. Pardo, “Modeling of airgap influence on DC voltage generation in a dynamo-type flux pump,” *Superconductor Science and Technology,* vol. 33, no. 3, pp. 035008, 2020.
[203] F. Pedregosa, G. Varoquaux, A. Gramfort *et al.*, “Scikit-learn: Machine learning in Python,” *the Journal of machine Learning research,* vol. 12, pp. 2825-2830, 2011.
[204] A. Botchkarev, “Performance metrics (error measures) in machine learning regression, forecasting and prognostics: Properties and typology,” *arXiv preprint arXiv:1809.03006*, 2018.
[205] X. Gao, Y. Asami, and C.-J. F. Chung, “An empirical evaluation of spatial regression models,” *Computers & Geosciences,* vol. 32, no. 8, pp. 1040-1051, 2006.
[206] M. Yazdani-Asrami, M. Taghipour-Gorjikolaie, W. Song *et al.*, “Prediction of nonsinusoidal AC loss of superconducting tapes using artificial Intelligence-based models,” *IEEE Access,* vol. 8, pp. 207287-207297, 2020.
[207] J. Leclerc, L. M. Hell, C. Lorin *et al.*, “Artificial neural networks for AC losses prediction in superconducting round filaments,” *Superconductor Science and Technology,* vol. 29, no. 6, pp. 065008, 2016.
[208] Z. Zhang, L. Ren, Y. Xu *et al.*, “AC loss prediction model of a 150 kJ HTS SMES based on multi-scale model and artificial neural networks,” *IEEE Transactions on Magnetics,* vol. 54, no. 11, pp. 1-5, 2018.
[209] H. Pan, and G. X. Shen, “Application of artificial neural network methods in HTS RF coil design for MRI,” *Concepts in Magnetic Resonance Part B: Magnetic Resonance Engineering: An Educational Journal,* vol. 18, no. 1, pp. 9-14, 2003.
[210] L. S. Richard, R. Bonifetto, S. Carli *et al.*, “Artificial Neural Network (ANN) modeling of the pulsed heat load during ITER CS magnet operation,” *Cryogenics,* vol. 63, pp. 231-240, 2014.
[211] D. P. Kingma, and J. Ba, “Adam: A method for stochastic optimization,” *arXiv preprint arXiv:1412.6980*, 2014.
[212] D. C. Liu, and J. Nocedal, “On the limited memory BFGS method for large scale optimization,” *Mathematical programming,* vol. 45, no. 1, pp. 503-528, 1989.
[213] S. Karsoliya, “Approximating number of hidden layer neurons in multiple hidden layer BPNN architecture,” *International Journal of Engineering Trends and Technology,* vol. 3, no. 6, pp. 714-717, 2012.
[214] M. J. Berry, and G. S. Linoff, *Data mining techniques: for marketing, sales, and customer relationship management*: John Wiley & Sons, 2004.
[215] L. P. Swiler, M. Gulian, A. L. Frankel *et al.*, “A Survey of Constrained Gaussian Process Regression: Approaches and Implementation Challenges,” *Journal of Machine Learning for Modeling and Computing,* vol. 1, no. 2, 2020.
[216] C. E. Rasmussen, and C. K. Williams, “Gaussian Processes for Machine Learning Cambridge,” *MA: the MIT Press.[Google Scholar]*, 2006.
[217] A. J. Smola, and B. Schölkopf, “A tutorial on support vector regression,” *Statistics and computing,* vol. 14, no. 3, pp. 199-222, 2004.
[218] L. Breiman, J. H. Friedman, R. A. Olshen *et al.*, *Classification and regression trees*: Routledge, 2017.
[219] J. L. Bentley, “Multidimensional binary search trees used for associative searching,” *Communications of the ACM,* vol. 18, no. 9, pp. 509-517, 1975.

[220] Z. Wen, H. Zhang, and M. Mueller, “Sensitivity analysis and machine learning modelling for the output characteristics of rotary HTS flux pumps,” *Superconductor Science and Technology,* vol. 34, no. 12, pp. 125019, 2021.

[221] J. Schmidt-Hieber, “Nonparametric regression using deep neural networks with ReLU activation function,” *The Annals of Statistics,* vol. 48, no. 4, pp. 1875-1897, 2020.

[222] I. A. Cruz, W. Chuenchart, F. Long *et al.*, “Application of machine learning in anaerobic digestion: Perspectives and challenges,” *Bioresource Technology,* vol. 345, pp. 126433, 2022.

[223] H. Akaike, “A new look at the statistical model identification,” *IEEE transactions on automatic control,* vol. 19, no. 6, pp. 716-723, 1974.

[224] G. Panchal, A. Ganatra, Y. Kosta *et al.*, “Behaviour analysis of multilayer perceptrons with multiple hidden neurons and hidden layers,” *International Journal of Computer Theory and Engineering,* vol. 3, no. 2, pp. 332-337, 2011.

[225] I. Choldun, J. Santoso, and K. Surendro, "Determining the number of hidden layers in neural network by using principal component analysis." pp. 490-500.

[226] D. Stathakis, “How many hidden layers and nodes?,” *International Journal of Remote Sensing,* vol. 30, no. 8, pp. 2133-2147, 2009.

[227] T. Vujicic, T. Matijevic, J. Ljucovic *et al.*, "Comparative analysis of methods for determining number of hidden neurons in artificial neural network." p. 219.

[228] D. J. Griffiths, "Introduction to electrodynamics," American Association of Physics Teachers, 2005.

[229] Z. Wen, H. Zhang, M. Tian *et al.*, “A statistical model for the design of rotary HTS flux pumps based on deep-learning neuron network,” *Superconductivity,* vol. 3, pp. 100017, 2022.